Keele University

Computer modelling of optical materials for laser applications: rare earth doping in $YLiF_4$ and $BaMgF_4$

A thesis submitted for the degree of Doctor of Philosophy in Chemistry

Thomas Edward Littleford

Keele University

June 2014

SUBMISSION OF THESIS FOR A RESEARCH DEGREE

Part I. DECLARATION by the candidate for a research degree. To be bound in the thesis

Degree for which thesis being submitted: Doctor of Philosophy in Chemistry
Title of thesis: Computer modelling of optical materials for laser applications: rare earth doping in $YLiF_4$ and $BaMgF_4$

Date of submission: 26th September 2013
(Date of submission must comply with Regulation 2D)
Original registration date: 28th September 2009

Name of candidate: Thomas E. Littleford
Research Institute: Research Institute for the Environment, Physical Sciences and Applied Mathematics
Name of Lead Supervisor: Dr Robert A. Jackson

I certify that:
(a) The thesis being submitted for examination is my own account of my own research.
(b) My research has been conducted ethically. Where relevant a letter from the approving body confirming that ethical approval has been given has been bound in the thesis as an Annex.
(c) The data and results presented are the genuine data and results actually obtained by me during the conduct of the research.
(d) Where I have drawn on the work, ideas and results of others this has been appropriately acknowledged in the thesis.
(e) Where any collaboration has taken place with one or more other researchers, I have included within an Acknowledgments section in the thesis a clear statement of their

contributions, in line with the relevant statement in the Code of Practice (see note).

(f) The greater portion of the work described in the thesis has been undertaken subsequent to my registration for the higher degree for which I am submitting for examination.

(g) Where part of the work described in the thesis has previously been incorporated in another thesis submitted by me for a higher degree (if any), this has been identified and acknowledged in the thesis.

(h) The thesis submitted is within the required word limit as specified in the Regulations.

Total words in submitted thesis (including the text and footnotes, but excluding references and appendices) is approximately 50,000.

Signature of candidate ..... Date .....

Note Extract from Code of Practice: If the research degree is set within a broader programme of work involving a group of investigators particularly if this programme of work predates the candidates registration the candidate should provide an explicit statement (in an Acknowledgments section) of the respective roles of the candidate and these other individuals in relevant aspects of the work reported in the thesis. For example, it should make clear, where relevant, the candidates role in designing the study, developing data collection instruments, collecting primary data, analysing such data, and formulating conclusions from the analysis. Others involved in these aspects of the research should be named, and their contributions relative to that of the candidate should be specified *(this does not apply to the ordinary supervision, only if the supervisor or supervisory team has had greater than usual involvement).*

Abstract

In the field of solid-state laser materials, $YLiF_4$ and $BaMgF_4$ are two actively researched systems, with $YLiF_4$ having been shown as a viable laser source. $BaMgF_4$ is less developed. The work presented here provides an atomistic computational chemistry study into the two materials.

A introduction to the field of optical materials and computational chemistry is given before a detailed description of the atomistic methodologies is provided. The work utilises the widely used and studied methods of this field. The interionic interactions are modelled using the pair-wise approximation, a Coulomb interaction for the long-range interaction, which is summed using an Ewald summation, and a Buckingham potential for the short-range interactions. Electronic polarisability of the fluoride ions is included through a core-shell model coupled with a spring. Energy minimisation of the lattice is achieved through geometry optimisation and the resulting structures reproduced the reported structure of $YLiF_4$ and $BaMgF_4$ to within 2%.

The intrinsic defect properties of the two materials are calculated through the Mott-Littleton method. For $YLiF_4$, the Frenkel defect energies were found to be lower than the Schottky energies, with the two lowest energy defect formations being a F Frenkel and a Li Frenkel. Thermal expansion coefficients of the lattice were also calculated using Free Energy minimisation techniques. For $BaMgF_4$, the Schottky defect energies are of similar magnitude to the Frenkel defects. Within the Frenkel defects the fluorine and magnesium Frenkel are 2.5 times smaller than the barium Frenkel defect. In comparison to the intrinsic defect energies for $YLiF_4$, the defect energies are greater.

To utilise these material in solid-state laser devices, the addition of rare earth dopant

ions to the lattice is needed, as it is these ions that provide the electronic structure required for the laser action. The solution energies for the incorporation of the rare earth ions were calculated at both cation sites in both materials. In $YLiF_4$ the dopant ions will dope at the yttrium site. In $BaMgF_4$, the doping site varies across the rare earth group, as does the charge compensation method. For ions La^{3+} to Nd^{3+} the preferred site is barium with a magnesium vacancy. The remaining rare earth ions dope at the magnesium site with either a barium or magnesium vacancy.

An attempt is made to calculate the doping limit of rare earth ions in each lattice. This is an important value to obtain so that a comparison across the rare earth ions can be made. It also allows different host lattices to be compared. Rare earth dopant solubility is of importance because, while for many devices the doping level is small, ideally the dopants should be homogenous throughout the host lattice and not clustered. In the case of $YLiF_4$ the doping limit was calculated to be between 0.69% for La^{3+} and 1.51% for Yb^{3+}. $BaMgF_4$ gives smaller maximum doping limit, and in some cases negative values, implying the lattice is less accepting of rare earth ions than $YLiF_4$.

The likelihood of transition metal ion defects being incorporated into a Yb:$YLiF_4$ lattice is studied as a result of the work into $YLiF_4$ as a laser cooling device. A new potential set was derived for various transition metal fluoride ions. The results suggest that the 1+ and 3+ transition metal ions are most likely to be incorporated into the lattice with Cu^{1+} and Ti^{3+} being the most likely.

The surface properties are also modelled using the same model parameters as in the bulk studies. Surface and attachment energies are given for the low index surfaces and these are used to predict surface morphologies. For $YLiF_4$ the equilibrium morphology is dominated by the (112) and (011) surfaces and the growth morphology by the (001) and (120) surfaces. For $BaMgF_4$ the morphologies are dominated by the (010) and (110) surfaces.

The segregation of rare earth dopants to the surfaces is calculated by comparing the difference between defect energy at the surface and in the bulk. For a number of surfaces of $YLiF_4$ a driving force for segregation is found. Simulation cells are scaled

to consider concentration effects of rare earth dopants at the surfaces. A Perl script is used to automate the creation of every configuration of the dopant ions at various concentrations. The lowest energy configurations are used to predict how the surface energy of each low index surface would change with the presence of dopant ions. This is used to predict the impact on surface morphology. In $YLiF_4$ the (110), (112), (012), (221), (021), (122) and (010) surfaces showed a reduction in surface energy with the presence of some of the rare earth ions. For $BaMgF_4$ all rare earth dopants segregated to the three surfaces studied, with the segregation force to the (010) surface the greatest. There is a correlation between the ionic radius mismatch between the lattice site and the rare earth ion, and the degree of segregation.

The content of this thesis is an important contribution to the research of these two materials, which should aid further research, both computational and experimental, into them.

Contents

List of Figures

List of Tables

Acknowledgements

This work would not have been possible without the following people.

Firstly, Rob Jackson for giving me the opportunity to study for a PhD and for his supervision and expertise during the work. Without his patience and guidance this thesis would not have been possible. I also need to thank Rob for the many debates about current affairs! For funding the research a huge thank you goes to AWE and all those there in the Computational Chemistry Team including Dave Plant.

I also need to thank Mark Read for the many discussions about the research while he was working at AWE. He is now based at the University of Birmingham. The surface work was aided by Steve Parker at the University of Bath, who offered advice with the METADISE code. Also, David Cooke at the University of Huddersfield gave suggestions, and provided his Perl Script, as a starting point to devise a defective surface energy methodology. To these three people I am grateful.

I have shared an office with a number of people during the course of the work at Keele University, and so thanks go to all those who have been on this journey with me, being a source of laughter, motivation and support.

Thanks also go to Philippa Douglas, Vicky Salmons, Kirsty Levantini, Kate Kirk for keeping me sane during the more difficult times of the research.

Finally, thank you to my Mum, Dad and the rest of the family for their continued support.

Thesis aims and outline

This thesis provides a detailed computational chemistry study into two, actively researched, solid-state laser materials $YLiF_4$ and $BaMgF_4$. The aim is to provide insight into the dopant chemistry of these materials and its impact on laser application. In detail, the thesis aims to:

a) produce an accurate bulk computer model of the systems,
b) calculate intrinsic and extrinsic defect energies,
c) confirm where the optically active rare earth ions will dope within the lattice,
d) calculate the solubility limits of the dopants,
e) extend the model parameters to produce a working surface model,
f) predict undoped surface morphologies,
g) calculate segregation energies of defects,
h) predict dopant effects on surface morphology,
i) identify any trends across the rare earth lanthanide series,
j) relate the results to the application of solid-state lasers,
k) evaluate the energies involved in impurity contamination in $YLiF_4$ as a laser cooling crystal.

The structure of the thesis is now given.

Chapter 1 introduces the field of computational chemistry and the main methodologies used in the field. An introduction to solid-state fluorides and optical materials, including the details of laser operation, is also given.

Chapter 2 provides the details behind the field of atomistic bulk modelling; introducing the code GULP, the mathematical description of the interactions between ions, Ewald summation, energy minimisation techniques and methods for calculating defect energies.

Chapter 3 describes atomistic surface modelling; introducing the code METADISE, surface classifications, energies, defects and morphologies and then outlining how defective surface energies can be predicted.

Chapters 4 and 5 provide the results of the modelling studies into the $YLiF_4$ and $BaMgF_4$. The results are presented by technique used in the same order as chapters 2 to 3.

Chapter 6 concludes the studies and outlines future work.

Chapter 1

Introduction

1.1 Computer modelling

Computational chemistry is the use of computer science to aid in the understanding of solids, molecules and reactions. It uses the mathematics and theorems of theoretical chemistry and incorporates them into computer programmes that allow structures and properties to be simulated. A good computer model of a material can be used to understand an experimentally seen occurrence, predict defect properties and even predict the structure of other materials.

The mathematics used within the field of computational chemistry is nothing new, however, it is only since the computer revolution that the field has grown due to the increasing computer power that enables more complex and useful simulations to be done. For example, some of the earliest work in computer modelling was into simple, ionic materials such as alkali halides [2]. Today far more complex simulations are carried out including phenomena such as, for example, oxygen adsorption on zirconia surfaces [3] and band-gap states of metal oxides [4] .

Computational chemistry studies aid experimental work rather than replace them. A computer simulation study can typically be completed with reduced cost in terms of both time and money. The results can then be used by experimentalists to provide them with viable structures, defect properties and other information as to ensure they concentrate on those structures that showed viability during the modelling stage. Take

for example, the study of the development of nuclear clocks by Schumm *et al* 2012. The cost of the isotope of thorium they are using is around $50,000 per milligram, so a modelling study was carried out prior to experimental work [5]. Another example is the field of nuclear research into UO_2 and PuO_2, where it is also cheaper and safer to model. An example of such work can be found in [6].

There are limitations to computational studies. Firstly, with all modelling techniques there are a number of approximations that have to be made. Any approximation must be limited and checked to ensure it does not produce unphysical outcomes. In most cases the approximations have been used for many years and have been validated across a range of materials to ensure they do not affect the results beyond acceptable error. Another limitation is that a model is always the ideal case, which may not be easy to reproduce at the experimental level through synthesis.

All models require the physics of the system to be described mathematically such that it reproduces the known structure. This means the interactions between the atoms in the system need to be described. There are a number of different techniques available to a computational chemist to achieve this all of which offer varying degrees of accuracy, type of result and computational expense. In general, it is possible to model the interatomic interactions in two ways; classically or quantum mechanically.

1.1.1 Atomistic simulations

In the classical approach force-fields are used with classical physics such as Coulombic and Van der Waals interactions. This approach takes no explicit account of the electronic structure of the system; it treats the ions as charged units. This has the disadvantage that no detail about electronic structure can be obtained, which may be of importance in certain materials if the phenomenon the model is attempting to simulate is due to electronic effects. However, because the technique uses relatively simple mathematics interacting between discrete units the computational cost is extremely low. This type of modelling can reproduce structures, calculate defect properties and lattice migrations and can be extended to look at surfaces and grain boundaries. It is usually used

in solid-state modelling because of the periodic nature of these materials. It should be noted that this technique requires experimental data on the material in order for the interatomic potentials to be empirically fitted. This adds the condition that the model can only be as good as the experimental data it is fitted to. Finally, classical approaches can also be taken to model non-static systems through molecular dynamics and Newton's Laws of Motion.

Some of the first atomistic calculations were done to determine Schottky defect energies in sodium chloride structured materials by Boswara and Lidiard [2, 7]. These, like all of the early simulated work, were highly ionic systems with simple structures [8]. In the 1970s transition metal oxides were also investigated [9, 10] where the major pioneering work in the field was carried out by the Harwell Laboratory. The focus was predominantly on uranium dioxide, UO_2, defect energies and fission products [11, 12, 13], but the methodologies developed are still used widely today and form a large part of this thesis.

Simulations of surfaces were a later development with the first fully developed code being MIDAS [14]. While this code allowed the modelling of a wide range of systems they were all limited to the condition of charge neutral surfaces. Defects within surfaces could only be modelled with the later CHAOS code [15]. Modern surface codes such as GULP/GDIS [16] and METADISE [17] utilise the fundamentals of these earlier codes.

1.1.2 Electronic simulations

It is also possible to model a system using its electronic structure. This requires the use of quantum mechanics. The technique requires the electronic structure of the whole system to be calculated, which for large systems can only be done with an approximation method such as Hartree Fock (HF) or Density Functional Theory (DFT). Electronic structure modelling is extremely computationally expensive but it can produce properties of the material that atomistic modelling cannot, such as Density of States (DOS) and charge density. There are two approaches to electronic modelling that describe the atomic orbitals in one of two ways; Plane Wave and Gaussian Basis

Set. Finally, electronic structure modelling can be done semi-empirically or *ab intio* (meaning from first principles of quantum mechanics).

1.1.3 Hybrid methods

The final method for modelling is a hybrid of the two previously mentioned techniques. In this approach a region around the defect centre, that is of interest, is modelled using an electronic structure method, and the remaining bulk is modelled using atomistic methods. This is a relatively new technique and is still in its infancy, however, it has been used successfully for a number of materials using the CHEMSHEL code [18, 19]. For examples see [20, 21].

1.1.4 Comparison

These three approaches for creating a model offer increasing levels of complexity (and computational time), however, they should not be seen as increasing in accuracy or suitability. Each chemical problem will require a different approach and the type of approach taken to modelling should be considered carefully. For example, if the simulation is to determine a simple intrinsic defect energy, choosing a hybrid or electronic approach is excessive. Alternatively, if the property under examination is a result of electronic effects an electronic (or hybrid) approach is required. Another important consideration is scalability. Atomistic methods scale to consider simulations of many atoms far easier than electronic methods. Typically an atomistic approach can consider thousands to tens of thousands of atoms in one simulations, whereas with an electronic approach the scale of the simulation would be limited to just tens to hundreds of atoms.

1.2 The solid state

Solid-state chemistry deals with the structure and properties of substances that have been cooled into a solid form of regular repeating arrays. X-ray diffraction is usually used to determine the structure of inorganic crystals because the crystals, whose atoms are spaced at a distance of the same order of magnitude as X-ray wavelengths, acts as a diffraction grating, and therefore the resulting diffraction pattern can be used to calculate the internal atomic positions. Due to the periodicity of crystals, symmetry can be used to define a unit that when repeated infinitely in all directions reproduces all the atomic positions of the crystal. This repeating unit is called the unit cell.

1.2.1 Space groups and crystal classification

The unit cell is expressed as three lengths ($a,\ b,\ c$), three angles (α, β, γ), and the minimum atomic coordinates needed to reproduce the structure. This leads to seven crystal systems as listed in Table 1.1. These seven classes of crystals can be of four different types, namely, primitive (**P**), body-centred (**I**), face-centred (**F**) or face-centred (**C**), where they have the following properties.

1. The primitive cell (**P**) has a lattice point at each corner.
2. The body-centred cell (**I**) has a lattice point at each corner and one in the centre of the cell.
3. The face-centred cell (**F**) has a lattice point at each corner and in the centre of each face of the cell.
4. The face-centred cell (**C**) has a lattice point at each corner, and one in the centres of one pair of opposite faces.

Combining the seven classes with the four types, the 14 Bravais lattices are produced. It is not possible to have all types in every class due to the symmetry requirements, hence there are only 14 Bravais lattices. The work in deducing these space lattices was first done by Frankenheim in 1835 (who said there were 15 space lattices), however,

System	Unit Cell
Triclinic	$\alpha \neq \beta \neq \gamma \neq 90°$ $a \neq b \neq c$
Monoclinic	$\alpha = \gamma = 90°$ $\beta \neq 90°$ $a \neq b \neq c$
Orthorhombic	$\alpha = \beta = \gamma = 90°$ $a \neq b \neq c$
Trigonal	$\alpha = \beta = \gamma \neq 90°$ $a = b = c$
Hexagonal	$\alpha = \beta = 90°$ $\gamma = 120°$ $a = b \neq c$
Tetragonal	$\alpha = \beta = \gamma = 90°$ $a = b \neq c$
Cubic	$\alpha = \beta = \gamma = 90°$ $a = b = c$

Table 1.1: The seven crystal systems.

Removed for copyright reasons

Figure 1.1: The 14 Bravais lattices. Taken from [23]

.

the system is now named after Bravais who noticed a mistake in Frankenheim's work pointing out that there are only 14 lattices [22]. Figure 1.1 shows the 14 Bravais lattices.

If the full symmetry of the crystal is accounted for there are 32 point groups. A point group is a set of symmetry operations around a fixed point that generates the other points. When this is combined with the Bravais lattices, removing those groups that break symmetry constraints, there are 230 space groups that a crystal can take. It is these space groups that are used to, firstly, describe the system in the smallest amount of detail, and secondly, reduce the terms in any model to increase computing efficiency.

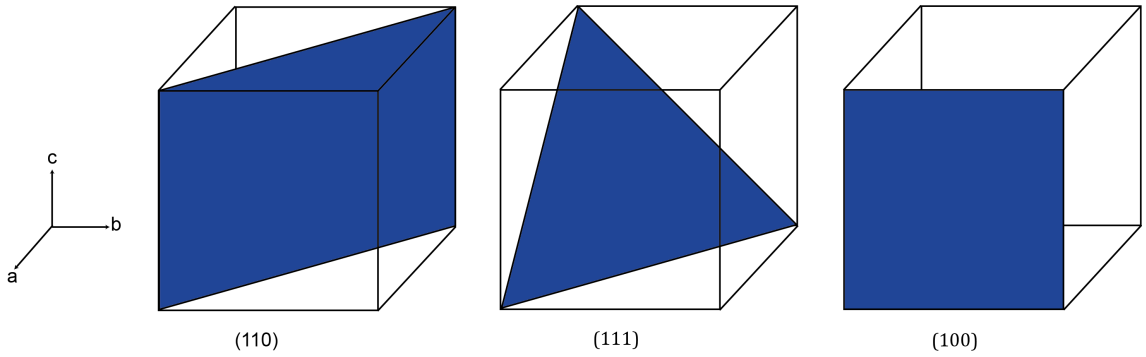

Figure 1.2: Example Miller indices. Shown are the (110), (111) and (100) surfaces. The origin is taken from the rear left corner.

1.2.2 Miller indices

Planes within the lattice are defined using the method popularised by W.H. Miller, and hence are known as Miller indices. In Figure 1.2 the first example is the (110) plane. The Miller index is the reciprocal of the intercept on the three unit cell vectors. Thus (110) intercepts **a** at 1, **b** at 1, and does not intercept **c**. In general terms, the Miller index is given by (hkl) where $\frac{a}{h}$, $\frac{b}{k}$, and $\frac{c}{l}$ are the intercepts with the unit cell. The location of the origin is required for the Miller index to be explicit as the intercept position is measured from the origin. Indices may be defined backwards from the origin resulting in a negative Miller index, which is written as $\bar{h}\bar{k}\bar{l}$. In surface modelling, it is sometimes necessary to calculate the perpendicular spacing between parallel Miller indices. These are known as d-spacings (d_{hkl}).

1.2.3 Bonding

Crystals can be held together through a number of types of bonding including metallic, covalent or ionic. In metallic bonding the regular array of metal cations are surrounded by a 'sea' of electrons occupying the space between the cations. The electrons are free to move providing the properties that characterise metals. Covalent bonds share electrons between two atoms resulting a strong directional bond.

The crystal systems considered in this thesis are all ionic. Ionic bonding forms between two oppositely charged ions. There is an attractive electrostatic force between

the cation and anion, which is given by the Coulomb Law:

$$F \propto \frac{q_1 q_2}{r^2} \tag{1.1}$$

where q_1 and q_2 are the charges on the ions and r is the interionic distance. There is also a repulsive force between like-charge ions. The ionic bond is non-directional and is long range with an inverse proportional relationship with ionic distance. In ionic crystals, the ions pack together such to maximise the Coulombic attraction while minimising the repulsion. The bonding within the systems studied in this thesis and how they are modelled is discussed in detail in Chapter 2.

1.2.4 Defects

Crystals as discussed above, with each ion occupying the correct lattice position in a regular array and aligned with the correct symmetry as defined by the spacegroup, can only exist in thermodynamic equilibrium at zero Kelvin. Any real-world crystal (*i.e.*, a crystal above 0 K) will contain some deviations from this ideal due to entropy.

All systems tend to increase their entropy and because a perfect crystal has low entropy, as it is highly ordered, the presence of defects increases the disorder and increases the entropy. Thus, the complete randomisation of the lattice ions would be the highest entropy state, however, the creation of defects requires energy and therefore, at any temperature, an equilibrium is established between the two terms to minimise the free energy. This can be seen with the Gibbs free energy equation, with the defect formation energy increasing the enthalpy term, H, and the increase in disorder increasing the entropy term, S:

$$G(p, T) = H - TS \tag{1.2}$$

There are a number of types of defects that can occur within crystals and they can be grouped into categories based on the dimensions of the defect. Within each category there are a large number of types of defects.

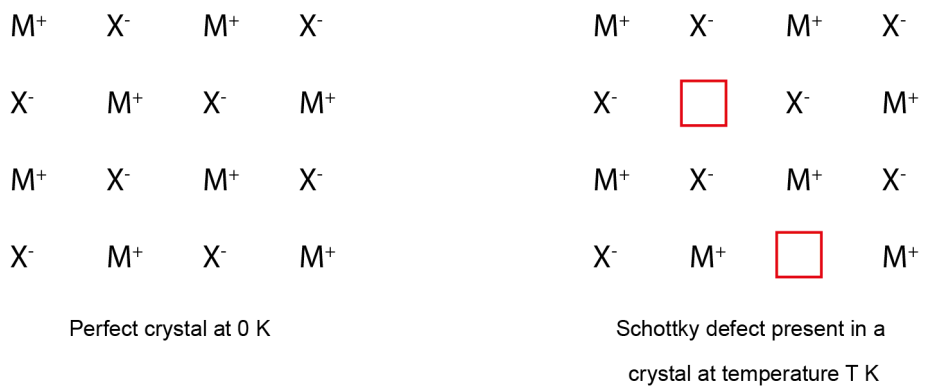

Figure 1.3: Diagram showing a perfect lattice at zero Kelvin on the left and a lattice containing a Schottky defect on the right. A cation and an anion vacancy is created to ensure charge neutrality. Adapted from [1].

1. **Point defects** - intrinsic and extrinsic

2. **Line defects** - dislocations

3. **Planar defects** - stacking faults, surfaces, grain boundaries

This thesis will only consider point defects and one type of planar defect - surfaces - however, all three groups are important and will be discussed briefly here.

Point defects are any defects that extend no further than a few interatomic distances [24] and are divided into two groups - intrinsic and extrinsic. Intrinsic point defects are imperfections that result from thermal effects and do not affect the chemical composition of the system. Vacant cation or anion lattice sites are one form of imperfection that can occur. Due to the requirement for charge neutrality stoichiometric units of vacancies must be created and these are known as Schottky defects [25, 26] (Figure 1.3). For example, in a MX_3 system the Schottky defect is a cation vacancy with three anion vacancies.

The second type of intrinsic point defect is the Frenkel defect [27] (Figure 1.4). This is created by an ion moving from its lattice site to an interstitial site leaving a vacancy. Ionic size and lattice spacing are extremely important in determining the concentration of Frenkel defects.

The presence of defects affects the physical properties of the system, for example, vacancies and interstitials can migrate within the lattice increasing conductivity. In

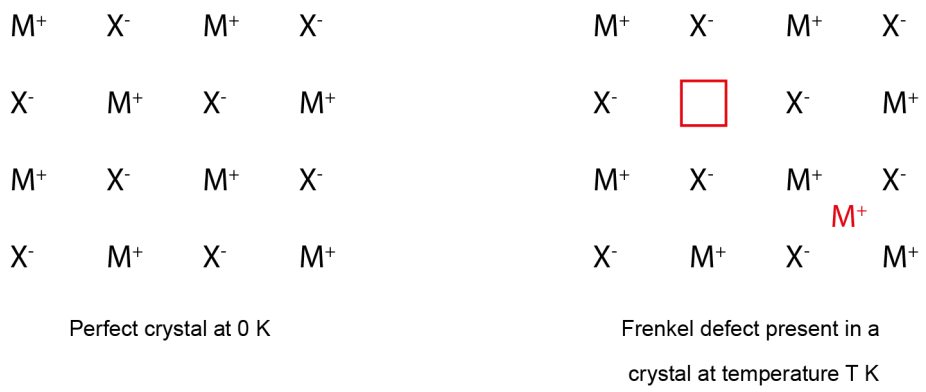

Figure 1.4: Diagram showing a perfect lattice at zero Kelvin on the left and a lattice containing a Frenkel defect on the right. A cation vacancy is created when the ion moves to a non-lattice interstitial site. Adapted from [1].

general, if the anion and cation differ in size, Frenkel defects are more common and the opposite is true for Schottky defects. However, crystallography is important in understanding the defects present too, as in close packed systems with little space in the lattice, Frenkel disorder is restricted due to the high energy of forming interstitial ions.

One final type of intrinsic defect that is extremely unlikely to occur in ionic systems, such as those in this work due to electrostatic repulsion, is antisite disorder. This is where two atoms within the lattice switch site.

Extrinsic point defects are different from intrinsic ones as they require a change in the chemical composition of the lattice, either through non-stoichiometry or the presence of impurity ions. These impurity ions may be as a result of contamination during crystal growth or purposely incorporated into the lattice to change the properties of the system in a useful way. The latter process is known as doping and forms the main focus of the defect simulations in this thesis.

Line defects are an extended defect that occur when ions are misaligned or vacancies form in a line and are known as dislocations. There are many types of dislocations, however they have not been studied in this work so no further discussion will be given here.

Planar defects are another type of extended defect, however, they occur in 2-dimensions. The most obvious of these is a surface, where the regular infinite array of

ions is only present in 2-dimensions and therefore, the ions at the surfaces are in a very different environment to the rest of the crystal. Two other planar defects include grain boundaries, which are the boundaries formed between seeds during crystal growth, and stacking faults, which is when a stack is out of sequence in the packing.

Defect formations are described throughout this thesis using the standardised Kröger-Vink notation [28]. In this notation the lattice site and charge on the defect is included and is given in general terms by:

$$X_s^c$$

where X is the species, s is the site, and c is the overall charge. To illustrate the types of notation consider the following examples in CaF_2.

Ca_{Ca} a calcium ion at a calcium lattice site, which is charge neutral.

$Ca_i^{\cdot\cdot}$ a calcium ion at an interstitial site, which has a charge of plus 2 (indicated by two $\cdot$).

$V_{Ca}^{\prime\prime}$ a calcium vacancy, which has a charge of minus 2 (indicated by two $\prime$). Note that V refers to both a vacancy and vanadium.

Kröger-Vink notation can be combined to form defect formation reactions. The reactions for Schottky and Frenkel defects, as discussed above, for a MF_3 system are now given.

$$\text{Schottky: } M_M + 3F_F \rightarrow V_M^{\prime\prime\prime} + 3V_F^{\cdot}$$
$$\text{Frenkel: } M_M + V_i \rightarrow M_i^{\cdot\cdot\cdot} + V_M^{\prime\prime\prime}$$

1.3 Optical materials

This research is concerned with modelling solid-state inorganic crystals that have been shown, or are actively being researched, as possible materials for use in an optical application. Examples of optical applications include lasers, scintillators and communication devices. In all of these examples the key to their useful optical properties is due to defects and impurities within the crystal structure.

Highly coloured naturally found crystals, such as Blue John, only have their intense colour due to defects within the lattice. Blue John is CaF_2 that is coloured due to the presence of electrons trapped at vacant F^- sites. Defects turn this simple crystal into a purple-blue attractive crystal that is used for ornamental purposes. This example shows how defects within a crystal can change its properties and value. For more technical applications it is often the addition of dopant ions to the lattice that produces systems with desirable optical properties for use in applications. The systems studied in this thesis are being researched as laser sources, where the laser-active dopants are rare earth ions. In most solid-state lasers the dopants used are either rare earth or transition metal ions.

It is the process of finding doped crystals that provide an electronic structure of practical use that drives this research. Being able to model accurately such materials and provide an understanding of their structures is vital to the continued search for better more tunable solid-state lasers and other optical devices.

1.3.1 Lasers

Laser stands for Light Amplification by Stimulated Emission of Radiation, although was originally termed optical maser, where maser was the process to describe earlier work involving amplification in the microwave region [29]. The theoretical origins of the laser came from the emerging quantum mechanical view of the atom in the early 1900s. The first working laser, however, was a pulsed ruby laser demonstrated by Maiman in 1960 [30], which was made from a synthetic ruby and produced pulses of red laser light with a wavelength of 694 nm. Around the same time a helium-neon gas laser [31] was

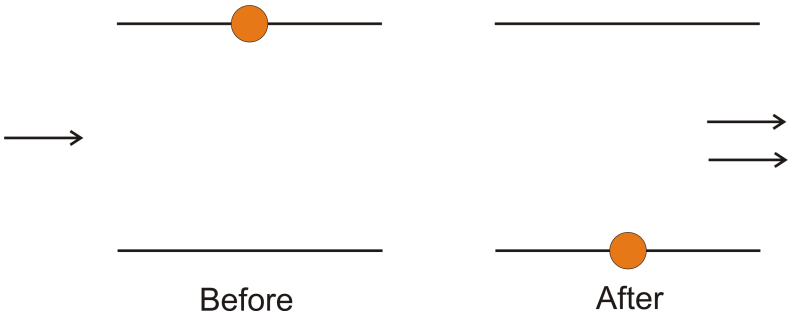

Figure 1.5: Diagram of stimulated emission. The incoming photons 'stimulates' the emission of the photon into the same spatial mode, resulting in amplification.

also demonstrated, which produced laser light with a wavelength of 633 nm. Lasers have a number of properties that make them useful for a variety of applications. They produce a narrow coherent beam of light that can propagate over large distances with little divergence and can be emitted as a continuous beam or pulsed.

1.3.2 Stimulated emission

The principle behind the laser operation is stimulated emission. To explain stimulated emission one must first define spontaneous emission. Spontaneous emission occurs within a lattice, where an excited ion in a high-energy state decays, after some time, to a lower energy level, resulting in a release of a photon. The emitted photon is in a random spatial direction. In the stimulated emission process, the photon emission is stimulated by incoming photons if they have a suitable energy (See Figure 1.5). The photon is emitted into the same spatial direction as the incoming photon, which results in the amplification of the incoming radiation [32].

1.3.3 Population inversion

At thermal equilibrium there will be a Boltzmann distribution of electrons, which populates the ground-state. This reduces the rate of stimulated emission and even prevents it unless there are a higher number of laser-active ions in a higher energy state than are in the ground-state. This can be achieved through pumping the system with energy and causing what is termed a population inversion. There are a number of ways

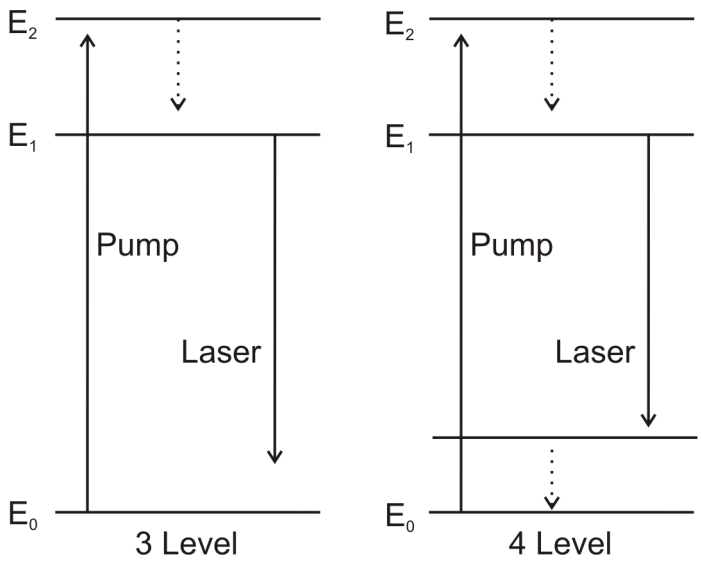

Figure 1.6: Diagram showing the differences between a 3 and 4 level laser system. The 4 level system has the lower laser level above the ground state unlike the 3 level system, resulting in a number of advantages.

to introduce energy into the system, with the most common being electrical discharge and optical irradiation [32].

In a system that contains two energy levels, E_1 and E_0, population inversion can never be reached. This is because the transition $E_{0\rightarrow1}$ would equal $E_{1\rightarrow0}$, and thus the two level would be equally populated. Laser systems, therefore, require at least a three-level system, where the pumping energy raises the ions into a high state, E_2, before decaying rapidly into a metastable state, E_1. The population inversion is created between the ground state, E_0 and the metastable state, E_1 as shown in Figure 1.6. An example of such a laser is the ruby laser [30]. A 4-level system has the lower laser level above the ground state, which quickly depopulates through non-radiative decay. The advantages of a 4-level system, over a 3-level, are that a lower threshold pump power is required and reabsorption of laser radiation is avoided. Nd:YAG (Nd^{3+}:$Y_3Al_5O_{12}$) is an example of such a laser [33]. In both cases the pumping level, E_2, can in practice be a band of close energies that all decay to the same metastable level. This increases the efficiency of the pumping.

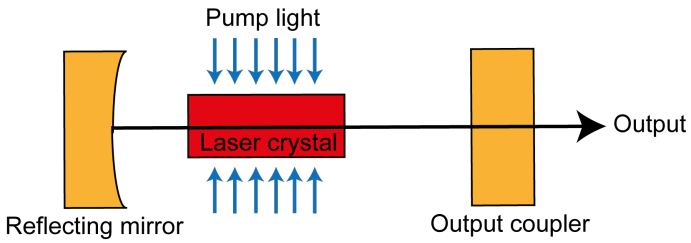

Figure 1.7: A laser schematic showing the basic set-up of a solid-state laser. Light oscillates between the two mirrors passing through the (optically pumped) laser crystal, resulting in the amplification of the light.

1.3.4 Solid-state lasers

Solid-state lasers are one type of laser system. These consist of doped, usually large band gap, materials where it is dopant ions that provide the laser transitions. The host lattice is still however important since it modifies the energy levels of the dopant ions, and the physical properties such as thermal conductivity affect the power levels at which the laser can operate. Figure 1.7 shows a schematic of a typical solid-state laser. Light circulates between the two mirrors and passes through the laser crystal. This light would normally become weaker on each cycle, however, the laser crystal (the gain medium) amplifies the light through stimulated emission. Pumping of the laser crystal is achieved either by an electrical current or through optical pumping with a lamp [34]. The latter of these is most common in rare earth lasers, like those studied in this work. Although excitation through flash lamps is cheap and can provide high powers, it has disadvantages because of the moderate lifetimes of the lamps and the strong thermal effects on the crystal [35]. The thermal effects can be reduced through pulsing of the lamp. It is crucial to ensure as much radiation as possible goes into the laser medium. Thus the laser material is often rod shaped and placed next to the flash lamp inside a container with highly reflective walls [36].

This type of laser is widely used in a variety of applications with one of the most common being Nd:YAG (Nd^{3+}:$Y_3Al_5O_{12}$), which produces a strong laser transition from $^4F_{3/2}$ to $^4I_{11/2}$ producing a wavelength of 1064 nm. (The origin of these levels is discussed in Section 1.3.8). Optically pumping the system with a lamp of wavelength 808 nm excites the electrons within the doped ion to a higher metastable state. On

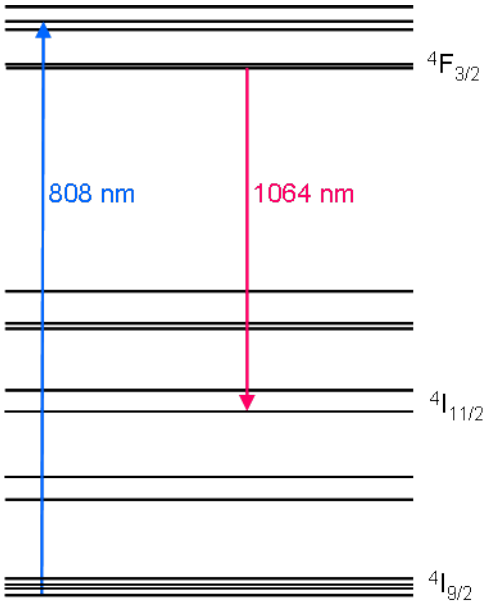

Figure 1.8: An example of laser operation. System shown is the typical operation of Nd:YAG. Pumping wavelength is 808 nm and the laser transition is 1064 nm.

relaxation of these electrons the emitted light is the laser action. This laser is a 4-level type laser as the lower laser level is sufficiently above the ground-state to be empty at room temperature [36]. Both continuous wave and pulsed operation is possible. Figure 1.8 shows the electronic configuration for Nd:YAG, the pumping (808 nm) wavelength and the laser action of 1064 nm.

Another example of a solid-state laser is the ruby laser (Cr^{3+}:Al_2O_3). The laser-active dopant in this laser is Cr^{3+} and is typically doped to about 0.05% weight [34]. The lower laser level is at the ground-state, thus ruby is a 3-level laser system. The main laser transition is between ^2E and $^4A_2$. These energy states have crystal field notation because, for transition metal dopants, the crystal field splitting has a larger importance then the spin-orbit coupling in rare earth ions (see Section 1.3.8) [34]. Pulsed operation is the most common due to the pumping requirements of a three-level system. Figure 1.9 shows the energy levels involved in the ruby laser.

When considering a solid-state laser material, the properties of the laser crystal that are required are:

- a laser transition in the desired wavelength,
- a host lattice with high transparency in the laser transition and pumping region,

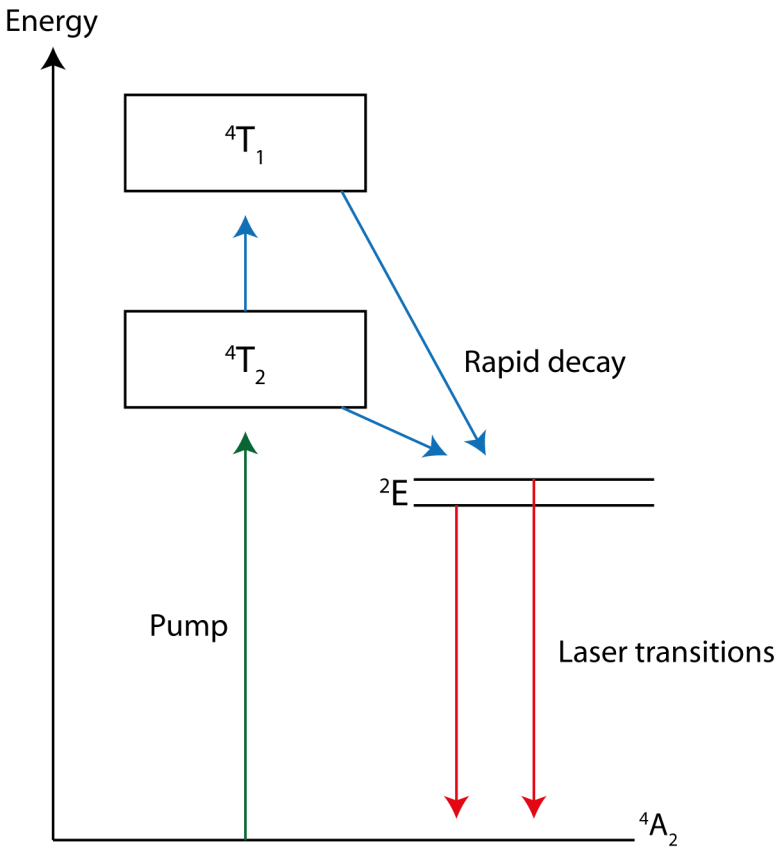

Figure 1.9: Schematic of the ruby laser showing: i) the energy levels of pumping from blue light ($^4T_1$) and from green light ($^4T_2$), ii) the metastable upper laser level, ^2E, and iii) the laser transitions back to $^4A_2$. Adapted from [34].

- an upper-state lifetime of length suitable for the laser type (*i.e.*, long for Q switched),
- a four-level system (see Section 1.3.3),
- a robust, chemically stable material with good thermal conductivity (to transfer pumping heat efficiently),
- a crystal which has good optical quality that can be cut and polished easily,
- and a host lattice with a high solubility of laser-active dopants with no tendency to cluster (see Section 1.3.10).

Within the laser operation there are a number of losses that have to be overcome and therefore there is a threshold gain coefficient that has to be reached for the laser action to proceed. One of the losses which occurs in solid-state lasers are Fresnel losses [34]. This is light that can be lost from the system from reflection at the laser medium - air interface. These can be minimised by, firstly coating the ends of the laser rod with antireflective coating, and secondly, by reducing the loss in a particular direction of polarisation through cutting the rod ends at the Brewster angle [34]. For Nd:YAG this angle is 61.2° [37] and is given generally by:

$$\theta_B = tan^{-1}\left(\frac{n_2}{n_1}\right) \tag{1.3}$$

where n_2 and n_1 are the refractive indices of the media. Cutting at this angle causes the laser output to be plane polarised. Other losses include scattering at the mirrors, diffraction around the mirror boundaries, transitions in the laser material other than the desired one, and scatting at defects within the crystal [34].

1.3.5 Gas laser

As well as solid-state lasers there are a wide variety of other types of lasers. This is one of the reasons why lasers are used in almost all industries as they are extremely versatile.

In comparison to solid-state laser media, gas lasers have a much lower density and therefore can only achieve a smaller population inversion, thus, gas lasers are usually large [35]. One advantage is their homogeneous nature and their efficient cooling. Gas lasers are usually excited within a gas discharge [35]. The following three brief examples demonstrate that the laser transition can take place between the energy levels of atoms, ions or molecules.

The helium-neon, HeNe, laser is a mixture of helium and neon in a 5 to 1 ratio [36]. The gas is contained in a narrow tube and a discharge is induced. The laser transition occurs between the energy levels of Ne (*i.e.*, an atomic gas laser). This laser is a 4-level type system but the details of the operation have many subtleties. A good description of the HeNe laser operation can be found in reference [34].

The helium-cadmium, HeCd, laser is an example of an ionic laser. The laser transitions take place between the electronic energy levels of the ion, thus ionisation has to occur first. Solid Cd metal is heated in a gas discharge to obtain a vapour. A process called Penning ionisation then takes place, which ionises and excites the Cd atoms through energy exchange with exited He atoms [36, 34]. This can be expressed as:

$$He^* + Cd \rightarrow (Cd^+)^* + e \tag{1.4}$$

where * indicates an excited state. The emission of an electron carries away any energy difference between the two excited states. Lasing takes place between Cd^* and the ground-state Cd^+, which then decays to Cd ground state with collisions at the tube walls. The lasing wavelengths are 325 nm and 442 nm [38].

The final example of a gas laser is the molecular carbon dioxide, CO_2, laser. This laser is one of the most important gas lasers as it is highly efficient and has high power output, making it possible to use the laser for application such as welding, cutting and weaponry [36]. The lasing transitions occur due to the energy levels resulting from the vibrational and rotational energy of the CO_2 molecule. The excitation of the CO_2 molecules takes places through an intermediate. The first vibrational level of nitrogen is very close to the asymmetric mode vibrational level of CO_2 and is used

as the intermediate [32, 38]. Laser transitions occur from this vibrational level to a range of other vibrational/rotational levels, with the strongest transition at 10.6 μm [38]. The high efficiency of this laser is due to a number of reasons. Firstly, the first excited state of nitrogen is 0.3 eV above the ground state, compared to the 20 eV for the HeNe laser, resulting in efficient pumping [34, 38]. Secondly, the excited nitrogen state is metastable, so once excited the nitrogen is highly likely to exchange its energy with CO_2 before relaxing back to the ground-state. Finally, helium is usually added to the system to aid in the transferring of heat and depopulating the lower laser levels [34, 38].

1.3.6 Liquid dye laser

Laser media can also be liquid based. Liquids are more homogeneous than solids and have a higher density of active atoms than gases making them a good laser medium. They also can be circulated for efficient cooling during operation. Liquid dye lasers are usually organic dyes dissolved in liquid solvents [35]. These solutions strongly fluoresce. An example is rhodamine 6G in ethanol [34]. The wide absorption band means optical pumping is usually used. Laser transitions occur between bands known as singlet states. These correspond to a total spin state of the molecule of zero. A detailed description of the energy levels can be found in reference [34].

1.3.7 Semi-conductor laser

As well as the doped, insulator solid-state laser, as discussed above, there are also semi-conductor lasers. These lasers are a type of solid medium laser in which population inversion is achieved by having a high density of electrons and holes [38]. This requirement means only a small region within the laser is active. The operation of semi-conductor lasers is very different to all other types considered. A detailed explanation can be found in reference [34]. Figure 1.10 shows the schematic of a simple gallium arsenide, GaAs, semi-conductor laser. The p-type GaAs and the n-type GaAs are shown, with dotted region between them the laser active zone. An external current

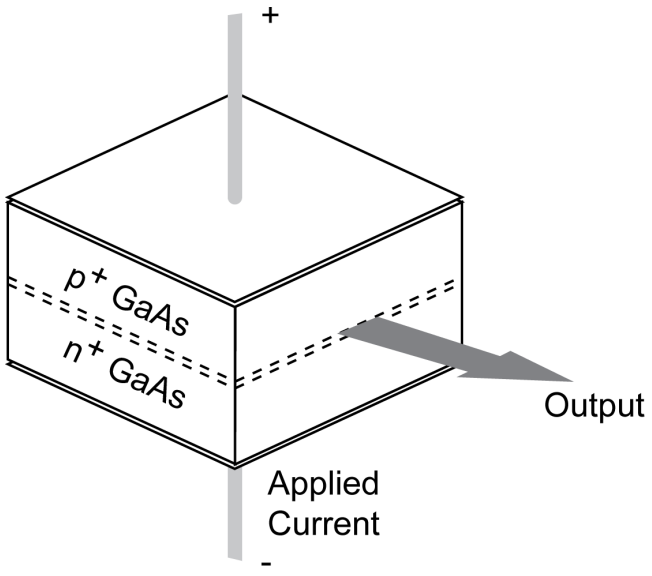

Figure 1.10: Schematic of the GaAs semiconductor laser. The p- and n- type sections are shown with the narrow band for the junction. The laser output is confined to this small region. The applied electrical current is also shown. Diagram adapted from [34].

is applied to drive the system. In practice, a more complicated design is used than this to ensure optimum output. The semi-conductor laser is one of the most commercially viable laser types due to the wide variety of applications they can be used for including laser printers and DVD players [34]. Their main advantage is the small size of the laser allowing them to be used in the miniaturisation of technology that is commonplace in this age. Disadvantages include the small active region and the low power output.

1.3.8 Electronic structure of rare earth ions

Rare earth ions are the usual dopants used in solid-state lasers due to their electronic structure providing the required transitions for laser action [35]. Nd^{3+} is a common dopant and has the electronic configuration

$$[Xe]4f^3$$

This means, like all rare earth ions, that the ion is characterised by the unfilled 4f subshell (Nd^{3+} has 3 electrons out of a capacity of 14 in the 4f subshell). The low lying energy levels of the dopant ion are determined by the forces acting on the electrons

in the unfilled shells [34]. The three main interactions, in order of importance for rare earth ions, are:

1. the inter-electron Coulomb force, which is the force acting between the electrons in the unfilled subshells,

2. the spin-orbit coupling, which is the coupling between the electron spin and the orbital angular momentum,

3. the crystal field splitting, which is the interaction between the host lattice ionic charges and the electrons in the unfilled subshells.

The crystal field term is the weakest of the three because the full 5s and 5p subshells in rare earth ions shield the $4f$ electrons. The inter-electron Coulomb interaction splits the electron configuration into terms related to the angular and spin momenta [34]. For example, the $4f^3$ subshell in Nd^{3+} is split into a number of terms including ^4F, where the usual spectroscopic notation for the total angular momentum, L, is used such that, F corresponds to value of $L = 3$, with $L = 0$ is S, $L = 1$ is P, etc. The superscript is the spin multiplicity and is equal to $2S + 1$, where S is the total spin quantum number. Thus ^4F corresponds to $L = 3$ $S = \frac{3}{2}$. A detailed explanation of this can be found in reference [34].

The spin-orbit coupling splits the terms up into multiplets by requiring the energy state to be dependent on the quantum number J (the total momentum quantum number). Therefore, the $4f$ term is split into 4 multiplets with $J = \frac{9}{2}, \frac{7}{2}, \frac{5}{2}, \frac{3}{2}$. These are determined from the sum of $\mathbf{L}$ and $\mathbf{S}$. The J term is written in subscript giving the energy levels written as $^{2S+1}L_J$. The crystal field will split these levels further although this is as far as needs to be considered here. Figure 1.11 shows the splitting of the $4f^3$ subshell in Nd^{3+} as described.

It is the electronic structure that make rare earth ions so useful in laser design because they provide metastable levels for population inversion and thus stimulated emission.

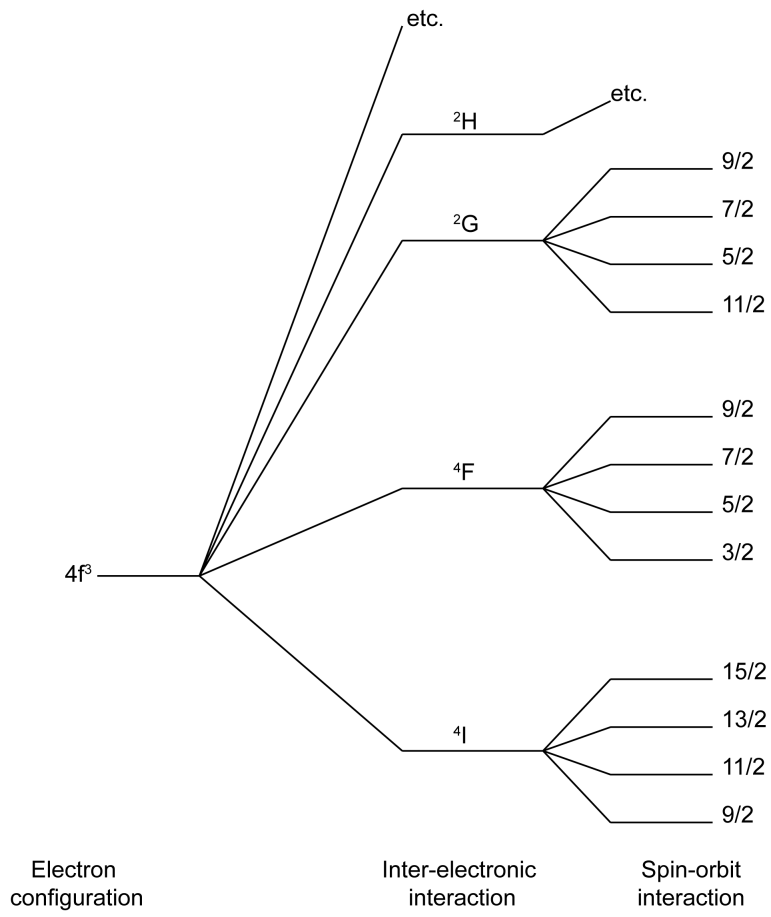

Figure 1.11: Diagram showing the energy level splitting of the $4f^3$ subshell in Nd^{3+}. Adapted from [34].

1.3.9 Q switching and tunablity

Q switching is the name given to the process where typically nanosecond, high energy pulses are generated. Rare-earth-doped laser crystals have weakly allowed transitions [32]. This results in long upper-state lifetimes, which means large amounts of energy can be stored making these crystals suitable for Q switching. Tunable lasers have output

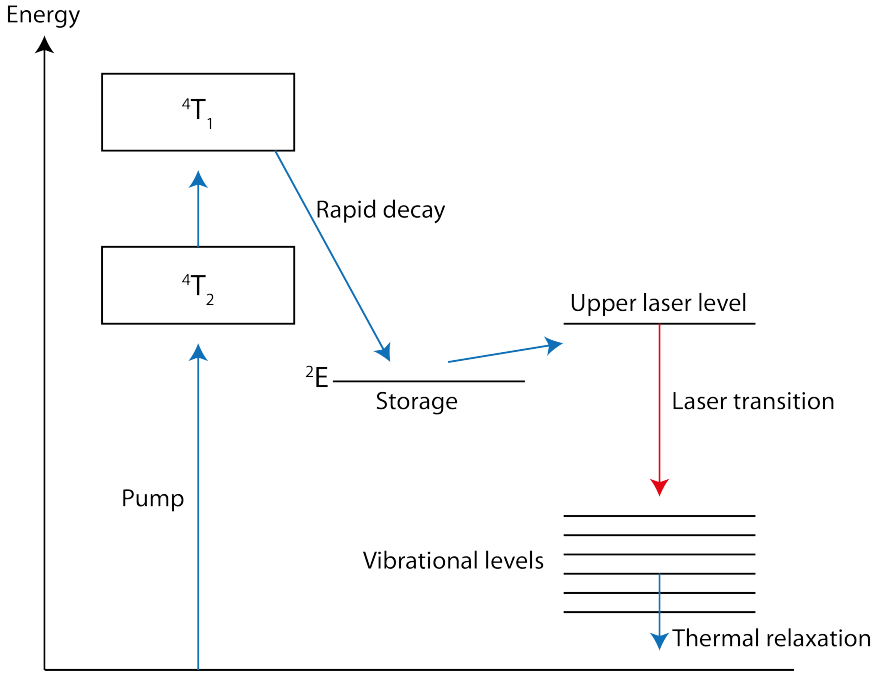

Figure 1.12: Energy level diagram for the Alexandrite tunable laser. Adapted from [34].

wavelengths that can be adjusted as required. An example is the Alexandrite laser, Cr:$BeAl_2O_4$. The active dopant Cr^{3+} can operate with a lasing wavelength between 700 nm and 820 nm [38]. Figure 1.12 shows the energy level diagram for this laser. Electrons are thermally excited from the ^2E storage level into the $^4T_2$ laser level. These transition to a band of vibrational levels that arise from lattice vibrations. In order to use this group of vibrational levels to create a tunable laser, a variable, very narrow bandwidth filter has to be introduced into the system [34]. The aim of the filter is to introduce little loss at the desired wavelength but high loss at all others. There are two common filter methods used with the first being the insertion of a prism into the system. The angle of the prism controls which wavelength hits the mirror and is reflected back through the system. It is also possible to use polarisation as a method to

filter the wavelengths (see reference [34] for further details). Applications of this type of laser include spectroscopy, laser cooling, fibre communications [34] and in some skin condition treatments [38].

1.3.10 Clustering and energy transfer

In an ideal laser, the laser-active ions within the host lattice would be uniformly spread. In reality, they are often not and may in some cases tend to form clusters. This process of clustering is usually undesirable and leads to a serious degrade of gain and power efficiency of the laser through quenching processes [32]. The quenching occurs because when laser-active ions are close enough, energy transfer between them can take place. There are a number of transfer processes that can occur and they all can have a positive or negative effect on the laser system depending on the exact nature of the process.

Energy transfers can take place to impurities within the crystal or to colour centres (defects within the structure). For example, if the excitation energy is transferred to crystal defects where non-radiative decay occurs, a loss in efficiency results. Energy can also transfer between ions of different species, which is often exploited in lasers, see references [39] and [40] for examples. Figure 1.13 shows a visualisation of this process. Here the pump energy is efficiently absorbed by the Yb^{3+} ions, which then transfer their excitation energy to the Er^{3+} ions. These then decay into a level that acts as the upper laser level for a transition to the ground state.

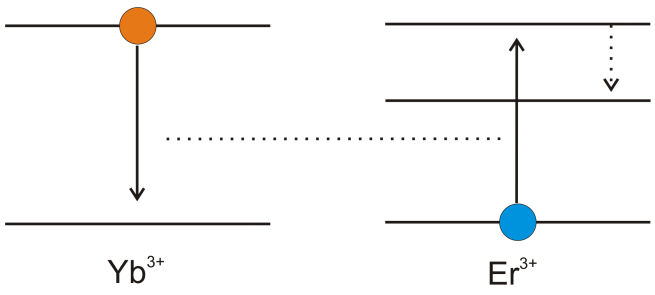

Figure 1.13: Diagram showing the useful energy transfer process between two different dopants. The pump energy is absorbed by by the Yb^{3+} ions, which, transfers to the Er^{3+} ions. Adapted from [32].

Cross relaxation is another type of energy transfer as shown in Figure 1.14. In this

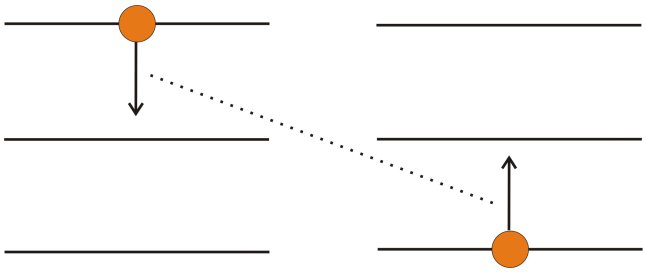

Figure 1.14: Diagram showing the cross relaxation energy transfer process. Ion 1 transfers part of its energy to another in the ground state resulting in both being at an intermediate level. Adapted from [32].

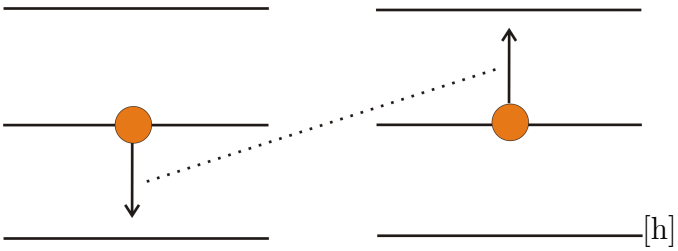

Figure 1.15: Diagram showing the upconversion energy transfer process. Ion 1 transfers its energy to another in the the same state. Adapted from [32].

process, an excited ion transfers part of its energy to another ion in the ground state, resulting in both ions being at an intermediate level.

Another process that can occur is energy transfers that depopulate the lower laser level. In systems where the lower laser level is long-lived, the laser action may self-terminate if the level is not depopulated, so these transfers are vital to the laser operation.

Cooperative upconversion is another process (Figure 1.15). In this case, the energy transfer from one ion raises another ion into a higher energy state. This can also be achieved though additional pumping, but upconversion has the advantage that only one pump source is required. Cooperative upconversion can also be degrading if it occurs in a laser where upconversion is not required.

These energy transfer processes show that unless the laser system requires a specific process to work, they should be minimised. Even systems where energy transfer is required, the type of transfer that occurs has be be selective to avoid degradation. All energy transfers can be avoided by reducing clustering, which in turn, can be reduced by selecting dopant ions that show less tendency to cluster in the host lattice, by

keeping the dopant concentration low, and by selecting a host lattice with a high dopant solubility [32].

1.3.11 Laser applications

Lasers are used in a large variety of applications in a vast range of areas from home electronics to scientific instruments to military uses. This section will briefly outline some of the possible uses of lasers. The applications considered can be split into five categories: measurement, machining, medicine, very high power, and optical information.

Measurement is one of the simplest applications of a laser. Optical alignment in which a laser beam is used to position an object or for guidance in construction, is the most basic of these. Extending this, laser beams can be used with interferometric techniques to measure short distances highly accurately. Interferometers, such as the Fizeau interferometer [41, 34], can be used to measure variation between a test and reference surface. The advantage of using a laser is that as the beam is coherent across large distances the surfaces can be separated, preventing damage to them. There are many more applications that are achieved through various interferometer set-ups that use lasers. Lasers can also be used to measure large distances through techniques such as pulse-echo. A typical hand-held military range-finder comprises a Nd:YAG laser that emits a pulse and has a detector that records the reflection of the beam off the distance object [42, 34, 43]. The time taken from emission to detection allows the distance to be calculated. This technique, which is often known as optical radar or lidar [44], can be extended to measure the topography of the Earth's surface for mapping through airborne systems to more complex techniques for measuring pollutants in the air. Optical radar has even been used to measure the distance to the moon to an accuracy of ± 0.15 m. This was achieved by using reflectors that were left on the surface of the moon during the Apollo missions [45]. Finally, in the measurement applications, lasers can detect rotation using laser gyroscopes [46]. These usually consist of a ring system with two lasers travelling in opposite directions. The system is adjusted so the total distance around the ring is an integer number of wavelengths. If the ring rotates,

the paths of the two beams will change (one becomes longer, the other shorter). This change can be used to measure the rotation speed.

An area in scientific applications is laser spectroscopy. Typically spectrometers use quartz halogen or xenon lamps to obtain monochromatic radiation, however, it is possible to use a laser source [34]. The advantage of using a laser source is the increased power compared to lamps and the smaller bandwidth, which leads to greater resolution and sensitivity. Laser uranium enrichment is another scientific application. Traditionally U-235 isotopes have been separated from nonfissile U-238 isotopes through centrifuge techniques and gas diffusion. These are both relatively inefficient processes. With the upsurge in interest in nuclear energy, attention is turning to laser enrichment, which is believed to offer a lower energy method [47]. The leading research company into the technique was Silex, which since 2008 is now owned by GE Hitachi Nuclear Energy [48]. The method Silex used is based around uranium hexafluoride gas that is cryogenically cooled and sprayed out of a nozzle at high speed. Rapid pulses from an infrared laser penetrates the gas. The laser is tuned to 16 μm which excites the U-235 atom selectively over the U-238. This allows the U-235 to be siphoned off.

Machining using lasers is a common application in industry [34]. Material processing applications include surface hardening, welding, cutting and drilling [36]. Surface hardening of ferrous materials involves heating the surface and then quenching [34]. This can be achieved with a high power laser which can produce a large amount of heat. The very localised heating that can be achieved with a laser allows it to be used to weld two metals together. There are many other types of welding techniques, but laser welding offers a few advantages. The first being that no physical contact is made with external components, and the second is the localised nature of the heating. In laser cutting, the high powered beam vaporises a narrow piece of material, cutting through it. It is necessary to keep the heat affected area as narrow as possible to prevent damage to the rest of the material. In industrial laser cutters an oxygen gas stream surrounds the laser beam to aid with the heating and to help remove the molten material from the area [34].

In the field of medicine, lasers can be used for cutting of tissue, as in particular the output of the CO_2 laser of 10.6 μm is strongly absorbed by water molecules. There are a number of advantages to laser cutting over conventional methods including the positioning of the beam can be highly accurate, there is limited damage to the adjacent tissue, and the laser has a cauterising effect on the nearby blood vessels reducing bleeding. The only disadvantage is the need for a laser system that is easily manoeuvrable. Argon-ion lasers are used in ophthalmology to treat detached retinas. The laser radiation is strongly absorbed by the red blood cells and the thermal effects from this re-attach the retina. Lasers can also be used to bleach some skin conditions and to remove tattoos [38].

Two theoretical laser uses that are being researched are based on very high power laser systems. It has long been the goal to produce nuclear fusion of light elements for power production. There are efforts to achieve the conditions needed for this with high powered lasers. The National Ignition Facility (Nif) in the US is close to producing a surplus of energy from the method and, in 2011, were joined by the Rutherford Appleton Laboratory and AWE in the UK [49]. Another high power laser application is weaponry. This requires very high power outputs and the systems must be compact, light and robust. Trials have been carried out and the one envisaged aim is to have a weapon situated in space capable of destroying missiles [50]. The US Army have developed a Laser-Induced Plasma Channel weapon, which has an optical power output of 50 billion Watts [51].

1.3.12 Laser cooling

Laser cooling, or optical refrigeration, of solids, which involves the refrigeration of a solid by exposing it to optical radiation, dates back to Pringsheim who theorised that phonon energy (thermal vibrations) could be removed by anti-Stokes fluorescence in 1929 [52]. Anti-Stokes fluorescence is the emission of higher energy photons than those which are absorbed, and hence can cause the removal of energy from the material. For the cooling to occur there needs to be high quantum efficiency and the anti-Stokes

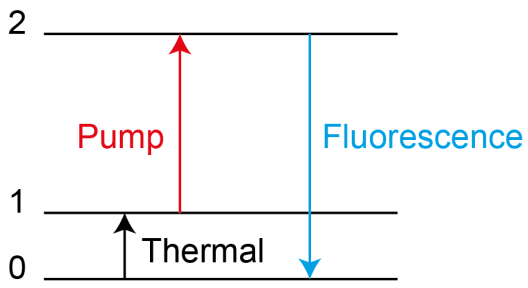

Figure 1.16: Diagram showing the anti-Stokes cooling process. The fluorescence is of higher energy than that of the pump light source, thus removing some phonon energy from the system. Adapted from [53].

fluorescence light has to leave the crystal without being reabsorbed [53]. Figure 1.16 shows the anti-Stokes process.

It was initially argued by Vavilov that laser cooling by anti-Stokes fluorescence contradicted the second law of thermodynamics because the process was reversible and therefore the energy yield would be equivalent to complete transformation of heat to work [54, 55, 53, 56]. However, Landau [57] proved that the process was irreversible by considering entropy. The incident laser light has a very small bandwidth and a defined direction compared to the fluorescence, which has a relatively wide bandwidth and is emitted in all directions. This change in entropy satisfies the second law of thermodynamics.

The first experimental evidence of anti-Stokes cooling in a solid was observed by Epstein in 1995 [58] in ytterbium-doped glass. Ytterbium, being a rare earth metal, is an ideal dopant for laser cooling of solids because the optically active 4f electrons are shielded by the filled 5s and 5p outer shells. This limits the interaction with the host lattice and reduces nonradiative decay. Fluoride glasses and crystals are often used as host lattices as these have low phonon energy, which help to reduce nonradiative decay further and increase quantum efficiency [53].

A number of applications have been suggested including a cryocooler [59], and a radiationally-balanced laser [60]. The concept behind a radiationally-balanced laser was proposed by Bowman in 1999 [60]. In any laser heat generation from the process of excitation and emission cause undesirable changes within the material such as thermal fracture and lensing. Bowman suggested that anti-Stokes fluorescence within the laser

host could balance out the heat generated by the laser generation.

Detailed reviews of laser cooling of solids can be found in references [56, 53].

1.3.13 Fluorides as lasers

Since the invention of the first laser, fluoride materials have been of interest [61]. Initially, the interest was in simple fluoride systems such as LaF_3, which has been subject to both experimental [62] and computational studies [63, 64]. More recently, interest has moved into mixed metal fluorides. Examples of these include $BaLiF_3$ doped with divalent ions [65] and with trivalent ions [66, 67, 68], BaY_2F_8 [69, 70, 71], $LiCaAlF_6$ and $LiSrAlF_6$ [72, 73, 74], and the K_2YF_5 family of materials [61]. Two further materials are $YLiF_4$ and $BaMgF_4$. These form the basis of the work in this thesis.

Fluorides are of interest due to favourable properties for the application of lasers as they readily dope with rare earth ions. They are also generally possess good thermo-mechanical properties with high optical damage threshold [61]. Any laser host lattice must withstand the pumping input, the laser output and any thermal effects of these to ensure a long-lived device. Other favourable properties of fluorides are the presence of a wide band gap, long radiative lifetimes and low phonon frequencies [61].

Chapter 2

Atomistic bulk modelling

2.1 Introduction: the code GULP

In this chapter the theories and methods that underpin atomistic modelling are described. The approach taken is to describe the system through empirically fitted interatomic potentials, which is then geometrically optimised through energy minimisation techniques. Defective lattices are then modelled using Mott-Littleton methods [75]. All bulk atomistic modelling was carried out using the General Utility Lattice Programme.

The General Utility Lattice Programme, GULP, was first published in 1997 [76] by Julian Gale. Its aim was to combine the features of the various atomistic codes into a single, fully-featured modern code. It was revised in 2003 [16] and the current version is 4.0 (although the work described in this thesis was carried out using version 3.4.7). The code allows full space-group information for periodic systems to be utilised along with a wide range of potential forms. System optimisation, supercells, Mott-Littleton defect approximations and index planes are among its features.

2.2 Interionic interactions

All systems studied in this thesis are inorganic ionic crystals, which means they consist of a series of alternatively charged ions that are held together through Coulomb electrostatic attraction. Therefore, these systems can be described using the classical ionic theory of Madelung [77] and Born [78, 79], in which the ions are treated as uniform charged spheres that interact through simple forcefields and no account of electronic structure is taken, although some electronic properties can be included through extensions, such as the Shell Model [80], to the basic forcefield model.

For a model to accurately represent a real-world structure all of the interactions between all of the species have to be included. The general form of this can be expressed as the following series sum:

$$\Psi(r) = \sum_{ij} \Psi_{ij}(r) + \sum_{ijk} \Psi_{ijk}(r) + \sum_{ijkl} \Psi_{ijkl}(r) + ... \tag{2.1}$$

where $\Psi_{ij}(r)$ is the interaction between pairs of ions ij, and $\Psi_{ijk}(r)$ is the interaction between triplets of ions ijk, etc. To evaluate this sum would be computationally expensive and so it is approximated to just the pair interactions, i.e.:

$$\Psi(r) = \sum_{ij} \Psi_{ij}(r) \tag{2.2}$$

This is the pair-wise potential approximation. It is valid because in ionic solids the pair term dominates [81]. The pair-wise approximation allows the long range Coulombic interaction to be given by:

$$V_{Coulomb} = \frac{1}{4\pi\epsilon_0} \frac{q_i q_j}{r_{ij}} \tag{2.3}$$

where ϵ_0 is the permittivity of free space, q_i and q_j are the ionic charges and r_{ij} is the interatomic distance. This interaction accounts for approximately 90% of the total energy [61]. The 1/r dependency in this potential is a very slowly converging if summed directly. The Coulombic term is therefore evaluated through Ewald summation [82] as discussed in Section 2.2.1.

The interactions between the ions provides the basis for the lattice energy of the system such that the lattice energy is given by:

$$E_{lattice} = \frac{1}{2}\sum_{ij}\left(\frac{1}{4\pi\epsilon_0}\frac{q_i q_j}{r_{ij}}\right) + \frac{1}{2}\sum_{ij}\phi_{ij}(r_{ij}) \tag{2.4}$$

where the first term is the long range Coulomb energy and the second is the total short range interaction energy. The short range interaction is discussed in Section 2.2.2.

2.2.1 Ewald summation

In order to evaluate the lattice energy (Equation 2.4), the sum of the Coulombic interaction across the ions is needed. The long range nature of this term results in the sum being problematic to calculate. The solution to this problem was devised by Paul Ewald in 1921 [82]. The method sums the interactions between ions and its array of periodic images. The original derivation is mathematically complex and beyond the scope of this thesis, therefore, a simplified explanation based on the derivation in Kittel 1976 [83] follows outlining the key points.

The total potential acting at a lattice point can be split into two parts with one, ϕ_1, in real space and the other, ϕ_2, in reciprocal space. This can be expressed as:

$$\phi = \phi_1 + \phi_2 \tag{2.5}$$

ϕ_1 is the real potential and is comprised of the point charges with an additional Gaussian charge distribution of the same magnitude but opposite sign superimposed on top (see Figure 2.1). The net result of this is to prevent neighbouring ions interacting. This potential is evaluated at the object ion and it comprises three components: the charge associated with the ion, the Gaussian distribution within a sphere of radius r_{ij} (i.e. distance to the nearest neighbour), and the Gaussian distribution of the ion outside the sphere.

The potential in reciprocal space, ϕ_2, comprises an array of Gaussian charge distribution with equivalent charge as the original point charges in the real crystal. However,

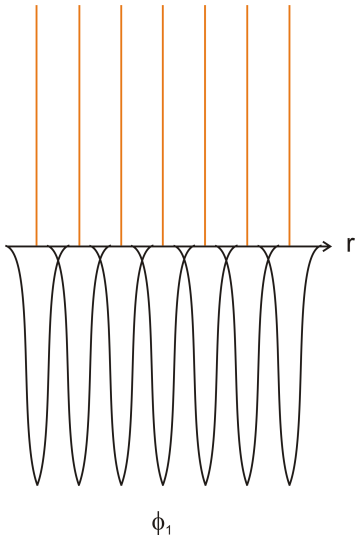

Figure 2.1: Graphical representation of the real part of the Ewald splitting. The red lines represent the point charges of the lattice ions and the black curves are the Gaussian distributions of equal magnitude but opposite sign superimposed on top. Adapted from [84].

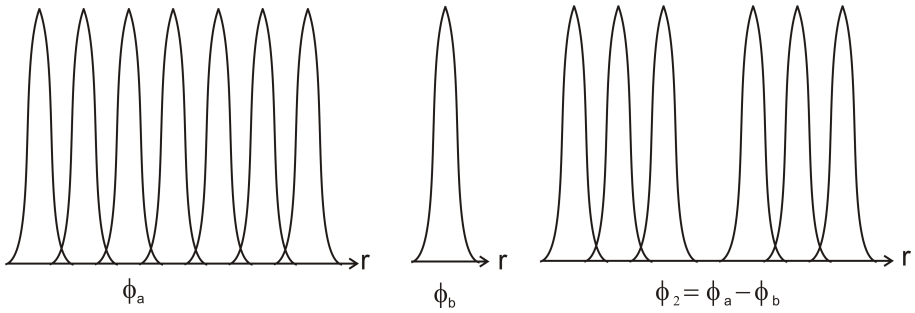

Figure 2.2: Graphical representation of the reciprocal part of the Ewald splitting. Guassian distributions are placed at the lattice ion locations, ϕ_a and ϕ_b represents the lattice ion itself. ϕ_b is taken away from ϕ_a to leave the potential used in Ewald splitting, ϕ_2. Adapted from [84].

because the Madelung constant, which allows electrostatic potentials in crystals to be calculated by approximating the ions as point charges, states that the individual ions do not feel their own electrostatic field [83], the reciprocal potential, ϕ_2, is made up of the Gaussian charge distribution, ϕ_a, minus the charge distribution of the ion, ϕ_b, such that:

$$\phi_2 = \phi_a - \phi_b \tag{2.6}$$

Figure 2.2 gives a graphical representation of the reciprocal potentials. The two components of the Ewald splitting combine to form the original point charge. The reason for the spitting is to achieve convergence. ϕ_a and its charge density can be

expanded in terms of a Fourier series and related though the Poisson's equation [85], yielding a charge density, ρ_k. The integral of the ϕ_a charge density Fourier series over the unit cell volume equals the integral of the Gaussian charge density for a single ion over the whole crystal. This charge density relationship can be substituted back into the ϕ_a Fourier series and this evaluated to give a summation for ϕ_a that can be converged. ϕ_b is the Gaussian distribution of the ion and can be evaluated as such.

Combining these results (Equation 2.5) enables ϕ to be calculated. In performing this mathematical treatment a parameter, η, can be optimised to determine the width of the Gaussian peaks, such that both parts converge rapidly. Catlow and Norgett [86] determined an optimal value for η and it is given by:

$$\eta = \left(\frac{N\pi^3}{V_2}\right)^{1/6} \tag{2.7}$$

where N is the total number of ions in the system and V is the unit cell volume.

2.2.2 Short range potential

The short range interaction is more complex than the long range one because it has to account for a number of phenomena. Electron cloud overlap occurs at short ionic distances, which results in a repulsion caused by two effects. Firstly, the Pauli Exclusion principal [87, 88], in a generalised form, states that no two fermions may occupy the same quantum state. This increases the energy of the electron configuration of the two overlapping electron clouds. Thus an increasing repulsive force occurs as the ions are moved closer together. The second repulsive term, which applies at very short interaction distances, arises from nuclear-nuclear interactions. The short range interaction also contains an attractive force, which occurs due to the spontaneous formation of instantaneous dipoles on adjacent electron clouds. This is known as the van der Waals interaction. Having this many terms in the short range interaction makes selection of a potential of suitable form less straightforward.

The first attempt to find a short range potential was done by Born and Landé [89]

and was in the form:

$$\phi = \frac{b}{r_{ij}^{n}} \tag{2.8}$$

where b and n are fitted variables. In early work n was set to 9 [90]. This potential worked well for some systems, but with more quantum mechanical knowledge it became clear it was insufficient. Born and Mayer [91] developed the following as a consequence:

$$\phi = Aexp\left(\frac{r_{ij}}{\rho}\right) \tag{2.9}$$

where A and ρ are variables. This potential is generally used when the ions have small polarisablities due to the potential form taking no account of the van der Waals interaction.

The Lennard-Jones potential [92] added the van der Waals interaction as determined by London [93, 94] to the Born and Landé equation (Equation 2.8):

$$\phi = \frac{b}{r_{ij}^{n}} - \frac{C}{r_{ij}^{6}} \tag{2.10}$$

where b and n are variables as before, with n usually set to 12. C is a variable that can be altered to adjust the van der Waals strength. This potential form is commonly used in the modelling of liquids and gases [95, 90].

The common potential form used in ionic solids modelling (examples of successful studies include [96, 97, 98]) and therefore the one used in this work is the Buckingham potential [99]. This potential takes the van der Waals term from the Lennard-Jones potential (Equation 2.10) and couples it to the Born-Mayer potential (Equation 2.9):

$$\phi = Aexp\left(\frac{-r_{ij}}{\rho}\right) - \frac{C}{r_{ij}^{6}} \tag{2.11}$$

where, as before, A, ρ and C are variables used to fit the potential to the structure.

One downside to the Buckingham potential is that at close interionic separation the positive C terms leads to an unphysical attractive term. This only becomes an issues if defects are placed in high energy locations in close proximity to lattice ions. There

are a number of ways to negate the attraction however. For cation-anion interactions Buckingham potentials are derived with the C parameter set to zero. These potentials now take the Born-Mayer form. As discussed above, this type of potential takes no account of van der Waals interactions. For anion-anion interactions, where van der Waals are more important an alternative known as the 4-range Buckingham potential is used. 4-range Buckingham potentials were derived by Jackson for UO_2 [100] and they has been used extensively since. In this work some of the ion interactions are modelled using this type of potential.

The 4-range Buckingham takes the form given in Equation 2.12. The potential is split into 4 ranges with the constraints that the functions and their first and second derivatives are continuous at the boundary points and also that the function possess a minimum stationary point at r_{min}. The potentials acts up to r_{max}, the short-range cut off. The polynomial constants are calculated by the spline fitting procedure embodied within GULP.

$$\phi^{Buck4}(r_{ij}) = \begin{cases} A_{ij} \exp\left(-\dfrac{r_{ij}}{\rho_{ij}}\right) & \text{if } r_{min} < r_{ij} \leq \text{cut}_1 \\ \displaystyle\sum_{m=0}^{5} a_m r_{ij}^m & \text{if } \text{cut}_1 < r_{ij} \leq r_{min} \\ \displaystyle\sum_{n=o}^{3} b_n r_{ij}^n & \text{if } r_{min} < r_{ij} \leq \text{cut}_2 \\ -\dfrac{C_{ij}}{r_{ij}^6} & \text{if } \text{cut}_2 < r_{ij} \leq r_{max} \end{cases} \tag{2.12}$$

There is a further potential form worth mentioning, as it is used in systems with covalent nature, the Morse Potential [95]:

$$\phi = D_{ij}[1 - exp(-\beta(r_{ij} - r_0))]^2 \tag{2.13}$$

where D_{ij} is the bond disassociation energy and β is a variable. An example of this potential in use can be found in the work of Basak 2003 [101].

All short range potentials by their nature are short range and so are only evaluated to a certain distance before being cut-off. The value for the cut-off may be determined

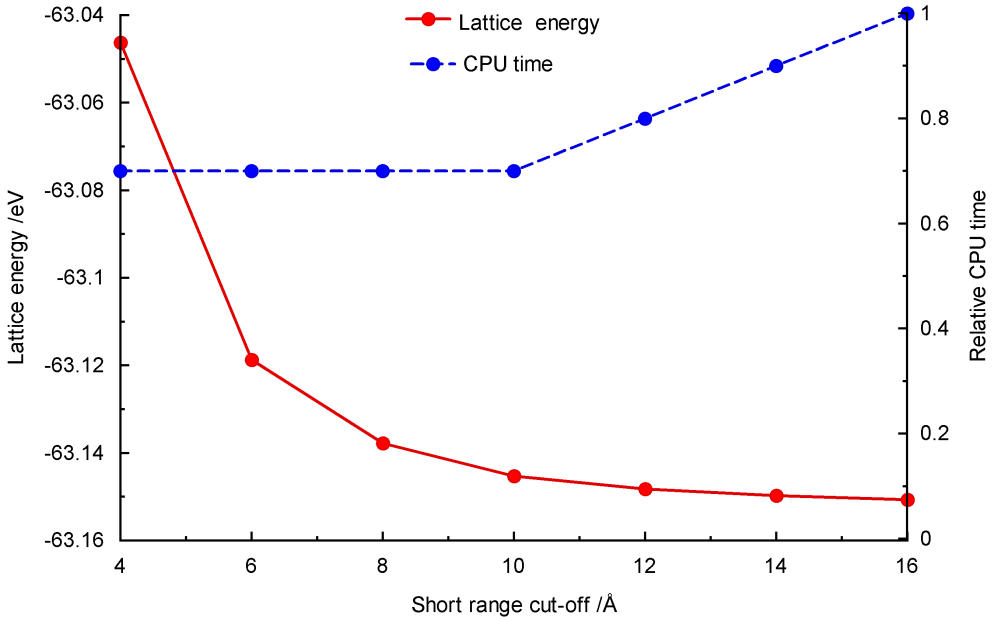

Figure 2.3: Plot of lattice energy convergence with short range potential scaling for $YLiF_4$. Also shown is the relative computation time. A cut-off of 10 Å was chosen.

by plotting lattice energy against cut-off and selecting a value where the lattice energy has plateaued and therefore the short range interaction contribution has reached its maximum, although it is usually sufficient to choose a typical value. See Figure 2.3 for the cut-off determination for $YLiF_4$.

The short range potential is coupled to the long range Coulomb potential to form the overall potential to describe the interaction between ions. Figure 2.4 shows the Mg-F Buckingham and Coulomb potentials used in this work as well as the overall potential.

2.2.3 Potential derivation

The short range potentials used within this work are all in the Buckingham form (although some have $C = 0$ so are technically Born-Mayer potentials). Where possible the potentials have been transferred from other models. The main advantage in this approach is that potentials that have been fitted to only one structure have effectively only be tested at one interionic distance and the inclusion of defects into the lattice can

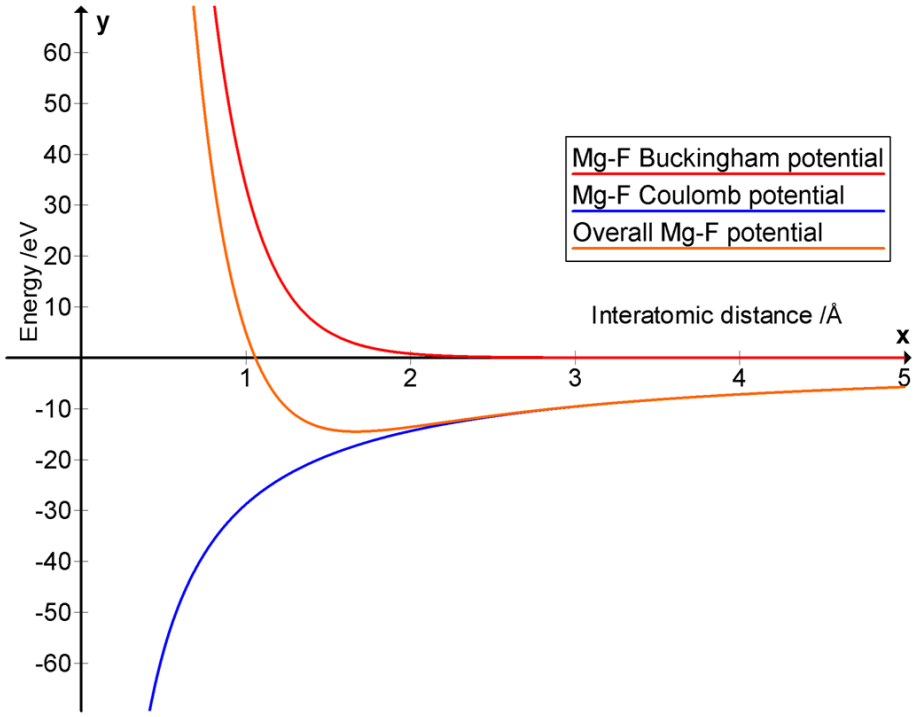

Figure 2.4: Plot showing the long range Coulombic Potential, the short range Buckingham potential and the potential resulting from combining these two. All potentials shown are the Mg-F potential used in this work.

alter this distance. Potentials that can be transferred (i.e. work for a range of systems) are therefore more robust, as they have been tested at a range of interionic distances corresponding to the different systems. This approach of fitting to a range of structures can be taken to derive new potentials, however it is time consuming (e.g. [102, 103]).

For the interactions where there were no reliable potentials to transfer to this current work, namely the transition metal fluorine potentials, new potentials were derived using the following method based on the approach taken by Read 2010 [104].

A GULP input file was generated using empirical data for the structure of the potential that needed fitting (i.e. for a Cr^{3+}-F potential the structure for CrF_3 was used to fit to). Geometry optimisation (see Section 2.3.2) was carried out for a range of Buckingham potential variable values and the outputs tabulated. The variable range was typically $A = 800$ eV to 4000 eV and $\rho = 0.2000$ Å to 0.4000 Å with C set to 0 eVÅ^6. By comparing the structural fit and the extent of minimisation (gnorm), a set of a few potentials were generated. These were compared to other physical properties,

if known, and the best potential selected. Fine tuning of the potential was then done through a similar method but with a finer step change in the variables to optimise the fit. The whole process was automated with the development of a fitting script.

The advantage of this approach is that a wide range of potentials could be examined very quickly, however, as discussed above, the limitation is that the potential has only been fitted to one structure and therefore one interionic separation. Another potential limitation is the experimental data. With empirical fitting, the end result can only be as good as the data it is fitted to. Comparing structural and physical data (such as elastic constants) can be problematic as they are usually determined experimentally from different techniques (power diffraction and single crystal) and crystals. The material examined may also have had defects within affecting the result.

During the course of this work, some transferred potentials were found to be giving unphysical results when applied to surface calculations. These were refitted using the method above. Another important note is that potentials have to be consistent. That is to say that a cation-fluoride potential is only compatible in models that use the same fluoride-fluoride potentials that was used in its derivation. It is for this reason that two different F-F potentials are used in this work.

2.2.4 Electronic polarisability

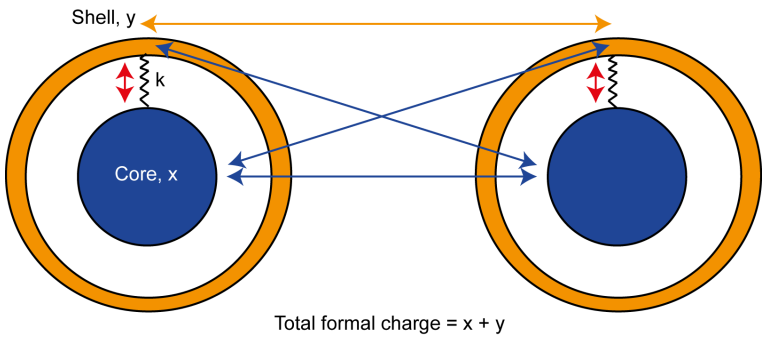

Figure 2.5: Shell Model devised by Dick and Overhauser [80] for polarisable ions. The (blue) core is surrounded by the massless (orange) shell, coupled together by a spring, which acts as the polarisation.

The Shell Model, which was devised by Dick and Overhauser [80], allows for electronic polarisability to be accounted for in the model. The concept of the model is to replace

the rigid, billiard-ball-type charged spheres representing the ions with a core-shell system. In the Shell Model, the ion is described by a massive core that is surrounded by a massless shell (Figure 2.5). The core and the shell are coupled together by a harmonic spring with a force constant k. When an electric field is applied to the ion, the shell moves relative to the core, creating a dipole and thus simulates dielectric polarisablity (Figure 2.6). The formal charge of the ion is split between the core and the shell, such that they sum to give the correct formal charge. The polarisability, α_e, of an isolated ion is given by [90]:

$$\alpha_e = \frac{1}{4\pi\epsilon_0}\left(\frac{Y^2}{k}\right) \tag{2.14}$$

where Y is the shell charge, ϵ_0 is the permittivity of free space, and k is the force constant. The model parameters; charge on the shell, charge on the core, and the spring constant are fitted empirically. In this work only the fluoride ions were treated with the Shell Model as these are the most polarisable and using a Shell Model adds to the computational expense.

The Shell Model has been used in many studies and shown to be very successful. Faux and Lidiard [105] also proved its value in defect calculations. One of the advantages of the Shell Model in calculations is that because the short range interactions are coupled to the shell (rather than the core), extra degrees of freedom are introduced into the relaxation. In effect, it adds many body terms since the position of the shells depends on the electrostatic interactions from all ions in the crystal. The model does however have some limitations. The limitations arise because of the two assumptions in the model, namely, that the potential is a function of the separation of the ions and not their directions, and that only dipolar distortions are allowed. Both of these assumptions mean the Shell Model is a centrosymmetric model, thus it implies the elastic constants C_{12} and C_{44} are equal for a cubic system. Experimentally, however, many materials are found where this is not true. This is known as the Cauchy Violation [106] and the Shell Model cannot reproduce this. Schroder created an extension to the model that allowed the radius of the shell to adjust to account for the case when $C_{12} < C_{44}$. This is known as the Breathing Shell Model [107]. Sangster [108] added a further enhancement by

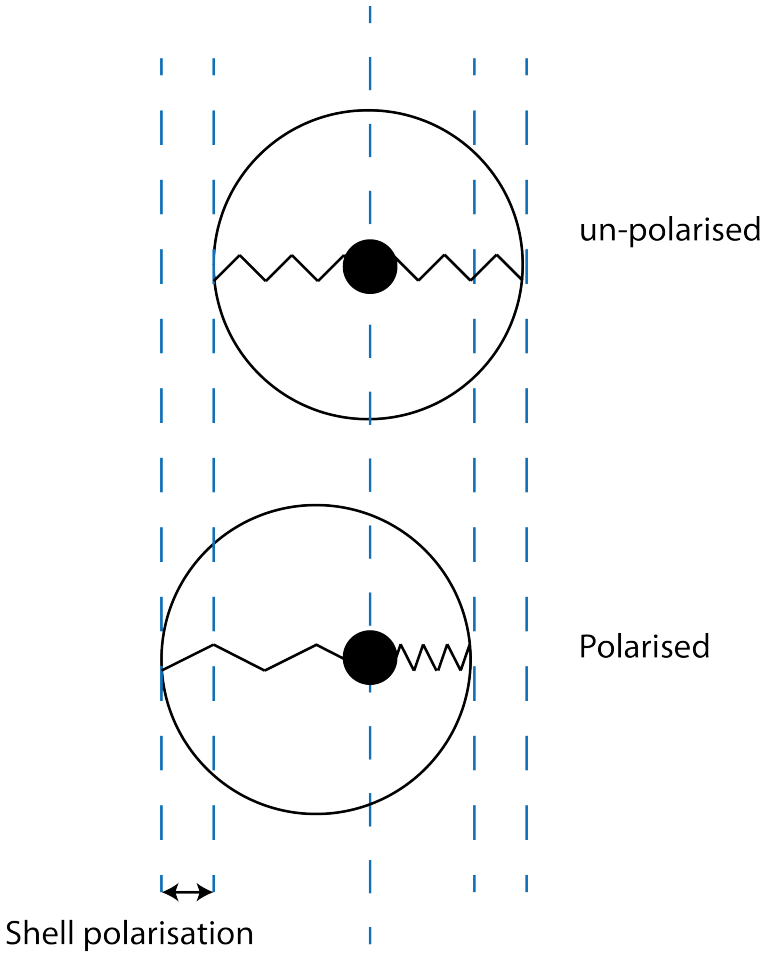

Figure 2.6: Diagram showing the polarisation effect with the Shell Model.

allowing the shell to distort in an ellipsoidal manner (the Breathing Shell Model only allows spherical distortion). However, these models are difficult to parameterise and add extra computational requirements. They are therefore not utilised in this work.

2.3 Perfect systems

2.3.1 Generation of structure

All material crystal structures were found using a literature search using the Inorganic Crystal Structure Database (ICSD). If multiple papers reported the structure the newest paper in terms of age that obtained the structure at ambient pressure and at the lowest temperature was chosen. The structure obtained was used as the starting input for all calculations.

2.3.2 Energy minimisation

All calculations are performed at 0 K, which is to say, lattice vibrations and configurational entropy are not accounted for in the model. Instead the minimum energy atomistic arrangement is achieved through minimisation techniques.

This is achieved by calculating all ionic interactions and each ion is then shifted proportionally to, and in the direction of, the force acting on it. The lattice energy can be minimised in a number of ways with the most common methods being either at constant pressure or constant volume. The latter of these determines the minimum energy from ionic coordinates only, whereas, the former accounts for strain not just in the ions but the also the unit cell and therefore offers a more realistic simulation. The computational expense is greater for constant pressure minimisation, however, it is now the standard form of minimisation due to the greater computer power today. To understand how the energy of the system can be minimised, consider the simpler case of constant volume minimisation. If U_{latt} is the lattice energy of a system with coordinates, r, then the lattice energy of the system with shifted coordinates, r', is,

$$U_{latt}(r') = U_{latt}(r) + g^T \cdot \delta + \frac{1}{2}(\delta^T \cdot \mathbf{H} \cdot \delta) \tag{2.15}$$

where g is the first derivative of the lattice energy with respect to ion coordinates,

$$g = \frac{\partial U_{latt}}{\partial r} \tag{2.16}$$

and δ is the displacement of an ion,

$$\delta = r' - r \tag{2.17}$$

and $\mathbf{H}$ is the second derivative of the lattice energy with respect to ion coordinate, which is known as the Hessian Matrix,

$$\frac{\partial^2 U_{latt}}{\partial r^2} \tag{2.18}$$

The first derivative of this shifted coordinate lattice energy with respect to displacement will be zero at equilibrium, as the forces will be zero.

$$\frac{\partial r'}{\partial \delta} = g + \mathbf{H}\delta \tag{2.19}$$

The ion displacement to achieve the energy minimum is therefore given by,

$$\delta = -\mathbf{H}^{-1} \cdot g \tag{2.20}$$

To consider constant pressure minimisation, strain in the cell is also minimised through the relaxation of the cell vectors. A detailed description of the mathematics for this can be found in [109].

Achieving the energy minimum takes cycles of the above procedure as the system will not reach a minimum in a single step. The ionic coordinates are shifted iteratively until the forces on the atoms are zero. There are a number of minimisation algorithms available to achieve this. The most common two are Conjugate Gradient, which is a first-order minimisation, and Newton-Raphson, which is a second-order minimisation.

Conjugate gradient is a more complex, but more accurate, form of a simple gradient

descent method. In a gradient descent, steps are taken proportional to the negative of the local gradient and a line search is used to determine the magnitude of the step, whereas with conjugate gradient method, steps are taken conjugate to each other. The problem with the simple gradient method is that the rate of convergence slows as the minimum is approached. Also, in shallow gradients zig-zagging occurs slowing the rate further and causes the line search to oscillate around the energy minimum [110]. The conjugate gradient method removes some of these problems, however, it does require more computational storage as the previous gradient is required at each step as well as the current.

The next stage of complexity is to consider second derivatives as well as first to increase the rate of convergence. This is achieved through the Newton-Raphson method. In this method the value of the displacement vector $\Delta\mathbf{x}$ is given by

$$\Delta\mathbf{x} = -\alpha\mathbf{H}^{-1} \cdot \mathbf{g} \tag{2.21}$$

where α is a scalar value, $\mathbf{g}$ is the first derivative of the vector and, as before, $\mathbf{H}$ is the Hessian Matrix (the second derivative matrix).

The Newton-Raphson method achieves fast convergence, however, the storage and calculation of the inverse Hessian is computationally expensive. Additionally, the Hessian may only change slightly from one step to the next and therefore it is not calculated explicitly at every step of the minimisation. Instead the Hessian is updated through changes in the gradient between cycles. There are a number of such updating schemes, with Broyden-Fletcher-Goldfarb-Shanno (BFGS) [111] being the one used in this work. In this scheme the initial step is to calculate the exact inverse Hessian and then it is updated for a number of cycles. It is however, sometimes necessary to recalculate the exact inverse Hessian again and in GULP this is triggered by one the the following possible situations that are all controlled by parameters set within the code (or altered by the input) [16]:

- The process has reached the maximum number of cycles

- The gradient vector and search vector angle has reached the threshold
- The energy decreased by more than the threshold in one cycle
- The energy cannot be lowered any further along current search vector

It is also possible to begin with an estimated inverse Hessian before preceding with the BFGS algorithm. This is useful if the system is large. Crystal symmetry is used whenever possible to reduce the convergence time of the optimisation. Symmetry allows the number of independent geometric variables to be reduced and defines certain atomic positions as special sites that are not allowed to vary.

The minimisation of total energy is stopped once the criteria for convergence has been met. Typically this is when the gradient norm (root mean square gradient) has reached 10^{-3}. The resulting structure is said to be geometry optimised.

The minimisation techniques discussed allow for the local minimum to be found, however, other minimisation methods can be taken to find other stationary points on the potential energy surface if required in modelling transition states for example, such as Rational Functional Optimisation or Nudged Elastic Band. Also, the techniques discussed take no explicit account of temperature and are effectively run at zero Kelvin. In many solid-state problems the inclusion of temperature is important, however, it is not a straightforward solution to include it. Firstly, the potentials used in the model are derived from empirical data. This causes a problem as the data has an implicit temperature built into it (the temperature at which the data was obtained). The net result is a temperature-free minimisation of a temperature-dependent structure. In practice this does not usually cause a problem. The problem is avoided if the potentials are derived from quantum mechanical methods at zero Kelvin, however, this approach relies on an accurate quantum mechanical model. Secondly, the approach to take to include temperature depends on the magnitude of the temperature and the level of detail required.

At very low temperatures the atoms in the system will vibrate harmonically around their lattice sites and this can be modelled using Lattice Dynamics and free energy

minimisation. Extensions to this can be used to allow for the anharmonic vibrations at higher temperatures, however, as the temperatures becomes high enough for diffusion to occur other approaches have to be taken. Molecular Dynamics, which utilises Newton's laws of motion is a common approach. Within this work, only Lattice Dynamics have been considered.

Free energy minimisation uses the quasi-harmonic approximation, which states the atoms vibrate harmonically while the cell parameters are adjusted to minimise the free energy. This approximation makes intuitive sense as most materials when heated undergo thermal expansion. It has also been shown to be valid until the temperature is approximately half the melting point of the material [16]. Within GULP two methods based on the Kantorovich analytical derivatives [112] of free energy are encoded. The first of these is the Zero Static Internal Stress Approximation (ZSISA) [113], in which the unit cell is minimised with respect to free energy, while the internal degrees of freedom are maintained at a minimum with respect to internal energy [16]. The second approach is Full Free Energy Minimisation (FFEM), in which both the unit cell and the internal degrees of freedom are minimised with respect to free energy. Both methods assume the second derivative matrices with respect to free energy, which are required for Newton-Raphson optimisation, can be approximated by ignoring the free energy contribution to them and using the internal energy Hessian instead. This is done because calculating these second derivatives, which corresponds to the fourth derivative of internal energy, is expensive.

2.3.3 Calculating material properties

Physical properties can be found from the derivatives of the lattice energy, which can be compared to experimental data. The second derivative with respect to strain gives the elastic constant matrix, $\mathbf{C}$, describing the mechanical hardness of the material with deformation. The elastic constant matrix in GULP is a 6x6 matrix, which is usually reduced through symmetry.

$$\frac{1}{V}\frac{\partial^2 U_{latt}}{\partial \varepsilon_i \varepsilon_j} = \mathbf{C} \tag{2.22}$$

Bulk (K) and shear (G) moduli also contain information relating to the hardness of the material with respect to various types of deformation. An equation of state, typically a third or fourth order Birch-Murgnahan equation [104], can be fitted to a plot of isotropic pressure versus volume to produce the bulk modulus from one the curve parameters. It is also possible to relate the bulk and shear moduli to the elastic constants, however, there is no unique way of doing this transformation. In this work the Voight approach is used.

$$K_{Voight} = \frac{1}{9}(C_{11} + C_{22} + C_{33} + 2(C_{12} + C_{13} + C_{23})) \tag{2.23}$$

$$G_{Voight} = \frac{1}{15}(C_{11} + C_{22} + C_{33} + 3(C_{44} + C_{55} + C_{66}) - C_{12} - C_{13} - C_{23}) \tag{2.24}$$

These terms may be reduced through symmetry, for example, in a cubic system $C_{11} = C_{22}$ etc. Two further moduli may be calculated from bulk and shear moduli; Young's modulus and Poisson's ratio. Under uniaxial tension the ratio of stress to strains defines the value of the Young's modulus for that axis.

$$Y = \frac{\sigma}{\epsilon} \tag{2.25}$$

The Young's modulus can be calculated from the bulk (K) and shear (G) moduli with the following equation:

$$Y = \frac{9KG}{3K + G} \tag{2.26}$$

Complementary to Young's modulus is Poisson's ratio (ν), which measures the change in the material at right angles to the uniaxial stress. Most materials shrink orthogonal to the applied tension and therefore most Poisson ratios are positive (with a maximum theoretical value of 0.5). The value may be obtained from the following equation.

$$\nu = \frac{3K - 2G}{2(3K + G)} \tag{2.27}$$

The most important properties, in terms of model fitting, are the dielectric constants. Furthermore, the dielectric properties are important in many contexts beyond the model fitting and the bulk properties. For example, the response of the material to a charged

defect depends on the inverse of the dielectric constant. The value of the constant varies with the electromagnetic frequency applied, and therefore for calculation purposes two extremes are usually taken. The static dielectric constant refers to the case where all degrees of freedom, both nuclear and electronic, respond to the electric field and provide screening. This can be calculated from the cartesian second derivative matrix of all particles and the charges of all particles. The other extreme is the high frequency dielectric constant, in which because the oscillation is greater than the maximum vibrational frequency of the material, only the electrons are able to respond to the electric field. The calculation is therefore identical except that the second derivative matrix now only includes cartesian components for any shells present within the model. For rigid ion models the high frequency dielectric tensor is a unit matrix.

The importance of the dielectric properties in fitting the model parameters arises because the dielectric tensor is related to the inverse second derivative matrix and therefore has many of the characteristics of the Hessian matrix. This allows a check for extreme values, particularly negatives ones, which might indicate an inadequate potential. Also, the high frequency dielectric constant is useful in fitting the parameters of the shell model due to the direct correlation.

Finally, the refractive indices of the material can be obtained from the dielectric constants.

$$n = \sqrt{\epsilon} \tag{2.28}$$

2.4 Defective systems

After the simulation of the bulk properties of the material the next stage is to consider defects within the lattice. This is of extreme importance as many of the key applications of solid-state systems utilise defects. Within this work, it is the addition of extrinsic dopants within the lattice that provides the key properties for applications. However, the properties of intrinsic defects that may be present alongside the dopants are also of importance.

There are two approaches to modelling defects in solids. The first is an extension of bulk simulations through supercells. This approach is usually taken when high concentrations of defects are to be modelled. The second approach uses a infinite dilution cluster method based on the pioneering work of Mott and Littleton [75]. The approach is therefore referred to as the Mott-Littleton method.

2.4.1 Mott-Littleton method

The Mott-Littleton method treats the problem with a two region strategy. The defect is located within a spherical region (called region 1) around a point known as the defect centre. The defect centre is, in the case of a single defect, usually at the same site as the defect. In multiple defect simulations the centre is usually located at the midpoint of the defects. A second region is defined outside of this first region, as region 2, that extends to infinity. In region 1, the ions are strongly perturbed by the defect and therefore all the interactions are calculated explicitly. Region 2 is split into two separate regions, region 2a and 2b (Figure 2.7). Ions that lie within region 2 are only weakly perturbed by the defect and so the energy is approximated.

The total energy of the system can be expressed as the sum of the energies within the two regions and between them:

$$U_{total}(x,\xi) = U_{11}(x) + U_{12}(x,\xi) + U_{22}(\xi) \tag{2.29}$$

where $U_{11}(x)$ is the energy of region 1 as a function of cartesian coordinates, x, $U_{22}(\xi)$

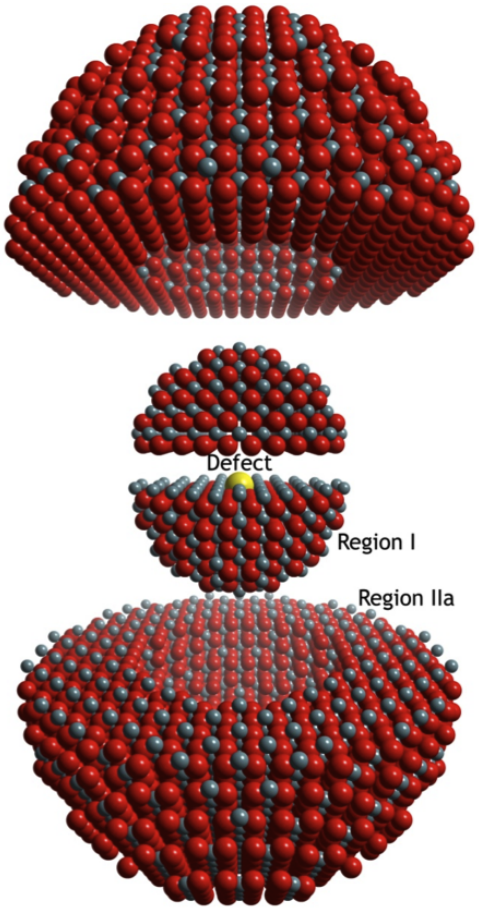

Figure 2.7: Diagram of the Mott-Littleton method used for defect calculations. The effect the defect has on Region 1 is calculated explicitly, whereas Region 2a is approximated. Image taken, with permission, from Read [104].

is the energy of region 2 as a function of cartesian displacement, ξ, and $U_{12}(x,\xi)$ is the energy of the interaction between the regions. It is possible to write the energy of region 2 as a harmonic function if it is assumed the forces acting on the region are small such that the response of the atoms in the region is harmonic.

$$U_{22}(\xi) = \frac{1}{2}\xi^T H_{22}\xi \tag{2.30}$$

In this expression H_{22} is the Hessian matrix for region 2. The displacements in region 2 will be the equilibrium values and so it it possible to write the following condition:

$$\left(\frac{\partial U_{total}(x,\xi)}{\partial \xi}\right)_x = \left(\frac{\partial U_{12}(x,\xi)}{\partial \xi}\right)_x + H_{22}\xi = 0 \tag{2.31}$$

Combining Equations 2.29, 2.30, and 2.31 removes the energy of region 2 from the total energy (along with the Hessian matrix which would be of infinite dimension).

$$U_{total}(x,\xi) = U_{11}(x) + U_{12}(X,\xi) - \frac{1}{2}\left(\frac{\partial U_{12}(x,\xi)}{\partial \xi}\right)_x \xi \tag{2.32}$$

The problem is simplified further by the cancellation of terms through calculating the defect energy rather than the individual contributions, where the defect energy is the difference between the energy of the perfect regions, U_{total}^{perf}, and the defective regions, U_{total}^{def}.

$$U_{defect}(x,\xi) = U_{total}^{def}(x,\xi) - U_{total}^{perf}(x,\xi) \tag{2.33}$$

One important difference in defect calculations compared to bulk ones is that the energy is optimised with respect to the forces rather than by energy. It is also vital to minimise the system before any defect calculation is performed due to the inclusion of region 2 displacements in the calculation.

Within region 2, the ions are treated in different ways in each of the two subregions. The forces on ions in region 2a are calculated explicitly and the displacements determined. In should be noted that within GULP a common approximation is used which only calculates the forces due to the defect species. Region 2b extents to infinity and so

the forces cannot be calculated explicitly. Instead, it is assumed that the only force acting is due to the Coulomb potential. This assumption is valid if the radius of region 2a is larger than that of region 1 plus the short-range potential cut-off. To simplify the calculation further, the electrostatic potential due to the defects in region 1 are represented by the monopole moment (the net charge) of the defect, thus the energy of region 2b is calculated as the 'induced relaxation energy due to the net charge of the defect' [16]. Further particulars of the exact mathematics used to calculate defect energies within GULP can be found within the GULP literature [16].

The size of the regions for the defect calculation is important. The larger the regions the more valid the approximations in the methodology become and hence the more accurate the defect energy becomes. However, the computational time increases dramatically with increasing region size. It is therefore necessary to find a balance between defect energy convergence (i.e. region sizes) and computation time. Figures 2.8 and 2.9 show the energy convergence for a Ce ion doped at a Ba site in $BaMgF_4$ with respect to the Mott-Littleton region sizes. Relative CPU time is also plotted. From this it can be seen that a region 1 size of at least 10 Å and a region 2 size of 13 Å is needed for convergence, with the CPU time increasing dramatically as the size of region 1 is increased while the size of region 2 has a smaller effect on the CPU time.

For the majority of the work within this thesis regions of 10 Å and 15 Å were used. Any results from larger region sizes are noted as such.

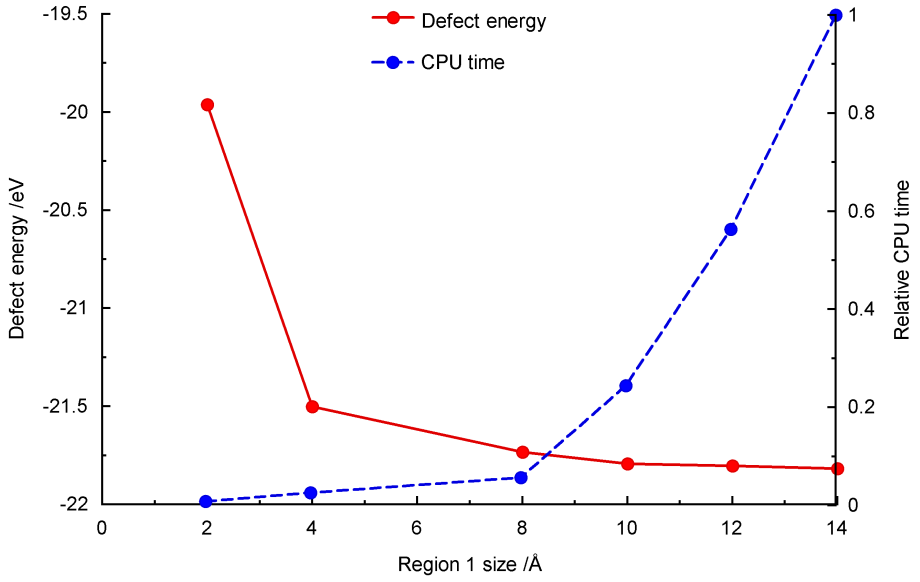

Figure 2.8: Convergence of defect energy with respect to region 1 size (region 2 size is held at 15 Å). The defect energy is for the substitution of a Ce^{3+} ion at a Ba site in $BaMgF_4$. CPU time is also given

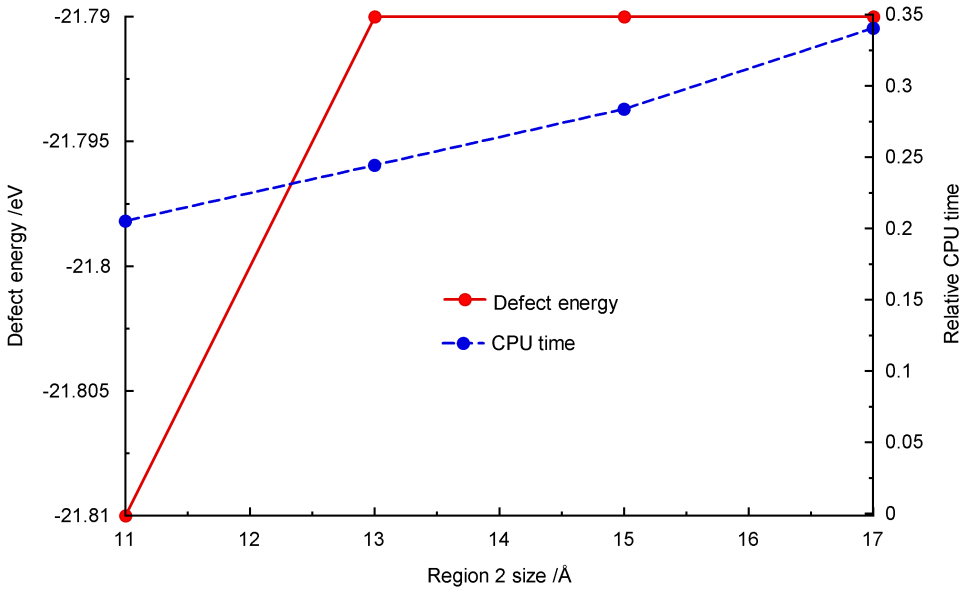

Figure 2.9: Convergence of defect energy with respect to region 2 size (region 1 size is held at 10 Å). The defect energy is for the substitution of a Ce^{3+} ion at a Ba site in $BaMgF_4$. CPU time is also given.

2.4.2 Rare earth dopants

The inclusion of dopants to the system requires potentials for the new ions. This work is concerned with the 14 rare earth elements, La to Lu (excluding Pm). Fortunately, Valerio and Jackson published a set of rare earth fluoride potentials in 2000 [114] that have been utilised in this work.

2.4.3 Solution energies

In order to be able to compare defect energies, for example different charge compensation mechanisms or different dopants, solution energies are used and not individual defect energies. Solution energies incorporate all of the terms in the reaction scheme (products minus reactants) and so can be directly compared. For example, consider the generic case of a dopant, D, within a lattice, MX, in Kröger-Vink notation (see Page 11), where the dopant has the same formal charge as the lattice cation.

$$DX + M_M \rightarrow D_M + MX$$

The solution energy for this reaction scheme would be:

$$E_{sol} = E_{latt}(MX) + E_{def}(D_M) - E_{latt}(DX) \tag{2.34}$$

2.4.4 Predicting doping limits

One important, and non-trivial, problem is predicting the doping limit of a particular dopant within a material. It is important to evaluate this as the level of solubility for dopant ions may have an effect on the application of the system. It is however, not a straight-forward problem to answer.

The first step is to write the doping reaction and generate the solution energy equation. To illustrate, consider the general doping reaction:

$$\alpha DX_3 + (1-\alpha)MNX_4 \rightarrow M_{1-\alpha}D_\alpha NX_4 + MX_3 \tag{2.35}$$

where D is the dopant, M and N are the lattice cations, X is the lattice anion and α is the mole fraction of dopant ions. The solution energy for this reaction would be:

$$E_{sol} = E_{latt}(M_{1-\alpha}D_{\alpha}NX_4) - [\alpha E_{latt}(DX_3) + (1-\alpha)E_{latt}(MX_3)] \tag{2.36}$$

The doping limit can be determined by setting E_{sol} to zero and solving for α. The problem arises with determining the lattice energy for the defective lattice, $E_{latt}(M_{1-\alpha}D_{\alpha}NX_4)$. A number of approaches to solve this problem have been suggested.

The first method considered here is the Jackson-Valerio (2011) method as published in [115]. In this the defective lattice energy is assumed to be equal to the perfect lattice plus the defect formation energy as determined from Mott-Littleton calculations, scaled by the mole fraction:

$$E_{latt}(M_{1-\alpha}D_{\alpha}NX_4) = (1-\alpha)E_{latt}(MNX_4) + \alpha E_{def}(D_M) \tag{2.37}$$

This approach does not take into account any defect-defect interactions as the defect energy is taken from an infinite dilution simulation and therefore the doping limit is the limit at which defects interact. The major problem with this method is that a divalent system such as CaF_2 does not work due to a reduction of terms through cancelling, resulting in a nonsensical equation.

The second method to determine the defect lattice energy is a modified version [116] of the previous [115]. Equation 2.36 remains the starting point, but the defective lattice is now considered to be equal to the perfect lattice plus α-amounts of the defect formation energy. The solution energy is given by:

$$\begin{aligned} E_{sol} = [E_{latt}(MNX_4) + \alpha E_{def}(D_M)] \\ - [\alpha E_{latt}(DX_3) + (1-\alpha)E_{latt}(MX3) + E_{latt}(NX)] \end{aligned} \tag{2.38}$$

For the case where $\alpha = 0$, i.e. there are no dopants present, the solution energy simplifies

to:

$$E_{sol} = E_{latt}(MNX_4) - [E_{latt}(MX_3) + E_{latt}(NX)] = E_{form}(MNX_4) \tag{2.39}$$

In this case the solution energy equals the formation energy of the perfect lattice. Rearranging Equation 2.36, with E_{sol} set to zero, to separate the α-terms and substituting for E_{form} gives:

$$\alpha = \frac{-E_{form}(MNX_4)}{E_{def}(D_M) + E_{latt}(MX_3) - E_{latt}(MX_3)} \tag{2.40}$$

This modified Jackson-Valerio method improves on some of the issues with the previous approach, however, the non-interacting defect assumption is still present.

Finally, it is possible to try to evaluate the defect lattice energy explicitly using supercells with varying concentrations of dopants, minimising the lattice energy and assuming a linear response to predict the maximum concentration of dopants. Besides the assumption of a linear response, the choice of minimisation freedom will affect the result. From a full constant pressure minimisation, with all degrees of freedom adjusted, the resulting optimised structure may barely resemble the initial structure when high concentrations of dopants are present. This leads to an inflation of the doping limit. The assumption of a linear response is also not valid and configurational entropy would need to be considered.

Within this work, a number of approaches are taken and the differences in the results discussed.

Chapter 3

Atomistic surface modelling

3.1 Introduction: the code METADISE

In any solid state system the surface structure and properties are of interest because it is at the surface that many reactions take place, and the surface properties may have an impact on any application the system is being investigated for use for. Modelling the surfaces is therefore an important, and vast, area of study.

Atomistic simulation of surfaces was pioneered by Tasker [14, 117] and Mackrodt and Stewart [118]. As with the early bulk simulations the first surface simulations were of simple systems such as cubic halides [117], MgO [119] and NiO [120]. After these, studies of more complex systems such as Cr_2O_3 [121] were carried out. The effects of oxidation [122] and temperature [123] on the surface structure were also later studied. In addition, methodologies for grain boundaries were developed with Duffy and Tasker studying the grain boundaries in NiO [124, 125].

In 1996, Watson et al. [126] published a new surface simulation code METADISE (Minimum Energy Techniques Applied to Dislocation, Interface and Surface Energies). This code aims to provide a full set of features to study linear and planar defects and is still under development today at the University of Bath.

All surface simulations within this work were carried out using METADISE (version 5.60), however there are other atomistic surface simulation codes that could have been used including MARVIN [127], which has been incorporated in GULP [16]. Electronic

surface modelling is also possible but it is more computationally demanding and does not provide this study with anything that atomistic methods cannot. In addition, it would have required a new set of modelling parameters, whereas using an atomistic approach allows for the same potentials and parameters as for the bulk simulations. Electronic surface modelling could not have been scaled to consider defect concentration effects easily either.

3.2 Perfect systems

Modelling surfaces involves cutting the unit cell at the Miller index under study and then systematically slicing through layers of atoms working through the repeat unit of that particular index to find the valid cuts. It is also possible to instead cut through individual atoms within each layer if required, however, this approach has not been taken in this work. A valid cut is one that is non-polar and therefore has a non-infinite surface energy. These can either be a type 1 or 2 surface as defined by Tasker [117]. In contrast, a type 3 surface has a dipole perpendicular to the surface and can only be studied if the surface is reconstructed to remove the dipole first. The three types of surfaces are shown in Figure 3.1. Once the valid surface planes have been found, the energy of them is calculated through energy minimisation techniques and this is used to predict morphologies and as a starting structure for any defect calculations.

3.2.1 Two region method

The approach taken by METADISE to simulate the surface is a two region one where the crystal is considered to be made up of planes of atoms periodic in two dimensions. Atoms in region 1, which lie close to the surface, are allowed to fully relax through minimisation techniques. The atoms in region 2 are fixed to represent the bulk. The size of region 1 is made sufficiently large so that the upper-most atoms relax completely without seeing the presence of region 2. This is checked through scaling of region sizes until convergence is achieved and lowest most ions in region 1 experience no displacement during relaxation, thereby ensuring there is no disjoint across the region boundary.

The interactions between the ions are described in exactly the same way as with bulk modelling with a long-range Coulombic term and a short-range potential. The energy of the system is calculated using the techniques discussed in Chapter 2, namely, energy minimisation through atomic coordinate shifting to achieve zero force. The only difference is with the calculation of the Coulombic term. In bulk simulations (i.e. 3-dimensional periodicity) the Ewald method is used to achieve convergence. For

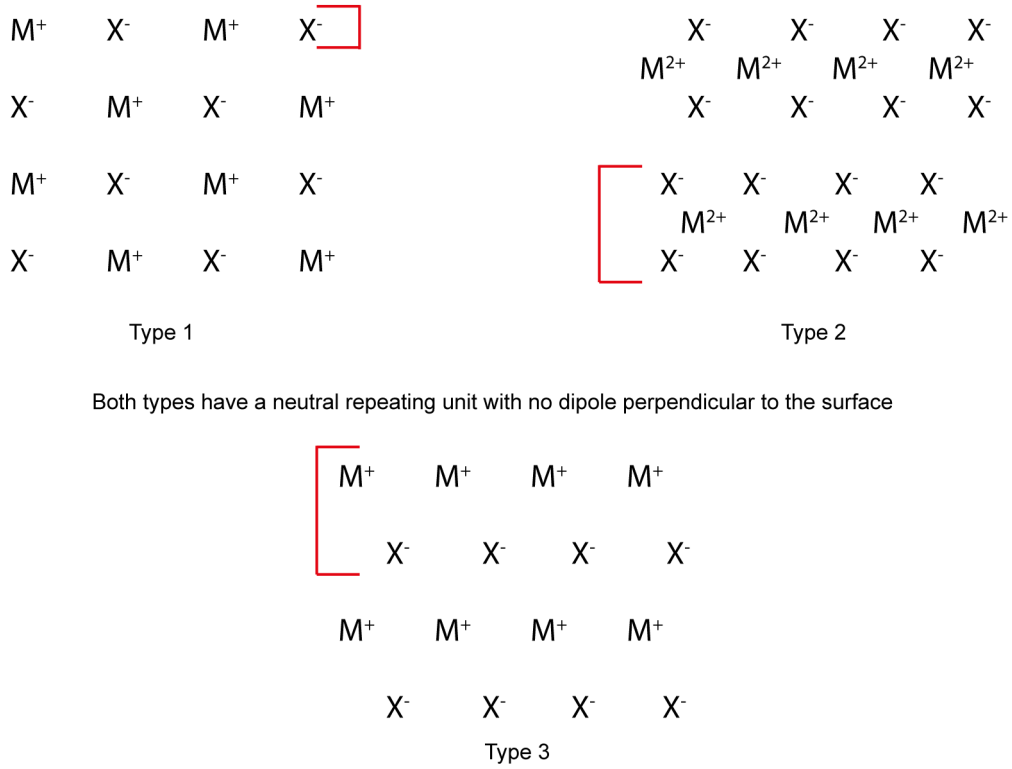

Figure 3.1: Figure showing the three types of surfaces as defined by Tasker [117]. Type 1 and 2 have repeat units that have no dipole perpendicular to the surface. The surface energy of these can be calculated, however, for type 3 there is a dipole and so the energy diverges. This dipole has to be removed before the surface energy can be calculated.

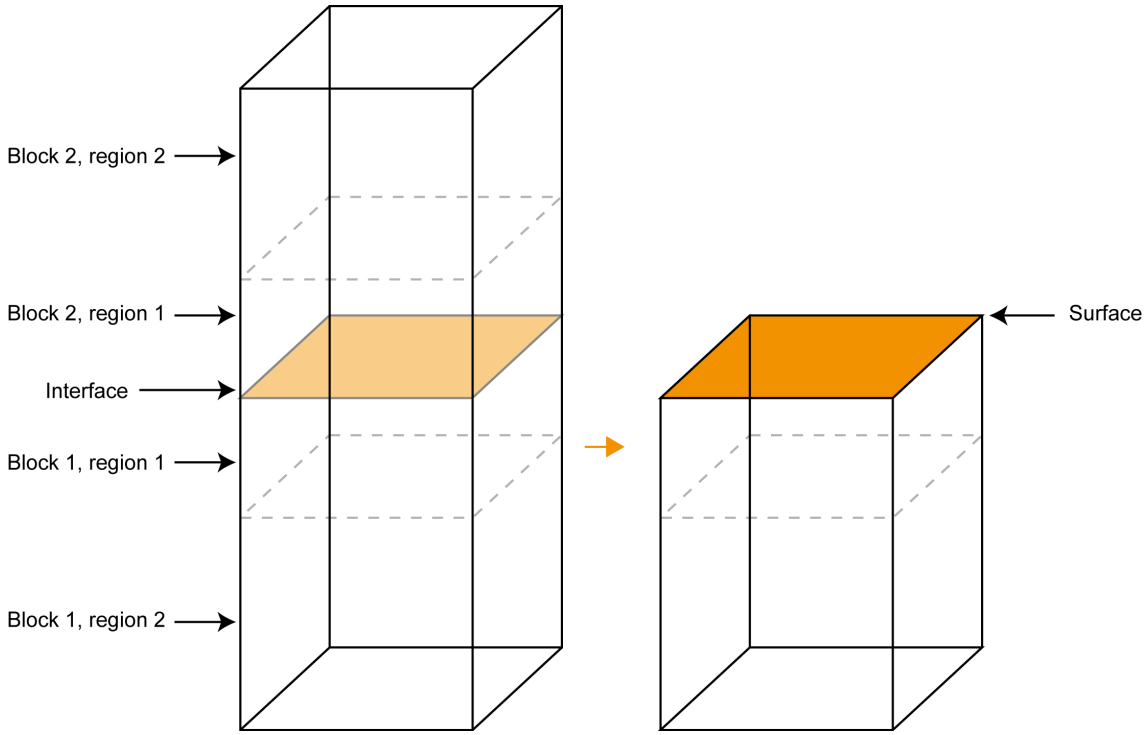

Figure 3.2: Two region approach in METADISE.

surface simulations (i.e. 2-dimensional periodicity) an analogue to the Ewald method is used that was developed by Parry [128].

3.2.2 Surface and attachment energy

Surface energy is defined as the energy per unit area needed to transform a bulk region into a surface region and is given by:

$$\gamma = \frac{E_{surf} - \frac{1}{2}E_{bulk}}{A} \tag{3.1}$$

where E_{surf} and E_{bulk} are the energies of the surface and bulk regions respectively and A is the surface area. The factor of a half arises due to the bulk calculation containing twice the number of the ions as the surface (Figure 3.2). A low, positive value indicates a stable surface.

It is also possible to express the energy of a surface in terms of attachment energy, which is defined as the energy released when a new layer of thickness d_{hkl} is added to the surface [129]. Although attachment energy is a thermodynamical quantity it can

be used as a pseudo-kinetic one [117] because it is a measure of the ease to which a new layer is added. The limitation with this method is that it is assumed there is bulk termination of the surface and no surface relaxation occurs [130]. Gay and Rohl with their MARVIN [127] code attempted to include relaxation into the attachment method, however it is unclear what this represents physically within the model [130]. This work therefore uses the two assumptions of bulk termination and no surface relaxation.

3.2.3 Morphology prediction

In 1901 Wulff, working from the earlier proposed theorem of Gibbs that the equilibrium form of a crystal should have minimal total surface free energy for a given volume [131], suggesting the equilibrium shape of a crystal is determined by the surface energies of its various surfaces such that the morphology is the shape that gives minimum total surface free energy [132].

The surface free energies can be assumed to be the surface energies obtained from static lattice simulations [133], because at 0 K, the surface free energy is a close approximation of the surface energy due to the entropy term in the surface free energy being small compared to the enthalpy term [134]. The height of the face is therefore proportional to the surface energy of that index. Thus, if two indicies have the same surface (free) energy they will have the same height. This theorem is only true if all surfaces form in equilibrium, thus a morphology plot using this technique is known as the equilibrium morphology.

Morphology predictions are important from an applicational viewpoint but they are also useful as a tool to check the model is simulating the system correctly. This is because it is difficult to compare surface energies to experimental results. Rather a comparison of the predicted morphology to the experimental morphology is made. One issue arises in this approach that experimental morphologies often depend on kinetic factors and not just thermodynamic ones [135]. Attachment energies have been used to try to overcome this problem by assuming the attachment energies are proportional to the growth rate for each surface producing a kinetic morphology [129, 136]. These

energies are exothermic and therefore the absolute value is taken when constructing the morphology such that those surfaces with low (absolute) attachment energy are the slow growing faces and therefore dominate the morphology. For the reasons discussed previously, attachment energies are not entirely satisfactory due to limitations in the calculation.

3.3 Defective systems

As with defect modelling in the bulk, there are broadly two approaches that can be taken for surface defects, either through a supercell in which the defect is repeated periodically throughout the crystal, or through an isolated approach. The work carried out in this thesis uses both methods depending on the type of calculation required.

3.3.1 CHAOS: infinite dilution method

For single defects, or small clusters of surface defects an infinite dilution approach was taken in a similar way to bulk defect modelling using the Mott-Littleton method. The CHAOS code developed by Duffy and Tasker [15] is integrated into METADISE and allows for such simulations.

CHAOS uses a two-region approach in which the crystal is divided into a region 1 and a region 2, with region 2 divided further in 2a and 2b. The interactions between ions in regions 1 and 2a are calculated explicitly, while those with the rest of the system are approximated using Mott-Littleton methods (see Section 2.4.1). Further approximations have to be made due to the unique properties of surface defect calculations; for example, the energy is calculated as a sum of planar and volume integrals rather than a summation [130, 120]. Also, the defect at the surface creates a dielectric discontinuity and therefore a dipole, which induces a dipole in region 2b. The interactions between region 1 and 2b therefore include these charged induced dipoles. It is assumed that the defect only effects the geometry locally around the defect and the rest of the crystal is only affected by the dipole. The sizes of regions 1 and 2a are selected as a trade-off between convergence and computation time.

3.3.2 Segregation energy

A useful value to calculate is the segregation energy of a defect. This is the difference between the energy of the defect within a bulk environment and the same defect at the

surface.

$$E_{seg} = E_{def}^{surf} - E_{def}^{bulk} \tag{3.2}$$

A negative segregation energy results from a lower defect energy at the surface, and thus a driving force for the defect to segregate to the surface exists. The driving force is proportional to the magnitude of the segregation energy. The segregation of defect ions to the surfaces would have an effect on the morphology of the system and may impact on the application of the material.

A number of theories, based on relative ion size, have been suggested to explain the segregation of defects [137, 138]. The primary drive for defect segregation, as suggested by McLean [139], is elastic strain induced by the defect ion in the lattice. The proposed relationship is given as:

$$E_{elastic} = \frac{6\pi B r^3 (\frac{\Delta r}{r})^2}{1 + \frac{3B}{4\mu}} \tag{3.3}$$

where r is radius of the lattice ion, Δr is the difference in radius between the defect and lattice ion, B is the bulk modulus of the defect and μ is the shear modulus of the lattice. μ is constant across all simulations and so if B is assumed to be constant across the rare earth ions, then the elastic strain, and hence the segregation energy, would be proportional to $(\frac{\Delta r}{r})^2$.

$$E_{strain} \propto \left(\frac{\Delta r}{r}\right)^2 \propto E_{seg} \tag{3.4}$$

A plot of segregation energy against $(\frac{\Delta r}{r})^2$ should produce a straight line plot if the above relationship is correct. This type of analysis has been performed for some systems, for example with haematite [140], and a highly significant correlation was found confirming the McLean theory. However, it was found that it was important to use the optimum segregation energy for the correlation to be high. The optimum segregation energy may not be equivalent to a single isolated defect at the surface, as defect-defect interactions may lower the energy at higher concentrations [140, 141, 142, 143].

3.3.3 Multiple defects

Considering isolated, infinite dilution defect energies and their segregation energies do not take into account binding energy between defects that may have an important impact. It also do not simulate real-world situations. It is therefore appropriate to attempt to consider clusters of defects within surface environments.

Using CHAOS and the same method as previously described, small clusters of defects can be considered. This resulting defect energy is the total defect energy for the cluster and includes the defect binding energy. This approach is advantageous due to the relative simplicity of the method and that while the defect is a cluster it is still in an infinite dilution meaning the configuration of the defects is less of an importance. However, to consider a large number of defects requires large region sizes to ensure convergence. The net result is this approach is best suited to small clusters of defects.

Furthermore, while the approach provides a defect energy (and therefore a segregation energy), it does not directly calculate the surface energy with the defects present. This is of importance if a prediction of the impact dopants on the equilibrium morphology is to be made. However, attempts have been made to relate segregation energy to the change in surface energy to overcome this limitation. This is discussed in the 'equilibrium segregation method' section.

Alternatively, a supercell approach allows for higher concentrations of defects and gives a direct calculation of the defective surface energy. In this method, the simulation cell is scaled such that there are many defect sites located at the surface, which are then filled with defects and the energy calculated as the difference between the energy of simulation cell with defects and the energy of the perfect simulation cell.

$$E_{def} = E_{surf}^{def} - E_{surf}^{perf} \tag{3.5}$$

3.3.4 Equilibrium segregation method

The first approach to calculate defective surface energies, which can then be used to study the impact of dopants on the crystal morphology, was put forward by Alfredsson

et al. (2007) and relates the segregation energy to the change in surface energy [144]. It will be referred to as the 'equilibrium segregation' (ES) method in this work.

Starting from a perfect, undoped surface, the surface energy is calculated as before using Equation 3.1. If a defect segregates to this surface, the energy is changed by the segregation energy, E_{seg}, amount. When n defects are present in the surface area, A, the defective surface energy is given by

$$\gamma_{def}(n) = \gamma_{perf} + \left(\frac{n}{A}\right) E_{seg} \tag{3.6}$$

This allows the surface energy to be calculated as a function of defect concentration using the CHAOS code to obtain segregation energies. If it is then assumed that the bulk contains an infinite reservoir of defects, each surface will reach a state where defects will segregate until the segregation energy is greater then zero independently from each other. This assumption is valid for large crystals with a high bulk to surface site ratio.

In low concentrations of defects, or small crystals, this assumption breaks down as the segregation process may complete at $n < n_{max}$, where n_{max} is the maximum number of defects for which there is still a segregation. In this case, a more complex analysis is needed as each surface cannot be considered independently from the other surfaces. The other extreme is where $n > n_{max}$, which may occur under non-equilibrium growth.

Equation 3.1 defines the surface energy as the difference between equal and stoichiometric regions of bulk and surface per surface area. The difficulties with calculating defective surface energies is that the surface (containing defects) may have a different stoichiometry to the bulk. The advantage to this method is that is resolves the issue of non-stoichiometry by not explicitly calculating a defective surface energy.

For low concentrations of defects, as a first approximation, the segregation energy can be assumed to be independent of the defect concentration. However, a more accurate surface energy can be obtained by modelling defect clusters in CHAOS to obtain the segregation energy. As the size of the cluster increases this calculation becomes increasingly more computationally demanding (due to the large region sizes required) and the configuration of the defects has to be considered.

3.3.5 Defective surface minimisation

An alternative approach is to consider the defects in the surface simulation block directly. It will be referred to as the 'defective surface minimisation' (DSM) method in this work. Defects are placed at surface sites within the simulation block and the energy of the block minimised in the usual way. The resulting block energy, E_{surf}^{def}, can be used to obtain the defective surface energy. As discussed previously, the difficultly is ensuring the bulk region is equivalent to the surface region. This is achieved by defining the defective bulk energy as

$$E_{bulk}^{def} = E_{bulk}^{perf} + E_{def} \tag{3.7}$$

where E_{def} is the defect energy, obtained through either Mott-Littleton or supercell calculations, for the same number of defects as in the surface region. The defective surface energy is therefore given by

$$\gamma_{def} = \frac{E_{surf}^{def} - \left(E_{bulk}^{perf} + E_{def}\right)}{A} \tag{3.8}$$

and this can be used to determine the lowest surface energy possible through systematically filling the defect sites from empty to full. Scaling the simulation cell increases the number of defect sites at the surface available and allows the effect of dopant concentration to be considered.

In considering large numbers of defects the configuration of the defects may be important. A Perl script was developed, based on a script created by David Cooke of Huddersfield University, to automate the generation of the defect configurations.

The simulation cell is first orientated to the index of interest and scaled to produce a large number of defect sites (typically around six). A perfect surface block is first minimised and the energy output, followed by one defect present, then two defects and so on considering all configurations of defects each time. The lowest surface energy block for each defect number is recorded along the corresponding configuration.

The advantage of using this approach as opposed to the ES method is that the defective surface block energy is calculated explicitly. This allows a full relaxation of

the surface block with the defects present, compared with just the addition of a defect energy in the ES method. The only assumption made in this method is that the bulk energy can be written as the perfect bulk plus a defect energy. This assumption is valid providing the defect energy is well minimised and results in the defective bulk block being stoichiometrically equivalent to the defective surface block.

It is possible to show that the two methods are equivalent and as such validate each other. Starting from ES equation (Equation 3.6):

$$\gamma_{def}(n) = \gamma_{perf} + \left(\frac{n}{A}\right) E_{seg}$$

$$\text{but,} \qquad E_{seg} = E_{def}^{surf} - E_{def}^{bulk}$$

$$\therefore \qquad \gamma_{def}(n) = \gamma_{perf} + \left(\frac{n}{A}\right) E_{def}^{surf} - E_{def}^{bulk}$$

$$\text{but,} \qquad E_{def}^{surf} = \left(E_{surf}^{def} - E_{surf}^{perf}\right)$$

$$\therefore \qquad \gamma_{def}(n) = \gamma_{perf} + \left(\frac{n}{A}\right) \left(E_{surf}^{def} - E_{surf}^{perf}\right) - E_{def}$$

$$\text{assume n=1 and} \qquad \gamma_{perf} = E_{surf}^{perf} - E_{bulk}^{perf}$$

$$\gamma_{def}(n) = \frac{-E_{bulk}^{perf} + E_{surf}^{def} - E_{def}}{A}$$

This is the same equation used in the DSM approach (Equation 3.8). The two methods are therefore equivalent. The only difference between them is the way the values to populate the equations are determined through simulation.

3.3.6 Defective morphology prediction

Obtaining defective surface energies for all low index surfaces using either method described above, allows predictions of the impact the defects have on the crystal morphology. Producing defective morphologies is not a trivial task however, as the effect of the defects depends on a number of factors.

The simplest scenario is when each surface reaches the lowest surface energy through having the optimum number of defects present. This will occur if each surface can reach

optimum defect coverage independently from the other surfaces. Providing the crystals are large, such that there is a high ratio of bulk to surface sites, and there is a high enough level of defects present this scenario would occur, as the remaining dopant ions would reside in the bulk. However, if there are too few defects present for all surfaces to reach their lowest surface energy, each surface cannot be considered independently. Instead, those surfaces with largest segregation energies would take the defects over those surfaces with lower segregation energies.

Chapter 4

$YLiF_4$

4.1 Structural description

$YLiF_4$ (YLF) is a material being researched as a solid state laser host lattice. It is particularly of interest because of the Y^{3+} cations present, which are of similar size and the same formal charge as the rare earth cations that provide the electronic structure for laser application.

The YLF crystal is obtained from a equimolar mixture of LiF and YF_3, and has the scheelite structure that belongs to the tetragonal crystal system with the centrosymmetric space group $I4_1/a$, with four formula units per cell. The structure is shown in Figure 4.1. Each Li^+ ion is located at the centre of a regular tetrahedron of four F^- ions and each Y^{3+} ion is surrounded by eight F^- ions forming a tetragonal dodecahedron [145] (Figures 4.2 and 4.3).

YLF is a naturally birefringent material, capable of producing linearly polarised output with virtually no depolarisation loss [146].

The structure used in this work was reported by Garcia [145].

4.1.1 Literature review

Since the 1970s rare earth doped YLF has been well known as a laser active medium. In the early days, research on this crystal was driven by the demand for Nd^{3+} -doped

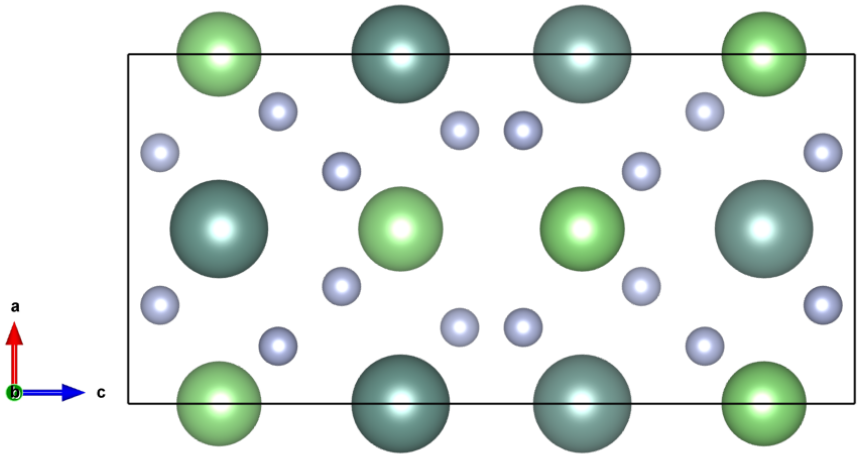

Figure 4.1: Unit cell of YLF as reported by [145]. The unit cell is 5.164 Å by 10.565 Å in size. The atoms are shown in relative ionic size.

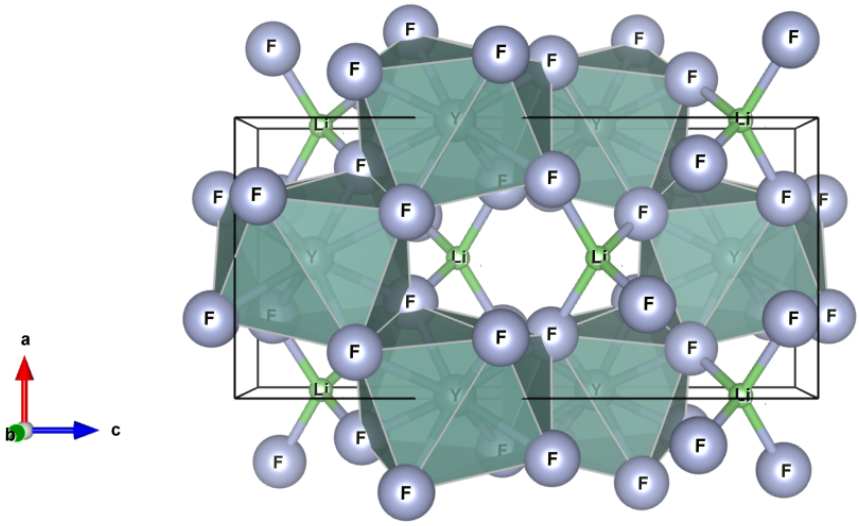

Figure 4.2: Unit cell of YLF showing the yttrium coordination. Each Y^{3+} ion is surrounded by eight F^- ions forming a tetragonal dodecahedron. The atoms are shown in relative ionic size.

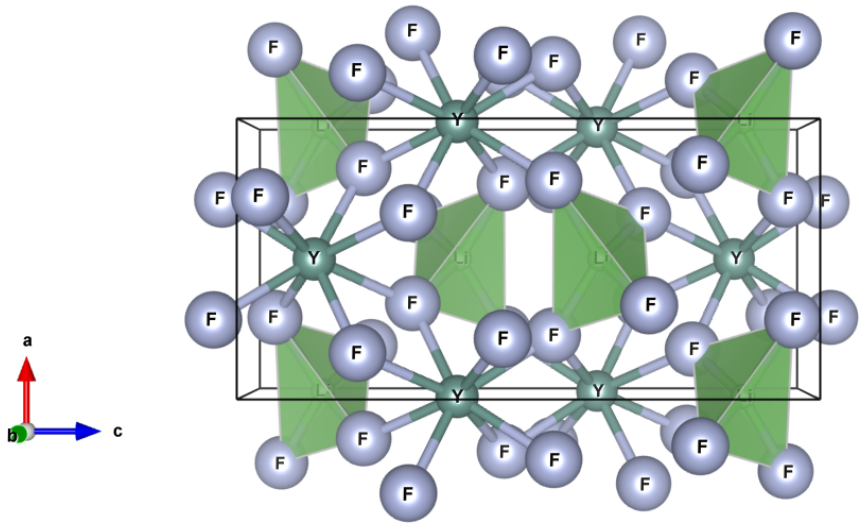

Figure 4.3: Unit cell of YLF showing the lithium coordination. Each Li^+ ion is surrounded by four F^- ions forming a regular tetrahedron. The atoms are shown in relative ionic size.

crystals, in particular because of some advantages of this host over the well researched and widely used Nd:YAG laser. Some of the advantages of YLF over YAG include longer fluorescence lifetime and smaller thermal lensing effect [147, 148]. There has been to date considerable research into YLF as a laser host lattice and it is also available as a commercial laser device [149]. YLF is particularly suited to UV laser applications because the YLF lattice has small absorption in the UV range.

Laser action in Ce:YLF was first demonstrated by Ehrlich [150], who observed a poor performance for this system resulting from the formation of permanent colour centres that absorb at the lasing transition. The Ce^{3+} ion is a good candidate for a UV tuneable laser source. The ground 4f state of Ce^{3+} splits into two levels, $^2F_{5/2}$ and $^2F_{7/2}$. The upper f level is not populated thermally at room temperature. The 5d state splits into four levels, and the transition between the 5d and 4s states provide a four level laser system. In 1993, the first demonstration of a large gain YLF laser system doped with Ce^{3+} was reported by Okada *et al.* [151]. Okada *et al.* reported a large gain and tunability when the crystal was excited at either 193 nm or 248 nm. In 1997, the local environment around the Ce^{3+} ion in YLF was studied further by Yosida *et al.* using electron spin resonance [152]. Baldochi in 1999 also reported the growth of Ce:YLF. Measurements revealed a dopant concentration of 0.15% with the initial melt

mixture at a doping concentration of 0.5% [153].

Other rare earth dopants have also been investigated. In 2001, Bensalah *et al.* reported the growth and properties of a YLF system co-doped with Tm^{3+} and Ho^{3+} building on the previous work into Tm, Ho:YLF [154, 155, 156]. The interest in co-doped systems arises due to the process where the energy is efficiently transferred from one dopant ion to the other. In this case the Tm^{3+} ions transfer energy to the Ho^{3+}. The paper reported that the distribution coefficients of the dopant ions were close to unity, as expected, due to the comparable ionic radius of the dopants. In 2007, Ranieri *et al.* reported the introduction of a third dopant ion to act as a second sensitiser. A YLF crystal co-doped with 0.5% Tm^{3+}, 20% Yb^{3+} and 1.3%$^{3+}$ Nd was grown. The paper concluded that the Nd^{3+} ion as a second sensitiser for Yb:Tm:YLF crystals 'improves the upconversion mechanism that gives rise to the Tm^{3+} blue emission in 475 nm and as such there is an efficient mechanism for energy transfer from Nd^{3+} to Yb^{3+} and from Yb^{3+} to Tm^{3+}' [157]. However, the paper did note that the concentration of Nd^{3+} must be around 0.8% to prevent back transfer from Yb^{3+} to Nd^{3+}, which is detrimental.

A Tm:YLF laser was reported in 2008 by Schellhorn [146]. This system was doped at 3.5% as this was found to be the optimum doping concentration because while 'increasing the Tm^{3+} doping level leads to a higher quantum yield (the number of ions excited to the upper laser level per absorbed pump photon), the rate of energy-transfer upconversion increases at higher doping levels and will give rise to an extra heat load in the laser crystal because of multiphonon relaxation of the up-converted ions' [146]. The lasing output was at 1910 nm.

A 1.7% doped Nd:YLF laser was reported by Santo *et al.* in 2006 with an output at 1047 nm (an IR laser) [158]. The doped YLF system was grown in fibres and it was reported that 'the Nd^{3+} incorporation and distribution is enhanced in the grown YLF fibres' [158] compared to bulk crystals. Another Nd:YLF laser was reported by Lu *et al.* in 2009 [159]. This was a 1% Nd^{3+} doped YLF laser system producing a laser transition of 1321 nm. The system was pumped directly into the emitting level by a diode laser at 880 nm. One of the most recent publications reports an Nd^{3+} doped YLF system

emitting at 1053 nm [160].

Yb^{3+} ions have also been incorporated in YLF. Yb-doped crystals have shown excellent properties such as efficiency, wide wavelength tunability and femtosecond pulse generation. These properties are due to the simple energy level structure of the Yb^{3+} ion. It consists of only two electronic multiplets, with a transition between them in the near infrared, leading to a relatively small quantum defect, low thermal loading, and reduced up-conversion losses [161, 162]. The strong electron-phonon interaction provides broad emission bandwidth also [163]. The system was doped to 5% and the output was in the wide range of 1009 to 1069 nm [164].

Other rare earth doped YLF laser systems reported in papers include Er^{3+} [165]. The successful growth of optically clear single crystals of YLF doped with rare earth ions depends not only on the growth process, but on the purity of the starting materials and the presence of certain complexes in the environment [153]. This has resulted a wide range of crystal growing techniques being used across the papers listed in this brief review.

In addition to the above experimental research into YLF a number of computer simulation studies have been carried out. Ogasawara *et al.* carried out a study in 2004 into the multiplet energy levels of all trivalent lanthanides in YLF using first-principles calculations [166]. The absorption spectra of Pr^{3+}, Ho^{3+}, and Tm^{3+} in YLF were also calculated. In 2009, Yin *et al.* published work into defect formation in the YLF lattice that may impact on the quality of the lasing action. F-type colour centres were modelled [167] as were Li vacancies [168]. The Yin group have also published a paper of DFT simulations of Yb^{3+} ions in YLF, concluding that the doping of Yb^{3+} can weaken the 330 nm absorption band [169]. They also note that 'it would be desirable to study different rare earth ions at the Y^{3+} site since this is the main experimental interest' [169] but that this is a difficult task with DFT simulations.

Rare earth doped YLF has also been reported as a laser cooling device, with a 5% Yb:YLF crystal having been shown to cool to 110 K [170].

This brief review highlights some of the work into YLF as a laser source. Most

research has focussed on the various growing techniques and spectrographic studies. Ce^{3+}, Nd^{3+}, Yb^{3+}, Tm^{3+}, Ho^{3+}, and Er^{3+} are the main rare earth ions that have been shown to produce laser systems of various qualities. There has been some limited computer simulation work, which has been DFT focussed.

4.2 Atomistic bulk modelling

4.2.1 Perfect system

In YLF, the ion interactions were modelled using potentials take from previous work on this material [110], and were in the form of electrostatic supplemented Buckingham potentials for the interactions between Y^{3+}-F^- and Li^+-F^-, while the F^--F^- interaction was modelled with a 4-range Buckingham potential (see page 38) and a Shell Model to represent the polarisability of these ions. The potentials used are given in Table 4.1. All potentials were cut so they acted between 0.0 Å and 10.0 Å. The values used in this work were selected based on a balance between convergence and computation time.

Interaction	A / eV	ρ / Å	C / eVÅ^6	Spline points		
Y^{3+}-F^-	1547.6200	0.3023	0.0000	-	-	-
F^--F^-	1127.7000	0.2753	15.8300	2.0000	2.7950	3.0310
Li^+-F^-	113.7200	0.3654	0.0000	-	-	-
Shell	F Shell q	$-1.59\ \|e\|$	K (F_{core}-F_{shell})	20.77 eVÅ^{-2}		

Table 4.1: Interatomic potentials used in the atomistic modelling of YLF taken from previous work [110]. All potentials are in the form of the Buckingham potential with the F^--F^- interaction described with a 4-range Buckingham potential.

These potentials accurately reproduce the system to within 2% of the observed [145] unit cell dimensions as shown in Table 4.2. Further properties, such as elastic constants and dielectric constants, can be used to confirm the model. Blanchfield and Saunders [171] report the elastic constants and bulk modulus (see Table 4.3). It should be noted that the potentials have not been fitted to the YLF structure, but rather taken from previous work for consistency, and therefore the fit to the reported elastic constants is rather poorer than might be expected if new potentials were fitted. Section 2.2.3 outlines the advantages of using transferred potentials where possible.

Parameter	Modelled /GPa	Reported [171] /GPa	Percentage difference /%
C_{11}	118.8	121.0	−1.8
C_{12}	49.2	60.9	19.2
C_{13}	62.1	52.6	18.1
C_{16}	−7.6	−7.7	−1.3
C_{33}	207.5	156.0	33.0
C_{44}	33.2	40.9	−18.8
C_{66}	24.0	17.7	35.6
Bulk modulus	88.0	80.0	10.0

Table 4.3: Comparison between reported elastic constants and bulk modulus, and modelled ones. Experimental values are quoted at room temperature.

Parameter	Modelled	Reported [145]	Percentage difference /%
a	5.193 Å	5.164	0.57
b	5.193 Å	5.164	0.57
c	10.565 Å	10.741	−1.64
$\alpha/\beta/\gamma$	90.000°	90.000°	0.00

Table 4.2: Comparison of modelled YLF unit cell parameters to the reported parameters [145].

Further physical properties are listed in Table 4.4 as calculated from the simulation.

4.2.2 Intrinsic defects

Defect calculations were performed using the Mott-Littleton method with region sizes of 10 Å and 15 Å for regions 1 and 2a respectively. These correspond to approximately 600 ions in region 1 and 1300 ions in region 2a. The lattice energies used throughout this chapter for defect calculations are listed Table 4.5; they were obtained from simulations using the potentials listed for consistency. The region sizes were chosen based on the need for converged defect energy values but also a sensible computation time.

Intrinsic defects are those that appear naturally within the system through thermal action and involve no non-native species. The first of these defects is the formation of a vacancy. Table 4.6 lists the formation energy of vacancies of the three constituent ions. It is assumed that all fluoride ions require the same energy to be removed from

Property	Modelled
Shear Modulus	36.2 GPa
Young's Modulus	x: 86.7 GPa z: 161.6 GPa
Poisson's Ratio	xy: 0.3 xz: 0.4 zx: 0.2 yz: 0.2
Static dielectric	xx: 9.2 yy: 9.2 zz: 8.8
High frequency dielectric	xx: 2.4 yy: 2.4 zz: 2.4
Static refractive indices	1: 3.0 2: 2.4 3: 2.4
High frequency refractive indices	1: 1.6 2: 1.6 3: 1.6

Table 4.4: Table listing physical properties of YLF obtained from the simulation.

System	E_{latt} /eV	Reference
YF_3	−52.465	calc.
LiF	−9.919	calc.
$YLiF_4$	−63.145	calc.
LaF_3	−49.701	[114]
CeF_3	−50.154	[114]
PrF_3	−50.596	[114]
NdF_3	−51.040	[114]
SmF_3	−51.244	[114]
EuF_3	−52.246	[114]
GdF_3	−52.238	[114]
TbF_3	−52.234	[114]
DyF_3	−52.850	[114]
HoF_3	−53.374	[114]
ErF_3	−53.466	[114]
TmF_3	−53.633	[114]
YbF_3	−53.961	[114]
LuF_3	−54.253	[114]

Table 4.5: Lattice energies of YF_3, LiF, $YLiF_4$ and all REF_3 studied as used in the calculation of solution energies.

Vacancy	Formation energy /eV
Y^{3+}	46.71
Li^+	7.91
F^-	4.73

Table 4.6: List of defect formation energies for the constituent ion vacancies in YLF.

the lattice as they are in similar environments. The second is interstitials, which are constituent ions at non-lattice sites. Table 4.7 lists the lattice sites considered in this thesis and the formation energy associated with forming an interstitial there for each of the three ions in this system. Figures 4.4 and 4.5 shows the location of these interstitial sites within the unit cell.

The Y^{3+} ion is the most energetically demanding to remove from the lattice requiring almost a 6 fold increase in energy over the Li^+ ion. It is therefore unlikely for Y^{3+} vacancies to be within the lattice. However, for the two interstitial sites studied, Y^{3+} has a favourable formation energy. In order to understand if Y^{3+} interstitials are likely to form, realistic models of the actual process involved have to be calculated. Interstitials are usually formed through Frenkel defects. A Frenkel defect is the movement of a ion

Lattice site		Formation energy /eV
a) 0.250, 0.000, 0.375	Y^{3+}	−34.88
	Li^{+}	−3.06
	F^{-}	−1.49
b) 0.250, 0.250, 0.250	Y^{3+}	−36.17
	Li^{+}	−5.18
	F^{-}	−0.98

Table 4.7: List of defect formation energies for the constituent ion interstitials in YLF.

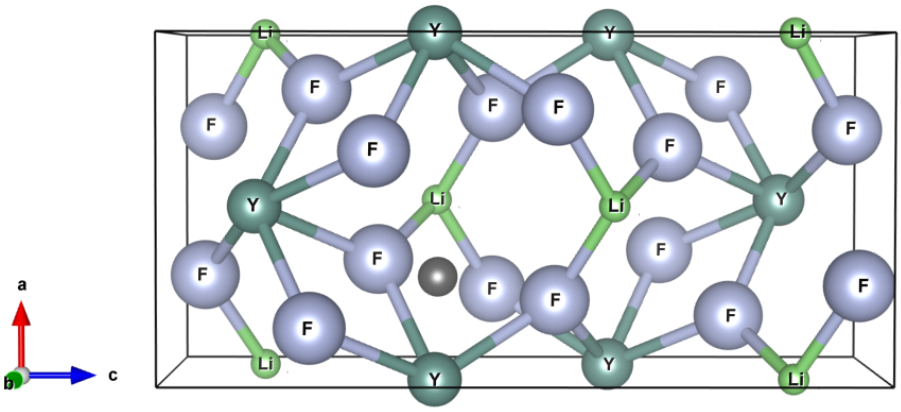

Figure 4.4: Unit cell of YLF showing the first interstitial site considered at fractional coordinates 0.250, 0.000, 0.375. The atoms are shown in relative ionic size.

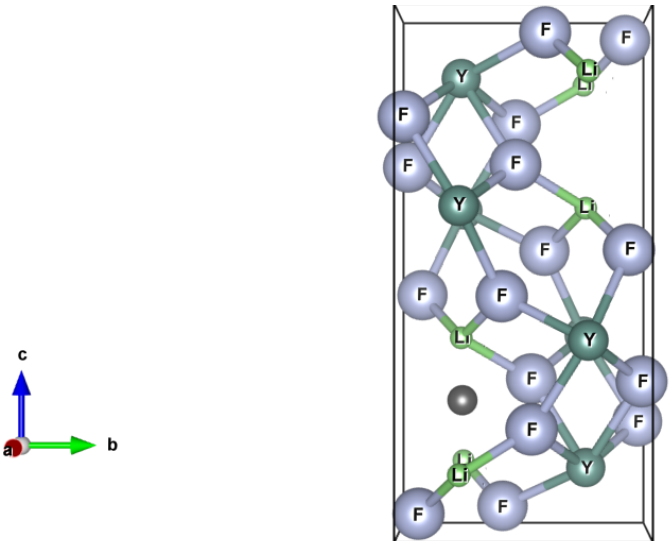

Figure 4.5: Unit cell of YLF showing the second interstitial site considered at fractional coordinates 0.250, 0.250, 0.250. The atoms are shown in relative ionic size.

from a lattice site to a non-lattice site. This is modelled by creating a vacancy and an interstitial. The other major form of intrinsic defect are Schottky defects. These are the creation of stoichiometric vacancies within the lattice. There are a number of types of Schottky defects that can be calculated; Schottky and pseudo-Schottky. The reaction schemes for all intrinsic defects studied are:

1. $E_{Frenkel} = E_{vac} + E_{int}$
2. $E_{Schottky} = Y_{vac} + Li_{vac} + 4(F_{vac}) + E_{latt}(YLiF_4)$
3. $E_{YF_3pseudo} = Y_{vac} + 3(F_{vac}) + E_{latt}(YF_3)$
4. $E_{LiFpseudo} = Li_{vac} + F_{vac} + E_{latt}(LiF)$

Defect	E_{def} /eV	E_{def}^{bound} /eV
Frenkel $(F)_a$	3.24	1.11
Frenkel $(F)_b$	3.75	2.34
Frenkel $(Y)_a$	11.83	2.54
Frenkel $(Y)_b$	10.53	2.03
Frenkel $(Li)_a$	4.85	3.35
Frenkel $(Li)_b$	2.73	1.41
Schottky	10.38	6.84
YF_3 pseudo-Schottky	8.42	4.32
LiF pseudo-Schottky	2.72	2.18

Table 4.8: List of intrinsic defects energies in YLF including Frenkel and Schottky defects. The Frenkel defects are considered at the two interstitial sites listed in Table 1.7

The intrinsic defect energies are given in Table 4.8. The Frenkel energies are subscripted 'a' and 'b' to correspond to the lattice site coordinates given in Table 4.7 for the interstitial location. The table lists two defect energies for each scheme. The first of these is obtained from adding the individual components that make up the total defect. For example, the Frenkel energy is obtained by adding the vacancy formation energy to the interstitial formation energy. The second value listed is for a bound defect energy. This is obtained from simulating the total defect in one calculation. For example, for the Frenkel defect a vacancy and an interstitial are modelled together. The advantage of this approach is that the binding energy of the two defects is included, which often

lowers the defect energy. The non-bound and the bound defect energies are both listed to provide a measure of the binding energy, as:

$$E_{binding} = E_{def}^{bound} - E_{def} \tag{4.1}$$

It can be seen from these that the lowest energy process is the formation of a F Frenkel at the (a) coordinate site, with the formation of a Li Frenkel at the (b) site at a similar low energy. These two intrinsic defects are therefore likely to dominate the YLF structure, although, most of the Frenkel defects modelled are at a relatively low energy (around 1 to 2 eV) and so are also likely. Schottky defects have defect energies greater than the Frenkel defects and are therefore less likely to form apart from at high temperatures.

The formation of Y^{3+} vacancies (Table 4.6) is a high energy process, which can be seen in the un-bound Y Frenkel defect energies. Despite this, the bound Y Frenkel defect energies are comparable to the other Frenkel defects. This is due to a large reduction in defect energy (due to a large binding energy) between the un-bound and bound simulations.

To quantify the likelihood of Frenkel and Schottky defects forming at a given temperature, the following equations may be used. In the Schottky equation (Equation 4.2), n_s is the number of Schottky defects, N is the number of lattice sites, E_{def} is the Schottky formation energy, k is the Boltzmann constant, and T is the temperature. In the Frenkel equation (Equation 4.3) n_f is the number of Frenkel defects, N_i is the number of interstitial sites available, and the other terms have the same meaning as before. These equations typically produce values that reveal intrinsic defects are very sparse at room temperatures, for example the Schottky defect energy in YLF gives the ratio of vacant sites as 3.7 x 10^{-59}. In reality, the ratio may be higher than this if the crystals are grown at a high temperature and cooled quickly.

$$n_s \approx N \exp\left(\frac{-E_{def}}{2kT}\right) \tag{4.2}$$

$$n_f \approx (NN_i)^{\frac{1}{2}} \exp\left(\frac{-E_{def}}{2kT}\right) \tag{4.3}$$

4.2.3 Rare earth dopant solution energies

The standard oxidation state of rare earth ions is 3+, as it is for yttrium, so when considering the doping of YLF, no charge compensation is required to maintain a neutral system if the rare earth ion dopes at the Y site. For doping at the lithium site there are a number of possible compensation methods. Two different Li substitution schemes, and the one Y scheme, are considered in this thesis.

1. $REF_3 + Y_Y \rightarrow RE_Y + YF_3$
2. $REF_3 + Li_{Li} \rightarrow RE^{\cdot\cdot}_{Li} + 2V^{'}_{Li} + 3LiF$
3. $REF_3 + Li_{Li} \rightarrow RE^{\cdot\cdot}_{Li} + V^{'''}_{Y} + V^{\cdot}_{F} + YLiF_4$

Solution energies for these reactions are given below and were used to calculate the energy required for each dopant reaction scheme.

$$\begin{aligned}
&1.\ E_{sol} = E_{latt}(YF_3) + E_{def}(RE_Y) - E_{latt}(REF_3) \\
&2.\ E_{sol} = 3(E_{latt}(LiF)) + 2(E^{Li}_{vac}) + E_{def}(RE_Y) - E_{latt}(REF_3) \\
&3.\ E_{sol} = E_{latt}(YLiF_4) + E^{F}_{vac} + E^{Y}_{vac} + E_{def}(RE_{Li}) - E_{latt}(REF_3)
\end{aligned} \tag{4.4}$$

The lattice energies used in all solution energy calculations are provided in Table 4.5. The potentials for the rare earth fluoride interactions were taken from [114] and are reproduced in Table 5.9. Upon carrying out the surface modelling work (see the next Chapter), two of the potentials were found to produce unphysical results. These were refitted using the methodology outlined in Section 2.2.3. Using these the solution energies for scheme 1 (doping at the Y site) can be calculated (Table 4.10).

The solution energies show that the doping process requires a small amount of energy and that the process becomes more favourable as the ionic radius of the dopant becomes smaller. This occurs because of the comparability of the host and dopant ionic radii. For

Interaction	A / eV	ρ / Å	C / eVÅ^6
La^{3+}-F^-	2817.74	0.2980	0.0
Ce^{3+}-F^-	2627.13	0.2980	0.0
Pr^{3+}-F^-	2453.39	0.2980	0.0
Nd^{3+}-F^-	2488.27	0.2950	0.0
Sm^{3+}-F^-	1764.57	0.3064	0.0
Eu^{3+}-F^-	2085.74	0.2950	0.0
Gd^{3+}-F^-	1667.02	0.3037	0.0
Tb^{3+}-F^-	1541.15	0.3065	0.0
Dy^{3+}-F^-	1536.68	0.3037	0.0
Ho^{3+}-F^-	2590.91	0.2809	0.0
Er^{3+}-F^-	1880.44	0.2920	0.0
Tm^{3+}-F^-	1390.19	0.3037	0.0
Tm^{3+}-F^-*	3173.80	0.2733	0.0
Yb^{3+}-F^-	2381.55	0.2808	0.0
Lu^{3+}-F^-	1448.23	0.2990	0.0
Lu^{3+}-F^-*	2901.80	0.2735	0.0

*Table 4.9: Rare earth fluoride potentials used in this work. Taken from [114]. The two potentials marked * were refitted for the defective surface modelling as the original potentials produced proved to be inadequate.*

RE	$E_{def}(RE_Y)$ /eV	Solution energy /eV
La	3.86	1.10
Ce	3.31	1.00
Pr	2.77	0.90
Nd	2.25	0.83
Sm	1.84	0.62
Eu	0.83	0.66
Gd	0.85	0.63
Tb	0.77	0.54
Dy	0.21	0.60
Ho	−0.37	0.54
Er	−0.50	0.50
Tm	−0.57	0.60
Yb	−0.99	0.51
Lu	−1.13	0.66

Table 4.10: Rare-earth dopant at Y site solution energies in YLF along with defect formation and lattice energies used in the calculations.

RE	E_{def} /eV	E_{def}^{bound} /eV	E_{sol} /eV	E_{sol}^{bound} /eV
La	−28.97	−14.62	6.79	5.32
Ce	−29.62	−15.52	6.59	4.88
Pr	−30.25	−16.12	6.41	4.72
Nd	−30.83	−16.67	6.27	4.61
Sm	−31.39	−17.19	5.92	4.30
Eu	−32.41	−18.19	5.90	4.30
Gd	−32.51	−18.27	5.79	4.21
Tb	−32.63	−18.38	5.66	4.09
Dy	−33.26	−19.00	5.65	4.09
Ho	−33.75	−19.51	5.68	4.12
Er	−33.99	−19.73	5.53	3.98
Tm	−34.20	−19.92	5.49	3.96
Yb	−34.47	−20.21	5.55	3.99
Lu	−34.85	−20.54	5.46	3.96

Table 4.11: Rare earth dopant at Li site solution energies in YLF along with the defect formation energies used in the calculations. Scheme 2; compensation of Li^+ vacancies.
$$E_{sol} = 3(E_{latt}(LiF)) + 2(E_{vac}^{Li}) + E_{def}(RE_Y) - E_{latt}(REF_3)$$

substitution at the Li lattice site two schemes were modelled. Table 4.11 lists the solution energy for scheme 2 which involves two Li^+ vacancies as charge compensation, as listed above in the reaction schemes. Vacancy defect energies needed for unbound calculations were given previously in Table 4.6. Table 4.12 shows the solution energy for scheme 3 (charge compensation via a Y^{3+} vacancy and F^- interstitial). Bound and unbound calculations are shown, which shows the effect of defect binding is approximately 1.5 eV.

The two charge compensation methods for doping at the Li site are of comparable energy when considering the bound solution energies. However, the energy for doping at the Y site is still more favourable. This is as expected due to the like charge of the cations and similar ionic radius. Figure 4.6 shows these solution energies graphically.

There is interest in co-doped YLF, for the reasons discussed in Chapter 1 relating to transfer techniques. Bensalah *et al* [40] looked at co-doping with Tm^{3+} and Ho^{3+}, as the addition of Tm^{3+} efficiently transfers the absorbed pumping energy into the Ho^{3+} metastable energy state. This was modelled, using the same method as above, and the bound solution energy calculated was 0.94 eV, which is comparable to the substitution of one dopant.

RE	E_{def}^{bound} /eV	E_{sol} /eV	E_{sol}^{bound} /eV
La	−17.98	9.02	4.54
Ce	−17.36	8.82	4.37
Pr	−16.75	8.64	4.20
Nd	−16.19	8.50	4.08
Sm	−15.67	8.15	3.77
Eu	−14.65	8.12	3.75
Gd	−14.57	8.02	3.67
Tb	−14.47	7.89	3.56
Dy	−13.85	7.88	3.56
Ho	−13.31	7.91	3.54
Er	−13.21	7.76	3.53
Tm	−13.06	7.72	3.55
Yb	−12.61	7.78	3.42
Lu	−12.44	7.96	3.54

Table 4.12: Rare earth dopant at Li site solution energies in YLF along with the defect formation energies used in the calculations. Scheme 3; compensation of Y^{3+} vacancies and F^- interstitials. $E_{sol} = E_{latt}(YLiF_4) + E_{vac}^F + E_{vac}^Y + E_{def}(RE_{Li}) - E_{latt}(REF_3)$

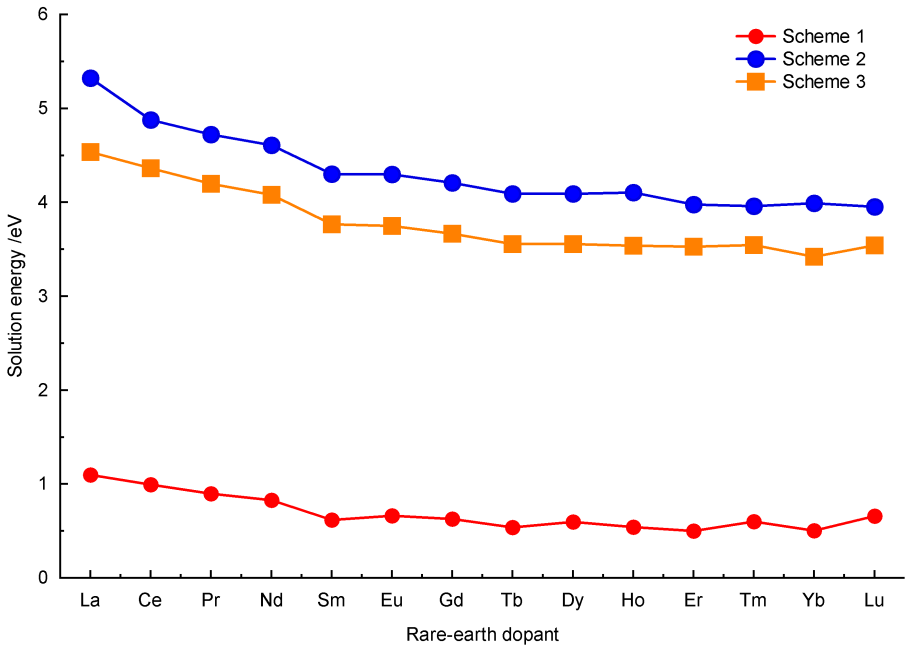

Figure 4.6: Plot of rare earth solution energies for the three schemes modelled.

4.2.4 Doping limit

As discussed in Section 2.4.4 an important, but non-trivial, calculation to make is to estimate the theoretical doping limit of the rare earth ions within the YLF lattice.

The first step in determining the doping limit is to write the solid-state reaction. In general form for YLF, with the rare earth ion doping at the Y site, this is:

$$xMF_3 + (1-x)\,YF_3 + LiF \rightarrow Y_{(1-x)}xM_Y^{\cdot}LiF_4 \tag{4.5}$$

where MF_3 is the rare earth fluoride and x is the mole fraction of dopant ions. The solution energy can be determined in the usual way and is given by:

$$E_{sol} = E_{latt}\left(Y_{(1-x)}xM_YLiF_4\right) - \\ \left[E_{latt}\left(xMF_3\right) + E_{latt}\left((1-x)\,YF_3\right) + E_{latt}\left(LiF\right)\right] \tag{4.6}$$

The doping limit can be determined by setting E_{sol} to zero and solving for x, the mole fraction of dopant ions. The problem arises with determining the lattice energy for the defective $YLiF_4$ lattice, $E_{latt}\left(Y_{(1-x)}xM_YLiF_4\right)$.

The first method considered to overcome this problem is the Jackson-Valerio 2011 method as published in [115]. In this, the defective lattice energy is assumed to be equal to the perfect $YiLF_4$ lattice plus the defect formation energy as determined from Mott-Littleton calculations. Both terms are adjusted by the mole fraction of dopant ions.

$$E_{latt}\left(Y_{(1-x)}xM_YLiF_4\right) = (1-x)\,E_{latt}\left(YLiF_4\right) + xE_{def}\left(M_Y\right) \tag{4.7}$$

The solution energy is then given by:

$$E_{sol} = \left[(1-x)\,E_{latt}\left(YLiF_4\right) + xE_{def}\left(M_Y\right)\right] - \\ \left[E_{latt}\left(xMF_3\right) + E_{latt}\left((1-x)\,YF_3\right) + E_{latt}\left(LiF\right)\right] \tag{4.8}$$

Table 4.13 lists the solution energy functions for each of the rare earth ions and the

RE	Function	Max % MF_3 /%
La	$E_{sol} = 64.24x - 0.76$	1.18
Ce	$E_{sol} = 64.14x - 0.76$	1.19
Pr	$E_{sol} = 64.04x - 0.76$	1.19
Nd	$E_{sol} = 63.97x - 0.76$	1.19
Sm	$E_{sol} = 63.76x - 0.76$	1.19
Eu	$E_{sol} = 63.81x - 0.76$	1.19
Gd	$E_{sol} = 63.77x - 0.76$	1.19
Tb	$E_{sol} = 63.69x - 0.76$	1.20
Dy	$E_{sol} = 63.74x - 0.76$	1.19
Ho	$E_{sol} = 63.69x - 0.76$	1.20
Er	$E_{sol} = 63.65x - 0.76$	1.20
Tm	$E_{sol} = 63.75x - 0.76$	1.19
Yb	$E_{sol} = 63.65x - 0.76$	1.20
Lu	$E_{sol} = 63.81x - 0.76$	1.19

Table 4.13: Concentration method for rare earth doping in YLF based on the Jackson-Valerio 2011 method [115]. x in the function is molefraction of MF_3 used. The max percentage is found by setting E_{sol} to zero.

maximum doping percentage based on this equation.

The results suggest that the YLF lattice is not very soluble to rare earth ions, with a maximum doping of 1.2%. The doping limit being constant across the rare earth ions is the other observation. In reality, it would be expected that the doping limit is low based on the criteria used, however, with the large difference in defect formation energies across the rare earth group a change in doping limit might be expected.

To understand these results it is important to consider the assumptions made in the calculation. Firstly, the defect formation energy is for a single, infinite dilution defect and does not take into account any defect-defect binding energy. Such binding energy often lowers the overall defect formation energy for multiple defect clusters and would increase the maximum doping limit. Therefore, the doping limit obtained from this calculation is the doping limit for *non-interacting* defects.

There are a number of problems with this approach, which may explain the consistent doping limit across the rare earth group. The calculation is highly sensitive to the lattice energies and is not affected by the defect energy (due to the relative magnitude of the numbers). The sensitivity is such that a small change of just 1% in a lattice energy, can alter the doping limit by up to 80%.

The second method to determine the defect lattice energy is a modified version [116] of the previous method [172]. Equation 4.6 remains the starting point, but the defective lattice is now considered to be equal to the perfect lattice plus x-amounts of the defect formation energy.

$$E_{latt}\left(Y_{(1-x)}xM_YLiF_4\right) = E_{latt}\left(YLiF_4\right) + xE_{def}(M_Y) \tag{4.9}$$

The difference in this approach to the previous is that the perfect lattice energy is not scaled by the mole fraction of dopant ions (compare Equation 4.7 to 4.9). This equation is more logical than the previous Jackson-Valerio method as the defect formation energy includes the change in the perfect lattice to the defective one. Also, in the previous method the Li and F amounts were scaled by the mole fraction as well the Y sites, despite these amounts not changing. This new approach is more robust and solves the problem that occurred with divalent dopants in the old method.

Considering the case when $x = 0$, i.e. there are no dopants present, the solution equation simplifies to:

$$E_{sol} = E_{latt}\left(YLiF_4\right) - \left[E_{latt}\left(YF_3\right) + E_{latt}\left(LiF\right)\right] = E_f\left(YLiF_4\right) \tag{4.10}$$

In this case, the solution energy equals the formation energy of $YLiF_4$. Rearranging Equation 4.6, with E_{sol} set to zero, to separate the $x-$terms and substituting for $E_{form}\left(YLiF_4\right)$ gives:

$$x = -\frac{E_{form}\left(YLiF_4\right)}{E_{def}\left(M_Y\right) + E_{latt}\left(YF_3\right) - E_{latt}\left(MF_3\right)} \tag{4.11}$$

Combining Equations 4.10 and 4.11 allows the doping limit, x, to be calcuated. Table 4.14 lists the calculated percentages of x using this methodology.

The immediate difference with the values from this method is a change across the rare earth group that is more in line with what is expected. Lu has double the doping limit of La (1.5% compared to 0.7%), which correlates with the solution energies for the

RE	Max % MF_3
La	0.69
Ce	0.76
Pr	0.85
Nd	0.92
Sm	1.23
Eu	1.15
Gd	1.22
Tb	1.41
Dy	1.28
Ho	1.40
Er	1.52
Tm	1.33
Yb	1.51
Lu	1.49

Table 4.14: Concentration method for rare earth doping in YLF based on a modified Jackson-Valerio method [116].

single defects. The largest value of 1.5% is still very low, however this calculation still assumes that the defects are non-interacting. This is an important value to know as in some applications it is important to have non-interacting defects. Even in applications were some interaction is not an issue, comparing the non-interacting defect doping limit for various systems/dopants gives a guide to the solubility allowing the optimal combination of lattice and dopant/s to be found.

It would be possible to extend this approach to consider interacting dopants by calculating the defect formation energy for clusters of 2, 3, 4, etc. dopants and using the lowest defect formation energy per dopant from these calculations in Equation 4.11. However, in practice this requires more calculations, does not provide any major advantage over the simpler single defect calculation, and, in the case of YLF, only increases the doping percentage slightly.

Another assumption made in this method is that the unit cell of the lattice is minimally effected by the presence of the dopant ions. This arises because the calculation is based on the energy of the formation of a single defect. High levels of doping may be possible under extreme conditions that distort the unit cell and destroy space-group symmetry. These conditions cannot be calculated using a single defect formation energy

calculation.

Within the literature, YLF is typically doped from around 0.1% to 2%. Some papers report higher concentrations ([146][164]) than that, however, most list the dopant concentration based on the ratio in the crystal melt. This may not be the dopant concentration in the resulting crystal.

The aim of calculating the maximum doping limit is to obtain a measure that can be compared across systems and doping reactions in a simple method. Additionally, for most applications the doping level is small and the resulting lattice is similar to the original. In conclusion, there is no reason to attempt to calculate the defective lattice energy directly as the modified Jackson-Valerio method provides an approach of worth.

4.2.5 Thermal effects

Most lattices expand with temperature and using free energy minimisation (see Section 2.3.2) the expansion of the lattice parameters can be modelled. Using this type of minimisation also allows the potentials to be tested with increasing temperature. Two methods for calculating the free energy were taken. The first, Full Free Energy Minimisation (FFEM) minimises the unit cell and the internal degrees of freedom with respect to the free energy, whereas the second, Zero Static Internal Stress Approximation (ZSISA) minimises only the unit cell with respect to the free energy with the internal degrees of freedom minimised with respect to the internal energy. Generally ZSISA is the more robust approach to take as FFEM tends to drive the system toward instability [16] through the creation of soft modes as a result of the coupling to the free energy. This was the case for YLF too. FFEM minimisation above 300 K oscillated around the minimum resulting in hundreds of cycles. Whereas, with ZSISA the number of minimisation cycles stayed low (less than 70) up to the highest modelled temperature (1000 K). The data from FFEM was therefore disregarded and the results that follow use the ZSISA approach.

Figure 4.7 shows the change in the 'a' parameter, 'c' parameter, volume, and free energy with temperature from 0 K to 1000 K. The calculations were performed at

constant pressure. The 'a' parameter initially increases in size with temperature, up to around 300 K, before there is a decrease in size. This is followed, at 600 K, by a flat region with no change in the parameter with increasing temperature. This no-change region may be a result of an inadequate approach or the potentials breaking down at this temperature. The inclusion of a Shell Model into the potential form can result in difficulties at higher temperatures, as the core and shell may separate. Another possibility is a phase change.

At higher temperatures, the 'c' parameter also shows a similar pattern of no change in its size. At lower temperatures there is an increase in size with temperature after 250 K. Before this the data fluctuates.

The unit cell volume increases (almost) linearly up to 600 K, despite the decrease in the 'a' parameter. After 600 K, as before, the volume stops increasing.

Overall, these three plots reveals that the volume of the unit cell increases linearly with temperature, with the increase a result of the 'a' parameter increasing between 0 K and 300 K, and then a result of the 'c' parameter increasing after 250 K. Data after 600 K is ignored. As discussed previously, the harmonic motion assumptions used in this method mean that the method tends to breakdown above half of the melting point of the material. In the case of YLF this limit is at 675 K.

The final plot in Figure 4.7 shows the change in free energy with temperature.

A line-of-best-fit was fitted to the 'a' vs temperature plot for values up to 300 K so that the thermal expansion coefficient could be calculated and compared to experimental data. The same was done for the 'c' parameter, but over the temperature range 250 K to 600 K. These regions were chosen because they are the linear section of the plots. The gradients of these lines were used to calculate the linear thermal expansion coefficient for the two axes using Equation 4.12, where L_0 is the initial parameter length and $\frac{\Delta L}{\Delta T}$ is the calculated gradient.

$$\alpha = \frac{1}{L_0}\frac{\Delta L}{\Delta T} \tag{4.12}$$

A similar analysis was carried out for the volume resulting in the volume thermal expansion coefficient. Table 4.15 lists these coefficients and any experimental data.

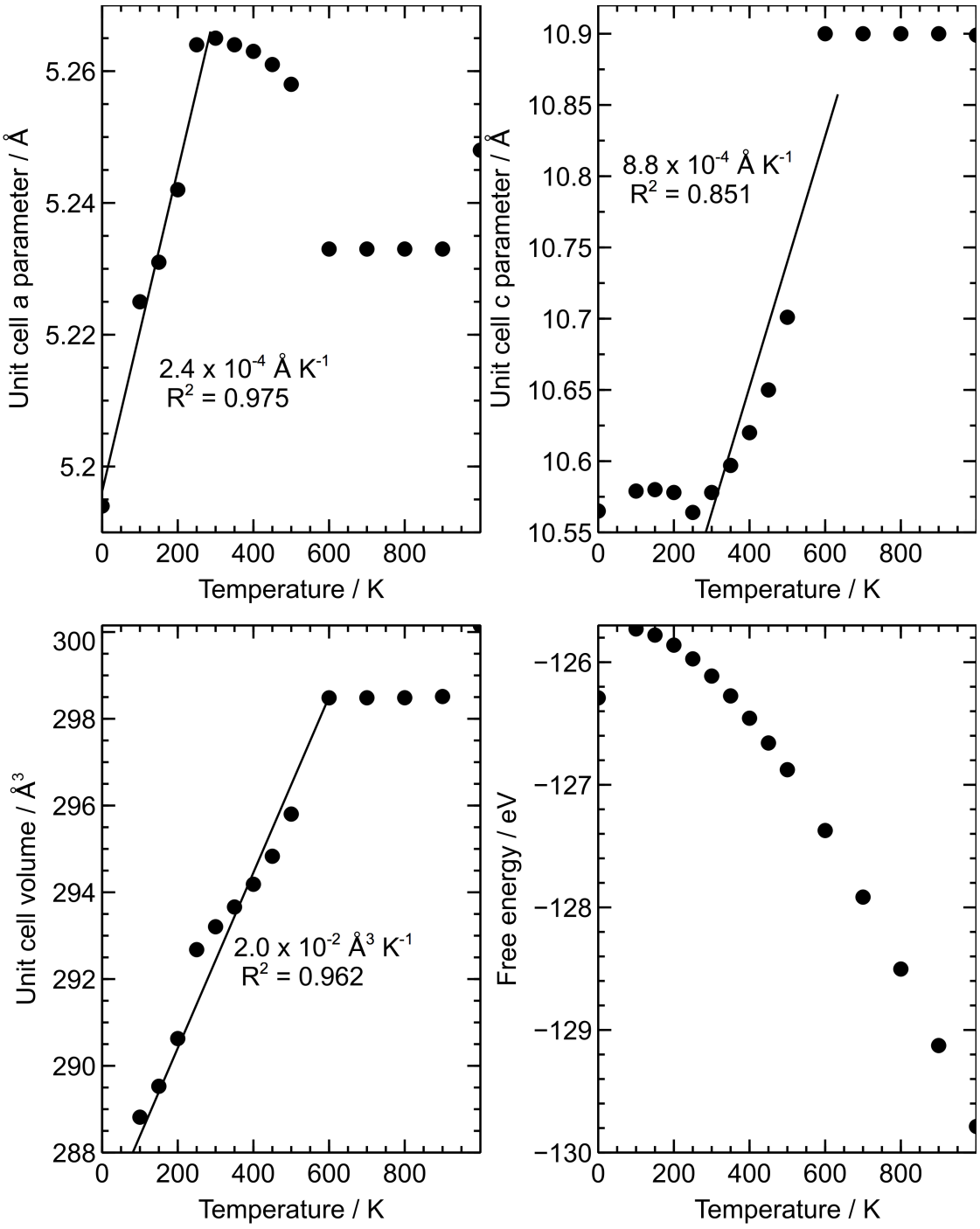

Figure 4.7: Plots of the free energy simulations for YLF using ZSISA. Plot top-left shows the change in the unit cell parameter 'a' with temperature. A function is fitted from 0 K to 300 K with the gradient displayed. The plot top-right shows the change in the unit cell parameter 'c' with temperature. A function is fitted from 250 K to 600 K with the gradient displayed. The plot bottom-left shows the overall change in volume with temperature. A function is fitted from 0 K to 600 K and the gradient displayed. The plot bottom-right shows the change in free energy with temperature.

Parameter	Thermal expansion coefficient	
	Modelled / K^{-1}	Reported [173] / K^{-1}
a	4.62×10^{-5}	1.33×10^{-5}
c	8.33×10^{-5}	8.30×10^{-6}
Volume	7.02×10^{-5}	-

Table 4.15: Comparison of calculated and reported thermal expansion coefficients.

Where data is available the coefficients calculated from the simulation are larger than the reported ones, although, for the 'a' parameter the value is in the same order of magnitude.

The discrepancies may be due to the approximations made in the thermal simulations. It is also important to note that the starting structure was obtained at room temperature yet is assumed to be the 0 K structure in the simulation. Nevertheless, the poor agreement with the experimental thermal expansion coefficients and the unstable FFEM suggest that the potentials are not suited to considering thermal effects and would have to be refitted before any non-static calculations were made.

Despite some concerns about the suitability of the potentials for non-static calculations, the results presented here are interesting. The decrease in the 'a' parameter of the unit cell between 300 K and 600 K has not been reported to date and should be the subject of further work.

4.2.6 Laser cooling

There is interest in YLF as a laser cooling crystal as well as a laser host matrix, with 5% Yb:YLF having been shown to cool to 110 K [170]. A lower temperature may not have been achieved due to defects with the crystals where undesirable non-radiative decay occurred. One class of defect are transition metal ions that act as acceptors for excitation energy from the excited rare earth ion. The use of crystals appears to offer an advantage over glasses that have been used in many other studies, as the growth of the crystal is in itself a purification process. It tends to exclude ions that are not part of the perfect crystal lattice, and it is selective for certain oxidation states for the impurities that do get incorporated. In YLF, to a first approximation, transition metal

Transition metal ion	Potential parameters		
	A /eV	ρ /Å	C /eVÅ^6
Co (II)	2514.01	0.2490	0.00
Cr (II)	744.55	0.3120	0.00
Cr (III)	1005.91	0.3044	0.00
Cu (I)	2860.66	0.2070	0.00
Cu (II)	2219.60	0.2540	0.00
Fe (II)	728.90	0.3060	0.00
Fe (III)	714.11	0.3300	0.00
Mn (II)	2929.58	0.2520	0.00
Mn (III)	1195.20	0.2910	0.00
Ni (II)	940.00	0.2980	0.00
Ti (III)	710.90	0.3390	0.00
V (II)	2971.00	0.2487	0.00
V (III)	709.50	0.3310	0.00

Table 4.16: List of derived transition metal fluoride potentials used in this work.

ions with oxidation states of 1+ and 3+ are likely to be incorporated more preferentially than 2+ and 4+ ions, as there are 1+ and 3+ sites in the crystal. While this may be a good initial guess, it is not necessarily true as non-isovalent defect incorporation may be equally as probably when binding energy between the defect and the charge compensation is considered.

As 2+ transition metals are believed to be most detrimental to laser cooling, Dr Hehlen from Los Alamos National Laboratory, NM, USA suggested to the Jackson research group at Keele University that this assumption might explain why Yb:YLF works as well as it does. In order to provide some evidence for this argument and to provide guidance on purification strategies to achieve sub-100 K laser cooling, a range of transition metal defect solution energies were calculated.

A new set of transition metal fluoride potentials was developed using the method outlined in Section 2.2.3. They were in the form of rigid-ion Buckingham potentials with a 'C' parameter set to zero. Table 4.16 lists the derived potentials and Table 4.17 lists the structures they were fitted too, along with the percentage difference between the modelled structure and the reported. All structures are reproduced to within 2% of the reported with the exception of CuF_2, which is within 3%.

These newly derived potentials were used to calculate the solution energy of incor-

Transition metal fluoride	Space group	Modelled structure a /Å	b /Å	c /Å	Reported structure a /Å	b /Å	c /Å	Percentage difference / % a	b	c	Reference
Co (II)	136	4.682	4.682	3.188	4.696	4.696	3.179	−0.30	−0.30	0.20	[174]
Cr (II)	14	4.841	4.843	3.378	4.732	4.718	3.505	2.30	2.64	−3.63	[175]
Cr (III)	167	4.869	4.869	13.696	4.986	4.986	13.214	−2.35	−2.35	2.97	[176]
Cu (I)	216	4.264	4.264	4.264	4.264	4.264	4.264	0.00	0.00	0.00	[177]
Cu (II)	14	3.208	4.734	5.554	3.309	4.569	5.362	−3.06	3.61	3.59	[178]
Fe (II)	136	4.733	4.733	3.274	4.693	4.693	3.301	0.84	0.84	−0.80	[179]
Fe (III)	167	5.070	5.070	13.728	5.194	5.194	13.335	−2.39	−2.39	2.95	[180]
Mn (II)	136	4.825	4.825	3.332	4.874	4.874	3.300	−1.00	−1.00	0.98	[181]
Mn (III)	15	9.049	5.109	13.051	8.920	5.047	13.475	1.45	1.23	−3.14	[182]
Ni (II)	52	4.604	4.601	3.134	4.648	4.647	3.075	−0.95	−0.99	1.93	[179]
Ti (III)	167	5.342	5.342	14.145	5.442	5.442	13.630	−1.84	−1.84	3.78	[183]
V (II)	136	4.774	4.774	3.281	4.806	4.806	3.237	−0.66	−0.66	1.36	[184]
V (III)	167	5.085	5.085	13.758	5.168	5.168	12.438	−1.60	−1.60	2.38	[185]

Table 4.17: Table listing the reported structures of the transition metal fluorides studied in this work. The modelled structures are also listed and the percentage difference between the two. All reported unit cell angles are 90 °except for CrF_2: $\beta = 96.52°$, MnF_3: $\beta = 92.64°$, CuF_2: $\beta = 121.11°$, and for TiF_3, VF_3, and Cr_3: $\gamma = 120°$. FeF_3: $\alpha = \beta = \gamma = 57.94°$.

Transition metal fluoride	Lattice energy / eV
CoF_2	−30.089
CrF_2	−27.929
CrF_3	−56.759
CuF	−11.394
CuF_2	−27.929
FeF_2	−28.691
FeF_3	−55.022
MnF_2	−29.055
MnF_3	−57.570
NiF_2	−29.996
TiF_3	−53.251
VF_2	−29.444
VF_3	−54.889

Table 4.18: List of lattice energies for the transition metal fluorides based on the derived potentials.

porating the transition metal into a Yb:YLF lattice. The lattice energies of the 13 transition metal fluorides, calculated using the potentials, are given in Table 4.18.

Eight different reaction schemes were considered for the transition metal (TM) incorporation.

For 1+ ions they were:

1A. $TMF + Li_{Li} \rightarrow TM_{Li} + LiF$

1B. $TMF + Y_Y \rightarrow TM_Y'' + 2V_F^{\cdot} + YF_3$

For 2+ ions:

2A. $TMF_2 + Y_Y \rightarrow TM_Y' + V_F^{\cdot} + YF_3$

2B. $TMF_2 + Y_Y + LiF \rightarrow TM_Y' + Li_i^{\cdot} + YF_3$

2C. $TMF_2 + Li_{Li} \rightarrow TM_{Li}^{\cdot} + F_i' + LiF$

2D. $TMF_2 + 2Li_{Li} \rightarrow TM_{Li}^{\cdot} + V_{Li}' + 2LiF$

For 3+ ions:

3A. $TMF_3 + Y_Y \rightarrow TM_Y + YF_3$

3B. $TMF_3 + 3Li_{Li} \rightarrow TM_{Li}^{\cdot\cdot} + 2V_{Li}^{'} + 3LiF$

Two approaches were taken to calculate the solution energy for the incorporation of the transition metal ions. In the first, the transition metal ion was added to a YLF lattice using a Mott-Littleton infinite dilution method with a single Yb^{3+} ion introduced as a defect at the same time. This approach did not allow for the 5% Yb doping, as used in the laser cooling paper by Seletskiy *et al.* (2011) [170], to be studied directly. However, it did include the binding energy between a single Yb^{3+} ion and the transition metal ion. Solution energies for this approach for the eight reaction schemes are given below. The Yb^{3+} defect energy, $E_{def}(Yb_Y)$, is subtracted off to provide the solution energy for just the transition metal ion incorporation.

$$
\begin{aligned}
1A.\ & E_{sol} = E_{latt}(LiF) + E_{def}(Yb_Y + TM_{Li}) - E_{latt}(TMF) - E_{def}(Yb_Y) \\
1B.\ & E_{sol} = E_{latt}(YF_3) + E_{def}(Yb_Y + TM_Y^{''} + 2V_F^{\cdot}) - E_{latt}(TMF) - E_{def}(Yb_Y) \\
2A.\ & E_{sol} = E_{latt}(YF_3) + E_{def}(Yb_Y + TM_Y^{'} + V_F^{\cdot}) - E_{latt}(TMF_2) - E_{def}(Yb_Y) \\
2B.\ & E_{sol} = E_{latt}(YF_3) + E_{def}(Yb_Y + TM_Y^{'} + Li_i^{\cdot}) - E_{latt}(TMF_2) - E_{def}(Yb_Y) \\
2C.\ & E_{sol} = E_{latt}(LiF) + E_{def}(Yb_Y + TM_{Li}^{\cdot} + F_i^{'}) - E_{latt}(TMF_2) - E_{def}(Yb_Y) \\
2D.\ & E_{sol} = E_{latt}(2LiF) + E_{def}(Yb_Y + TM_{Li}^{\cdot} + V_{Li}^{'}) - E_{latt}(TMF_2) - E_{def}(Yb_Y) \\
3A.\ & E_{sol} = E_{latt}(YF_3) + E_{def}(Yb_Y + TM_Y) - E_{latt}(TMF_3) - E_{def}(Yb_Y) \\
3B.\ & E_{sol} = E_{latt}(3LiF) + E_{def}(Yb_Y + TM_{Li}^{\cdot\cdot} + 2V_{Li}^{'}) - E_{latt}(TMF_3) - E_{def}(Yb_Y)
\end{aligned}
\tag{4.13}
$$

Table 4.19 lists the resulting solution energies from the infinite dilution method. The table is ordered alphabetically by the transition metal ion.

The second approach used a Mean Field to approximate the 5% Yb^{3+} doped YLF lattice. A Mean Field calculation assigns partial charges to the Y sites within the lattice, such that each site is a hybrid ion consisting of 95% Y^{3+} and 5% Yb^{3+}. The potentials are scaled to match. The transition metal ions were then incorporated using

Transition metal ion	Reaction scheme	Solution energy / eV
Co (II)	2A	3.56
Co (II)	2B	3.41
Co (II)	2C	3.93
Co (II)	2D	3.39
Cr (II)	2A	3.29
Cr (II)	2B	3.21
Cr (II)	2C	4.29
Cr (II)	2D	3.30
Cr (III)	3A	2.85
Cr (III)	3B	5.01
Cu (I)	1A	1.49
Cu (I)	1B	5.23
Cu (II)	2A	3.54
Cu (II)	2B	3.39
Cu (II)	2C	3.92
Cu (II)	2D	3.37
Fe (II)	2A	3.49
Fe (II)	2B	3.38
Fe (II)	2C	3.68
Fe (II)	2D	3.21
Fe (III)	3A	2.72
Fe (III)	3B	4.96
Mn (II)	2A	3.22
Mn (II)	2B	3.11
Mn (II)	2C	4.43
Mn (II)	2D	3.44
Mn (III)	3A	2.58
Mn (III)	3B	4.06
Ni (II)	2A	4.98
Ni (II)	2B	4.87
Ni (II)	2C	5.94
Ni (II)	2D	4.95
Ti (III)	3A	2.43
Ti (III)	3B	4.34
V (II)	2A	3.32
V (II)	2B	3.22
V (II)	2C	4.42
V (II)	2D	3.43
V (III)	3A	2.71
V (III)	3B	4.97

Table 4.19: Table listing the solution energies for the 13 transition metal ions studied using the eight infinite dilution reaction schemes. The corresponding solution energy equations are given in Equation 4.13.

a Mott-Littleton method into the Mean Field lattice. This approach simulates the same doping percentage as used in the Seletskiy *et al.* paper. A downside to this is that, for any reaction schemes involving defects at an Y site, the defect energy is for the hybrid Yb^{3+}-Y^{3+} site rather than a pure Y^{3+} one. The solution energy equations for this second approach are given below.

$$
\begin{aligned}
1A.\ \ & E_{sol} = E_{latt}(LiF) + TM_{Li} - E_{latt}(TMF) \\
1B.\ \ & E_{sol} = E_{latt}(YF_3) + TM_{Y}^{''} + 2V_{F}^{\cdot} - E_{latt}(TMF) \\
2A.\ \ & E_{sol} = E_{latt}(YF_3) + TM_{Y}^{'} + V_{F}^{\cdot} - E_{latt}(TMF_2) \\
2B.\ \ & E_{sol} = E_{latt}(YF_3) + TM_{Y}^{'} + Li_{i}^{\cdot} - E_{latt}(TMF_2) \\
2C.\ \ & E_{sol} = E_{latt}(LiF) + TM_{Li}^{\cdot} + F_{i}^{'} - E_{latt}(TMF_2) \\
2D.\ \ & E_{sol} = E_{latt}(2LiF) + TM_{Li}^{\cdot} + V_{Li}^{'} - E_{latt}(TMF_2) \\
3A.\ \ & E_{sol} = E_{latt}(YF_3) + TM_{Y} - E_{latt}(TMF_3) \\
3B.\ \ & E_{sol} = E_{latt}(3LiF) + TM_{Li}^{\cdot\cdot} + 2V_{Li}^{'} - E_{latt}(TMF_3)
\end{aligned}
\tag{4.14}
$$

Table 4.20 lists the resulting solution energies from the Mean Field method. The table is ordered alphabetically by the transition metal ion as before.

Table 4.21 summaries the solution energies for both methods and is ordered by solution energy. The tables shows there is good agreement with the order of the transition metal ions across the two methods. Additionally, for each ion the reaction scheme that was the lowest energy was the same across both methods. All 1+ ions substituted at the Li site (scheme 1A). This was expected as the lattice ion and the defect ion have the same formal charge. Likewise, all 3+ ions substituted at the Y site (scheme 3A) for the same reason. The six most favoured substitutions are the 1+ and 3+ ions, with the 2+ ions at higher solution energy.

For the 2+ ions the lowest energy reaction was varied. For ions Mn^{2+}, Cr^{2+}, V^{2+}, and Ni^{2+}, the preferred substitution was at the Y^{3+} site with a Li^{+} vacancy. Whereas, Fe^{2+}, Cu^{2+}, and Co^{2+} substituted at the Li^{+} site with a Li^{+} vacancy. The ionic radius of the Y^{3+} ion is larger than the Li^{+} ion, which correlates with those transition metal

Transition metal ion	Reaction scheme	Solution energy / eV
Co (II)	2A	2.21
Co (II)	2B	2.58
Co (II)	2C	4.62
Co (II)	2D	2.09
Cr (II)	2A	1.92
Cr (II)	2B	1.84
Cr (II)	2C	2.44
Cr (II)	2D	2.01
Cr (III)	3A	1.35
Cr (III)	3B	4.41
Cu (I)	1A	−0.01
Cu (I)	1B	4.23
Cu (II)	2A	2.19
Cu (II)	2B	2.50
Cu (II)	2C	3.70
Cu (II)	2D	2.08
Fe (II)	2A	2.11
Fe (II)	2B	2.11
Fe (II)	2C	3.54
Fe (II)	2D	1.94
Fe (III)	3A	1.22
Fe (III)	3B	4.39
Mn (II)	2A	1.83
Mn (II)	2B	1.75
Mn (II)	2C	2.76
Mn (II)	2D	2.14
Mn (III)	3A	1.08
Mn (III)	3B	3.97
Ni (II)	2A	3.59
Ni (II)	2B	3.19
Ni (II)	2C	5.32
Ni (II)	2D	3.65
Ti (III)	3A	0.93
Ti (III)	3B	4.26
V (II)	2A	1.95
V (II)	2B	1.53
V (II)	2C	3.14
V (II)	2D	1.92
V (III)	3A	1.20
V (III)	3B	4.40

Table 4.20: Table listing the solution energies for the 13 transition metal ions studied using the eight Mean Field reaction schemes. The corresponding solution energy equations are given in Equation 4.14.

ions that substitute at the Y^{3+} site rather than the Li^{+} (with the exception of Ni^{2+}).

The results suggest that the assumption that 2+ defect ions are unlikely to be present in Yb:YLF, which is one reason why the system works well as a laser cooling crystal, is correct. The solution energy for the incorporation of all 2+ defect ions studied were greater than the 1+ and 3+ defects ions. The most likely defect ions to be incorporated into the Yb:YLF lattice are Cu^{+1} and Ti^{3+}, which both have small solution energies of less than 1 eV (based on Mean-Field simulation). The other 3+ ions, Mn^{3+}, V^{3+}, Fe^{3+}, Cr^{3+}, also have small solution energies but are greater than 1 eV (but less than 1.5 eV). The six ions mentioned would incorporate into the Yb:YLF lattice if present and therefore if a purer Yb:YLF lattice is desired these ions should be removed from the growing conditions. The 2+ ions with the lowest solution energies, that should also be considered during the production of the Yb:YLF crystal are V^{2+}, Mn^{2+}, Cr^{2+}, and Fe^{2+} which have energies less than 2 eV.

Infinite dilution			Mean field		
Transition metal ion	Reaction scheme	Solution energy / eV	Transition metal ion	Reaction scheme	Solution energy / eV
Cu (I)	1A	1.49	Cu (I)	1A	−0.01
Ti (III)	3A	2.43	Ti (III)	3A	0.93
Mn (III)	3A	2.58	Mn (III)	3A	1.08
V (III)	3A	2.70	V (III)	3A	1.20
Fe (III)	3A	2.72	Fe (III)	3A	1.22
Cr (III)	3A	2.85	Cr (III)	3A	1.35
Mn (II)	2B	3.11	V (II)	2B	1.53
Fe (II)	2D	3.21	Mn (II)	2B	1.75
Cr (II)	2B	3.21	Cr (II)	2B	1.84
V (II)	2B	3.22	Fe (II)	2D	1.94
Cu (II)	2D	3.37	Cu (II)	2D	2.08
Co (II)	2D	3.39	Co (II)	2D	2.09
Ni (II)	2B	3.87	Ni (II)	2B	3.19

Table 4.21: Solution energies for the transition metal doping schemes using both methods ordered by solution energy. The table shows there is good agreement across both methods.

4.2.7 Summary

In summary, the intrinsic thermal defects for YLF have been modelled and the defect formation energies calculated. These show that the Frenkel defect energies are lower than the Schottky energies, with the two lowest energy defect formations being a F Frenkel and a Li Frenkel.

The interionic potentials used in this work were tested at various temperatures and were found to be inadequate above 600 K, however, this may have been due to the harmonic motion approximation used in the calculations. As such, if non-static simulations were to be performed the potentials should be refitted or the model parameters adjusted. The thermal expansion profiles up to 600 K revealed that the 'a' lattice parameter increases linearly in size with temperature up to 300 K but then decreases. The 'c' lattice parameter increases linearly only after 250 K. Despite this, overall the volume increases linearly however. This unusual decrease in the 'a' parameter should be the subject of a future study. The thermal expansion coefficients calculated were different to those listed in the literature - 4.62 x 10^{-5} K^{-1} calculated, 1.33 x $10^{-5}\,K^{-1}$ reported.

Solution energies for the doping of rare earth ions into the lattice were also calculated and concluded that doping at the Y site is the most favourable process as the Li site has a five-fold increase in energy compared to the Y site. This forms the basis of all further defect work into YLF.

Various methods were considered to calculate the doping limit for the dopant ions within the YLF lattice. A modified Jackson-Valerio [116] was determined to provide a good measure of the doping limit and could be used to compare the doping solubility of various dopant ions within a lattice, or a dopant ion's solubility in various host lattices. The limit calculated is strictly for non-interacting defect ions and as such always provides small doping limits, however, as a tool for comparing trends across dopants or host lattices it could be extremely useful. The maximum doping was calculated for Yb^{3+} at 1.51%.

Finally, the likelihood of transition metal ion defects being incorporated into a

Yb:YLF lattice was studied as a result of the work into YLF as a laser cooling device. The results suggest that the 1+ and 3+ transition metal ions are most likely to be incorporated into the lattice with Cu^{1+} and Ti^{3+} being the most likely. In order to ensure an optimal crystal for the laser cooling application 1+ and 3+ transition metal ions should be not allowed to contaminate the growing environment. The 2+ ions have higher solution energies.

The impact of this work in the field of lasers comes from a number of results. Firstly, the confirmation that the rare earth ions will substitute at the Y site is an important result when considering the structure of these doped materials. The large difference in the solution energies between substituting at the Y and Li sites effectively means that rare earth ions will be exclusively at Y cation sites within the lattice unless very harsh conditions (high temperature and fast quenching) are used during crystal growth. Secondly, the ability to calculate the doping limit for each of the rare earth ions provides a useful measure when designing a laser system. For high power laser applications, high concentrations of dopant ions would be required and therefore a dopant with higher solubility in the host lattice should be selected.

4.3 Atomistic surface modelling

The surface structure of any ionic material is an important property especially when doping is required for application purposes. The surface properties of YLF were studied using METADISE with the same potential set as used in the bulk modelling work. The results are presented in this section.

4.3.1 Methodological detail

The bulk studies given in Section 4.2.3 showed that rare earth dopants are most likely to dope at the Y site. This was used as the basis for the surface work in this section.

All potentials and cut-offs remained the same as those used before and are listed in Table 4.1. Mott-Littleton region sizes for surface defects, using the CHAOS code, were 9 Å and 35 Å for regions 1 and 2a respectively. Region 1 was chosen as a balance between converged values and calculation size. Region 2 was set to a suitable value based on the region size criteria built into the code. Within CHAOS some combinations of region sizes result in charged spheres and these must be avoided.

4.3.2 Surface and attachment energies

Surface and attachment energies were calculated for all of the valid cuts up to the 2nd index. Table 4.22 lists these for the most stable cut along with the area of each surface. The lowest surface energy corresponds to the (112) surface, which is therefore the most stable, and the second most stable is the (011) surface. The slowest growing surface is the index with the highest attachment energy and that is the (001) surface.

The lowest energy (i.e. most stable) repeat unit for each surface is given in Figure 4.8. Each box represents the surface atomic makeup, with the ions at a height of 0.0 Å being the surface termination. The block is repeated to generate the full structure. In some cases, the repeating unit is large. These repeat units contain a mirror plane, such that the ions above the mirror are reflected below it to form the complete repeat unit. Most surfaces are anion terminated, with the exceptions of (110), (121), and (221).

Index	Surface area /$\mathring{A}^2$	Surface energy /Jm^{-2}	Attachment energy /eV/unit-cell
(001)	26.972	0.718	−0.101
(010)	54.869	0.657	−0.161
(011)	61.140	0.596	−0.160
(012)	76.946	0.750	−0.367
(021)	113.004	0.645	−0.972
(110)	77.597	0.717	−0.308
(111)	82.151	0.635	−0.401
(112)	94.505	0.560	−0.260
(120)	122.691	0.744	−0.139
(121)	125.621	0.725	−0.584
(122)	134.027	0.766	−1.220
(210)	122.691	0.818	−1.225
(211)	125.621	0.645	−0.853
(221)	157.520	0.838	−1.147

Table 4.22: Surface and attachment energies for YLF along with the surface area of each index. Attachment energy is scaled per unit cell. Indices up to index 2 were modelled and the energies quoted are for the most stable cut.

Of these exceptions only one surface, (110), has a mixed cation termination.

4.3.3 Morphology predictions

The morphologies of YLF were constructed using a Wulff construction. Both the equilibrium (surface energy based) and the growth (attachment based) morphology were drawn and they are shown in Figure 4.9. The two morphologies show considerable differences. The (001) surface dominates the growth morphology (46.74%), whereas in the equilibrium morphology it is a much smaller surface (2.28%). Also, the (112) surface, which dominates the equilibrium morphology, does not appear in the growth based model. Table 4.23 lists the percentage surface area coverage for the surfaces appearing in the equilibrium and growth morphologies, as well as the coverage in the unrelaxed equilibrium morphology. These values are based on unrelaxed surface energies and are largely meaningless, however, they allow the extent of relaxation in the surfaces to be seen. For example, the high index surface (211) appears in the equilibrium morphology (1.78%) due to a large reduction in surface energy through relaxation. It does not appear in the unrelaxed morphology. Two other surfaces, (010) and (111), also appear

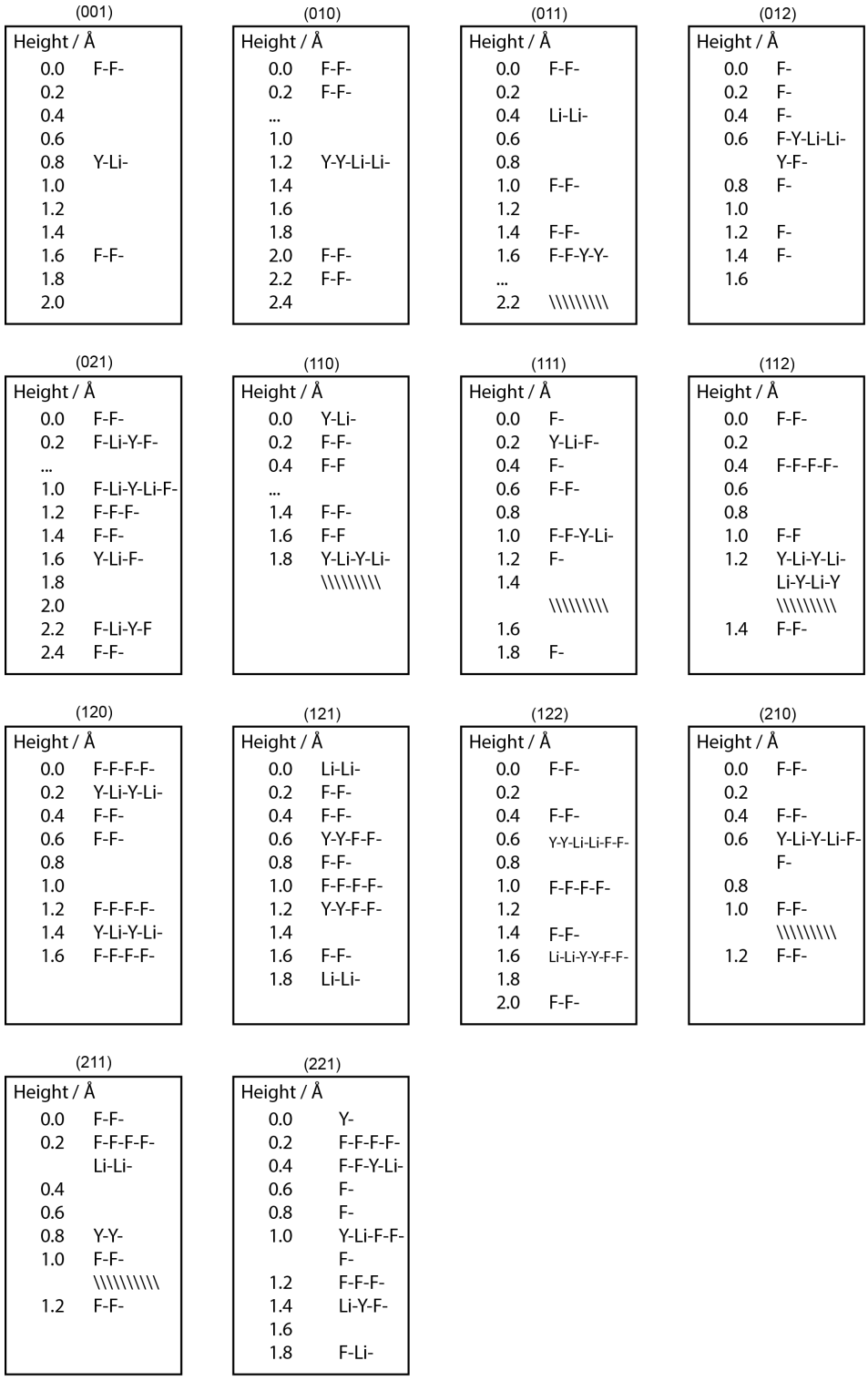

Figure 4.8: The lowest energy (i.e. most stable) terminations the low index surfaces of YLF. Each box contains the repeat unit for that surface. The uppermost ions form the surface termination layer. Note that some height scales are abbreviated for space reasons. Some boxes contain a mirror plane, indicated by \\\, for the same reason. The ions above the mirror are reflected below it to form the complete repeat unit.

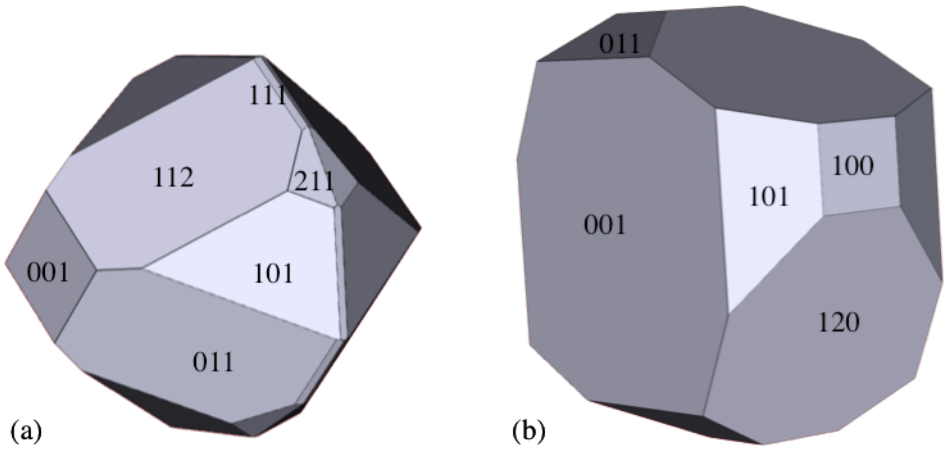

Figure 4.9: Equilibrium (a) and growth morphologies of YLF (b).

Surface	Percentage coverage		
	Unrelaxed	Equilibrium	Growth
(001)	1.22%	2.28%	46.74%
(010)	-	0.71%	5.31%
(011)	49.42%	30.07%	13.17%
(111)	-	6.30%	-
(112)	49.36%	58.86%	-
(120)	-	-	34.78%
(211)	-	1.78%	-

Table 4.23: Surface area percentage coverage of each surface appearing in predicted morphologies.

only after relaxation. The stability of these three surfaces reduces the size of the (011) surface in the equilibrium morphology.

Many other studies have found a similar situation in which the two morphologies are different from each other [17][186][133]. This is to be expected because morphologies depend on a number of factors, including the conditions during growth, and therefore the prediction results depends on which model (and which assumptions) are used. There is currently no experimental data to compare these predictions with, but other studies [17][186][133] show that the predictions made by these methods are reliable. The reader can therefore have confidence in their reliability.

4.3.4 Rare earth dopant segregation

YLF is of interest when doped with rare earth lanthanide ions. This may affect the energy of some surfaces, particularly where there is strong segregation. Any significant change in surface energy will alter the morphology.

The results from the bulk modelling (Section 4.2.3) showed that the rare earth ions would dope at the Y^{3+} site and the defect energies for these were calculated (Table 4.10). To extend this bulk work, the morphologically dominating surfaces, (112), (001) and (011), were doped at the Y^{3+} sites at different depths from the surface working down into the crystal. These three surfaces were chosen because they account for 91% of the total equilibrium morphology. While the (111) surface is more dominant in this mode, the (001) surface was studied because it also appears strongly in the growth morphology. The plots in Figures 4.104.11 show the difference in energy between doping at a particular depth on a surface compared to the bulk (i.e. the segregation energy). A negative value indicates there is a driving energy for the dopant to lie at that surface depth rather than in the bulk. As expected, the difference in energy tends to zero with increasing depth, due to the defect energy tending towards the bulk defect energy.

These plots show surface segregation to the morphologically important surfaces, however it is to a much greater extent with the (112) surface. At the (001) surface, for the first seven rare earth cations the lowest energy position is around 3.8 Å from the surface, with the lowest being for La^{3+}. The amount of segregation decreases moving across the row of rare earth cations, with ions from Tb^{3+} onwards having little segregation. The two exceptions are Tm^{3+} and Lu^{3+}, where the energy minimum is at the nearest Y^{3+} site to the surface. A very similar trend is seen for the (011) surface but with the minimum occurring at around 7 Å. The difference in energy at this depth compared to the bulk is very small suggesting that surface segregation to this face is unlikely.

The (112) surface segregation plot has a more complicated profile with defect energies not reaching bulk values until 9 Å in depth. Rare earth cations Tb^{3+} to Er^{3+} and Yb^{3+} to Gd^{3+} show no segregation to this surface while Tm^{3+} and Lu^{3+} show a small

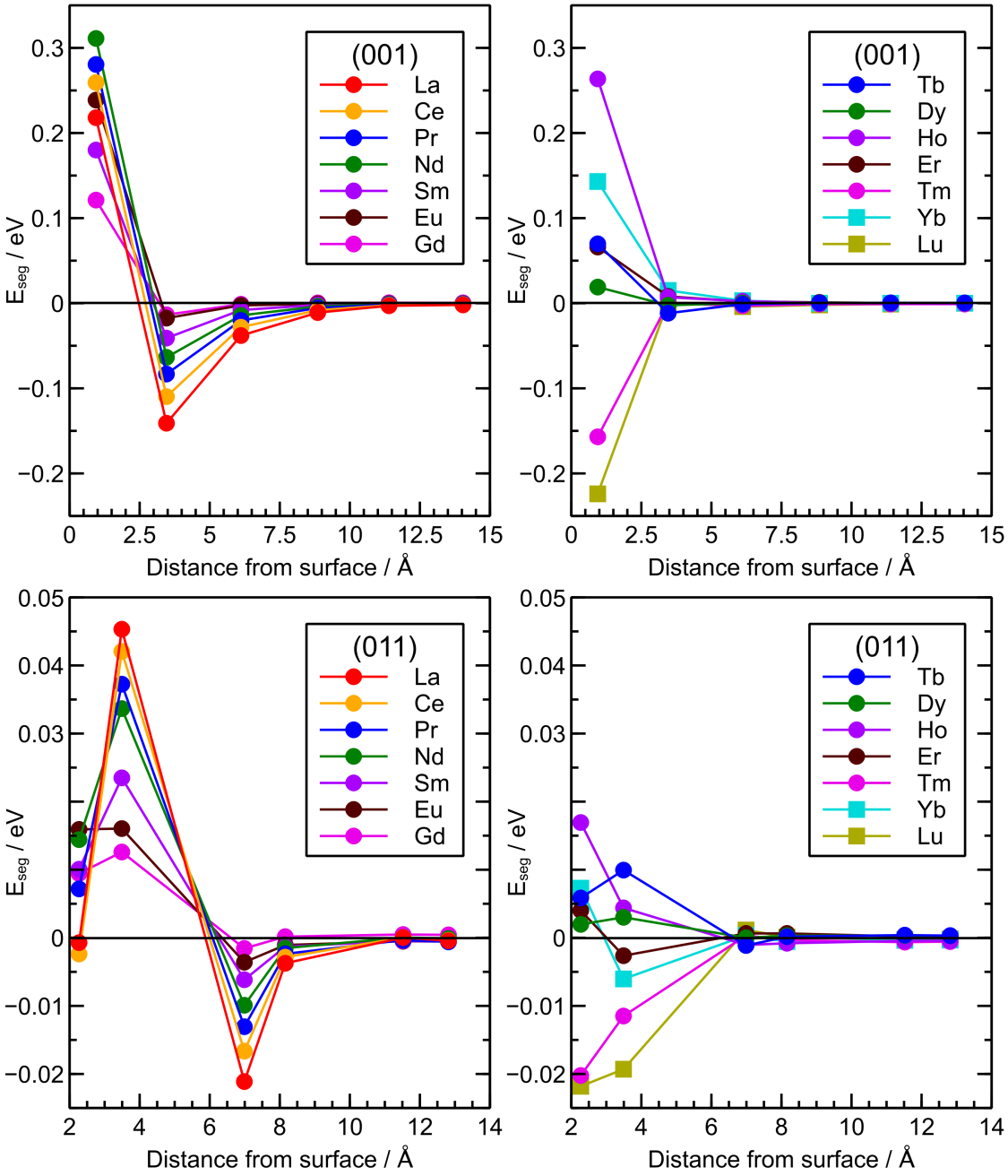

Figure 4.10: Plots showing the difference in defect energy at a surface depth and the bulk for surfaces (001) and (011). A negative energy indicates there is a driving forces for the dopant to lie at that depth rather than in the bulk.

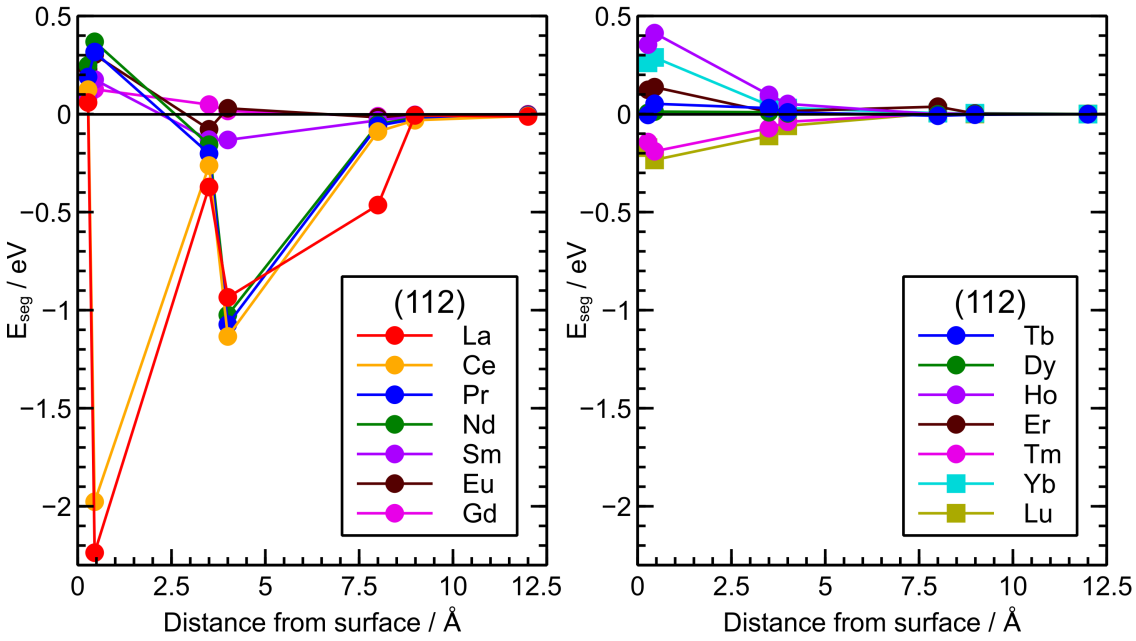

Figure 4.11: Plots showing the difference in defect energy at a surface depth and the bulk for the (112). A negative energy indicates there is a driving forces for the dopant to lie at that depth rather than in the bulk.

tendency. However, the cations La^{3+} to Sm^{3+} show a large segregation to this surface. The deep surface depth of strong segregation suggests there are many sites for dopants at this surface, indicating there may be clustering towards this face. Clustering of the dopant ions can cause energy transfer between them due to the small interionic separation. This can result in the degradation of their activity [32]. To study this further, higher concentrations of dopant ions would need to be considered.

The primary driving force for isovalent dopant segregation is elastic strain induced in the lattice [139]. This results in dopants with ionic radius most different to the lattice ion radius segregating most. The ionic radius of Y^{3+} is 1.019 Å and the rare earth cations have ionic radii starting at 1.16 Å for La^{3+}, decreasing across the period to 0.977 Å for Lu^{3+}. The ionic radius of Ho^{3+} is the most similar to Y^{3+}, being just 0.4% different (see Table 4.24). This radii mismatch explanation fits with the segregation profile for the three surfaces studied, that showed strong segregation for the first four cations in period. The positive value for segregation energy for Ho ions also agrees as there would be small elastic strain induced to the close match in radii of the cations.

Ion	Ionic radius /Å	Percentage difference to Y^{3+} /%
Y^{3+}	1.019	0.0
La^{3+}	1.160	13.8
Ce^{3+}	1.143	12.2
Pr^{3+}	1.126	10.5
Nd^{3+}	1.109	8.8
Sm^{3+}	1.079	5.9
Eu^{3+}	1.066	4.6
Gd^{3+}	1.053	3.3
Tb^{3+}	1.040	2.1
Dy^{3+}	1.027	0.8
Ho^{3+}	1.015	0.4
Er^{3+}	1.004	−1.5
Tm^{3+}	0.994	−2.5
Yb^{3+}	0.985	−3.3
Lu^{3+}	0.977	−4.1

Table 4.24: Ionic radii of Y^{3+} and the rare earth dopant ions. Radius information taken from [187].

4.3.5 Multiple defects

To study more realistic levels of doping, and to consider the effect dopants may have on the surface morphology, more than one dopant ion had to be included. Two methods are outlined in Chapter 3 - defective surface minimisation (DSM) and equilibrium segregation (ES) - that are equivalent, however, the results that follow use the DSM approach as this method allows for the configuration of the rare earth ions to be considered more easily and the defects are minimised within the simulation cell without resorting to the CHAOS infinite dilution code.

In the DSM approach more than one dopant was included in the simulation cell directly. The simulation cells for all low index surfaces were grown such that they contained around six Y^{3+} sites in the surface layer. Rare earth dopants ions were then progressively added to these sites from 0% to 100% coverage of the surface layer. All configurations of the dopant ions were considered, however only the lowest energy ones are reported here. The minimised (defective) simulation cell was used to calculate the

surface energy for that number of dopant ions, as given in Equation 3.8

$$\gamma_{def} = \frac{E_{surf}^{def} + \left(E_{bulk}^{perf} + E_{def}\right)}{A} \tag{3.8}$$

For each of the low index surfaces the change in surface energy is plotted against dopant concentration per surface area. This allows the effect of multiple dopants at the surface to be seen. In some cases the dopants have a stabilising effect and reduce the surface energy. It is important to note that the rare earth dopant ions have all been placed in the same layer, which is the layer of Y^{3+} ions nearest to the surface. The depth of this layer varies for each of the surfaces depending on the repeat unit. This is of importance because the depth profiles in the previous section highlighted that the uppermost layer of Y^{3+} ions was not necessarily the lowest energy position when considering single dopant ions.

Figure 4.12 shows the plots for the (001) surface. In this surface, all dopant ions have a destabilising effect and increase the surface energy. The single dopant ion depth profile for this surface revealed that the uppermost surface site had a positive segregation energy and so this result is not surprising. However, for some dopant ions, La^{3+}, Ce^{3+} and Pr^{3+}, there is a non-linear change in surface energy meaning that clusters of multiple dopant ions are more stable than single ones. Although the reduction in energy is not sufficiently great to reduce the energy below the perfect YLF surface energy. The dopant ion that has the smallest destabilising effect on the surface is Dy^{3+}.

As stated above, the Tm^{3+}-F^- and Lu^{3+}-F^- potentials were refitted for this surface modelling. This was because at this stage, the results produced unphysical results for this surface. The original rare earth fluoride potential derivation paper revealed that these two systems reproduced the lattice structure more poorly than the others, and so they were refitted for this work. Note, that the earlier bulk results were obtained with the original published potentials. A check was carried out to see the difference the newly fitted potentials made on the bulk defect energies and was it found to be small.

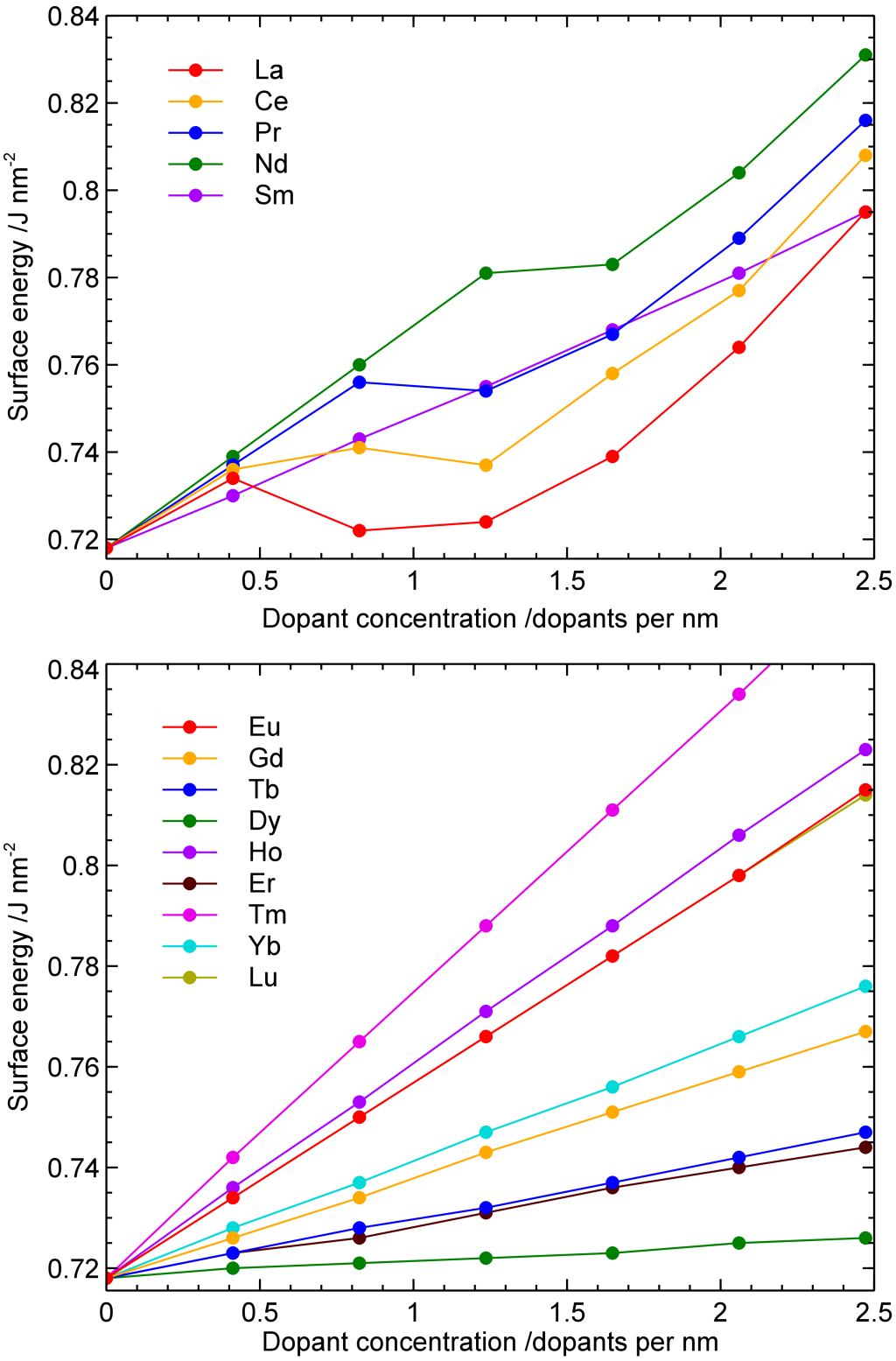

Figure 4.12: Surface energy against dopant concentration for the (001) surface. The rare earth ions are split across two graphs for clarity.

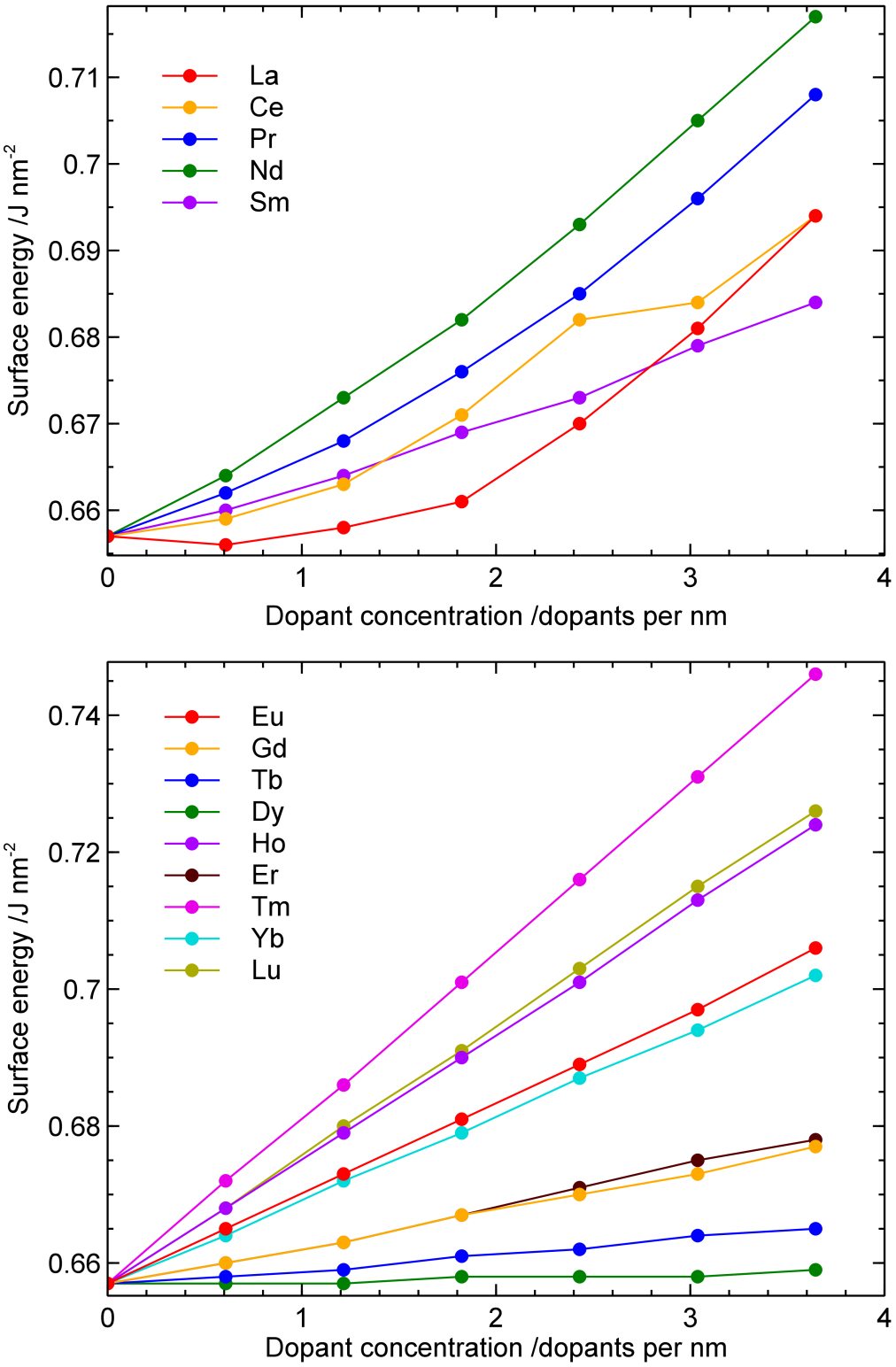

Figure 4.13: Surface energy against dopant concentration for the (010) surface. The rare earth ions are split across two graphs for clarity.

The (010) surface (Figure 4.13) is also destabilised by most rare earth ions, with the exception of La^{3+} and Dy^{3+}. The presence of Dy^{3+} ions at this surface has little effect on the energy of the surface, with only a small increase in energy at the higher dopant concentrations. There is a slight decrease in surface energy with one La^{3+} ion present on the surface (0.2%), however the surface energy increases dramatically at higher doping levels. As with the (001) surface, the three dopants that have the smallest impact on the surface energy are Dy^{3+}, Er^{3+} and Tb^{3+}. Likewise the dopant that has the largest effect again is Tm^{3+}.

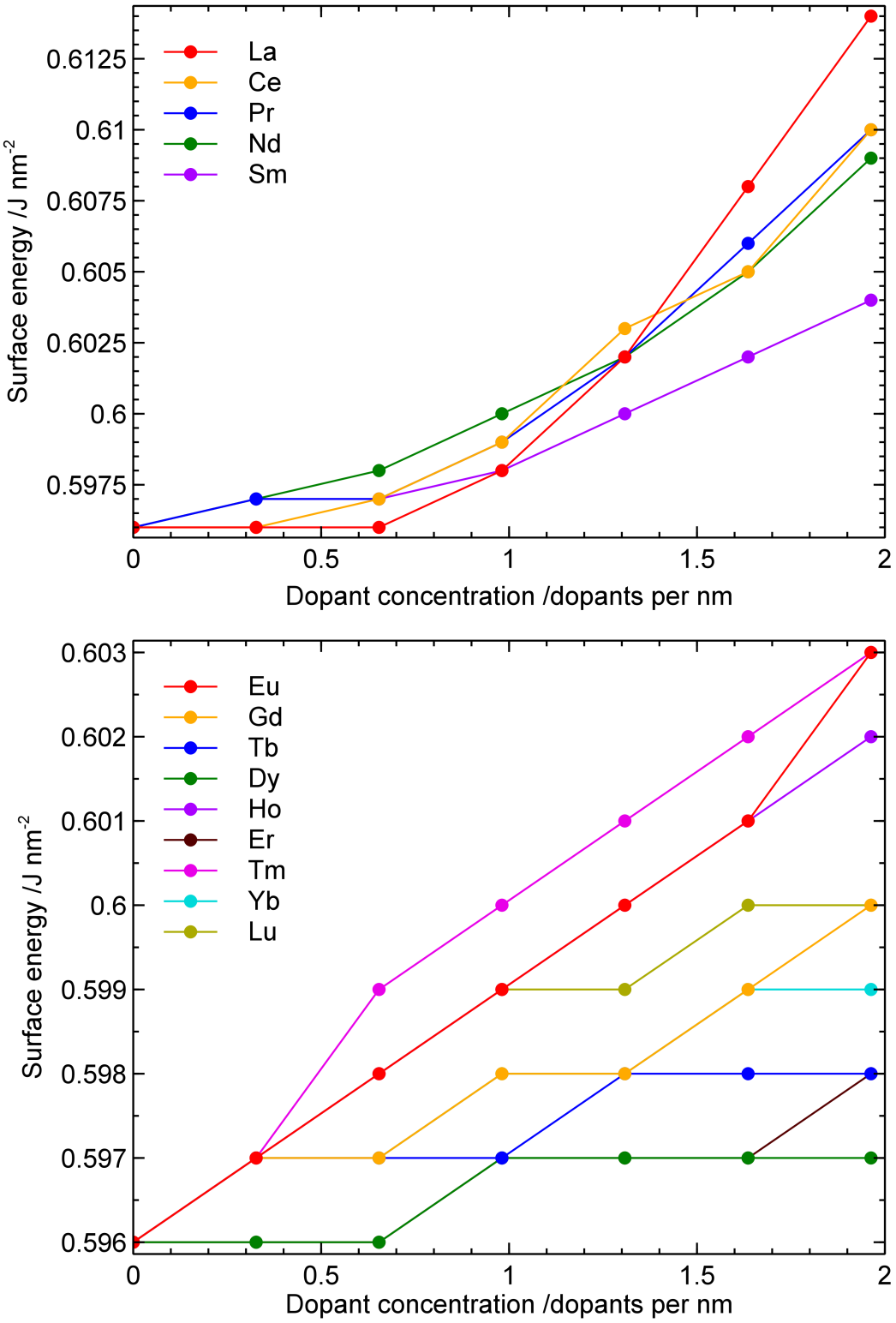

Figure 4.14: Surface energy against dopant concentration for the (011) surface. The rare earth ions are split across two graphs for clarity.

The (011) surface has a more complicated plot (Figure 4.14). None of the dopant ions reduce the surface energy below that of a perfect surface, however, for some of the dopant ions (La^{3+}, Pr^{3+}, Gd^{3+}, Tb^{3+}, Dy^{3+}, Er^{3+}, Yb^{3+}, Lu^{3+}) zero-gradient sections where the addition of another dopant ion does not increase the surface energy occur. For example, the surface energy of an Dy^{3+} doped face does not increase from the perfect surface until there is 1 dopant per nm. The surface energy remains at this value up to (at least) 2 dopants per nm. This implies that this surface is less affected by the presence of the dopants and that clusters of dopants are equally as likely. The dopant that has the largest impact in the surface energy is La^{3+}, which at the maximum doping level increases the surface energy by 3%. Comparing this to the largest increase in surface energy for the two previously discussed surfaces - (001) Tm^{3+} results in a 29% increase, (010) Tm^{3+} results in a 14% increase - it reveals that this surface is less effected by the dopant ions. The repeat unit for this surface shows that the Y^{3+} layer (i.e. the dopant layer) is relatively deep within the crystal, and is a mixed layer of Y^{3+} cations and F^- anions. The layers immediately around the Y^{3+} layer are also anion layers. It may be the close proximity of these anion that help to reduce the energy of the dopant-filled surface. In the two previous surfaces discussed, (001) and (010), the Y^{3+} layer is a mixed cation layer with Li^{3+} ions.

The (012) surface is the first surface that the inclusion of rare earth ion dopants reduces the surface energy and stabilises the surface. The layer in which the rare earth ions dope in this surface is a mixed layer that contains all three constituent ions of YLF. La^{3+} and Ce^{3+} ions reduce the surface energy with up to 1.3 dopants per nm before the energy increases at higher dopant concentrations (Figure 4.15). In the case of La^{3+} ions the reduction in energy is around 4%. All other rare earth ions show an increase in surface energy with increasing concentration of dopant ions. While La^{3+} ions decrease the surface energy of this surface at lower concentrations, the surface energy quickly increases at higher concentrations. The three lowest surface energies at the maximum concentration are, as with all surfaces, Dy^{3+}, Er^{3+} and Tb^{3+}. These dopant ions consistently produce shallow gradient plots meaning that they do not impact on

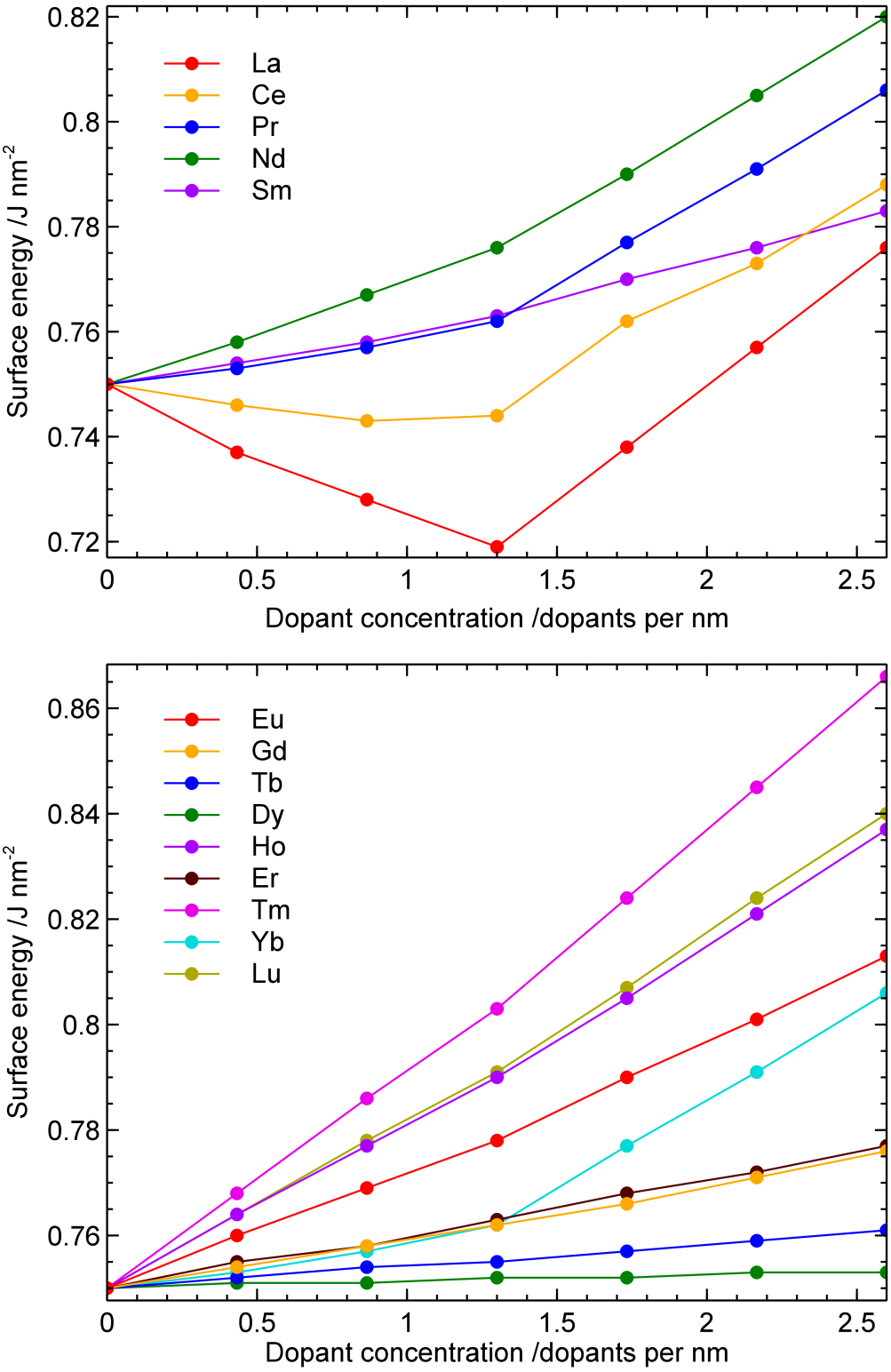

Figure 4.15: Surface energy against dopant concentration for the (012) surface. The rare earth ions are split across two graphs for clarity.

the stability of the surface to any great degree. These three rare earth ions are most similar in ionic radius to Y^{3+}, with the exception of Ho^{3+}. The mismatch in ionic radii for these ions is between 2% and −2%. This explains the pattern seen in the results. However, Ho^{3+}, in the surfaces discussed so far, is one of the dopant ions that effects the surface energy the most, despite it having the closest ionic radius match to Y^{3+}.

The (021) surface has a similar mixed ion doping layer. A similar trend (Figure 4.16) is seen for the surface, with La^{3+}, Ce^{3+} and Pr^{3+} showing some decrease in surface energy. For La^{3+} the maximum decrease in surface energy occurs for 0.7 dopants per nm with a reduction of 1.5%. Again Dy^{3+}, Er^{3+} and Tb^{3+} are the three dopant ions that alter the surface energy the least.

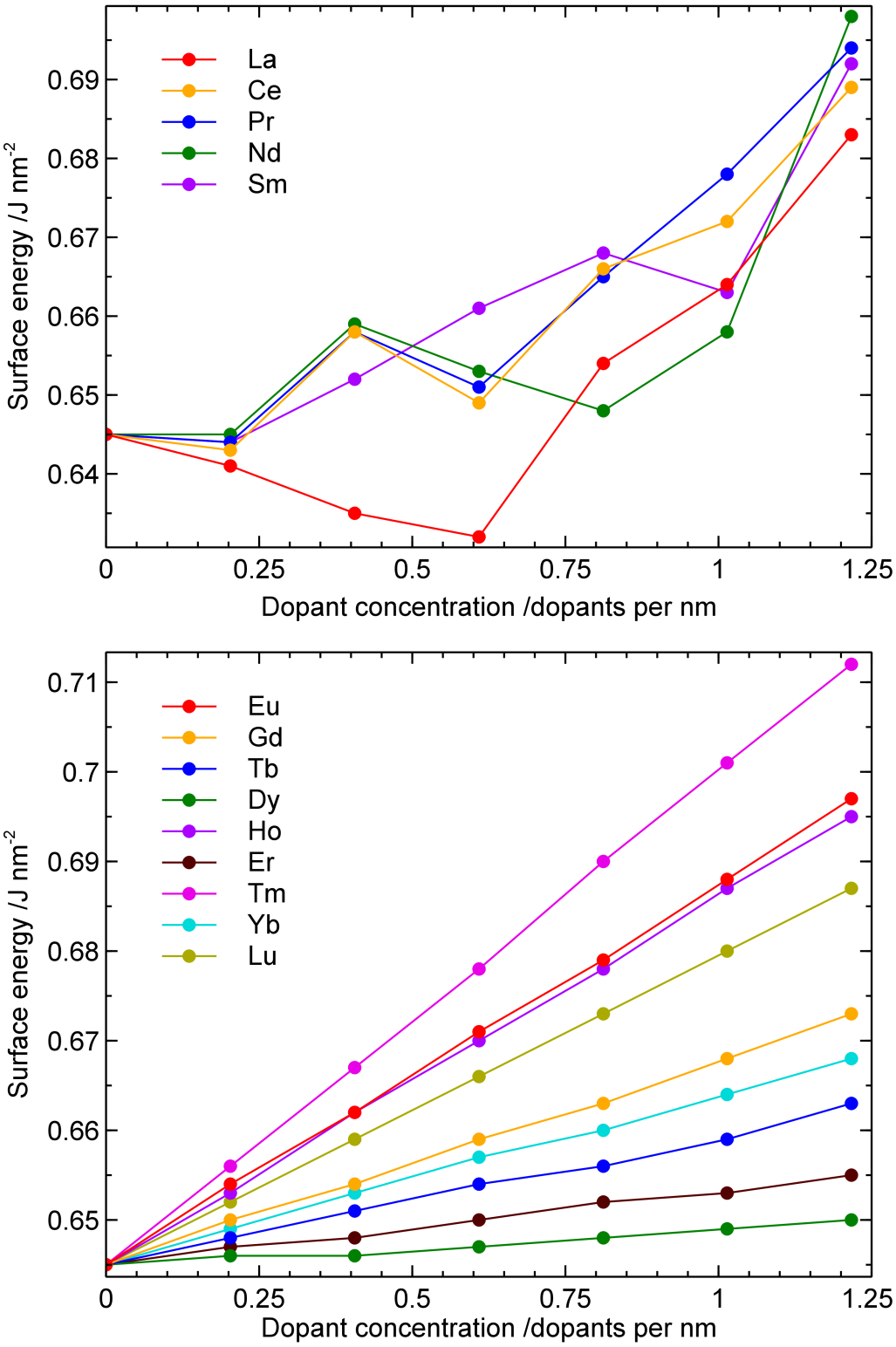

Figure 4.16: Surface energy against dopant concentration for the (021) surface. The rare earth ions are split across two graphs for clarity.

The plots for the (110) surface are very different to the first five surfaces discussed (Figure 4.17). This surface is the first surface in which the doping layer is at the surface termination (i.e. 0 Å). All rare earth dopant ions, apart from Dy^{3+} and Er^{3+}, reduce the surface energy to some degree. La^{3+} produces the greatest reduction in surface energy (14.5%), then Ce^{3+}, then Pr^{3+}, and then Nd^{3+}. This aligns with the theory of defect segregation due to elastic strain induced by the mismatch of ionic radii.

Doping within the (111) surface is also in a mixed Y-Li-F layer like in the surfaces (012) and (021). However, unlike with those surfaces no reduction in surface energy is seen (Figure 4.18). Again Dy^{3+}, Tb^{3+} and Er^{3+} cause the least effect on the surface energy.

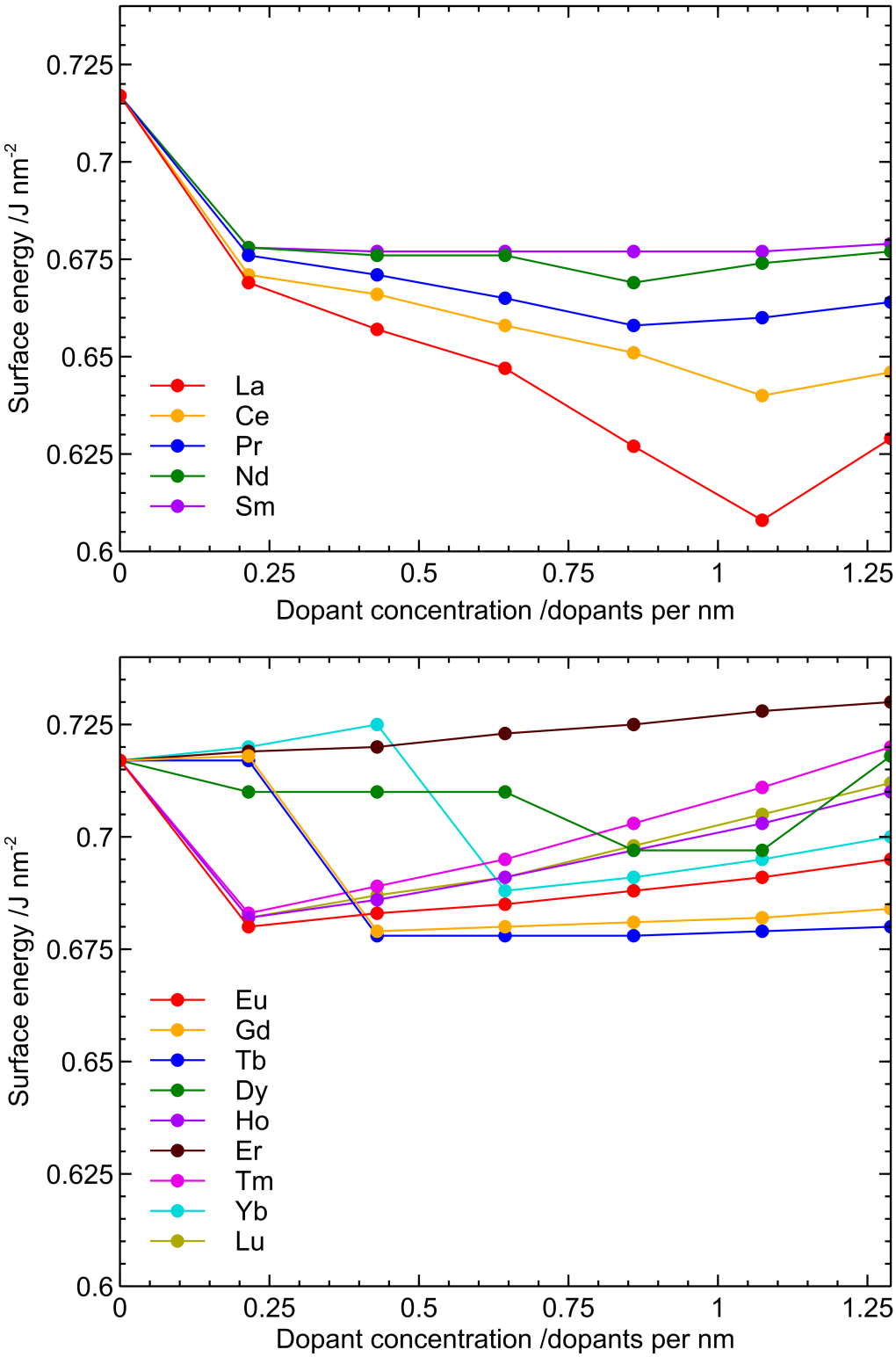

Figure 4.17: Surface energy against dopant concentration for the (110) surface. The rare earth ions are split across two graphs for clarity.

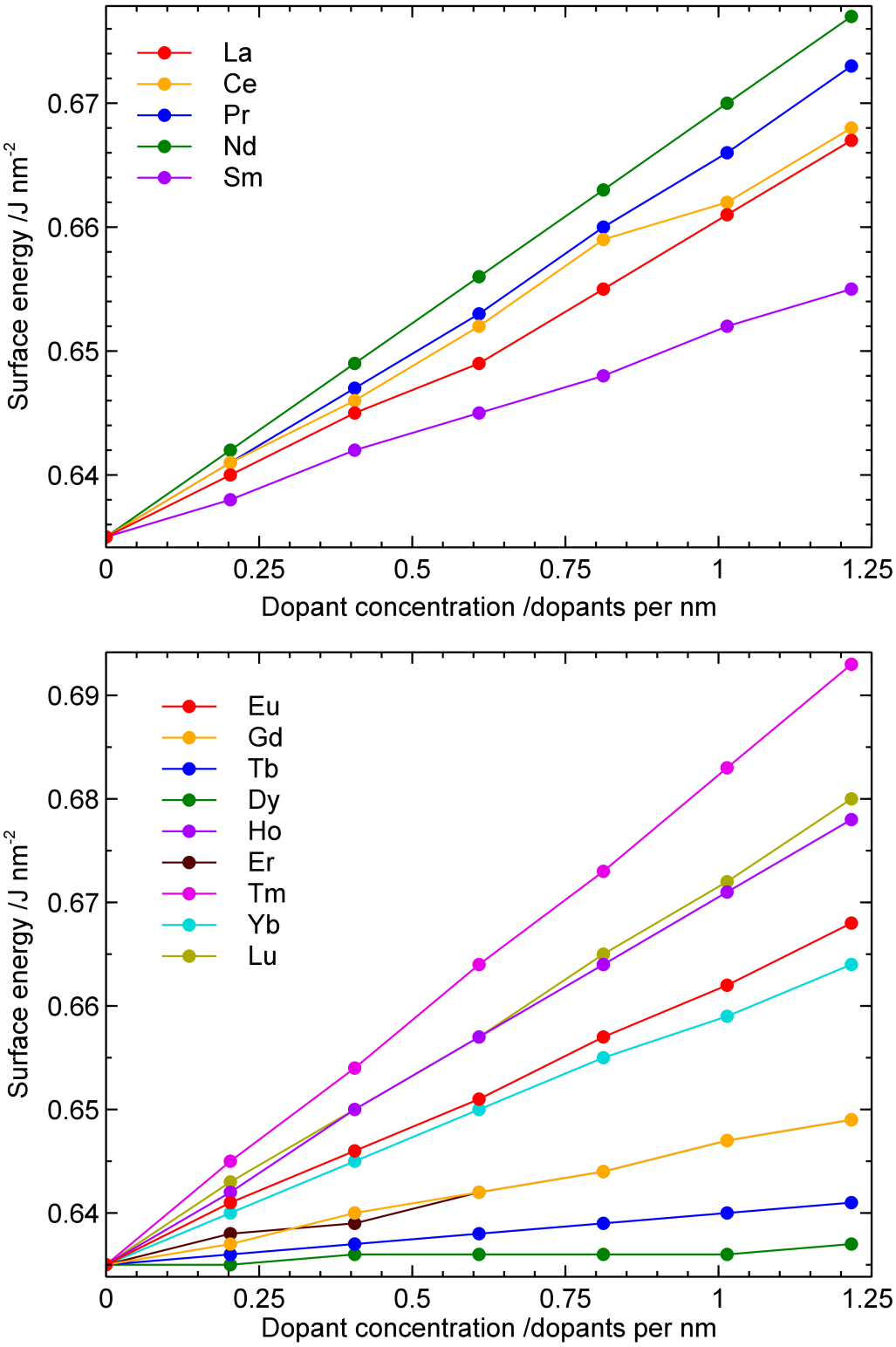

Figure 4.18: Surface energy against dopant concentration for the (111) surface. The rare earth ions are split across two graphs for clarity.

(112) is the first surface to show significant reductions in surface energy across the rare earth series. At this surface, dopants ions La^{3+} through to Dy^{3+} (with the exception of Eu^{3+}) reduce the surface energy. The largest decrease occurs for around 2 La^{3+} ions per nm. The reduction is equal to 7.7%. While this is not the largest percentage decrease, this surface is unique in that it accepts more of the rare earth ions than any of the others. The maximum doping level is also greater than the other others. The three dopant ions that affect the surface energy least are Tb^{3+}, Dy^{3+}, and Gd^{3+}. These are slightly different to the previous surfaces, where Gd^{3+} was the fourth ion not third. The opposite is true at this surface.

Although the doping layer at the (120) surface is similar to that at the (001) surface, the plots produced are linear in style and show no decreases in energy due to clustering from this linear increase. In common with all surfaces, Dy^{3+}, Tb^{3+} and Er^{3+}, are the ions that increase the surface energy the least (with Gd^{3+} being the next ion).

The (121) surface shows an almost identical pattern to the (120) surface. The only exception being Sm^{3+}, which has a lower surface energy.

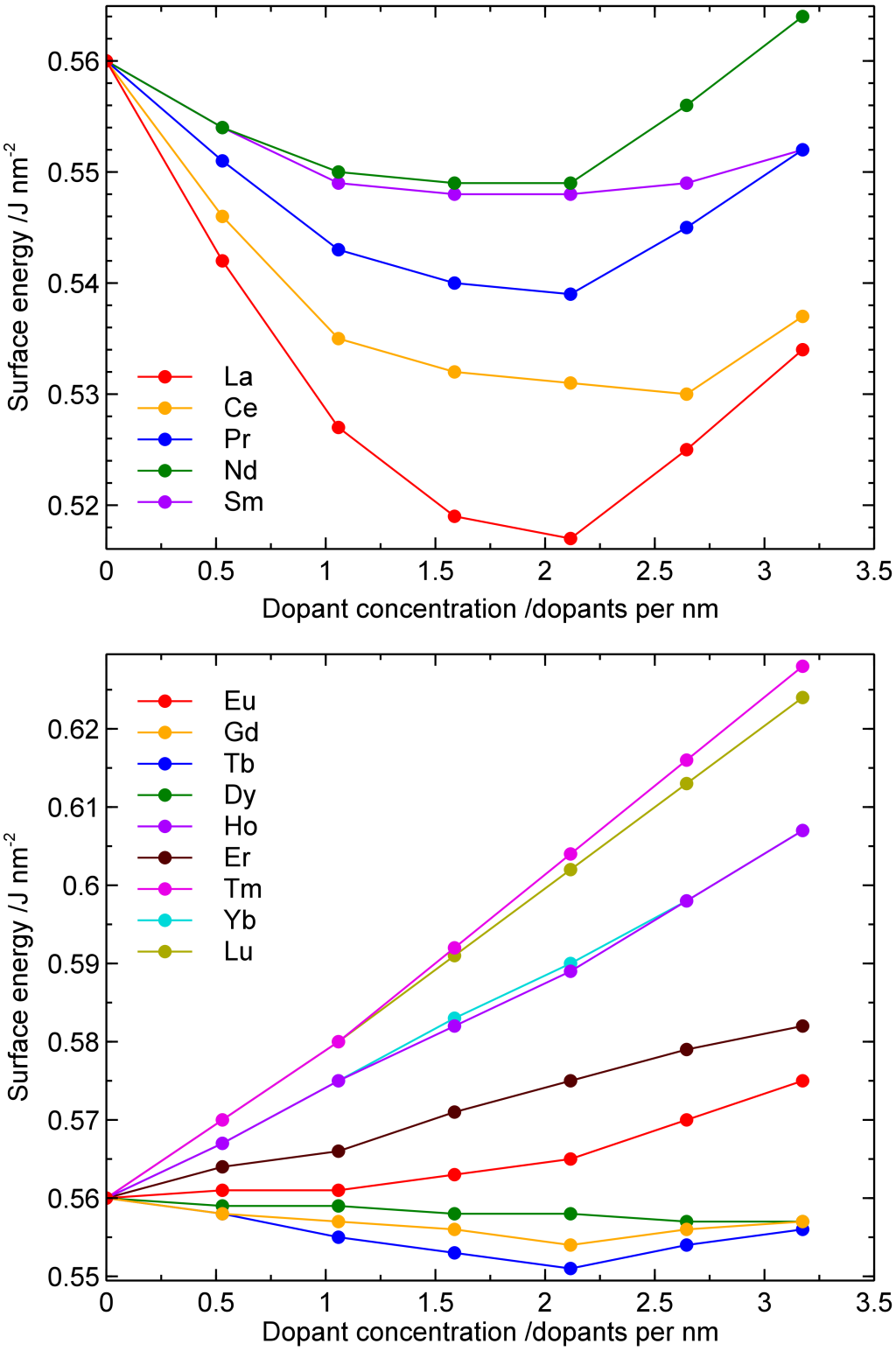

Figure 4.19: Surface energy against dopant concentration for the (112) surface. The rare earth ions are split across two graphs for clarity.

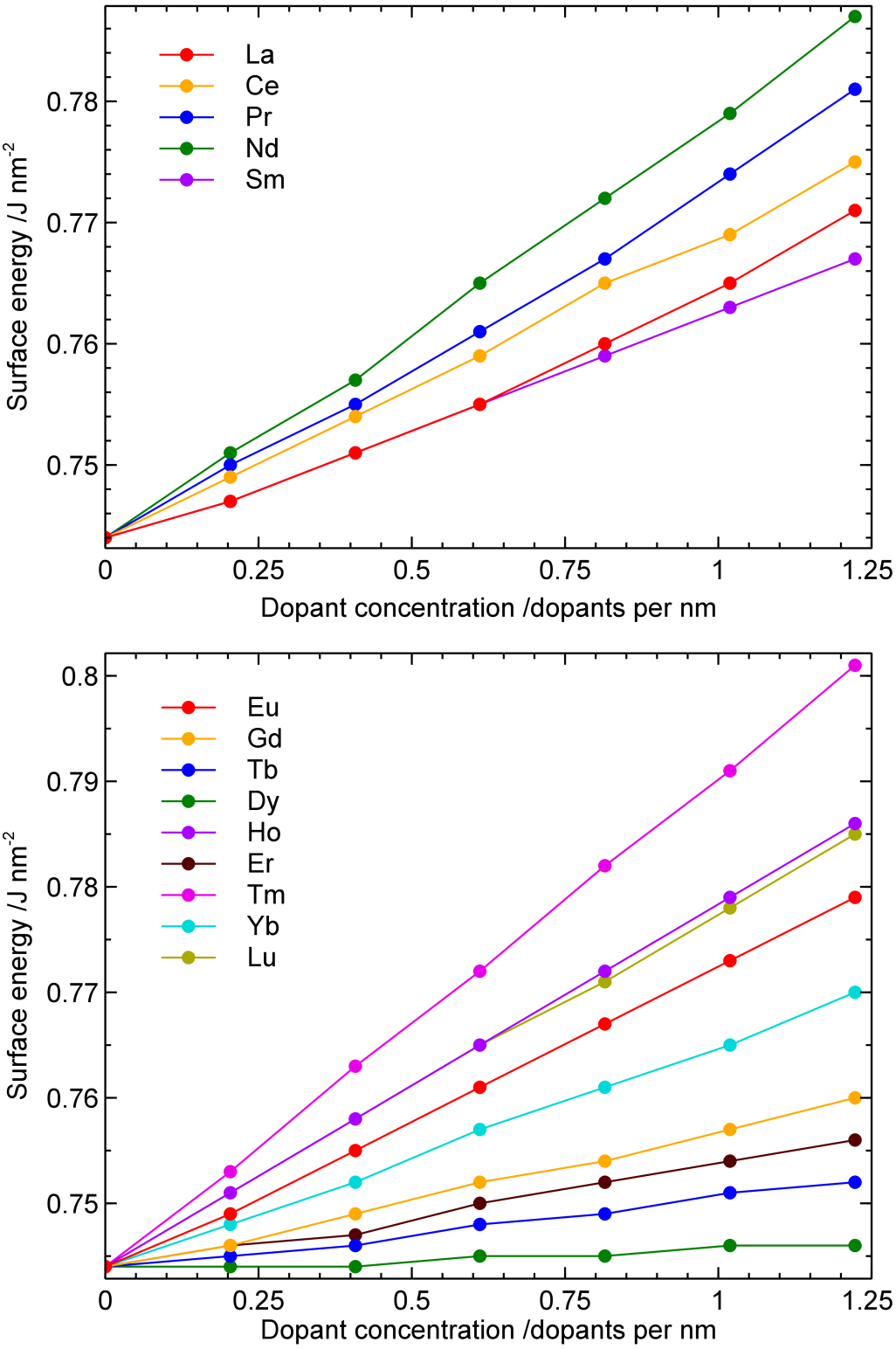

Figure 4.20: Surface energy against dopant concentration for the (120) surface. The rare earth ions are split across two graphs for clarity.

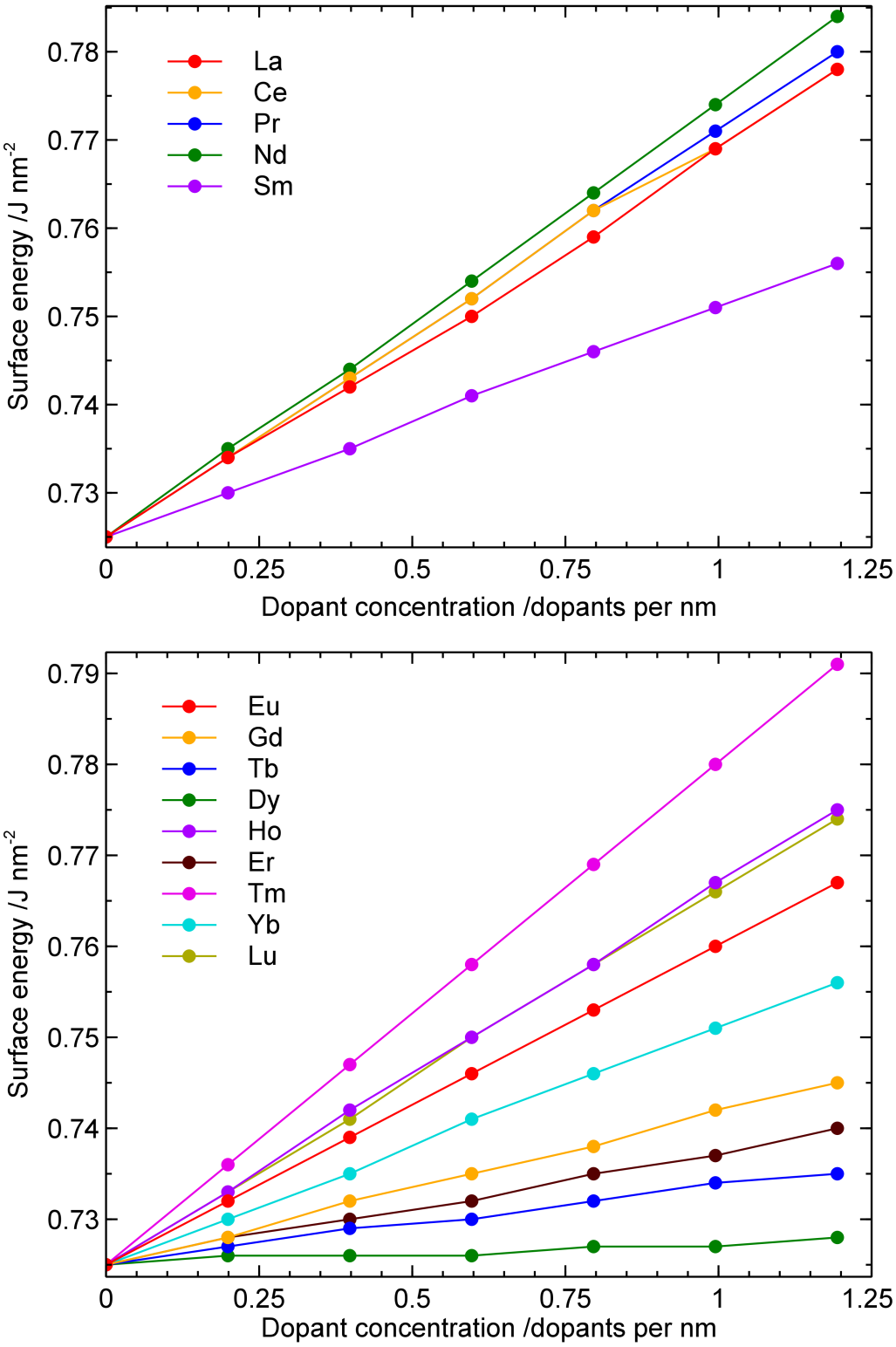

Figure 4.21: Surface energy against dopant concentration for the (121) surface. The rare earth ions are split across two graphs for clarity.

For the smaller rare earth ions (Sm^{3+} onwards), the effect at the (122) surface is similar to the previous two surfaces, with an (almost) linear increase in surface energy with dopant concentration. However, the first four rare earth ions (La^{3+}, Ce^{3+}, Pr^{3+}, and Nd^{3+}) show a decrease in surface energy with dopant concentration, with La^{3+} giving the largest reduction at 0.68 Å equal to 0.7%. This is a small decrease in surface energy compared to other surfaces. The doping layer at this surface is a mixed cation and anion layer, similar to the (012) and (021) surfaces, which also showed a decrease in surface energy (albeit to a larger extent). The largest doping concentration modelled at this surface is smaller than many of the other surfaces, due to the mixed ion make up of the surface.

The (210) surface shows no decrease in surface energy with increasing concentration of dopant ions. The trends seen match those seen in the other surfaces.

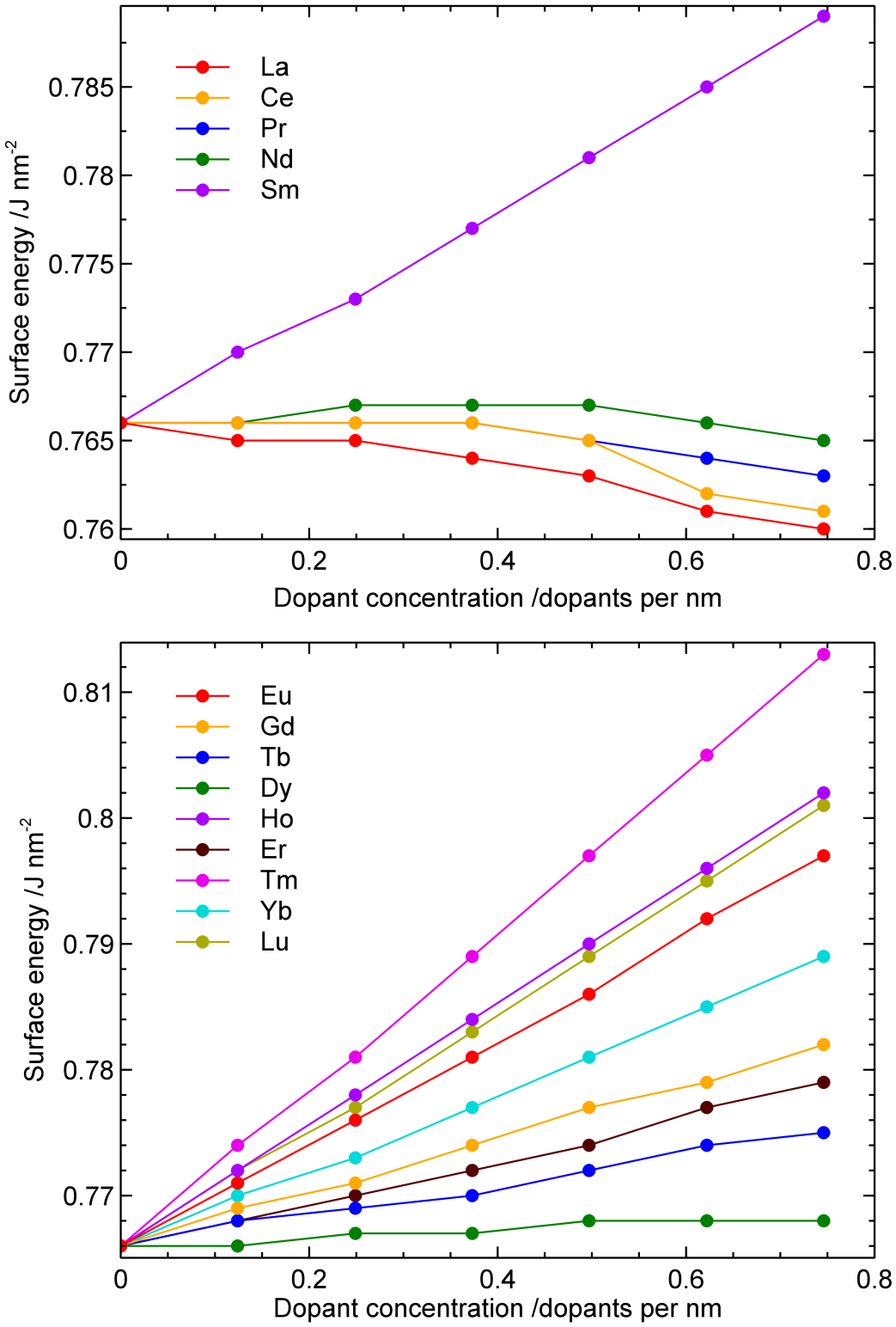

Figure 4.22: Surface energy against dopant concentration for the (122) surface. The rare earth ions are split across two graphs for clarity.

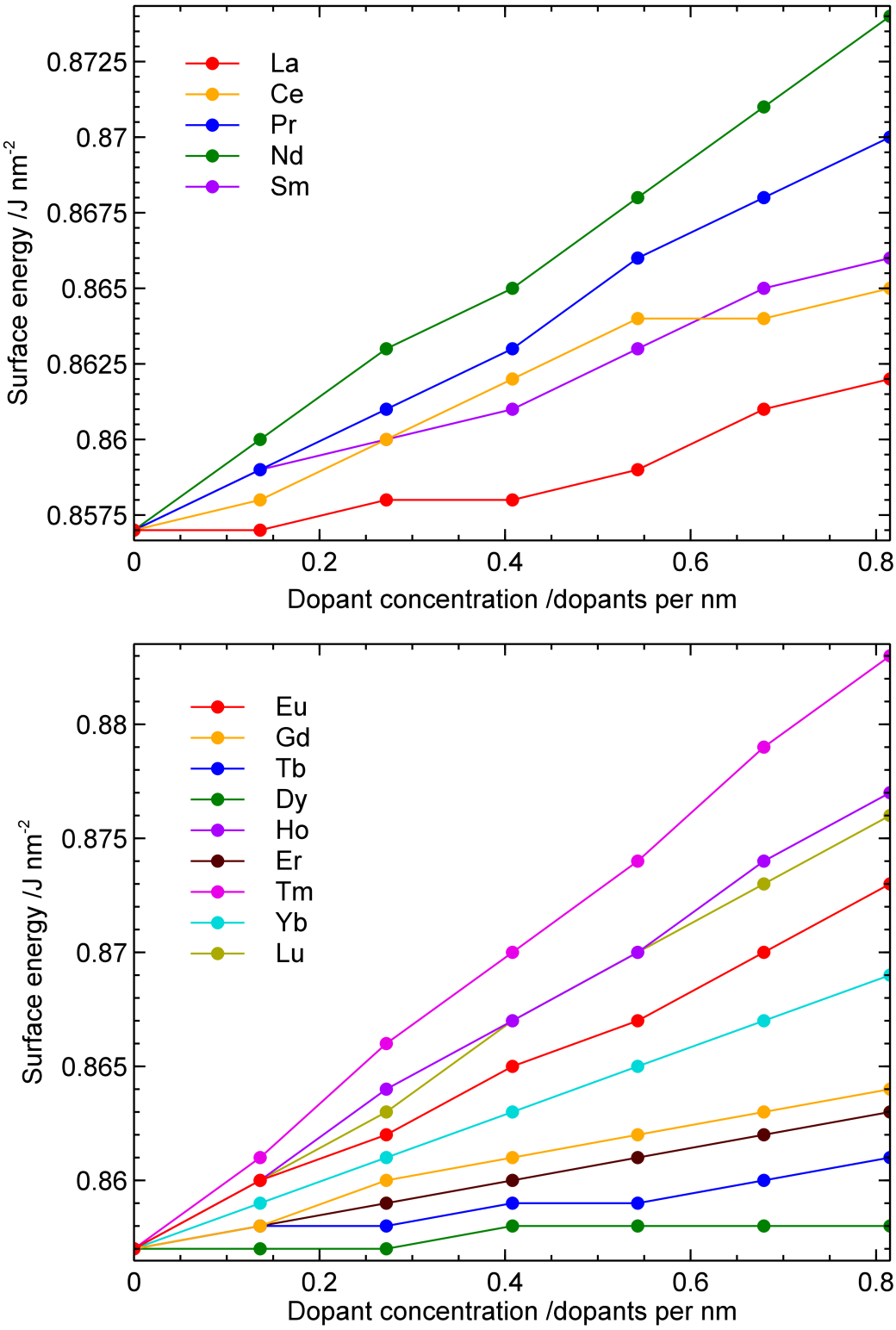

Figure 4.23: Surface energy against dopant concentration for the (210) surface. The rare earth ions are split across two graphs for clarity.

The final two surfaces, (211) and (221) are both of a different type to all those considered so far. The doping layer at these surface contains just Y^{3+} ions. The Y^{3+} layer at the (211) surface is at a depth of 0.8 Å. No reduction in surface energy is seen.

At the (211) the Y^{3+} layer is at the surface termination. The only other surface termination doping considered was at the (110) surface, at which most rare earth ions decreased the surface energy with La^{3+} reducing the energy by 14.5%. Here most rare earths do not decrease the energy, with the exceptions of La^{3+}, Ce^{3+}, and Nd^{3+}. Again La^{3+} provides the largest decrease in surface energy (3.1%).

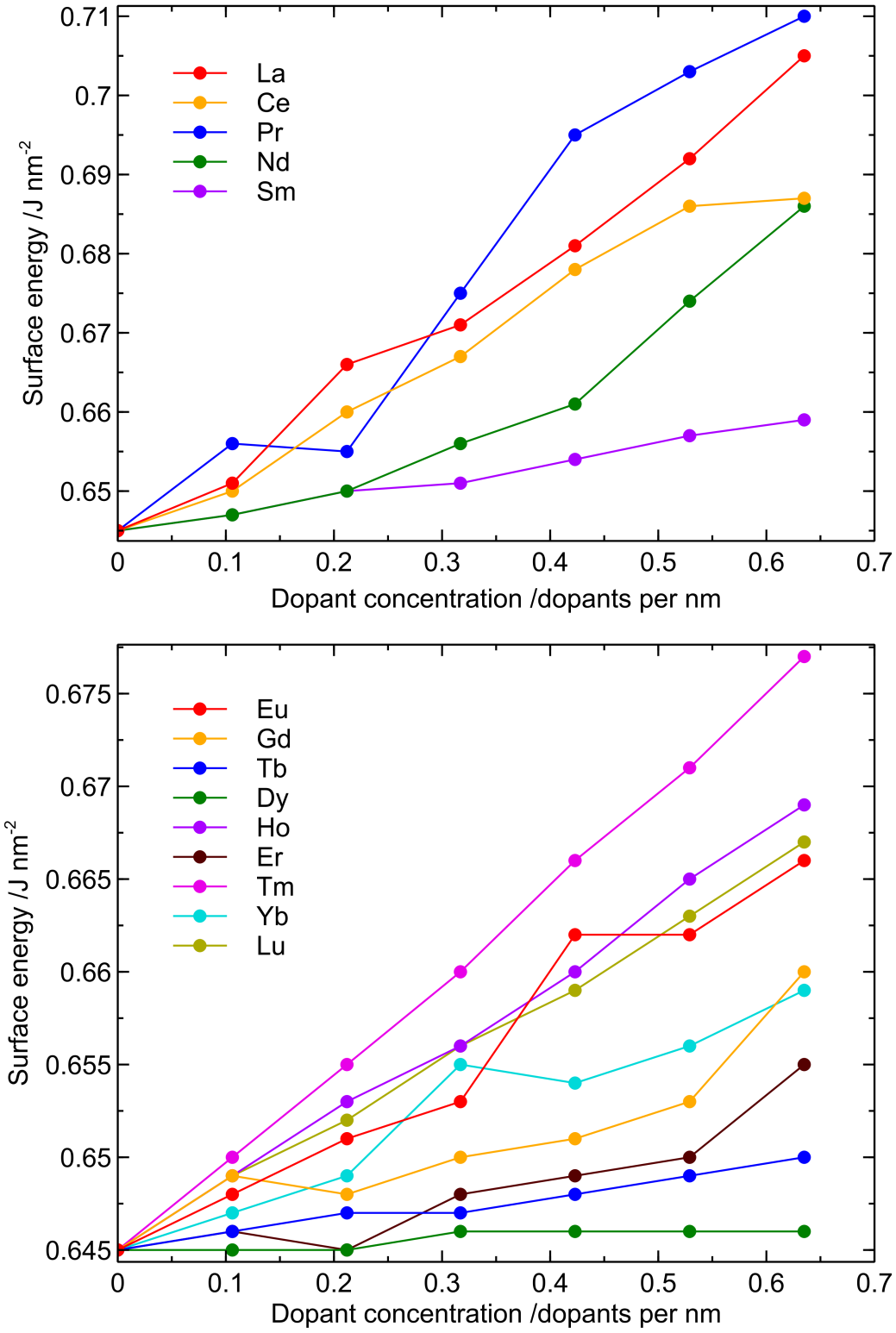

Figure 4.24: Surface energy against dopant concentration for the (211) surface. The rare earth ions are split across two graphs for clarity.

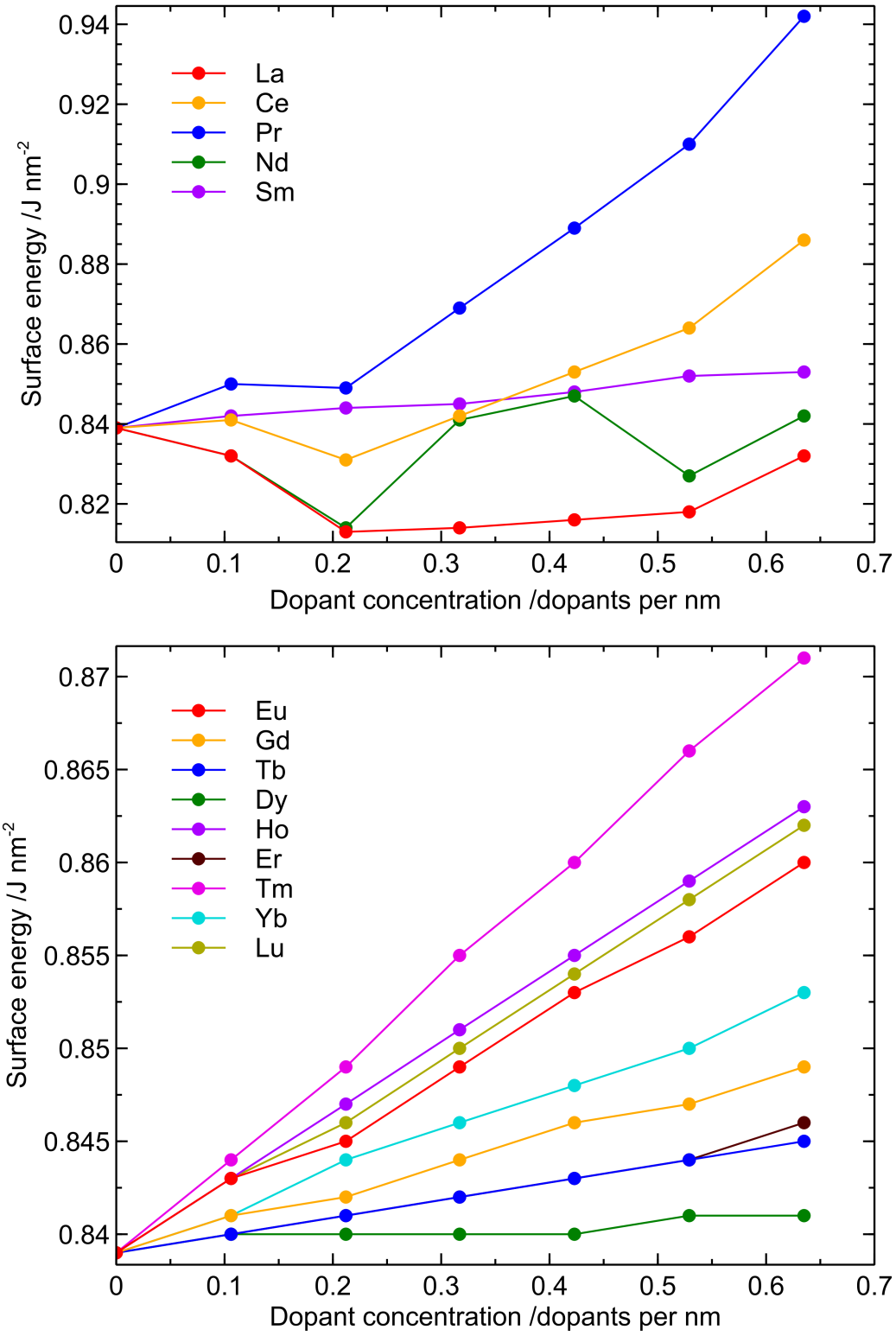

Figure 4.25: Surface energy against dopant concentration for the (221) surface. The rare earth ions are split across two graphs for clarity.

Looking more generally at the results from the low index defective surface energies, it is seen that those rare earth ions with similar ionic radii to Y^{3+} tend to affect the surface energy least. This is expected because similar ionic radii between dopant and lattice site ion means a small elastic strain induced in the lattice. As segregation energy is proportional to elastic strain, and the defective surface energy is proportional to segregation energy, the defective surface energy should be minimally affected.

$$\gamma_{def} \propto E_{seg}$$
$$\text{and } E_{seg} \propto E_{strain}$$
$$\therefore\ \gamma_{def} \propto E_{strain}$$

The exception to this is Ho^{3+}, which has the closest ionic radius to that of the Y^{3+} ion. Ho^{3+} consistently across all surfaces was one of the highest energy dopant ions. There is no obvious explanation for this, and it should be examined further. A possible cause is with the potential. The rare earth fluoride potentials used in this work have not been used in surface modelling before, and as seen some of them broke down during use. It is possible that the Ho^{3+}-F^- potential is also inadequate and should be further tested by refitting.

Table 4.25 lists the seven surfaces that for La^{3+} doping the surface energy decreased. The table gives the maximum percentage change in surface energy and the concentration at which that occurs. It also lists the remaining surfaces along with the increase in surface energy for La^{3+} when doped with six rare earth ions. The top three surfaces, (111), (112) and (012), have the La^{3+} ion doped in a mixed layer that contains F^- ions. There are also layers of F^- ions either side of the doping layer. The next surface, (211), has the dopants in a pure Y^{3+} layer with Li^+ in the surrounding layers. This highlights what is generally true, that there appears to be no immediately obvious relationship between doping layer environment and defective surface energy.

As outlined previously, there is an alternative method to achieve the same result as presented here that is referred to as the ES method (equilibrium segregation method).

Surface	Percentage change in surface energy /%	Concentration of La^{3+} /dopants per nm
(110)	−14.5	0.61
(112)	−7.7	2.12
(012)	−4.1	1.30
(221)	−3.1	0.21
(021)	−1.5	0.63
(122)	−0.7	0.76
(010)	−0.2	0.61
(210)	0.6	0.82
(011)	3.0	1.96
(120)	3.6	1.22
(111)	5.0	1.22
(121)	7.3	1.19
(211)	9.3	1.59
(001)	10.7	1.16

Table 4.25: Change in surface energy with La^{3+} ions present. For those surfaces where the change reduces the surface energy, the value quoted is for the maximum reduction. For the other surfaces, the value quoted is for doping with six La^{3+} ions.

In this method the dopant ions are embedded in a CHAOS simulation and the defect energy calculated. From this the segregation energy is determined and this is used to determine the defective surface energy using Equation 3.6. The two methods are equivalent and should produce the same results, however, this was not found to be the case. To provide an example of the difference, Table 4.26 lists the defective surface energies for one to three La^{3+} and Eu^{3+} ions at the (001) and (112) surfaces obtained using both methods. The lowest energy configuration of dopant ions obtained from the DSM method was used in the ES simulation. There is a slight difference in the surface energies, which the author attributes to the defect formation energy as a result of convergence with the CHAOS code and the nature of the isolated simulation cell.

4.3.6 Dopant ion configurations

For each concentration of dopants there are a number of possible arrangements within the surface layer. All surface energies quoted previously are for the configuration of dopant ions that was the lowest energy. Across all of the low index surfaces and all rare earth ions there are many different configurations that form the lowest energy. Detailing

Dopant	Number of dopants	Surface energy from DSM /J nm^{-2}	Surface energy from ES /J nm^{-2}
(001) La	1	0.734	0.706
	2	0.722	0.699
	3	0.724	0.783
(001) Eu	1	0.734	0.777
	2	0.750	0.835
	3	0.766	0.893
(112) La	1	0.734	0.706
	2	0.722	0.699
	3	0.724	0.783
(112) Eu	1	0.734	0.777
	2	0.750	0.835
	3	0.766	0.893

Table 4.26: Difference in La^{3+} doped surface energies obtained from DSM and ES methods. The ES surface energy is determined from calculating the defect energy at the surface, for the same configuration of dopant ions as the DSM method, using CHAOS. The difference in the energy arises due to the methodology used and should be equal.

all configurations would be time consuming and provide little information of importance. Instead a few examples from the (001) surface are presented to highlight the general trend shown in Figure 4.26. Comparing the configuration of Ce^{3+} to Sm^{3+} (for low numbers of dopant ions) the trend seen is that Ce^{3+} ions tend to sit in different planes within the doping layer, while Sm^{3+} sits in the same plane. This trend is true across the rare earth series, with the first few ions (La^{3+} to Eu^{3+}) separating across different planes and the latter ions residing in the same plane. This can be explained with ionic radius and lattice strain, as the first few ions are larger than the Y^{3+} ion they replace. As the doping level increases, the number of possible configurations decreases and the rare earth ions are forced to reside in the same plane as each other. The configurations shown in Figure 4.26 represent just a few of the lowest energy configurations, as for the lower concentration systems there are more than one configuration that produces the same energy.

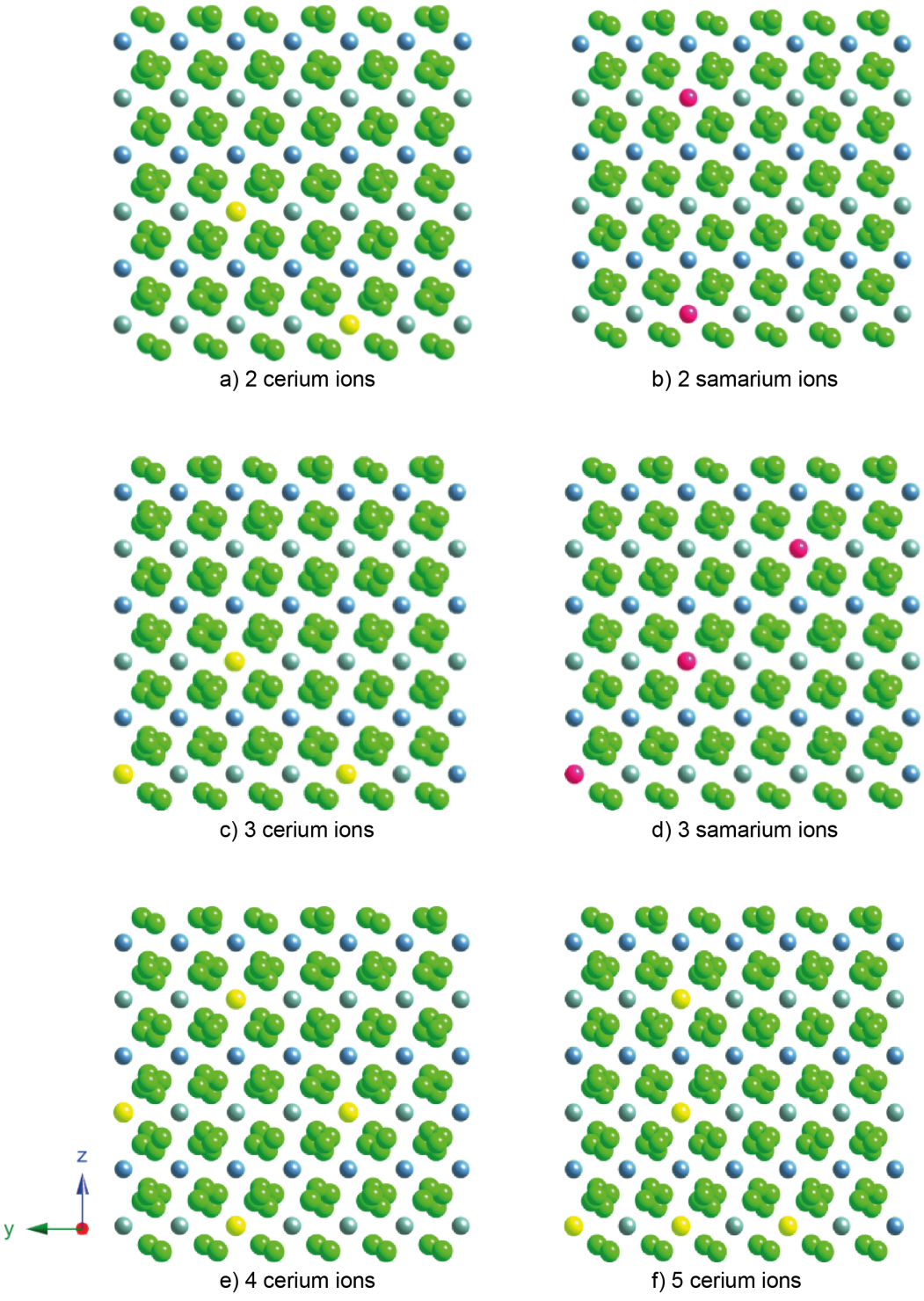

Figure 4.26: Selected dopant ion configurations at the (001) surface. a) shows the lowest energy configuration for 2 Ce^{3+} ions, b) for 2 Sm^{3+} ions, c) for 3 Ce^{3+} ions, d) for 3 Sm^{3+} ions, e) for 4 Ce^{3+} ions, and d) for 5 Ce^{3+} ions. There may be more than one configuration has the same energy but only one is shown here. The plots are orientated such that x-plane is into the page (i.e. the view is of the surface layer with the bulk crystal below into the page).

4.3.7 McLean relationship

Throughout the defective surface work, the explanation given for many of the trends seen has been elastic strain induced in the lattice through ionic radii mismatch between the dopant ion and the lattice ion it replaces. To confirm this quantitatively the relationship proposed by McLean [139] can be used. The proposed relationship is:

$$E_{elastic} = \frac{6\pi B r^3 (\frac{\Delta r}{r})^2}{1 + \frac{3B}{4\mu}} \tag{3.3}$$

where r is the radius of the lattice ion, Δr is the difference in radius between the defect and lattice ion, B is the bulk modulus of the defect and μ is the shear modulus of the lattice. μ is constant across all simulations and so if B is assumed to be constant across the rare earth ions, the segregation energy would be proportional to $(\frac{\Delta r}{r})^2$.

The segregation energies used in the plot are the optimum segregation and therefore are not for equal dopant concentrations. Previous studies [140, 141] have shown the importance of concentration in determining the segregation energy because segregation energy is not independent of surface coverage. The values were calculated by obtaining the surface defect formation energy by calculating the difference between the defective surface block energy and the perfect surface block energy.

Plotting $(\Delta r/r)^2$ against segregation energy produced a non-linear complicated plot. Unlike with other studies, for example [188, 140], where the fit was excellent here the McLean relationship did not fit with the segregation data. However, if just the first rare earth ions are considered (i.e. La^{3+} to Nd^{3+}) linear plots are produced (Figure 4.27). These four rare earth ions are the most the dissimilar in ionic size to the host Y^{3+} site and therefore should induce the largest strain in the lattice. The rare earth ions Tm^{3+}, and Lu^{3+} also fit to some degree with the linear trend created by the first four rare earth ions. These are the two potentials that were refitted for this work.

The plots show that all surfaces fit to the linear trend predicted by the McLean relationship and all of the linear lines have negative gradients meaning those dopants with largest difference in ionic size have the lowest segregation energy.

The rest of the rare earth series have not been plotted, as the data is extremely

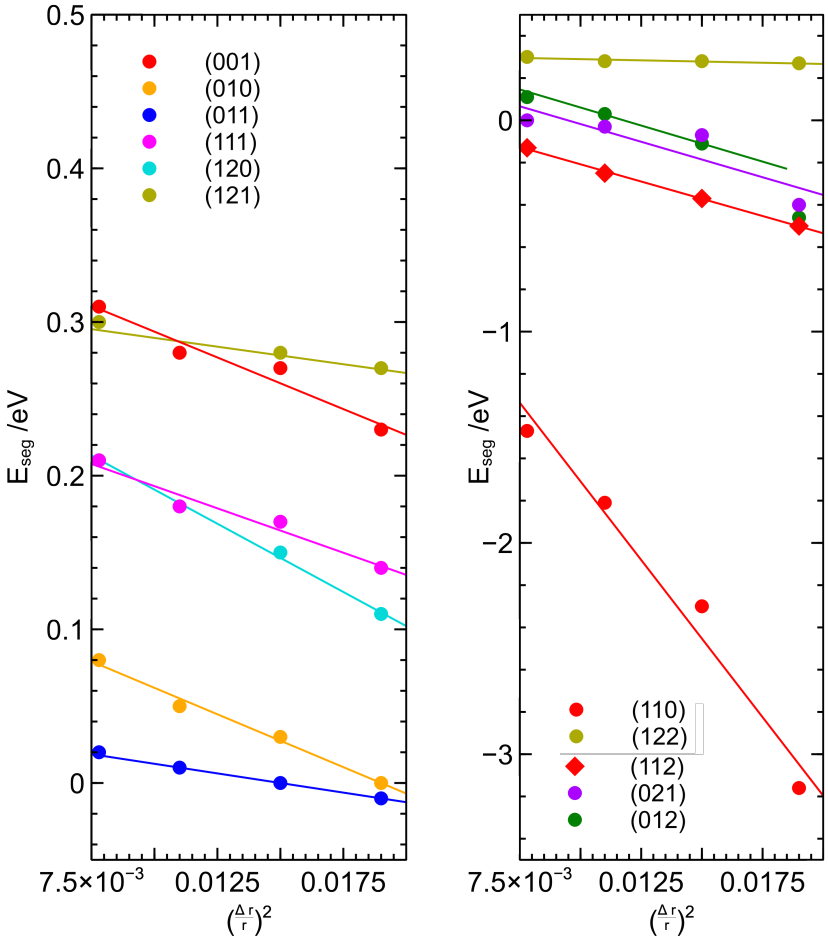

Figure 4.27: Plot of relative ionic size of dopant against segregation energy for the first four rare earth ions (La^{3+} to Nd^{3+}) as proposed by McLean [139].

scattered resulting in a poor linear fit. However, the linear fit for them are all positive. This is not the trend that is predicted but may be a result of the similarity in the ionic size of these dopants to the host Y^{3+} site.

There are a number of reasons why the plots do not produce a linear trend as predicted by McLean. It may be due to poor potentials. Two potentials were refitted during the work as they were found to be inadequate and these two rare earth ions lie closer to the linear trend than the other ions. The theory appears to work for those ions that show strong segregation but breaks down for the ions that do not in YLF. This may be true for other systems too. Finally, the McLean plot assumes that the bulk modulus of the rare earth ions is constant.

4.3.8 Defective morphology

It has been shown that surfaces with dopants present have different surface energies. This will lead to a different equilibrium morphology prediction as the size of each interface is proportional to the surface energy. In order to consider the changes dopant ions may have on the crystal morphology, a number of properties have to be defined. Firstly, as the morphology prediction is based on surface energy the crystal must be at equilibrium for the Wulff construction to be valid. Secondly, the two properties of the system that can change are the crystal size and the level of doping. These two properties affect the parameters of the prediction.

Crystal size is important as large crystals will have a high ratio of bulk to surface sites and can therefore accommodate higher concentrations of dopant ions in non-surface sites compared to small crystals. This relates to the doping level to produce four possible scenarios.

Large crystal, low doping In this case not all surfaces would reach optimum surface energy as the doping level is too low. Surfaces with the greatest segregation energy would reach the optimum surface energy first. If there was very low doping then all dopants may reside in surface sites.

Small crystal, low doping In the case of very low doping not all surfaces would reach the optimum surface energy. Surfaces with the greatest segregation energy would reach the optimum surface energy first. This scenario is very similar to the previous.

Large crystal, high doping All surfaces would reach the optimum surface energy with the remaining dopant ions residing in the bulk.

Small crystals, high doping Dopant ions would be forced to surface sites if the ratio of bulk to surface sites was low and there was high doping levels.

The simplest of these to model is the scenario of large crystals and high doping. While this is referred to as high doping, the doping level only needs to be great enough

to all surfaces to reach the optimum surface energy. As for YLF most surface energies are increased with the presence of the rare earth dopants the level of doping required for this scenario is relatively low. Figures 4.28 and 4.29 show the morphology predictions for the rare earth ions considered in this work along with the percentage change from the perfect YLF morphology.

The most obvious difference in the morphologies is that the (111) surface, which appears in the perfect YLF morphology, is replaced by the (110) surface when La^{3+}, Ce^{3+}, Pr^{3+}, and Nd^{3+} ions are present. Table 4.25 shows that the (110) surface was the surface most greatly affected by the present of dopant ions. It is therefore unsurprising that the surface energy is reduced enough for it to replace the (111) surface. For La^{3+} ions the (110) surface energy changed by -14.5% whereas the (111) surface changed by 5%. For Sm^{3+} doped YLF neither the (111) or the (110) surface appears in the morphology. The extra surface area is taken up by the (112) surface in this case. For the rare earth ions from Eu^{3+} to Lu^{3+} the (111) appears again. The latter rare earth doped YLF morphologies are all similar to the perfect YLF morphology.

The first five rare earth ions (La^{3+}, Ce^{3+}, Pr^{3+}, Nd^{3+} and Sm^{3+}) show the greatest difference from the perfect YLF morphology. This is due to these ions having the strongest segregation tendency. For all five ions the (112) surface area is increased. The (112) surface was the second most affected surface by the presence of dopants (Table 4.25). The next four surfaces in decreasing order of dopant segregation are the (012), (221), (021) and (122). These do not decrease in energy sufficiently to appear in any of the morphologies.

The (211) surface is the other surface that changes across the morphologies. This is despite the surface energy of this surface not changing, as all dopant ions cause an increase in the surface energy. The surface energy for this surface is therefore the perfect (211) surface energy for all rare earth ion doped systems. The change in the surface area coverage is caused by the change in the surface energies of other surfaces.

While the relative size of each surface alters across the rare earth ions, the overall shape of the morphology remains consistent. Even the (111) surface being replaced

with the (110) does not alter the overall shape.

The three other scenarios can be considered qualitatively from the results shown for the large crystal with high doping. If the crystals are large, but the doping level is lower then only those surfaces with large segregations energies would reach optimum surface energy. The morphology predictions would therefore be very similar to those shown as the surfaces that change the most in surface area coverage are those with the largest segregation energy.

In the two scenarios with small crystals, the low doping would again produce morphology predictions very similar to those shown. In the case of high doping, dopant ions may be forced to surface sites, providing there is enough energy. In this case the morphologies would be different, however, it is not easy to predict them as the Wulff construction theory relies on equilibrium growth. To make an attempt to predict the morphologies, the smallest positive segregation energies would be assumed to be where the dopants would be forced to reside after the negative segregation sites were filled. The surfaces that have the greatest reduction in energy with dopant ions present are most likely to be the surfaces with the lowest positive segregation energies also. The morphology predictions are therefore likely to contain the same surfaces as before, just in different ratios of surface area coverage. As the doping level is increased, other surfaces would start to appear.

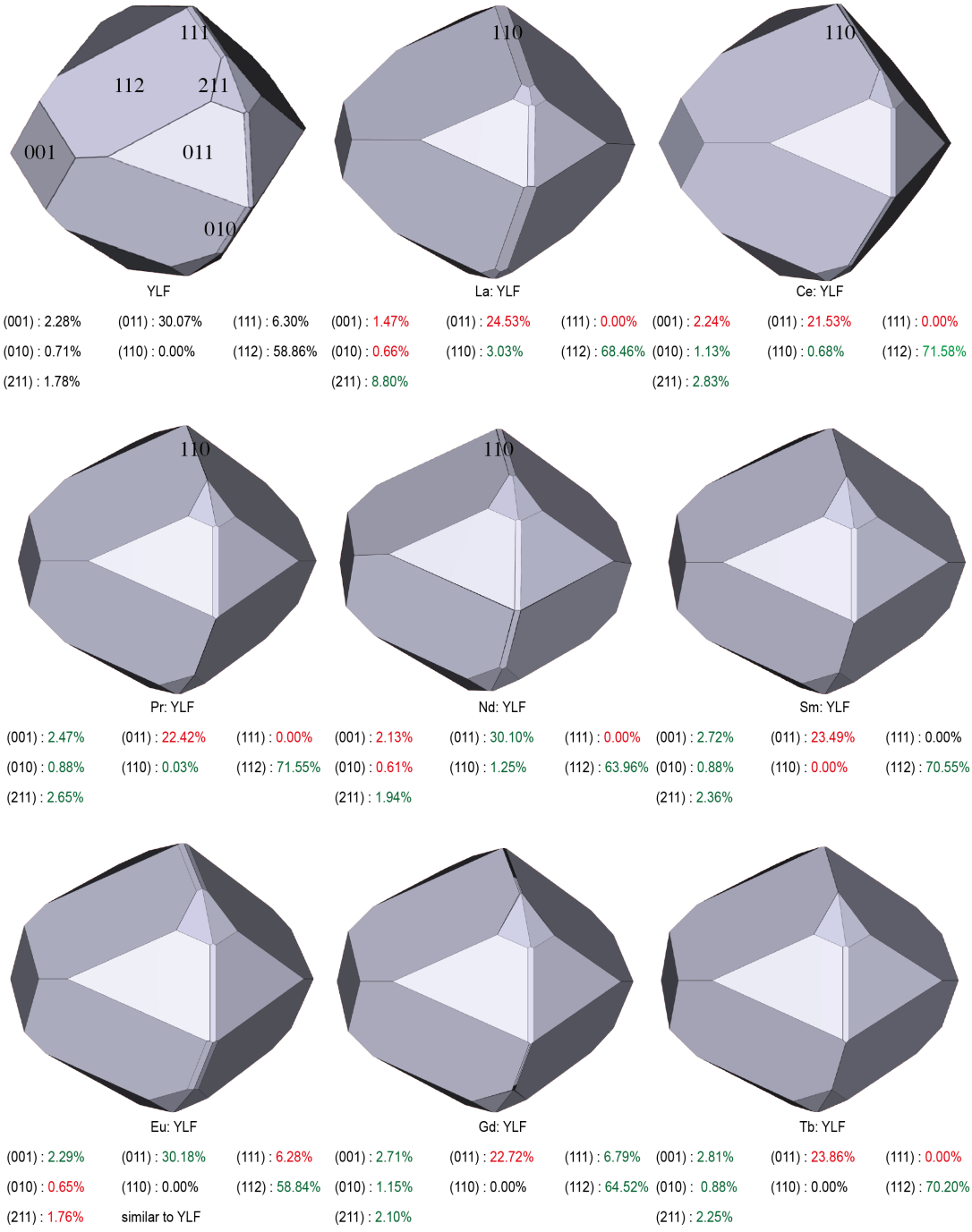

Figure 4.28: Morphology predictions based on defective surface energy for dopant ions La^{3+} to Tb^{3+}. Surface area percentages are given and colour coded. Surfaces that increase in area from the perfect YLF morphology are green. Those that decrease are red. Only the surfaces that change from the perfect YLF morphology are labeled.

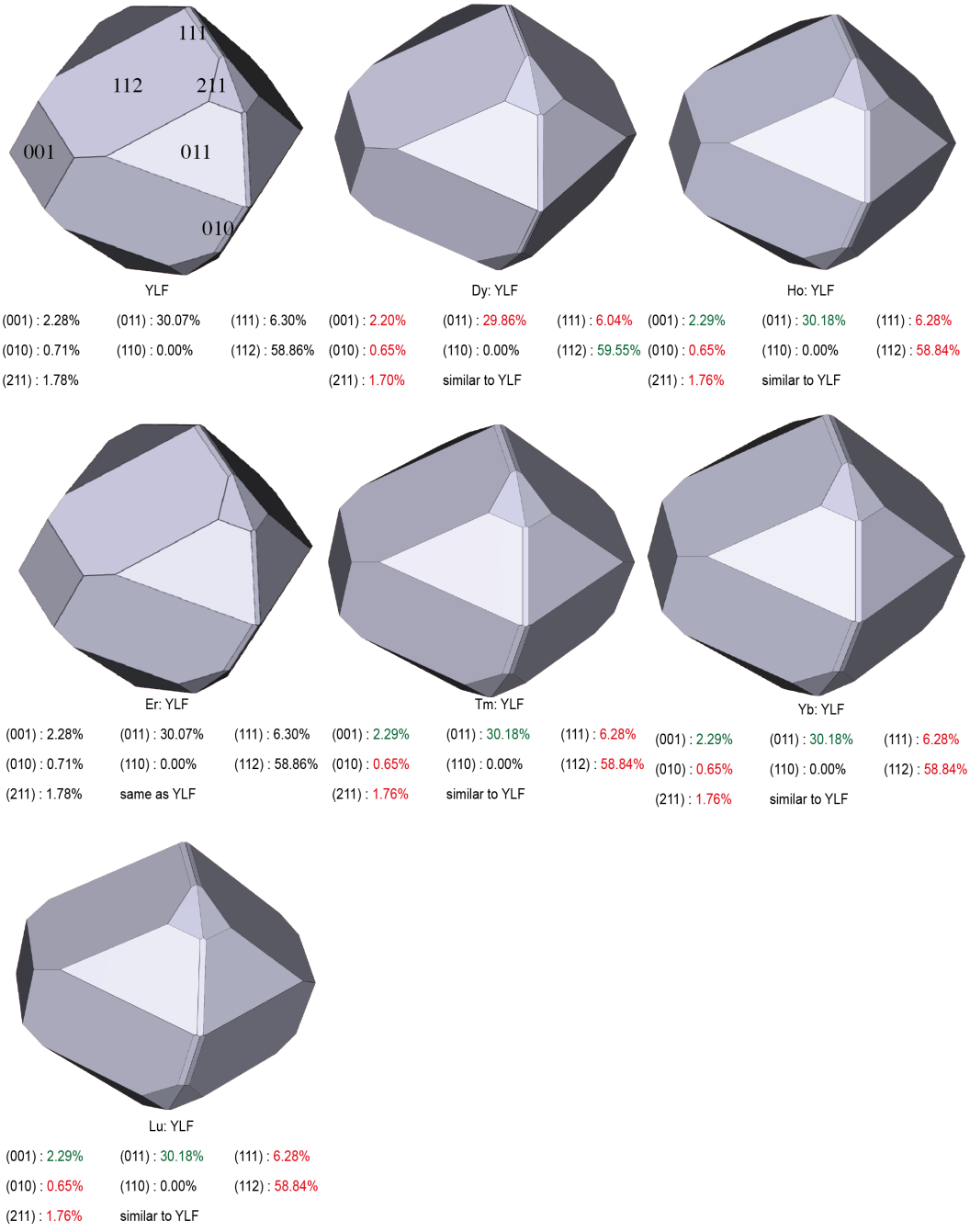

Figure 4.29: Morphology predictions based on defective surface energy for dopant ions Dy^{3+} to Lu^{3+}. Surface area percentages are given and colour coded. Surfaces that increase in area from the perfect YLF morphology are green. Those that decrease are red. Only the surfaces that change from the perfect YLF morphology are labeled.

4.3.9 Summary

Surface and attachment energies were calculated for YLF and were used to predict the equilibrium and growth morphologies. The equilibrium morphology was dominated by the (112) and (011) surfaces as these had the lowest surface energies. The rest of the morphology consisted of the (001), (010), (111) and (211) surfaces. The growth morphology was dominated by the (001) and (120) surfaces as these were the slowest growing faces. The rest of the growth morphology consisted of the (010) and the (011) surfaces.

Rare earth dopant segregation to the surfaces that appear in the morphologies were calculated. This revealed that there was segregation to all surfaces studied - (001), (011), (112) - but was to a much greater degree for the (112) surface. At the (112) surface the defect energies did not reach their bulk values until a depth of 9 Å; far greater than with the other two surfaces. Common across all three surfaces was that the first rare earth ions in the group have stronger segregation tendencies than the latter ones, with La^{3+} producing the largest segregation energy of them all. As the primary driving force for defect ion segregation is elastic strain induced in the lattice by a mismatch in defect ion radius to lattice host radius, this result was as expected.

To analyse the segregation of defects further a methodology was established to consider clusters of multiple defects at the surfaces of all low index faces and the effect they had on the surface energy. The same trend was seen from these results in that those rare earth ions with similar ionic radius to Y^{3+} tend to affect the surface energy least. One exception to this appeared. Ho^{3+}, which has the closest ionic radius to that of the Y^{3+} ions, had one of the greatest impacts on the surface energy. Considering the case of La^{3+}, as this ion produced the greatest reduction in surface energy, the surface that changed the most in energy was the (110) surface, which saw a reduction of 14.5% in surface energy. The next surfaces in decreasing size of the reduction in energy are: (112), (012), (221), (021), (122) and (010). The remaining surfaces all showed increases in surface energy with the presence of La^{3+} ions (and therefore all rare earth ions).

Using the defective surface energies it was possible to predict the defective mor-

phology. In the case of large crystals, such that there is a high ratio of bulk to surface sites, and high doping levels, all surfaces would reach the optimum surface energy with the remaining dopant ions residing in the bulk. For systems with La^{3+} to Nd^{3+} ions present the (111) surface is replaced by the (110) surface in the morphology. For Sm^{3+} neither the (111) or the (110) surface appears. As expected for the latter rare earth ions the predicted morphology is similar to the perfect YLF morphology. Despite the surfaces that appear in the morphology changing, and the relative ratios of surface areas changing, the overall shape does not change.

The results from this work into the surface properties of YLF provide important information needed for the design, development and improvement of this laser material. For example, ideally a doped laser crystal would be homogeneous as clustering of defects makes cutting and polishing any crystals more difficult, and dopant ions that lie close to each other can cause problems through energy transfer processes that may degrade the laser action. The calculated segregation of dopant ions can be used to provide an insight into possible clustering of dopant ions. It is shown that the latter rare earth ions are more suited for this application as they tend to cluster less. The dominance of the (112) surface in the surface morphology and the stabilisation of this surface with the presence of dopant ions may have an impact on the quality of the crystal and must therefore be considered.

4.4 Future work

This work into YLF has raised a number of interesting results that should be examined further. Firstly, the unusual decrease in the 'a' parameter with increasing temperature should be investigated further. To achieve this, the potentials need to be improved for non-static simulations. Stiffening the spring constant in the Shell Model may be enough and should be tried as a first approach.

To extend the work in the prediction of the impact dopant ions have on the morphology, the other scenarios of crystal size and doping level could be examined explicitly. The work carried out so far assumed the dopant ions were at the uppermost cation layer to the surface termination. The depth profiles of the morphologically important surfaces revealed that often the defect energies do not reach bulk values until a deep depth. The work carried out in this thesis could therefore be repeated but at the second cation layer down.

The simulation cells could be scaled further to see if the same results are produced. The surfaces in this work were filled from 0% to 100% and so with larger simulation cells the effect of concentration and surface coverage could be examined further.

Finally, as it is the electronic properties of the rare earth dopant ions that provides this system with its useful properties, detailed electronic structure modelling should be carried out. This would not be a trivial task as yttrium and the rare earth ions are large complex elements that would cause problems in this type of modelling, particularly if concentration effects were to be looked at.

Chapter 5

$BaMgF_4$

5.1 Structural description

BMF has the formula $BaMgF_4$ and is a material that is actively being researched for its optical properties that arise when doped with rare earth ions. These properties open up the possibility of practical applications for the material, mainly in the area of solid state lasers that operate in the IR (infrared), UV (ultraviolet), and near UV region.

BMF consists of Ba^{2+} ions surrounded by six F^- ligands forming a trigonal prism and two F^- ligands in a plane containing the Ba^{2+} ion perpendicular to the c-axis. There are four crystallographically distinct fluorine sites. Mg^{2+} ions and six F^- ligands form a distorted octahedron. Structural and electronic calculations indicate the octahedral distortion arises because the undistorted unit cell is unable to accommodate the energetically preferred Mg - F1 bond lengths, forcing the F1 anion outward to achieve the favoured separation [189]. This distortion and rotation gives rise to the ferroelectric spontaneous polarisation, directed along the c-axis [190, 191, 192]. BMF belongs to the orthorhombic crystal system with the space group $Cmc2_1$. The structure is shown in Figure 5.1 as reported by [193] with unit cell parameters of a = 4.13 Å, b = 14.52 Å, c = 5.82 Å.

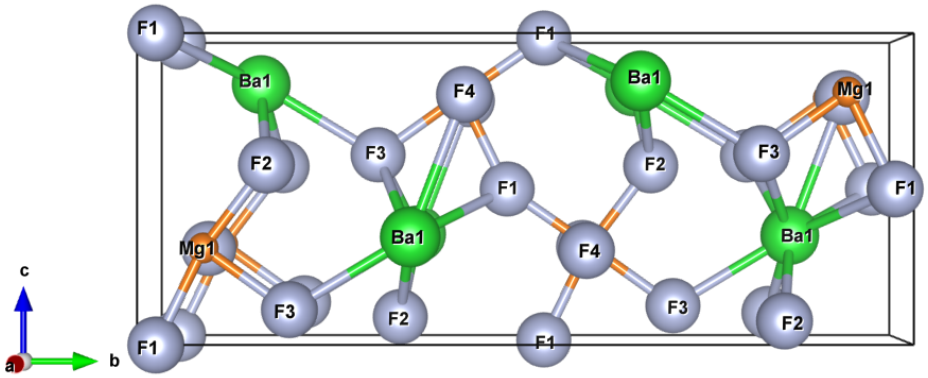

Figure 5.1: Unit cell of BMF as reported by [193] with unit cell parameters of a = 4.13 Å, b = 14.52 Å, c = 5.82 Å. Atoms are shown in relative ionic size.

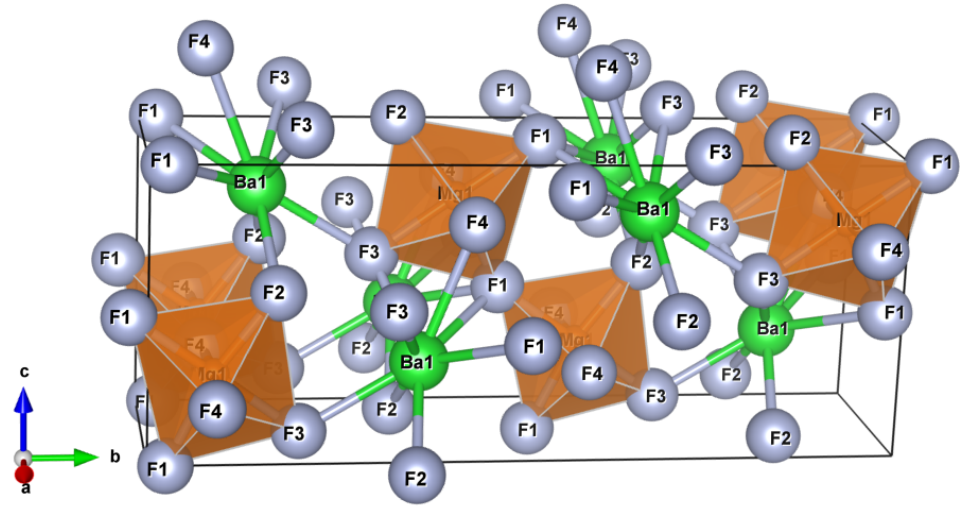

Figure 5.2: Unit cell of BMF showing the magnesium coordination. Atoms are shown in relative ionic size.

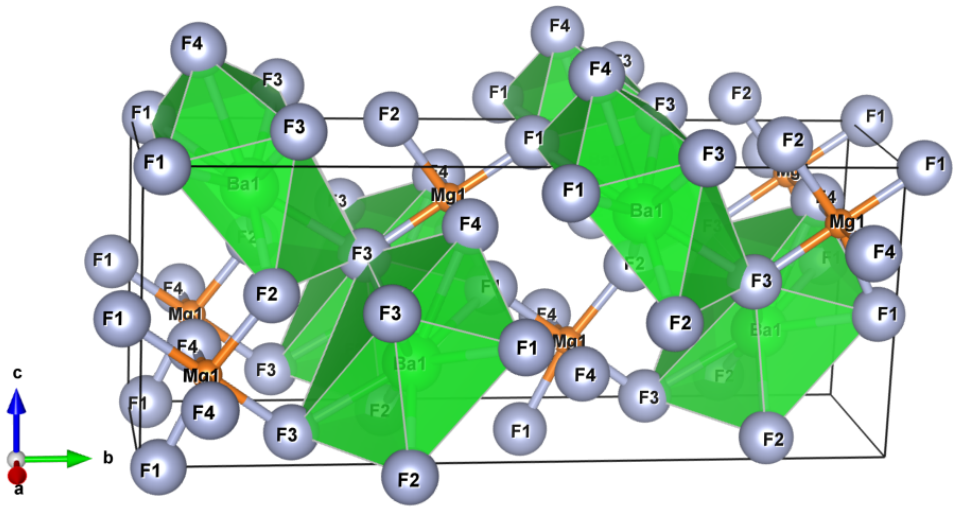

Figure 5.3: Unit cell of BMF showing the barium coordination. Atoms are shown in relative ionic size.

5.1.1 Literature review

BMF is of interest as a UV laser host lattice due to a number of its properties. It is colourless and transparent down to approximately 130 nm [194, 195]. BMF has a large bandgap to cover the UV/VUV (ultraviolet/vacuum ultraviolet) wavelength region, which is more generally true of fluoride single crystals. They tend to have a larger bandgap than oxides and that is why fluoride single crystals have high potential in UV/VUV laser applications [196]. Pyroelectric and piezoelectric properties of BMF have been reported [190], as have ferroelectric properties with thin films of BMF having been investigated for memory applications [197, 198].

In the area of laser development, BMF has been studied less widely than YLF and is, to date, not available as a working, commercial laser device. It is still however, a candidate and the BMF lattice offers a number of advantages. Shimamura and Villora in 2011, after a range of studies into solid-state laser materials, concluded there is 'high potential for BMF as a laser source with generation at 193 nm' [196]. Kodama *et al.* [199] grew Ce:BMF crystals with various concentrations of Na^+ ions from 0% to 2.5% as charge compensation. The Ce^{3+} ion concentration was 0.5% in all cases. The aim was to produce a tunable laser, however, on being irradiated with an intense 266 nm laser, colour centres were formed that caused the material to turn brown (green at high

temperature). Despite this, the material is still believed to offer potential as a tunable laser [200].

Kuck and Sokolska (2002) report the growth and characteristics of Pr^{3+} doped BMF [201] as an alternative to the Ce^{3+} doped systems. The use of other dopants has been reported including Yb^{3+} by Garcia-Santizo [202] and Nd^{3+} by Munoz-Santiuste [203].

There have been a small number of electronic structure modelling studies into BMF. In 2010, Huang *et al.* published a plane-wave pseudopotential study into BMF which reported the electronic band structure of the material [204]. A further computational paper was published by Watanabe *et al.* in 2006 outlining work into the $4f5d$ transition in Ce^{3+} doped crystals including BMF [205]. Most recently, Janssens, Williams and Clarke reported the growth of Ce^{3+}, Nd^{3+}, and Eu^{3+} doped BMF nanoparticles [206]. Based on the photoluminescence results the authors remark that the Ce^{3+} and Eu^{3+} ions occupy two distinct crystal sites.

Research has not just focussed on BMF as a laser source but also as a possible scintillator device. The scintillation properties of BMF have been reported [207, 208, 209] and in 2010, Yanagida *et al.* carried out further studies and concluded 'BMF is generally a suitable candidate for radiation measurements with high counting rate' [210].

A study by Posse, Friese and Grzechnik (2011) into the stability of BMF at high pressure revealed BMF undergoes a reversible phase transition to the paraelectric phase at pressures between 5 and 6 GPa [211].

5.2 Atomistic - bulk modelling

5.2.1 Perfect system

The ion interactions were modelled using potentials taken from previous work on this material [96]. Electrostatic supplemented Buckingham potentials were used for the interactions between Ba^{2+}-F^- and Mg^{2+}-F^-, while the F^--F^- interaction was modelled with a Shell Model to represent the polarisability of the ions. The Mg^{2+}-F^- potential was modified to reproduce the BMF structure and the MgF_2 lattice. The potentials used are given in Table 5.1.

These potentials produce a model which is within 1.6% of the observed lattice parameters [193] (Table 5.11). Further properties such as elastic constants can be compared to ensure the model reproduces the system accurately. Elastic constant data is reported in Table 5.3. The fit of the elastic constants is variable, however, it should be noted that the potentials used in this work were not fitted to the elastic constants. The accurate reproduction of the lattice parameters and that successful use of the potentials in other work [96] provides support to the model's accuracy.

Further physical properties are listed in Table 5.4 as calculated from the simulation.

All potential cut-offs were set to 0.0 Å and 10.0 Å, and all defect calculations were performed using the Mott-Littleton method with region sizes of 10 Å and 15 Å. These correspond to approximately 500 ions in region 1 and 1100 ions in region 2a. The lattice energies used throughout this chapter for defect calculations are listed Table 5.5, and they were obtained from simulations using the potentials listed for consistency. The region sizes were chosen based on the need for converged defect values but also a

Interaction	A /eV	ρ /Å	C /eVÅ^6	F shell q	K (F_{core}-F_{shell}) /eVÅ^{-2}
Ba^{2+}-F^-	3090.2000	0.2987	0.0000	-	-
F^--F^-	1153.6000	0.1365	0.0000	-2.321 $\|e\|$	48.40
Mg^{2+}-F^-	1140.0000	0.2664	0.0000	-	-

Table 5.1: Interatomic potentials used in the atomistic modelling of BMF taken from previous work [96] with the exception of Mg^{2+}-F^-, which was modified. All potentials are in the form of the Buckingham potential.

Parameter	Modelled	Observed [193]	Percentage difference /%
a	4.17 Å	4.13 Å	0.97
b	14.37 Å	14.52 Å	1.03
c	5.91 Å	5.82 Å	1.55
$\alpha/\beta/\gamma$	90.00°	90.00°	0.00

Table 5.2: Comparison of modelled BMF unit cell parameters to the observed parameters.

Parameter	Modelled /GPa	Reported [212] /GPa	Percentage difference /%
C_{11}	114.3	104.0	−9.9
C_{12}	34.1	28.7	−18.8
C_{13}	52.8	63.7	17.19
C_{22}	75.6	81.0	6.7
C_{23}	30.2	35.8	15.6
C_{33}	89.1	130.0	31.5
C_{44}	16.8	32.1	47.7
C_{55}	46.0	55.1	16.5
C_{66}	25.2	24.7	−2.0

Table 5.3: Comparison between reported elastic constants and modelled ones. Experimental values are quoted at room temperature.

Property	Modelled
Shear Modulus	28.4 GPa
Bulk Modulus	57.0 GPa
Young's Modulus	x: 79.0 GPa y: 62.1 GPa z: 65.5
Static dielectric	xx: 11.1 yy: 9.0 zz: 7.7
High frequency dielectric	xx: 2.2 yy: 2.1 zz: 2.1
Static refractive indices	1: 2.7 2: 3.0 3: 3.3
High frequency refractive indices	1: 1.5 2: 1.5 3: 1.5

Table 5.4: Table listing physical properties of BMF obtained from the simulation.

System	E_{latt} /eV	Reference
BaF_2	−23.940	calc.
MgF_2	−29.920	calc.
$BaMgF_4$	−54.052	calc.
LaF_3	−49.701	[114]
CeF_3	−50.154	[114]
PrF_3	−50.596	[114]
NdF_3	−51.040	[114]
SmF_3	−51.244	[114]
EuF_3	−52.246	[114]
GdF_3	−52.238	[114]
TbF_3	−52.234	[114]
DyF_3	−52.850	[114]
HoF_3	−53.374	[114]
ErF_3	−53.466	[114]
TmF_3	−53.633	[114]
YbF_3	−53.961	[114]
LuF_3	−54.253	[114]

Table 5.5: Lattice energies of BaF_2,MgF_2 and all REF_3 studied used in the calculation of solution energies.

sensible computation time.

5.2.2 Intrinsic defects

Intrinsic defects are those that appear naturally within the system through thermal action and involve no non-native species. The first of these defects is the formation of a vacancy. Table 5.6 lists the formation energy of vacancies of all three constituent ions. There are four unique F^- positions in the system so they are treated separately, with an average value also given. The second is interstitials, which are constituent ions at non-lattice sites. Table 5.7 lists the lattice sites considered in this thesis and the formation energy associated with forming an interstitial there for the each of the three ions in this system.

The results show, as expected, the formation energy of a F^- vacancy is considerably lower in energy than the cation vacancies. Cation vacancies are therefore unlikely to appear in the lattice, however, the formation energies for cation interstitials are favourable. Vacancies and interstitials occur in the lattice in the form of Frenkel defects.

Vacancy	Formation energy /eV
Ba	19.23
Mg	25.15
F1	4.70
F2	4.55
F3	4.55
F4	4.56
F(av)	4.59

Table 5.6: List of defect formation energies for constituent ions vacancies in BMF.

Lattice site		Formation energy /eV
a) 0.2500, 0.7151, 0.3028	Ba	−12.01
	Mg	−21.18
	F	−1.49
b) 0.5000, 0.5710, 0.5385	Ba	−9.47
	Mg	−18.64
	F	−0.79

Table 5.7: List of defect formation energies for constituent ions interstitials in BMF.

To calculate the likelihood of Frenkel defects occurring, the solution energy has to be calculated.

The reaction schemes for all intrinsic defects studied are:

1. $E_{Frenkel} = E_{vac} + E_{int}$
2. $E_{Schottky} = Ba_{vac} + Mg_{vac} + 4(F_{vac}) + E_{latt}(BaMgF_4)$
3. $E_{BaF_3pseudo} = Ba_{vac} + 2(F_{vac}) + E_{latt}(BaF_2)$
4. $E_{MgFpseudo} = Mg_{vac} + 2(F_{vac}) + E_{latt}(MgF_2)$

The intrinsic defect energies are give in Table 5.8. The Frenkel energies are subscripted ‘a’ and ‘b’ to correspond to the lattice site coordinates given in Table 5.7. Two defect formation energies are given. The first of these is obtained from adding the individual components that make up the total defect. For example, the Frenkel energy is obtained by adding the vacancy formation energy to the interstitial formation energy. The second value listed is for a bound defect energy. This is obtained from simulating the total defect in one calculation. For example, for the Frenkel defect a

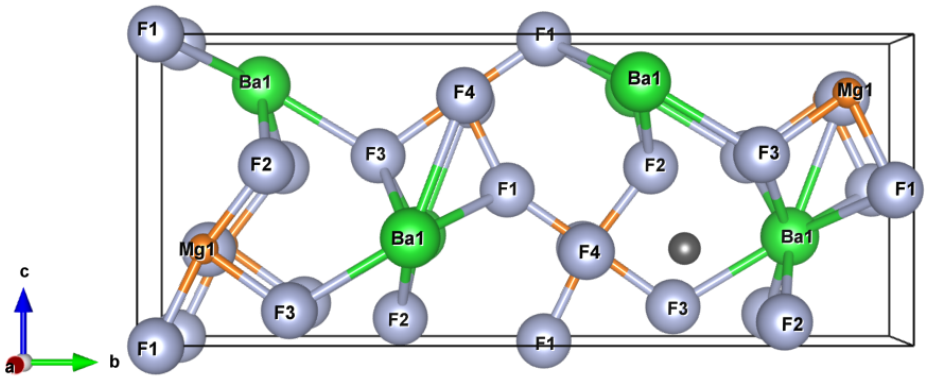

Figure 5.4: Unit cell of BMF showing the first interstitial site considered at fractional coordinates 0.2500, 0.7151, 0.3028. The atoms are shown in relative ionic size.

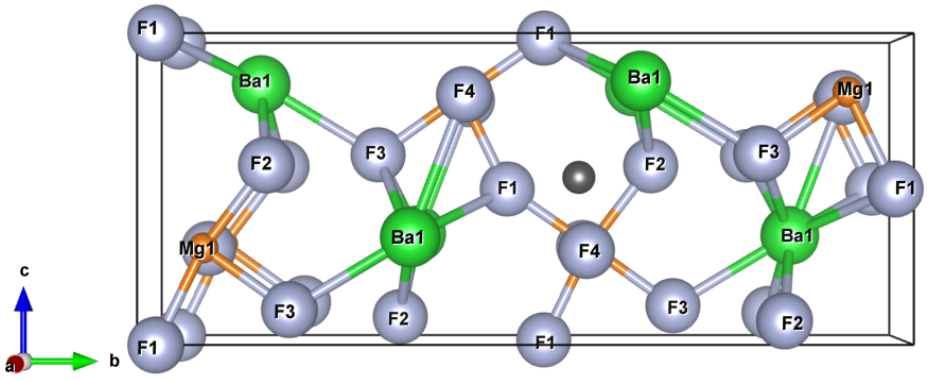

Figure 5.5: Unit cell of BMF showing the second interstitial site considered at fractional coordinates 0.5000, 0.5710, 0.5385. The atoms are shown in relative ionic size.

Defect	E_{def} /eV	E_{def}^{bound} /eV
Frenkel $(F)_a$	3.10	2.11
Frenkel $(F)_b$	3.80	3.11
Frenkel $(Ba)_a$	7.22	5.41
Frenkel $(Ba)_b$	9.76	9.47
Frenkel $(Mg)_a$	3.97	2.62
Frenkel $(Mg)_b$	6.51	2.71
Schottky	8.69	3.20
BaF_2 pseudo-Schottky	4.47	2.10
MgF_2 pseudo-Schottky	4.41	1.59

Table 5.8: List of intrinsic defects energies in BMF including Frenkel and Schottky defects. Both bound and unbound defect energies are given.

vacancy and an interstitial is modelled together. The advantage of this approach is that the binding energy of the two defects is included, which often lowers the defect energy. The non-bound and the bound defect energies are both listed to provide a measure of the binding energy, as:

$$E_{binding} = E_{def}^{bound} - E_{def} \tag{4.1}$$

It can be seen from these that the formation of Ba Frenkel defects are high energy, with both the F and Mg Frenkel defect energies smaller. Schottky defects are of a similar magnitude to the F and Mg Frenkel due to a large binding energy. The lowest energy defect is the formation of a MgF_2 pseudo-Schottky. In comparison with the defect energies obtained for YLF in the previous chapter the energies for BMF are greater.

In summary, the intrinsic defects most likely to dominate the BMF lattice are F Frenkel, MgF_2 pseudo-Schottky and BaF_2 pseudo-Schottky.

5.2.3 Rare earth dopant solution energies

The optically important rare earth dopants all have a standard oxidation state of 3+. However, there are no cations within the BMF lattice with this charge therefore charge compensation is required in all cases. Six different reaction schemes were considered and they are:

1. $2REF_3 + 3Ba_{Ba} \rightarrow 2RE^{\cdot}_{Ba} + V^{''}_{Ba} + 3BaF_2$
2. $2REF_3 + 2Ba_{Ba} + Mg_{Mg} \rightarrow 2RE^{\cdot}_{Ba} + V^{''}_{Mg} + 2BaF_2 + MgF_2$
3. $REF_3 + Ba_{Ba} \rightarrow RE^{\cdot}_{Ba} + F^{'}_{i} + BaF_2$
4. $REF_3 + Mg_{Mg} \rightarrow RE^{\cdot}_{Mg} + F^{'}_{i} + MgF_2$
5. $2REF_3 + 3Mg_{Mg} \rightarrow 2RE^{\cdot}_{Mg} + V^{''}_{Mg} + 3MgF_2$
6. $2REF_3 + 2Mg_{Mg} + Ba_{Ba} \rightarrow 2RE^{\cdot}_{Mg} + V^{''}_{Ba} + 2MgF_2 + BaF_2$

The solution energies for these reactions are:

1. $E_{sol} = \frac{1}{2}[3(E_{latt}(BaF_2) + E^{Ba}_{vac} + 2(E_{def}(RE_{Ba})) - 2(E_{latt}(REF_3))]$
2. $E_{sol} = \frac{1}{2}[E_{latt}(MgF_2) + 2(E_{latt}(BaF_2)) + E^{Mg}_{vac} + 2(E_{def}(RE_{Ba})) - 2(E_{latt}(REF_3))]$
3. $E_{sol} = E_{latt}(BaF_2)) + E(F_i) + E_{def}(RE_{Ba}) - E_{latt}(REF_3)$ (5.1)
4. $E_{sol} = E_{latt}(MgF_2)) + E(F_i) + E_{def}(RE_{Mg}) - E_{latt}(REF_3)$
5. $E_{sol} = \frac{1}{2}[3(E_{latt}(MgF_2)) + E^{Mg}_{vac} + 2(E_{def}(RE_{Mg})) - 2(E_{latt}(REF_4))]$
6. $E_{sol} = \frac{1}{2}[E_{latt}(BaF_2 + 2(E_{latt}(MgF_2)) + E^{Ba}_{vac} + 2(E_{def}(RE_{Mg})) - 2(E_{latt}(REF_3))]$

The potentials for the rare earth fluoride interactions were taken from [114] and are reproduced in Table 5.9. Upon carrying out the surface modelling work of YLF (see the previous Chapter), two of the potentials were found to produce unphysical results. These were refitted using the methodology outlined in Section 2.2.3.

Table 5.10 lists the defect formation energies for rare earth dopants at both cation sites and also the formation energy of a F interstitial at the 'a' lattice site. This interstitial site was used for reaction schemes 3 and 4. The defect formation energies are smaller for the rare earth ion at the Ba^{2+} site than at the Mg^{2+} site, however, to evaluate which reaction scheme is the lowest energy, the solution energies have to be calculated. All solution energies were calculated using both bound and unbound defects in order to provide a measure of binding energy. Table 5.11 lists the solution energies for the six reaction schemes. The scheme highlighted in red for each rare earth ion is

Interaction	A / eV	ρ / Å	C / eVÅ^6
La^{3+}-F^-	2817.74	0.2980	0.0
Ce^{3+}-F^-	2627.13	0.2980	0.0
Pr^{3+}-F^-	2453.39	0.2980	0.0
Nd^{3+}-F^-	2488.27	0.2950	0.0
Sm^{3+}-F^-	1764.57	0.3064	0.0
Eu^{3+}-F^-	2085.74	0.2950	0.0
Gd^{3+}-F^-	1667.02	0.3037	0.0
Tb^{3+}-F^-	1541.15	0.3065	0.0
Dy^{3+}-F^-	1536.68	0.3037	0.0
Ho^{3+}-F^-	2590.91	0.2809	0.0
Er^{3+}-F^-	1880.44	0.2920	0.0
Tm^{3+}-F^-	1390.19	0.3037	0.0
Tm^{3+}-F^-*	3173.80	0.2733	0.0
Yb^{3+}-F^-	2381.55	0.2808	0.0
Lu^{3+}-F^-	1448.23	0.2990	0.0
Lu^{3+}-F^-*	2901.80	0.2735	0.0

*Table 5.9: Rare earth fluoride potentials used in this work. Taken from [114]. The two potentials marked * were refitted for the defective surface modelling as the original potentials produced proved to inadequate.*

the lowest energy scheme. For the first rare earth ions (La^{3+}, Ce^{3+}, Pr^{3+}, and Nd^{3+}) the preferred doping site is the Ba^{2+} site with Mg^{2+} vacancies. For some of these ions a F^- interstitial instead of the vacancy as charge compensation is similar in solution energy. The solution energy for Sm^{3+} doping is the same for both the Mg^{2+} and Ba^{2+} sites. The remaining rare earth ions dope at the Mg^{2+} site with vacancies as charge compensation.

The ionic radius of Ba^{2+} is 1.42 Å while the ionic radius of Mg^{2+} is 0.89 Å. Rare earth ion radii range from 1.16 Å for La^{3+}, decreasing across the period to 0.98 Å for Lu^{3+}. (Radius information taken from [187]). This provides an explanation for why the larger rare earth ions reside at the Ba^{2+} site.

These results are summarised into two graphs with one for each cation site; Figures 5.6 and 5.7. The graphs reveal that the solution energies at the Ba^{2+} site are more constant across the rare earth ions compared to the Mg^{2+} site. At the Mg^{2+} there is a clear decrease in solution energy for the latter rare earth ions.

The solution energy results allow all simulations with rare earth doping from now on to be considered as listed in Table 5.12.

RE	$E_{def}(RE_{Ba})$ /eV	$E_{def}(RE_{Mg})$ /eV
La	−21.38	−14.04
Ce	−21.79	−14.72
Pr	−22.20	−15.40
Nd	−22.62	−16.00
Sm	−22.96	−16.81
Eu	−23.74	−17.77
Gd	−23.74	−18.02
Tb	−23.81	−18.21
Dy	−24.32	−18.96
Ho	−24.87	−19.20
Er	−24.99	−19.70
Tm	−25.05	−20.15
Yb	−25.46	−20.14
Lu	−25.58	−20.89
	$E_{def}(F_i)$ /eV	−1.49

Table 5.10: Defect formation energies at both cation sites in BMF and F interstitial energy. Values are used to calculate solution energies for all reaction schemes.

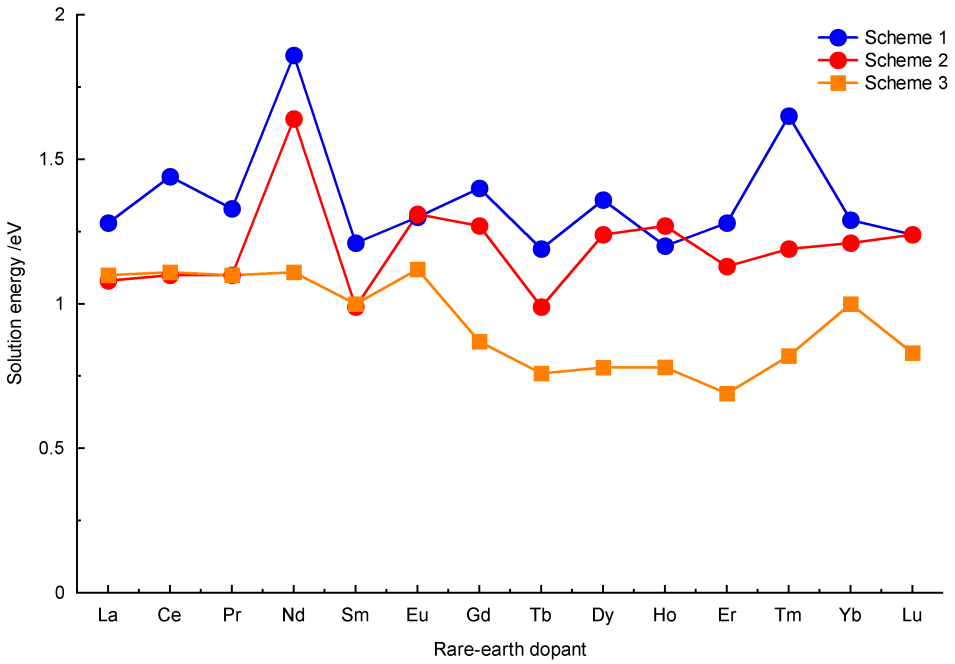

Figure 5.6: Plot of rare earth solution energy for the three schemes for doping at the Ba^{2+} site.

	Scheme 1 /eV		Scheme 2 /eV		Scheme 3 /eV		Scheme 4 /eV		Scheme 5 /eV		Scheme 6 /eV	
RE	E_{sol}	E_{sol}^{bound}	E_{sol}	E_{sol}^{bound}	E_{sol}	E_{sol}^{bound}	E_{sol}	E_{sol}^{bound}	E_{sol}	E_{sol}^{bound}	E_{sol}	E_{sol}^{bound}
La	2.03	1.28	2.00	1.08	2.89	1.10	4.25	2.46	3.36	2.11	3.39	2.47
Ce	2.07	1.44	2.04	1.10	2.93	1.11	4.02	2.37	3.12	1.87	3.16	2.28
Pr	2.10	1.33	2.07	1.10	2.96	1.10	3.78	2.13	2.89	1.69	2.92	2.08
Nd	2.12	1.86	2.10	1.64	1.94	1.11	3.63	1.99	2.73	2.33	2.77	1.95
Sm	1.99	1.21	1.96	0.99	2.85	1.00	3.02	1.39	2.13	0.98	2.16	1.39
Eu	2.21	1.30	2.18	1.31	3.07	1.12	3.06	1.50	2.17	1.06	2.20	1.22
Gd	2.21	1.40	2.18	1.27	3.07	0.87	2.81	1.25	1.92	0.88	1.95	0.91
Tb	2.12	1.19	2.10	0.99	2.99	0.76	2.61	0.87	1.72	0.69	1.75	0.69
Dy	2.24	1.36	2.21	1.24	3.10	0.78	2.48	0.92	1.59	0.70	1.62	0.58
Ho	2.20	1.20	2.17	1.27	3.07	0.81	2.76	1.01	1.87	0.74	1.90	0.84
Er	2.19	1.28	2.16	1.13	3.05	0.69	2.36	0.62	1.47	0.48	1.50	0.63
Tm	2.26	1.65	2.23	1.19	3.12	0.82	2.07	0.50	1.18	0.27	1.21	0.15
Yb	2.21	1.29	2.18	1.21	3.07	1.00	2.41	1.38	1.51	0.63	1.55	0.69
Lu	2.28	1.24	2.25	1.24	3.24	0.83	1.95	0.37	1.06	0.14	1.09	0.01

Table 5.11: Rare earth dopant solution energies in BMF for all six reaction schemes. The energies marked in red is the lowest energy reaction for that rare earth ion.

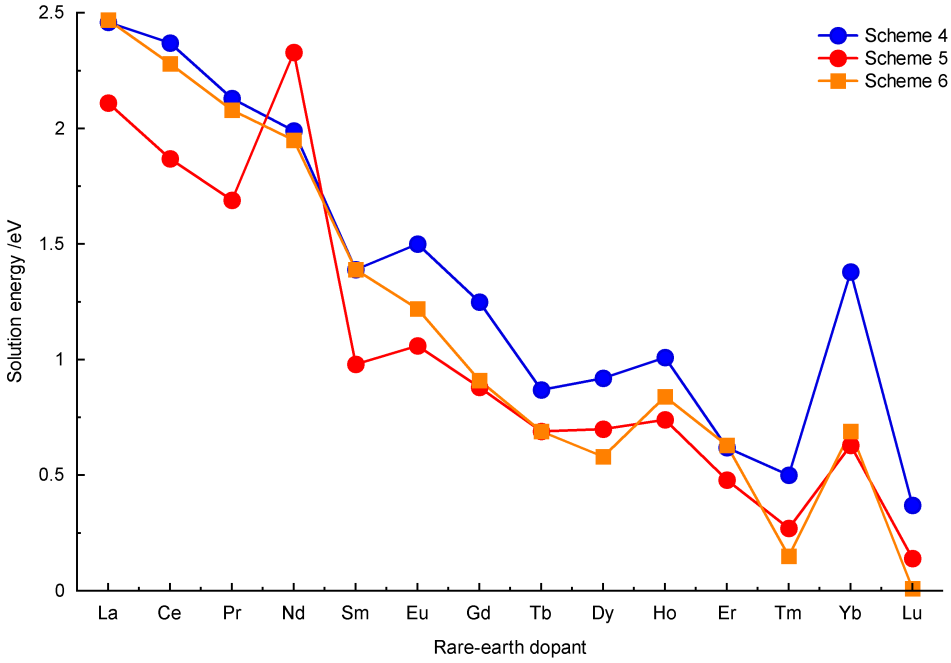

Figure 5.7: Plot of rare earth solution energy for the three schemes for doping at the Mg^{2+} site.

RE	Scheme	Doping method
La	2	$RE^{\cdot}_{Ba} + V''_{Mg}$
Ce	2	$RE^{\cdot}_{Ba} + V''_{Mg}$
Pr	2	$RE^{\cdot}_{Ba} + V''_{Mg}$
Nd	2	$RE^{\cdot}_{Ba} + V''_{Mg}$
Sm	6	$RE^{\cdot}_{Mg} + V''_{Ba}$
Eu	6	$RE^{\cdot}_{Mg} + V''_{Ba}$
Gd	6	$RE^{\cdot}_{Mg} + V''_{Ba}$
Tb	5/6	$RE^{\cdot}_{Mg} + V''_{Ba}$ or $RE^{\cdot}_{Mg} + V''_{Mg}$
Dy	5	$RE^{\cdot}_{Mg} + V''_{Mg}$
Ho	6	$RE^{\cdot}_{Mg} + V''_{Ba}$
Er	6	$RE^{\cdot}_{Mg} + V''_{Ba}$
Tm	5	$RE^{\cdot}_{Mg} + V''_{Mg}$
Yb	6	$RE^{\cdot}_{Mg} + V''_{Ba}$
Lu	5	$RE^{\cdot}_{Mg} + V''_{Mg}$

Table 5.12: Table summarising the doping method that was calculated as the lowest energy scheme for each rare earth.

5.2.4 Doping limit

As discussed in Section 2.4.4 an important, but non-trivial, calculation to make is to estimate the theoretical doping limit of the rare earth ions within the BMF lattice.

The first step in determining the doping limit is to write the solid-state reaction. As there are three different reaction schemes considered in BMF (Table 5.12) there are three solid-state reactions. In general form, where MF_3 is the rare earth fluoride and x is the mole fraction of dopant ions, they are:

Scheme 2:

$$xMF_3 + (1-x)BaF_2 + (1-0.5x)MgF_2 \rightarrow Ba_{(1-x)}xM_{Ba}^{\cdot}Mg_{(1-0.5x)}(0.5x)V_{Mg}^{''}F_4$$

$$E_{sol} = E_{latt}[Ba_{(1-x)}xM_{Ba}^{\cdot}Mg_{(1-0.5x)}(0.5x)V_{Mg}^{''}F_4] - [E_{latt}(xMF_3) + E_{latt}((1-x)BaF_2) + E_{latt}((1-0.5x)MgF_2)] \quad (5.2)$$

Scheme 5:

$$xMF_3 + BaF_2 + (1-1.5x)MgF_2 \rightarrow BaM_{Mg}^{\cdot}(0.5x)V_{Mg}^{''}Mg_{(1-1.5x)}F_4$$

$$E_{sol} = E_{latt}[BaM_{Mg}^{\cdot}(0.5x)V_{Mg}^{''}Mg_{(1-1.5x)}F_4] - [E_{latt}(xMF_3) + E_{latt}(BaF_2) + E_{latt}((1-1.5x)MgF_2)] \quad (5.3)$$

Scheme 6:

$$xMF_3 + (1-0.5x)BaF_2 + (1-x)MgF_2 \rightarrow Ba_{(1-0.5x)}xM_{Mg}^{\cdot}(0.5x)V_{Ba}^{''}Mg_{(1-x)}F_4$$

$$E_{sol} = E_{latt}[Ba_{(1-0.5x)}xM_{Mg}^{\cdot}(0.5x)V_{Ba}^{''}Mg_{(1-x)}F_4] - [E_{latt}(xMF_3) + E_{latt}((1-0.5x)BaF_2) + E_{latt}((1-x)MgF_2)] \quad (5.4)$$

The solution energy are determined in the usual way. The doping limit can be determined by setting the solution energy to zero and solving for x, the mole fraction of dopant ions. The problem arises with determining the lattice energy for the defective $BaMgF_4$ lattice. The first method considered to overcome this problem is the Jackson-Valerio 2011 method as published in [115]. In this, the defective lattice energy is assumed to be equal to the perfect $BaMgF_4$ lattice plus the defect formation energy as determined from Mott-Littleton calculations. Both terms are adjusted by the mole fraction of dopant ions.

Scheme 2:

Assume:

$$E_{latt}[Ba_{(1-x)}xM_{Ba}^{\cdot}Mg_{(1-0.5x)}(0.5x)V_{Mg}^{''}F_4] = (1-x)E_{latt}(BaMgF_4) + 0.5xE_{def}(2M_{Ba}^{\cdot} + V_{Mg}^{''})$$

Then:

$$E_{sol} = (1-x)E_{latt}(BaMgF_4) + 0.5xE_{def}(2M_{Ba}^{\cdot} + V_{Mg}^{''}) - [E_{latt}(xMF_3) + (1-x)E_{latt}(BaF_2) + (1-0.5x)E_{latt}(MgF_2)] \quad (5.5)$$

Scheme 5:

Assume:

$$E_{latt}[BaM_{Mg}^{\cdot}(0.5x)V_{Mg}^{''}Mg_{(1-1.5x)}F_4] = (1-x)E_{latt}(BaMgF_4) + 0.5xE_{def}(2M_{Mg}^{\cdot} + V_{Mg}^{''})$$

Then:

$$E_{sol} = (1-x)E_{latt}(BaMgF_4) + 0.5xE_{def}(2M_{Mg}^{\cdot} + V_{Mg}^{''}) - [xE_{latt}(MF_3) + E_{latt}(BaF_2) + (1-1.5x)E_{latt}(MgF_2)] \quad (5.6)$$

RE	Function	Max % MF_3
La	$E_{sol} = 52.34x - 0.19$	0.39
Ce	$E_{sol} = 52.51x - 0.19$	0.39
Pr	$E_{sol} = 52.39x - 0.19$	0.39
Nd	$E_{sol} = 52.84x - 0.19$	0.38
Sm	$E_{sol} = 58.02x - 0.19$	0.35
Eu	$E_{sol} = 58.10x - 0.19$	0.35
Gd	$E_{sol} = 57.92x - 0.19$	0.35
Tb	$E_{sol} = 57.73x - 0.19$	0.35
Dy	$E_{sol} = 51.64x - 0.19$	0.39
Ho	$E_{sol} = 57.79x - 0.19$	0.35
Er	$E_{sol} = 57.52x - 0.19$	0.35
Tm	$E_{sol} = 51.21x - 0.19$	0.39
Yb	$E_{sol} = 57.68x - 0.19$	0.35
Lu	$E_{sol} = 51.07x - 0.19$	0.40

Table 5.13: Concentration method for rare-earth doping in BMF. X in the function is mole-fraction of MF_3 used. The max percentage is found by setting E_{sol} to zero.

Scheme 6:

Assume:

$$E_{latt}[Ba_{(1-0.5x)}xM_{Mg}^{\cdot}(0.5x)V_{Ba}^{''}Mg_{(1-x)}F_4] = (1-x)E_{latt}(BaMgF_4) + 0.5xE_{def}(2M_{Mg}^{\cdot} + V_{Ba}^{''})$$

Then:

$$E_{sol} = (1-x)E_{latt}(BaMgF_4) + 0.5xE_{def}(2M_{Mg}^{\cdot} + V_{Ba}^{''}) - [xE_{latt}(MF_3) + (1-0.5x)E_{latt}(BaF_2) + (1-x)E_{latt}(MgF_2)] \quad (5.7)$$

Table 5.13 lists the solution energy functions based on this Jackson-Valerio assumption and the calculated doping limit for each of the rare earth ions. This shows that BMF does not readily accept high levels of doping of rare earth ions with levels at approximately 0.4%. However, as discussed in the previous chapter, there are significant problems with this method. The results for BMF highlight them again.

A modified version of the Jackson-Valerio method has the same starting point, but the defective lattice is now considered to be equal to the perfect lattice plus x-amounts

of the defect formation energy.

$$E_{latt}^{def}\left(BMF\right) = E_{latt}\left(BaMgF_4\right) + xE_{def} \tag{5.8}$$

The difference in this approach to the previous is that the perfect lattice energy is not scaled by the mole fraction of dopant ions. This equation is more logical than the previous Jackson-Valerio method as the defect formation energy includes the change in the perfect lattice to the defective one. This new approach is more robust and solves the problem that occurred with divalent dopants in the old method.

Considering the case when $x = 0$, i.e. there are no dopants present, the solution energy equations simplify to:

$$E_{sol} = E_{latt}\left(BaMgF_4\right) - \left[E_{latt}\left(BaF_2\right) + E_{latt}\left(MgF_2\right)\right] = E_f\left(BaMgF_4\right) \tag{5.9}$$

In this case, the solution energy equals the formation energy of $BaMgF_4$. Rearranging the solution energy equations (Equations 5.2, 5.3 and 5.4), with E_{sol} set to zero, to separate the $x-$terms and substituting for $E_{form}\left(BaMgF_4\right)$ gives:

Scheme 2:

$$x = -\frac{E_{form}\left(BaMgF_4\right)}{E_{def}\left(2M_{Ba}^{\cdot} + V_{Mg}^{''}\right) + E_{latt}\left(MgF_2\right) + 2E_{latt}\left(BaF_2\right) - 2E_{latt}\left(MF_3\right)} \tag{5.10}$$

Scheme 5:

$$x = -\frac{E_{form}\left(BaMgF_4\right)}{E_{def}\left(2M_{Mg}^{\cdot} + V_{Mg}^{''}\right) + 3E_{latt}\left(MgF_2\right) - 2E_{latt}\left(MF_3\right)} \tag{5.11}$$

Scheme 6:

$$x = -\frac{E_{form}\left(BaMgF_4\right)}{E_{def}\left(2M_{Mg}^{\cdot} + V_{Ba}^{''}\right) + 2E_{latt}\left(MgF_2\right) + E_{latt}\left(BaF_2\right) - 2E_{latt}\left(MF_3\right)} \tag{5.12}$$

Combining Equations 5.9 and 5.10/5.11/5.12 allows the doping limit, x, to be calcuated. Table 5.14 lists the calculated percentages of x using this methodology. Some of the percentages are negative, implying that with the conditions imposed by

RE	Max % MF_3	Scheme
La	−0.06	2
Ce	−0.07	2
Pr	−0.06	2
Nd	−0.08	2
Sm	0.03	6
Eu	0.02	6
Gd	0.03	6
Tb (5)	−0.04	5
Tb (6)	0.03	6
Dy	−0.04	5
Ho	0.03	6
Er	0.03	6
Tm	−0.04	5
Yb	0.03	6
Lu	−0.03	5

Table 5.14: Concentration method for rare earth doping in BMF based on a modified Jackson-Valerio method [116].

the calculations the BMF lattice is insoluble to rare earth ions. Those values that are positive are for Scheme 6, but these are also very small positive numbers.

5.2.5 Thermal effects

Most lattices expand with temperature and using free energy minimisation (see Section 2.3.2) the expansion of the lattice parameters can be modelled. Using this type of minimisation also allows the potentials to be tested with increasing temperature. Two methods for calculating the free energy were taken. The first, Full Free Energy Minimisation (FFEM) minimises the unit cell and the internal degrees of freedom with respect to the free energy, whereas the second, Zero Static Internal Stress Approximation (ZSISA) minimises only the unit cell with respect to the free energy with the internal degrees of freedom minimised with respect to the internal energy.

FFEM minimisation failed above 150 K with the simulation oscillating around the minimum resulting in hundreds of cycles. The Shell Model parameters were therefore removed from the potentials as it is often the separation of core and shell that causes issues. Using rigid ion potentials solved the minimisation problem and the simulations minimised in a few cycles up to 1000 K. With ZSISA, the minimisations were less

Parameter	Thermal expansion coefficient Modelled / K^{-1}
a	1.62×10^{-5}
b	1.52×10^{-5}
c	1.16×10^{-5}
Volume	4.53×10^{-5}

Table 5.15: Calculated thermal expansion coefficients for BMF.

successful with some data points having to be removed due to an unsatisfactory gradient normal. Figure 5.8 shows the change in the 'a' parameter, 'b' parameter, 'c' parameter, and volume with temperature from 0 K to 1000 K using the ZSISA simulation. The calculations were performed at constant pressure. The data points are slightly scattered but, particularly for the unit cell volume, show a linear increase in size with temperature. The scatter and the poor minimisation of some data points (that are not included in the plots) reveals that the potentials are not suitable for non-static minimisation.

Figure 5.9 shows the change in the lattice parameters using FFEM with rigid ion potentials. These plots all produce good linear trends, with a sight curve at low temperatures. The fit is good in all cases, which implies that the original potentials fail because of the Shell Model. If non-static simulations were to be carried out either the spring constant coupling the shell to the core for the fluoride ions would need to be stiffened, or rigid ion potentials used, to prevent the potentials failing.

Lines-of-best-fit were fitted to the plots so that the thermal expansion coefficients could be calculated. The gradients of these lines were used to calculate the linear thermal expansion coefficient for the three axes using Equation 4.12, where L_0 is the initial parameter length and $\frac{\Delta L}{\Delta T}$ is the calculated gradient.

$$\alpha = \frac{1}{L_0}\frac{\Delta L}{\Delta T} \tag{4.12}$$

A similar analysis was carried out for the volume resulting in the volume thermal expansion coefficient. Table 5.15 lists these coefficients.

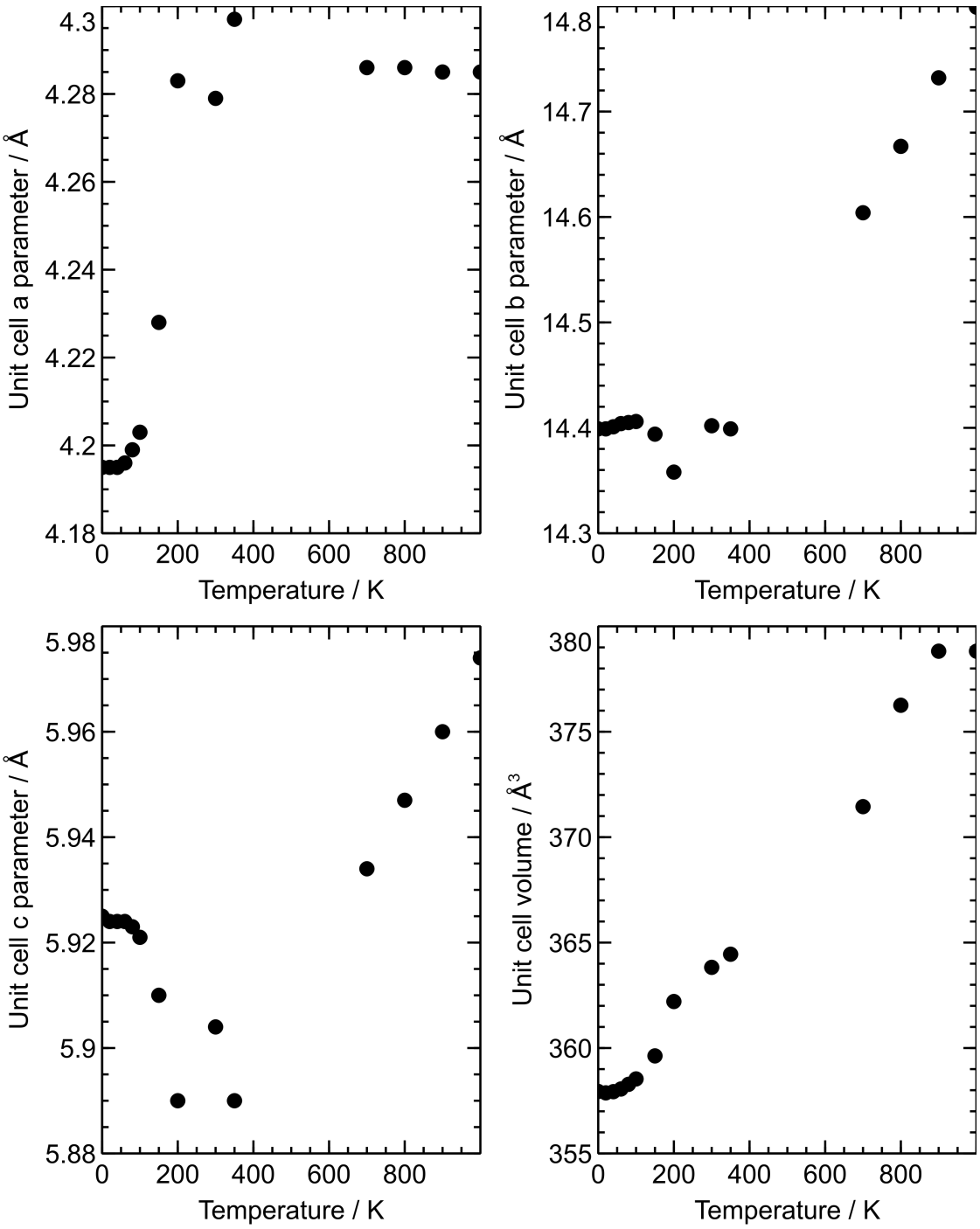

Figure 5.8: Plots of the free energy simulations for BMF using ZSISA. Plot top-left shows the change in the unit cell parameter 'a' with temperature. The plot top-right shows the change in the unit cell parameter 'b' with temperature. The plot bottom-left shows the change in the unit cell parameter 'c' with temperature. The plot bottom-right shows the overall change in volume with temperature.

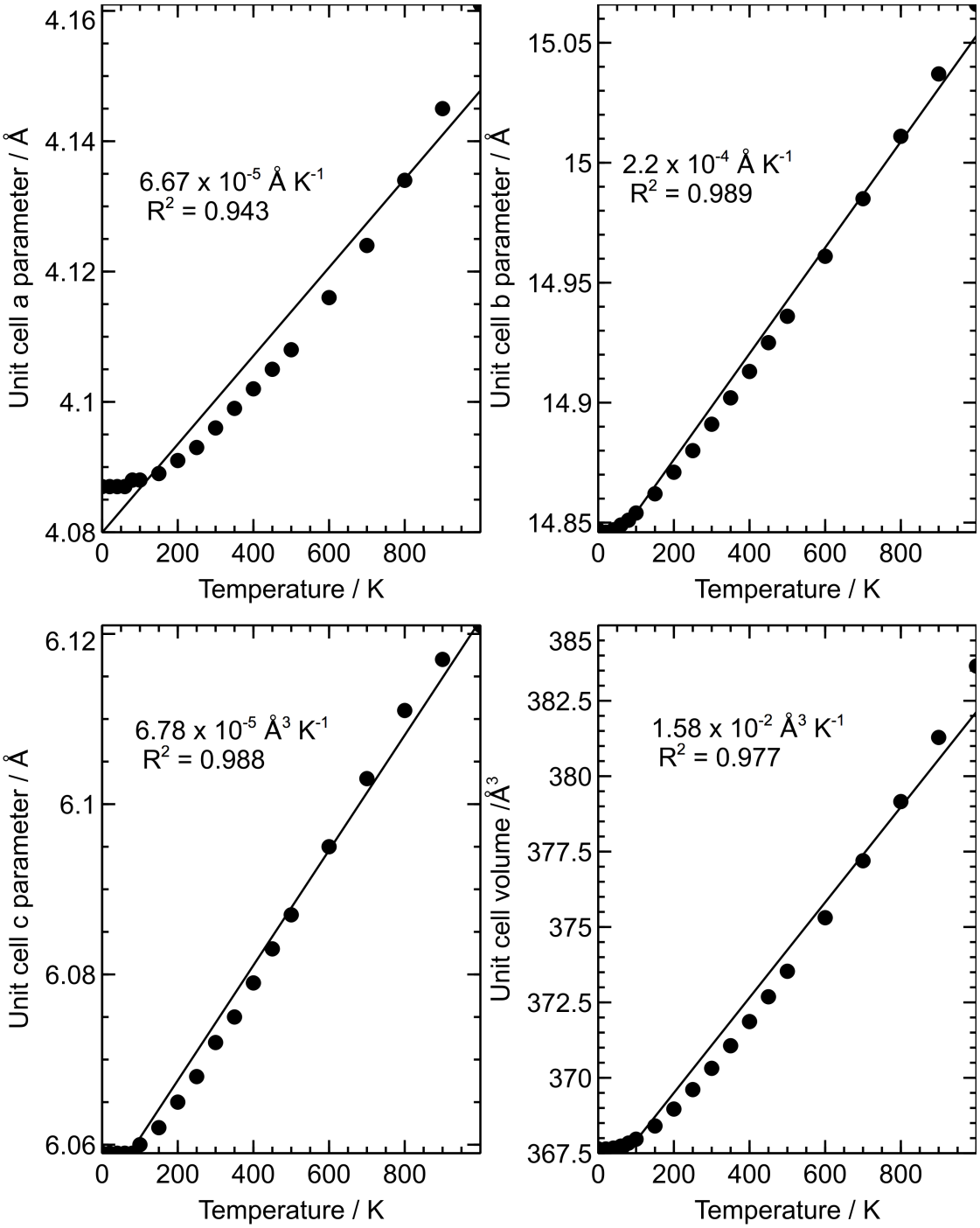

Figure 5.9: Plots of the free energy simulations for BMF using FFEM with rigid ion potentials. Plot top-left shows the change in the unit cell parameter 'a' with temperature. The plot top-right shows the change in the unit cell parameter 'b' with temperature. The plot bottom-left shows the change in the unit cell parameter 'c' with temperature. The plot bottom-right shows the overall change in volume with temperature. A function is fitted to all plots and the gradients displayed.

5.2.6 Summary

In summary, the intrinsic thermal defects for BMF have been modelled and the defect formation energies calculated. These show that the Schottky defect energies were of similar magnitude to the Frenkel defects. Within the Frenkel defects the fluorine and magnesium Frenkel are 2.5 times smaller than the barium Frenkel defect. In comparison to the intrinsic defect energies for YLF in the previous chapter, the BMF defect energies are greater. Solution energies for the doping of rare earth ions into the lattice have also been calculated. As there is no cation site with the same formal charge as the dopant ions, various reaction schemes were considered. There was a correlation between the dopant ionic radius and the cation radius the dopant replaced in the lattice, such that the larger rare earth ions (La^{3+}, Ce^{3+}, Pr^{3+} and Nd^{3+}) dope at the larger of the two lattice cation sites (i.e. the Ba^{2+} site) while the rest dope at the Mg^{2+} site. The rare earth doping solution energies are small with none greater than around 1.1 eV. This puts them in the same order of magnitude as the solution energies for YLF.

The doping limit of rare earth ions was also calculated. Using the original Jackson-Valerio method the doping limit was calculated to be around 0.4%. Issues with this method have been documented throughout this thesis and therefore the doping limit was also calculated using the modified Jackson-Valerio method. This produced limits which were negative implying that using the criteria assumed in the method, namely non-interacting defects with minimal unit cell distortion, the lattice does not readily accept rare earth dopant ions.

The impact of this work in the field of lasers is similar to that for YLF bulk results. Calculating which rare earth ions will substitute at which cation site within the lattice is an important result when considering the structure of these doped materials. As for YLF, the ability to calculate the doping limit for each of the rare earth ions in BMF provides a useful measure when designing a laser system. As BMF shows smaller solubility of rare earth dopant ions than YLF, it is likely that YLF is a more suitable laser host lattice especially for high power lasers.

5.3 Atomistic - surface modelling

The surface structure of any ionic material is an important property especially when doping is required for application purposes. The surface properties of BMF were studied using METADISE with the same potential set as used for bulk modelling work. The results are presented in this section.

5.3.1 Methodological detail

The bulk studies given in the previous Section showed that rare earth dopants are doped at both cation sites depending on the rare earth ion. The charge compensation method also varied between rare earth ions. Table 5.16 listed the reaction scheme(s) for each rare earth ion dopant and it is reproduced here for clarity. These were used as the basis for the surface work in this section. All potentials and cut-offs remained the same as those used before and are listed in Table 5.1. Mott-Littleton region sizes for surface defects using the CHAOS code were 9 Å and 35 Å for regions 1 and 2a respectively. The rare earth ion potentials are listed in Table 5.9.

5.3.2 Surface and attachement energies

Surface and attachment energies have been calculated for all of the valid cuts up to the 3rd index. Table 5.17 lists these for the most stable cut along with the surface area of each surface. The lowest surface energy corresponds to the (010) surface, which is therefore the most stable, followed by the (110) surface. The slowest growing surface is the index with the highest attachment energy and that is the (010) surface. Compared to the surface energies obtained for YLF, these are smaller surface energies. There are only nine unique surfaces that are non-polar up to the 3rd index. This is partly due to the symmetry of the unit cell and partly due to a number of surface being a Type 3 as defined by Tasker [14], with the (001) surface being an example.

The first repeat unit for each of the surfaces is given in Figure 5.10. All of the surfaces are very different, with the lowest index ones having large repeat units compared

RE	Scheme	Doping method
La	2	$RE^{\cdot}_{Ba} + V''_{Mg}$
Ce	2	$RE^{\cdot}_{Ba} + V''_{Mg}$
Pr	2	$RE^{\cdot}_{Ba} + V''_{Mg}$
Nd	2	$RE^{\cdot}_{Ba} + V''_{Mg}$
Sm	6	$RE^{\cdot}_{Mg} + V''_{Ba}$
Eu	6	$RE^{\cdot}_{Mg} + V''_{Ba}$
Gd	6	$RE^{\cdot}_{Mg} + V''_{Ba}$
Tb	5/6	$RE^{\cdot}_{Mg} + V''_{Ba}$ or $RE^{\cdot}_{Mg} + V''_{Mg}$
Dy	5	$RE^{\cdot}_{Mg} + V''_{Mg}$
Ho	6	$RE^{\cdot}_{Mg} + V''_{Ba}$
Er	6	$RE^{\cdot}_{Mg} + V''_{Ba}$
Tm	5	$RE^{\cdot}_{Mg} + V''_{Mg}$
Yb	6	$RE^{\cdot}_{Mg} + V''_{Ba}$
Lu	5	$RE^{\cdot}_{Mg} + V''_{Mg}$

Table 5.16: Table summarising the doping method that was calculated as the lowest energy scheme for each rare earth.

to the rest. The (100), (130), and (310) surfaces are the only ones to have cations in the termination layer, although they are not purely cation layers. The remaining surfaces all have fluoride terminations.

5.3.3 Morphology predictions

It was not possible to construct a morphology prediction using the surface energies listed, because no surface is defined in the z-direction. The morphology requires a plane

Index	Surface area $/\mathring{A}^2$	Surface energy $/Jm^{-2}$	Attachment energy /eV
(010)	24.681	0.243	−0.025
(100)	84.994	0.546	−0.182
(110)	88.505	0.448	−0.251
(120)	98.289	0.698	−0.467
(130)	122.723	0.553	−0.552
(210)	171.771	0.552	−0.637
(230)	185.415	0.646	−1.012
(310)	256.174	0.527	−0.527
(320)	259.717	0.527	−1.260

Table 5.17: Surface and attachment energies for BMF along with surface area of each index. Attachment energy is scaled per unit-cell. Indices up to index 3 were modelled and the energies quoted are for the most stable cut.

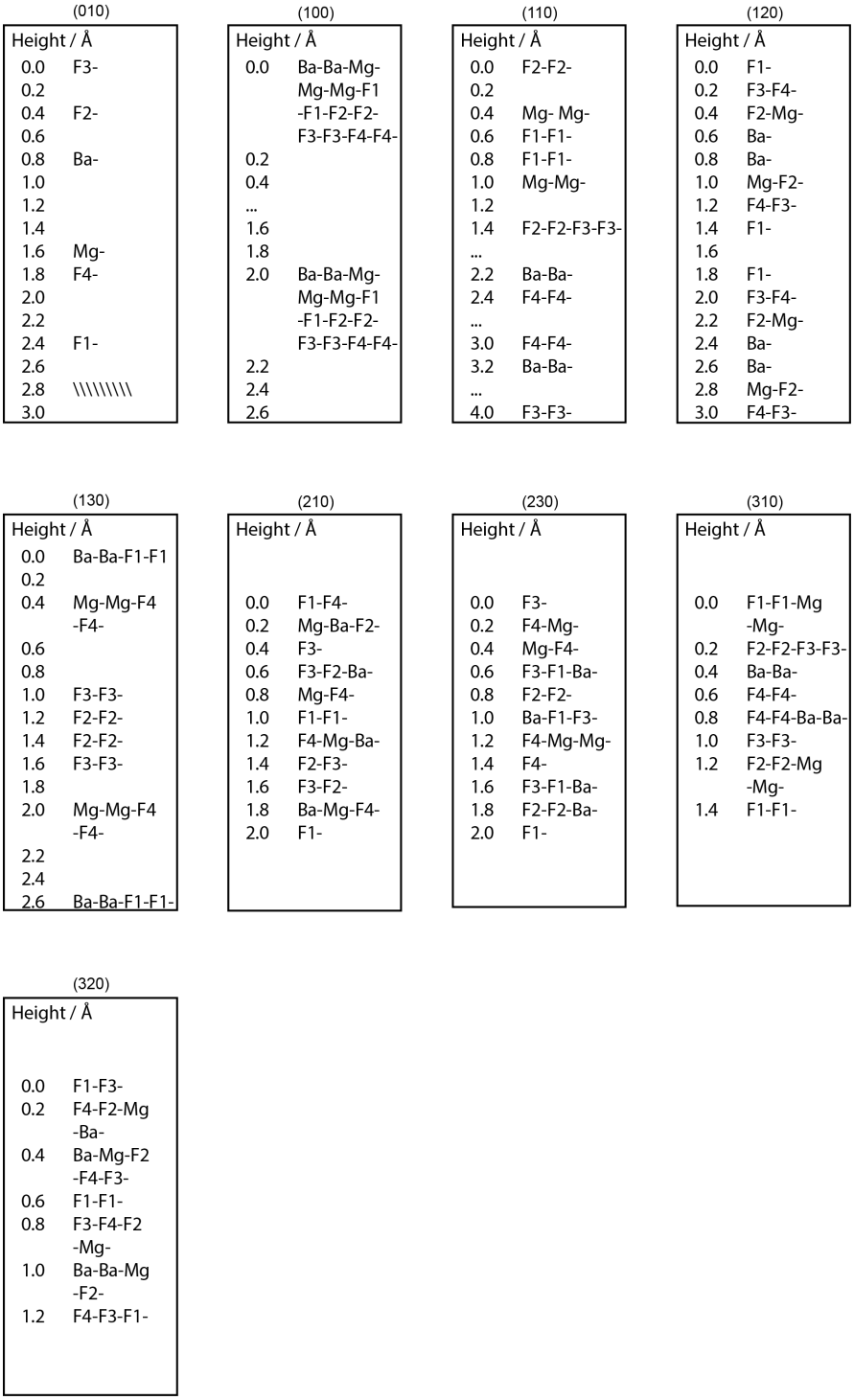

Figure 5.10: Terminations of the low index surfaces of BMF. Each box contains the repeat unit for that surface. The uppermost ions form the surface termination layer. Note that some height scales are abbreviated for space reasons. Some boxes contain a mirror plane, indicated by \\\, for the same reason. The ions above the mirror are reflected below it to form the complete repeat unit.

in this in order to bound the construction. The lowest index surface in the z-direction is the (001) surface. (Also because the unit cell is non-centrosymmetic the $(00\bar{1})$ surface). This surface is a polar surface and as such is not listed in the surface energy table above because the surface energy could not be calculated. It should be possible to directly calculate the surface energy of these polar surfaces by removing the dipole. This can sometimes be achieved through moving ions from the termination layer to the bottom of the simulation cell, thus creating vacancies at the surface. However, for the (001) surface in BMF this proved not to remove the dipole. Dipoles were attempted to be removed for the next two surfaces as well - (011) and (111) surfaces. No simple solution was found and so the morphology was constructed using values chosen rather than calculated.

In testing, it was found that the second order indices, (201), (211), and (221), never appeared in the morphology. The remaining surfaces, (001), (011), (111), (101), (021), and (121), were systematically tested to provide good prediction as to which would appear in the morphology. In the simplest case of the surfaces all having the same surface energy the morphology prediction, contained the (001) and the (011) surfaces, with the (001) surface being the larger of the two. The surface energy value chosen was as a value greater than the other calculated indices to reflect the stability of such a surface. Then by increasing the energy of each surface in turn, a list can be produced of the likelihood of each surface appearing in the morphology. It was found to be as follows: (001) >(011) >(101) >(021) >(111) >(121)

The same order was assumed for the attachment energy based morphology. The morphologies of BMF were constructed using a Wulff construction. Both the equilibrium (surface energy based) and the growth (attachment based) morphology were drawn. The two morphologies are shown in Figure 5.11. They show a similar plate-like shape terminated with the (001) surface. The energy value given for the polar surfaces only affected the length of the (010), (100) and (110) surfaces in the morphology prediction and not the shape.

The surface area coverages are given in Table 5.18. The unrelaxed values are based

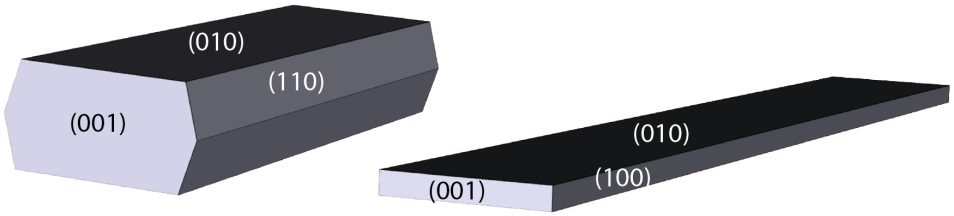

Figure 5.11: Equilibrium and growth morphologies of BMF.

Surface	Percentage coverage		
	Unrelaxed	Equilibrium	Growth
010	63.57%	51.58%	86.57%
100	29.31%	-	11.98%
110	-	33.43%	-
001	3.56%	7.49%	0.72%

Table 5.18: Percentage coverage of each surface appearing in predicted morphology.

on unrelaxed surface energies and are largely meaningless, however, they allow the extent of relaxation in the surfaces to be seen. For example, the (110) surface does not appear in the unrelaxed morphology but does feature prominently in the equilibrium morphology due to a reduction in surface energy through relaxation. The largest surface in both the equilibrium and the growth morphologies is the (010) surface. The only difference between the two predictions is that the (100) surface appears instead of the (110) surface in the growth morphology.

These morphology predictions are less than ideal due to the polar nature of many of the surfaces. In order to produce more accurate predictions further work is needed to remove the dipole in these surface so that surface energies can be calculated. Despite this, the surface energies for the non-polar surfaces have been calculated explicitly and a thorough test of the possible likelihood of the polar surfaces appearing in the morphology done. As such, some confidence can be taken with the morphology prediction.

5.3.4 Rare earth dopant segregation

BMF is of interest when doped with rare earth lanthanide ions. This may affect the energy of some surfaces, particularly where there is strong segregation. Any significant

change in surface energy will alter the morphology.

To study the doping of rare earth ions at the surface, a methodology was needed to calculate which of the defects, the dopant ion or the charge compensation, would segregate to the surface. The procedure used was to dope the rare earth ion at the cation site nearest to the surface. The cation being either Ba^{2+} or Mg^{2+} depending on which reaction scheme was calculated to be the lowest energy for that rare earth (as discussed in Table 5.12). The dopant was then moved systematically down through the system deeper into the simulation cell from cation site to cation site. The defect formation energy at a deep depth should be equal to that obtained through bulk studies. Due to the charged nature of these individual defects the two energies did not always agree. To overcome this a normalising correction factor was added to the METADISE values. This normalisation factor was obtained by comparing the defect formation energy at a deep depth in METADISE to the value obtained from GULP bulk studies. A similar method was used for the charge compensation defects. Only those surfaces that appear in the morphology were considered (i.e. (010), (100) and (110)).

The full tables of the results can be found in Appendix 1. The tables list the defect formation energy for each rare earth ion at the first four cation sites from the surface and the value for the bulk. The segregation energies are also listed along with the correction factor that was used. The same is listed for the charge compensation methods.

All defects showed a tendency to segregate to the surface of the three morphologically important surfaces. It was therefore assumed that the defect cluster (i.e. the rare earth ion plus the charge compensation) would segregate to the surface together. Defect clusters were placed at the lowest energy sites, based on the individual defect results, and a bound defect energy obtained. This was compared to bulk modelling studies in GULP and a cluster segregation calculated. Figure 5.12 shows the segregation of these defect clusters for each rare earth ion to the morphologically important surfaces. (The values are tabulated in Appendix 1.)

It can be seen from this plot that the (010) surface has the greatest degree of segregation for all rare earth ions, followed by the (110) surface and then the (100)

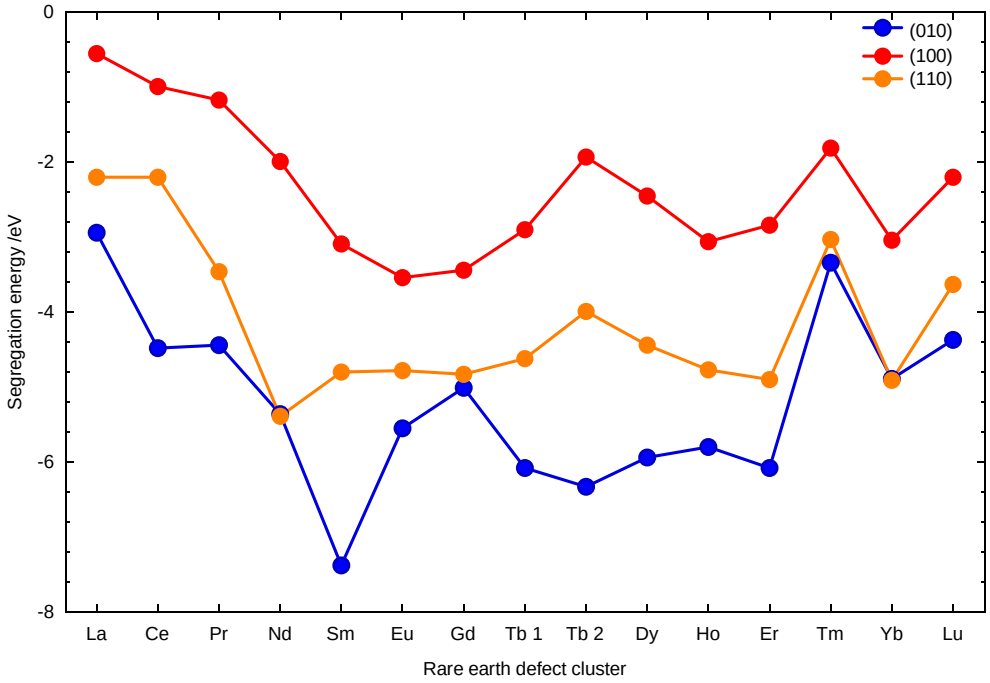

Figure 5.12: Plot showing the difference in defect energy at the surface depth and the bulk for the defect cluster of each rare earth ion and the appropriate charge compensation method.

surface. All three surfaces do, however, show considerable segregation of the single defect cluster. This maybe an important consideration with this system. The three surfaces have very different repeat units. The major difference is that for the (100) surface the termination layer contains cations. Therefore the rare earth dopant ions would be at the termination of the surface whereas in the other two surfaces they would reside slightly below the termination.

Considering just those rare earth ions that dope at the Ba^{2+} site (La^{3+} to Nd^{3+} and $Tb1^{3+}$) there is a decrease in segregation along the group with Tb^{3+} giving a segregation tendency around twice as large as La^{3+}. The ionic radius of Ce^{3+} is the closest in size to that of Ba^{2+}, with the difference increasing through the group of rare earth ions. This difference will create increasing strain in the lattice and as such would increase the segregation tendency. From Sm^{3+} onwards the rare earth ion is doped at the Mg^{2+} site. The opposite trend with ionic radii is true here. Lu^{3+} has the closest radius to Mg^{2+} and therefore it is expected that the segregation becomes less from Sm^{3+} to Lu^{3+}. This is the trend seen.

5.3.5 Summary

In summary, the surface energies and attachment energies of the non-polar, low index surfaces of BMF have been calculated. These were, along with a sensible value for the polar (001) surface, used to predict the equilibrium and growth morphologies. Both morphologies were flat, plate-like shapes dominated by the (010) and (110) surfaces.

Rare earth dopant ions were placed at various cation sites at these morphologically important surfaces, working from the termination layer down into the crystal. It was found that all rare earth dopants had a negative segregation energy implying there was a driving force for the ions to segregate to the surface. The same was found for the vacancy charge compensation defects. Using this, it was assumed that the dopant ion and charge compensation defect cluster would segregate towards the surface together, rather than one segregating and the other remaining in the bulk. The defect cluster energies were calculated and the overall segregation energy found. This revealed that

all rare earth dopants segregated to the surfaces, with the segregation force to the (010) surface the greatest. There was a correlation between the ionic radius mismatch between the lattice site and the rare earth ion, and the degree of segregation.

The results from this work into the surface properties of BMF provide important information needed for the design, development and improvement of this laser material. Ideally a doped laser crystal would be homogeneous as clustering of defects can cause problems through energy transfer processes that may degrade the laser action. The results shown here show that the segregation of dopant ions is significant in BMF. This segregation can be used as a measure of possible clustering of dopant ions.

5.4 Future work

This work into the bulk and surface properties of BMF has shown it to be an interesting material with many complex properties. The current published literature on BMF contains various difficulties research groups have had in developing a laser system, and reveals many complex properties. The work in this thesis lays the initial foundations for further computer modelling of BMF and the dopant behaviour within it. To extend the work, time would need to be taken to remove the dipoles from the polar surfaces so that the surface energies could be calculated. The work here has shown that the dipoles cannot be removed through any simple procedure, such as vacancy creation, and therefore, the surface reconstruction would be of considerable interest once found. Calculated surface energies would allow more accurate morphologies to be obtained.

Rare earth segregation should also be considered to all low index surfaces and not just the three considered in this work. Continuing this to model concentration effects is the logically next step as the work showed the dopant clusters would segregate to the surface. Knowing how many dopants would segregate before the energy becomes unfavourable would allow defective morphology predictions to be made. Due to the many combinations of dopant ions and charge compensation ions, plus the complex surface profiles in BMF, this would be a resource heavy task.

The work in this thesis assumed the rare earth dopants ion had their usual formal charge of +3. Some of the rare earth ions (Nd, Dy, Sm, Eu, Tm and Yb) do exist in a +2 state albeit with less stability than the +3 charge. This would make an important study as the lattice cations are both +2. To achieve this work, new potentials for the rare earth ions would have to be derived.

Finally, as it is the electronic properties of the rare earth dopant ions that provides this system with its useful properties, detailed electronic structure modelling should be carried out. This would not be a trivial task as the rare earth ions are large complex elements that would cause problems in this type of modelling, particularly if concentrations effects were to be looked at.

Chapter 6

Conclusions

In conclusion, two solid-state laser host lattices have been simulated using atomistic techniques. A set of potentials for the host lattices, $YLiF_4$ (YLF) and $BaMgF_4$ (BMF), are given along with potentials for the rare earth fluoride dopant ions. A new potential set is derived for various transition metal fluoride ions also.

Both systems are actively being researched as laser sources as well for use in other devices, such as scintillators and memory devices. YLF has been subject to a wide range of research since the 1970s, with a number of new papers on the properties of the material or the growth of YLF crystals every year. The work in this thesis has provided research into the bulk and surface properties, with particular focus on rare earth ion dopants.

Using well established methodologies, the perfect YLF lattice was reproduced to within 2% of the reported structure. Intrinsic thermal defects were modelled and the defect formation energies calculated. These shows that the Frenkel defect energies are lower than the Schottky energies, with the two lowest energy defect formations being a F Frenkel and a Li Frenkel.

The interionic potentials used for YLF are tested at various temperatures and are found to be inadequate above 600 K however this may be due to the approximation of harmonic vibration assumed in the model breaking down. Therefore, for any future non-static simulations the potentials would have to be refitted or the model parameters adjusted. The thermal expansion profiles up to 600 K reveal that the 'a' lattice

parameter increases linearly in size with temperature up to 300 K but then decreases. The 'c' lattice parameter increases linearly only after 250 K. Despite this, overall the volume increases linearly. This unusual decrease in the 'a' parameter should be the subject of a future study. The thermal expansion coefficients are calculated.

Solution energies for the doping of rare earth ions into the lattice are also calculated and this reveals that doping at the Y site is the most favourable process as the Li site has a five-fold increase in energy compared to the Y site.

Various methods are considered to calculate the doping limit for the dopant ions within the YLF lattice. A modified Jackson-Valerio method was determined to provide a good measure of the doping limit and can be used to compare the doping solubility of various dopant ions within the lattice, or a dopant ion's solubility in various host lattices. The limit calculated is strictly for non-interacting defect ions and as such produced small doping limits, however, as a tool for comparing trends across dopants or host lattices it is extremely useful. The maximum doping is calculated for Yb^{3+} at 1.51%. The lowest is for La^{3+} at 0.69%. These values suggest that the YLF lattice will readily accept rare earth dopants at low concentrations without interacting. This suggests a homogeneous doping of up to 1.5% rare earth ion should be possible. This agrees with the values in the literature.

The likelihood of transition metal ion defects being incorporated into a Yb:YLF lattice was studied as a result of the work into YLF as a laser cooling device. The results suggest that the 1+ and 3+ transition metal ions are most likely to incorporate into the lattice with Cu^{1+} and Ti^{3+} being the most likely. In order to ensure an optimal crystal for the laser cooling application 1+ and 3+ transition metal ions should not be allowed to contaminate the growing environment. The 2+ ions have higher solution energies.

The detailed bulk studies were followed by simulations of the surface of YLF. An atomistic approach was taken for this, using the same potentials as the bulk study. The advantage of an atomistic approach with surface studies was that the simulation cells can be scaled easily to consider concentration effects. This is not possible with

electronic structure simulation techniques and the facilities available.

Surface and attachment energies are calculated and were used to predict the equilibrium and growth morphologies. The equilibrium morphology is dominated by the (112) and (011) surfaces. The rest of the morphology consisted of the (001), (010), (111) and (211) surfaces. The growth morphology is dominated by the (001) and (120) surfaces as these are the slowest growing faces. The rest of the growth morphology consists of the (010) and the (011) surfaces.

Rare earth dopant segregation to the surfaces that appear in the morphologies were calculated. This revealed that there is segregation to all surfaces studied - (001), (011), (112) - but it is to a much greater degree for the (112) surface. At the (112) surface, the defect energies do not reach their bulk values until a depth of 9 Å; far greater than with the other two surfaces. Common across all three surfaces is that the first rare earth ions in the group had stronger segregation tendencies than the latter ones, with La^{3+} producing the largest segregation energy.

To analyse the segregation of defects further, a methodology was established to consider clusters of multiple defects at the surfaces of all low index faces and the effect they had on the surface energy. Those rare earth ions with similar ionic radius to Y^{3+} tend to affect the surface energy least. Ho^{3+}, which has the closest ionic radius to that of the Y^{3+} ions, is an exception to this, as it has one of the greatest impacts on the surface energy. Considering the case of La^{3+}, as this ion produced the greatest reduction in surface energy, the surface that changes the most in energy is the (110) surface, with a reduction of 14.5% in surface energy. The next surfaces in decreasing size of the reduction in energy are: (112), (012), (221), (021), (122) and (010). The remaining surfaces all show increases in surface energy with the presence of La^{3+} ions (and therefore all rare earth ions).

The defective surface energies were used to predict the defective morphology i.e. a prediction of what the morphology may be when the YLF lattice is doped. In the case of large crystals, such that there is a high ratio of bulk to surface sites, and high doping levels, all surfaces would reach the optimum surface energy with the remaining

dopant ions residing in the bulk. For systems with La^{3+} to Nd^{3+} ions present, the (111) surface is replaced by the (110) surface in the morphology. For Sm^{3+} neither the (111) or the (110) surface appear. As expected for the latter rare earth ions the predicted morphology is similar to the perfect YLF morphology. Despite the surfaces that appear in the morphology changing, and the relative ratios of surface areas changing, the overall shape does not change.

This work into YLF has raised a number of interesting results that should be examined further. Firstly, the unusual decrease in the 'a' parameter with increasing temperature should be investigated further. To extend the work in the prediction of the impact dopant ions have on the morphology the other scenarios of crystal size and doping level could be examined explicitly. The work carried out so far assumed the dopant ions were at the uppermost cation layer to the surface termination. The depth profiles of the morphologically important surfaces revealed that often the defect energies do not reach bulk values until a deep depth. The work carried out in this thesis could therefore be repeated but at the second cation layer down. The simulation cells could be scaled further to examine the effect of concentration and surface coverage further. Finally, as it is the electronic properties of the rare earth dopant ions that provides this system with its useful properties, detailed electronic structure modelling should be carried out. This would not be a trivial task as yttrium and the rare earth ions are large complex elements that would cause problems in this type of modelling, particularly if concentrations effects were to be looked at.

A similar approach was taken for the second material studied, $BaMgF_4$ (BMF). This material has been subject to less research and has not been successfully used in a viable, commercial laser device to date. There has nonetheless been a number of studies into the properties of BMF including crystal growth, pyroelectric and piezoelectric properties, and the properties of rare earth dopants within the lattice. The work in this thesis has aimed to produce an insight into this material through both bulk and surface simulations to provide experimentalists information for future development of the system.

Using an atomistic approach, the intrinsic thermal defects for BMF were modelled and the defect formation energies calculated. These showed that the Schottky defect energies are of similar magnitude to the Frenkel defects. Within the Frenkel defects the fluorine and magnesium Frenkel are 2.5 times smaller than the barium Frenkel defect. In comparison to the intrinsic defect energies for YLF, the BMF defect energies are greater. Solution energies for the doping of rare earth ions into the lattice were also calculated. As there is no cation site with the same formal charge as the dopant ions, various reaction schemes were considered. There is a correlation between the dopant ionic radius and the cation radius the dopant replaced in the lattice, such that the larger rare earth ions (La^{3+}, Ce^{3+}, Pr^{3+} and Nd^{3+}) dope at the larger of the two lattice cation sites (i.e. the Ba^{2+} site) while the rest dope at the Mg^{2+} site. The rare earth doping solution energies are small with none greater than around 1.1 eV. This puts them in the same order of magnitude as the solution energies for YLF.

The doping limit of rare earth ions was also calculated. Using the original Jackson-Valerio method the doping limit is calculated to be around 0.4%. Using the modified Jackson-Valerio method, some limits are negative implying that using the criteria assumed in the method, namely non-interacting defects with minimal unit cell distortion, the lattice does not readily accept rare earth dopant ions. This result does not mean that no rare earth dopants will dope into the BMF lattice, but it does reveal that the BMF lattice accepts rare earth dopant ions less easily than the YLF lattice. The literature provides many examples of studies where the authors have had unusual spectrographic results [199], with some authors suggesting two different dopant environments exist [206]. Taken as a whole, the results lead to the conclusion of a complex dopant picture with BMF that should be studied further.

BMF was also subject to surface studies. The surface energies and attachment energies of the non-polar, low index surfaces were calculated. These were, along with a sensible value for the polar (001) surface, used to predict the equilibrium and growth morphologies. Both morphologies are flat, plate-like shapes dominated by the (010) and (110) surfaces.

Rare earth dopant ions were placed at various cation sites at these morphologically important surfaces, working from the termination layer down into the crystal. It is found that all rare earth dopants have a negative segregation energy implying there is a driving force for the ions to segregate to the surface. The same was found for the vacancy charge compensation defects. It was, therefore, assumed that the dopant ion and charge compensation defect cluster would segregate towards the surface together. The defect cluster energies were calculated and the overall segregation energy found. This revealed that all rare earth dopants segregated to the surfaces, with the segregation force to the (010) surface being the greatest. There is a link between the ionic radius mismatch between the lattice site and the rare earth ion, and the degree of segregation.

The work in this thesis lays the initial foundations for further computer modelling of BMF and the dopant behaviour within it. To extend the work, the dipoles from the polar surfaces would need to be removed, so that the surface energies could be calculated. The work here has shown that the dipoles cannot be removed through any simple procedure, such as vacancy creation, and therefore, the surface reconstruction would be of considerable interest once found. Calculated surface energies would allow more accurate morphologies to be obtained.

Rare earth segregation should also be considered to all low index surfaces and not just the three considered in this work. Modelling concentration effects should be done also, as knowing how many dopants would segregate before the energy becomes unfavourable would allow defective morphology predictions to be made. Due to the many combinations of dopant ions and charge compensation ions, plus the complex surface profiles in BMF, this would be a resource heavy task.

The work in this thesis assumed the rare earth dopants ion had their usual formal charge of +3. Some of the rare earth ions do exist in a +2 state. This would make an important study as the lattice cations are both +2. To achieve this work, new potentials for the rare earth ions would have to be derived.

Comparing BMF and YLF, this thesis has concluded that YLF is more suited to the incorporation of rare earth ions both in terms of (non-interacting) doping limit and

the impact the dopants have on the surface morphology, although the intrinsic defect formation energies were found to be smaller in YLF. BMF has been shown to be a complex material, that requires further study.

The impact of this work is two-fold. Firstly, while many of the techniques used are tried and tested methods, some of the analysis carried out is novel and important not just for the work described here but also for use in further studies into other systems. For example, the ability to quickly calculate doping limits so that comparisons can be made across possible dopant ions in a useful tool in material design for applications. Equally being able to compare alternative host lattices with the same dopant ion offers valuable knowledge from a material design point of view. The work on doping limits in this body of research is therefore an important contribution to the field and the methodology will be used in many future studies. Another important methodological contribution from this work is the technique to calculate defective surface energies and ultimately the impact defects have on the morphology of the crystal. This has vast implications for research as crystal morphology is of huge importance in many applications, in particular ones where the surface chemistry is key (for example catalysts). Even in those applications where the morphology is of less importance, the ability to calculate the likelihood of defect segregation to surface sites is useful. Finally, the derivation of transition metal fluoride potentials is a good contribution as they can be utilised in any future modelling of such materials.

The second impact of the research is from the results from the studies into the laser host materials themselves. Both YLF and BMF are of interest as laser host materials. The results from this body of work provide important information needed in the design, development, and improvement of these laser materials. For example, ideally a doped laser crystal would be homogeneous as clustering of defects makes cutting and polishing any crystals more difficult, and dopant ions that lie close to each other can cause problems through energy transfer processes that may degrade the laser action. This work has calculated the segregation of dopant ions, which can be used to provide an insight into possible clustering. In general, it is shown that the latter rare earth ions are

more suited for this applications as they tend to cluster less. The contrast between the two systems studied is also an important result that suggests efforts should be focussed on YLF as a laser system over BMF.

The work carried out in the thesis has fulfilled the aims of the study. Insight into two solid-state laser lattices has been given with bulk and surface properties examined. The content is an important contribution to the research of these two materials, which should aid further research, both computational and experimental, into them. The work has raised a number of important questions that should be the aim of further work.

Finally it is worth repeating that, computational modelling is a vital tool in chemistry and material science, that can provide insight into a materials, help explain observed phenomena, and even make predictions.

References

[1] N. N. Greenwood. *Ionic crystals, lattice defects and nonstoichimetry*. Butterworth and Co., London, second edition, 1968.

[2] I. M. Boswarva and A. B. Lidiard. The energy of formation of Schottky defects in ionic crystals. *Philosophical Magazine*, 16(142):805–826 1967.

[3] X. Xia, R. J. Oldman, and C. R. A. Catlow. Oxygen adsorption and dissociation on yttria stabilized zirconia surfaces. *Journal of Materials Chemistry*, 22(17):8594–8612, 2012.

[4] A. Walsh, C. R. A. Catlow, K. H. L. Zhang, and R. G. Egdell. Control of the band-gap states of metal oxides by the application of epitaxial strain: The case of indium oxide. *Physical Review B*, 83(16):161202 2011.

[5] R. A. Jackson, J. B. Amaral, M. E. G. Valerio, D. P. DeMille, and E. R. Hudson. Computer modelling of thorium doping in LiCaAlF 6 and LiSrAlF 6 : application to the development of solid state optical frequency devices. *Journal of Physics: Condensed Matter*, 21(32):325403 2009.

[6] S. R. Walker, R. A. Jackson, and M. S. D. Read. Atomistic modelling of actinide oxides for nuclear fuel applications. *physica status solidi (c)*, 10(2):197–201 2013.

[7] I. M. Bos Warva. The energy of formation of Schottky defects in caesium halides. *Philosophical Magazine*, 16(142):827–844 1967.

[8] C. Stanek. *Atomic Scale Disorder in Fluorite and Fluorite Related Oxides*. Thesis, Imperial College, 2003.

[9] C. R. A. Catlow, B. Fender, and D. G. Muxworthy. Defect Interactions and Order-Disorder in Transition Metal Oxides. *Le Journal de Physique Colloques*, 38(C7):C7–67–C7–71 1977.

[10] C. R. A. Catlow and D. G. Muxworthy. The electronic structure of divalent transition metal oxides. *Philosophical Magazine Part B*, 37(1):63–71 1978.

[11] R. A. Jackson, A. D. Murray, and C. R. A. Catlow. Calculation of the Basic Defect Energies of UO2. *Physica B*, 131:136–138, 1985.

[12] C. R. A. Catlow. Point Defect and Electronic Properties of Uranium Dioxide. *Proceedings of the Royal Society A: Mathematical, Physical and Engineering Sciences*, 353(1675):533–561 1977.

[13] R. A. Jackson and C. R. A. Catlow. Trapping and solution of fission Xe in UO2. *Journal of Nuclear Materials*, 127(2-3):161–166 1985.

[14] P. W. Tasker. R.9130. Technical report, AERE Harwell, 1978.

[15] D. M. Duffy and P. W. Tasker. R.11059. Technical report, AERE Harwell, 1983.

[16] J. Gale and A. Rohl. The General Utility Lattice Program (GULP). *Molecular Simulation*, 29(5):291–341 2003.

[17] G. W. Watson, P. M. Oliver, and S. C. Parker. Computer simulation of the structure and stability of forsterite surfaces. *Physics and Chemistry of Minerals*, 25(1):70–78 1997.

[18] P. Sherwood. Chemshell; www.chemshell.org.

[19] P. Sherwood, A. H. de Vries, M. F. Guest, G. Schreckenbach, C. R. A. Catlow, S. A. French, A. A. Sokol, S. T. Bromley, W. Thiel, A. J. Turner, S. Billeter, F. Terstegen, S. Thiel, J. Kendrick, S. C. Rogers, J. Casci, M. Watson, F. King, E. Karlsen, M. Sjø voll, A. Fahmi, A. Schäfer, and C. Lennartz. QUASI: A general purpose implementation of the QM/MM approach and its application to problems in catalysis. *Journal of Molecular Structure: THEOCHEM*, 632(1-3):1–28 2003.

[20] T. W. Keal, P. Sherwood, G. Dutta, A. A. Sokol, and C. R. A. Catlow. Characterization of hydrogen dissociation over aluminium-doped zinc oxide using an efficient massively parallel framework for QM/MM calculations. *Proceedings of the Royal Society A: Mathematical, Physical and Engineering Sciences*, 467(2131):1900–1924 2011.

[21] J. To, A. A. Sokol, S. A. French, and C. R. A. Catlow. Hybrid QM/MM Investigations into the Structure and Properties of Oxygen-Donating Species in TS-1. *Journal of Physical Chemistry C*, 112(18):7173–7185 2008.

[22] C. Hammond. *The Basics of Crystallography and Diffraction*. Oxford University Press, Oxford, 1997.

[23] I. J. Ford. http://www.cmmp.ucl.ac.uk/˜ijf/3c25/bravais.gif Accessed October 2012.

[24] A. Kelly and G. W. Groves. *Crystallography and Crystal Defects*. Longman Group Limited, London, first edition, 1970.

[25] W. Schottky and C. Wagner. Theorie der geordneten Mischphasen. *Zeitschrift für Physikalische Chemie*, 11B:163–210, 1930.

[26] W. Schottky. Über den Mechanismus der Ionenbewegung in festen Elektrolyten. *Zeitschrift für Physikalische Chemie*, 29B:335–355, 1935.

[27] J. Frenkel. Über die Wärmebewegung in festen und flüssigen Körpern. *Zeitschrift fr Physik*, 35(8-9):652–669 1926.

[28] F. A. Kroger and H. J. Vink. *Solid State Physics - Advances in Research and Applications*. Academic Press, New York, 1957.

[29] B. A. Lengyel. *Introduction to Laser Physics*. John Wiley and Sons Inc, New York, 1966.

[30] T. H. Maiman. Stimulated Optical Radiation in Ruby. *Nature*, 187(4736):493–494 1960.

[31] A. Javan, W. Bennett, and D. Herriott. Population Inversion and Continuous Optical Maser Oscillation in a Gas Discharge Containing a He-Ne Mixture. *Physical Review Letters*, 6(3):106–110 1961.

[32] R. Paschotta. *Encyclopedia of Laser Physics and Technology*. Wiley-VCH, 2008.

[33] J. E. Geusic, H. M. Marcos, and L. G. Van Uitert. Laser oscillation in Nd-doped yttrium aluminium, yttrium gallium and gadolinium garnets. *Applied Physics Letters*, 4(10):182, 1964.

[34] J. Wilson and J. F. B. Hawkes. *Lasers Principles and Applications*. Prentice Hall International, Helmel Hempstead, UK, 1987.

[35] O. Svelto. *Principles of Lasers*. Plenum Press, New York, third edition, 1989.

[36] W. T. Silfvast. *Laser Fundamentals*. Cambridge University Press, Cambridge, UK, 1996.

[37] D. B. Coyle, R. B. Kay, P. R. Stysley, and D. Poulios. Laser for space-based vegetation topographical altimetry. *Applied Optics*, 43(27), 2004.

[38] Q. Peng, A. Juzeniene, J. Chen, L. O. Svaasand, T. Warloe, K.-E. Giercksky, and J. Moan. Lasers in medicine. *Reports on Progress in Physics*, 71(5):056701 2008.

[39] X. Zhang, P. Hong, M. Bass, and B. Chai. Blue upconversion with excitation into Tm ions at 780 nm in Yb- and Tm-codoped fluoride crystals. *Physical Review B*, 51(14):9298–9301 1995.

[40] A. Bensalah, K. Shimamura, V. Sudesh, H. Sato, K. Ito, and T. Fukuda. Growth of Tm, Ho-codoped YLiF4 and LuLiF4 single crystals for eye-safe lasers. *Journal of Crystal Growth*, 223(4):539–544 2001.

[41] NASA; http://engineer.jpl.nasa.gov/practices/2404.pdf Accessed October 2012. Guideline for use of the Fizeau interferometer in optial testing.

[42] S. M. Nejad and S. Olyaee. Low-Noise High-Accuracy TOF Laser Range Finder Shahram Mohammad Nejad and Saeed Olyaee Optoelectronic and Laser Laboratory, Iran University of Science and Technology, Narmak, 16846, Tehran, Iran. *American Journal of Applied Science*, 5(7):755–762, 2008.

[43] Saab. Laser Rangefinder; http://www.saabgroup.com/Global/Documents%20and%20 Accessed October 2012.

[44] C. Weitkamp. *Lidar: Range-Resolved Optical Remote Sensing of the Atmosphere*. Springer, 2005.

[45] P. L. Bender. Laser measurements of the lunar distance. *Reviews of Geophysics*, 13(3):271, 1975.

[46] W. M. Macek and D. T. M. Davis. Rotation rate sensing with travelling-wave ring lasers. *Applied Physics Letters*, 2(3):67, 1963.

[47] S. Upson. Laser Uranium Enrichment Makes a Comeback. *IEEE Spectrum* 2010.

[48] Cameco Joins GE Hitachi Enrichment Venture; http://www.cameco.com/media/news_releases/2008/?id Accessed June 2012, 2008.

[49] BBC. UK joins laser nuclar fusion project; http://www.bbc.co.uk/news/science-environment-1484 Accessed October 2012, 2011.

[50] BBC. Laser gun zaps missile; http://news.bbc.co.uk/1/hi/sci/tech/782696.stm Accessed October 2012, 2000.

[51] BBC. Lightning laser weapon developed by US Army; http://www.bbc.co.uk/news/technology-18630622 Accessed October 2012, 2012.

[52] P. Pringsheim. Zwei bemerkungen uber den unterschied von lumineszenz und temperaturstrahlung. *Zeitschrift fur Physik*, 57(11-12):739–746, 1929.

[53] G. Nemova and R. Kashyap. Laser cooling of solids. *Reports on Progress in Physics*, 73(8):086501 2010.

[54] S. I. Vavilov. Some remarks on the Stokes of fluorescent liquids. *Journal of Physics-USSR*, 9:68–73, 1945.

[55] S. I. Vavilov. Photoluminescence and thermodynamics. *Journal of Physics-USSR*, 10:499–501, 1946.

[56] X. L. Ruan and M. Kaviany. Advances in Laser Cooling of Solids. *Journal of Heat Transfer*, 129(1):3, 2007.

[57] L. D. Landau. On the thermodynamics of photoluminescence. *Journal of Physics-USSR*, 10:503–6, 1946.

[58] R. I. Epstein, M. I. Buchwald, B. C. Edwards, T. R. Gosnell, and C. E. Mungan. Observation of laser-induced fluorescent cooling of a solid. *Nature*, 377(6549):500–503, 1995.

[59] B. C. Edwards, J. E. Anderson, R. I. Epstein, G. L. Mills, and A. J. Mord. Demonstration of a solid-state optical cooler: An approach to cryogenic refrigeration. *Journal of Applied Physics*, 86(11):6489, 1999.

[60] S. R. Bowman. Lasers without internal heat generation. *IEEE Journal of Quantum Electronics*, 35(1):115–122, 1999.

[61] E. M. Maddock. *Computer modelling of solid state inorganic materials for optical applications*. Thesis, Keele University, 2010.

[62] W. T. Carnall, G. L. Goodman, K. Rajnak, and R. S. Rana. A systematic analysis of the spectra of the lanthanides doped into single crystal LaF3. *The Journal of Chemical Physics*, 90(7):3443–3457 1989.

[63] R. A. Jackson, M. E. G. Valerio, J. B. Amaral, M. A. Couto dos Santos, and E. M. Maddock. Computer modelling of the optical properties of rare-earth dopant metal fluorides. *Physics of the Solid State: C*, 4(3):1185–1188, 2007.

[64] M. Stephan, M. Zachau, M. Gröting, O. Karplak, V. Eyert, K.C. Mishra, and P.C. Schmidt. A theoretical investigation of 4f5d transition of trivalent rare earth ions in fluorides and complex oxides. *Journal of Luminescence*, 114(3-4):255–266 2005.

[65] M. E. G. Valerio, R. A. Jackson, and J. F. d. Lima. Computer modelling of BaLiF 3 : II . Defects produced by divalent dopants. *Journal of Physics: Condensed Matter*, 10:3353–3358, 1998.

[66] M. E. G. Valerio, J. F. De Lima, and R. A. Jackson. Computer modelling of BaLiF 3 : III. Substitution of La 3+ , Nd 3+ and Y 3+ rare earth ions. *Radiation Effects and Defects in Solids*, 151(1-4):249–254 1999.

[67] M. A. Couto dos Santos, M. E. G. Valerio, R. A. Jackson, and J. F. de Lima. Predicting the spectroscopic behaviour of Eu3+ in BaLiF3 via defect modelling and crystal field parameter calculations. *Chemical Physics Letters*, 369(1-2):90–94 2003.

[68] Y. Tan and C. Shi. Ce3+Eu2+ energy transfer in BaLiF3 phosphor. *Journal of Physics and Chemistry of Solids*, 60(11):1805–1810 1999.

[69] M. E.G. Valerio, V. G. Ribeiro, A. C.S. de Mello, M. A.C. dos Santos, S. L. Baldochi, V. L. Mazzocchi, C. B.R. Parente, R. A. Jackson, and J. B. Amaral. Structural and optical properties of Nd- and Tb-doped BaY2F8. *Optical Materials*, 30(1):184–187 2007.

[70] N. Y. Kirikova, V. E. Klimenko, V. A. Kozlov, V. N. Makhov, N. M. Khaidukov, and T. V. Uvarova. . *Nuclear Instruments and Methods in Physics Research Section A: Accelerators, Spectrometers, Detectors and Associated Equipment*, 259:351–353, 1995.

[71] J. B. Amaral, M. A. Couto dos Santos, M. E. G. Valerio, and R. A. Jackson. Computer modelling of BaY2F8: defect structure, rare earth doping and optical behaviour. *Applied Physics B*, 81(6):841–846 2005.

[72] J. B. Amaral, A. C. Lewis, M. E. G. Valerio, and R. A. Jackson. Computer modelling of divalent, trivalent and tetravalent ion doping in LiCaAlF 6 and LiSrAlF 6. *Journal of Physics: Condensed Matter*, 16(47):8733–8741 2004.

[73] J. B. Amaral, D F Plant, M. E. G. Valerio, and R. A. Jackson. Computer modelling of defect structure and rare earth doping in LiCaAlF6 and LiSrAlF6. *Journal of Physics: Condensed Matter*, 15(17):2523–2533 2003.

[74] S. A. Payne, C. D. Marshall, A. J. Bayramian, and J. K. Lawson. . In Wieslaw Strek, Edward Lukowiak, and Barbara Nissen-Sobocinska, editors, *SPIE Proceedings*, volume 3176, pages 68–73 1997.

[75] N. F. Mott and M. J. Littleton. Conduction in polar crystals. I. Electrolytic conduction in solid salts. *Transactions of the Faraday Society*, 34:485, 1938.

[76] J. D. Gale. GULP: A computer program for the symmetry-adapted simulation of solids. *Journal of the Chemical Society, Faraday Transactions*, 93(4):629–637, 1997.

[77] E. Madelung. Molekulare Eigenschwingungen. *Zeitschrift für Physikalische Chemie*, 11(898), 1910.

[78] M. Born. *Atomtheorie des Festen Zustandes*. Teubner, Leipzig, 1923.

[79] M. Born. *Handbuch der Physik*. Springer, Berlin, 1933.

[80] B. Dick and A. Overhauser. Theory of the Dielectric Constants of Alkali Halide Crystals. *Physical Review*, 112(1):90–103 1958.

[81] J. H. Harding. Computer simulation of defects in ionic solids. *Reports on Progress in Physics*, 53(11):1403–1466 1990.

[82] P. P. Ewald. Die Berechnung optischer und elektrostatischer Gitterpotentiale. *Annalen der Physik*, 369(3):253–287, 1921.

[83] C. Kittel. *Introduction to Solid State Physics*. John Wiley and Sons Inc, New York, 1976.

[84] M. Levy. *Crystal Structure and Defect Properties in Ceramic Materials*. Thesis, Imperial College, 2005.

[85] J. Ball. *Computer Simulation of Disorder in Ceramic Materials*. PhD thesis, Imperial College, 2006.

[86] R. Catlow and M. J. Norgett. AERE-M2936. Technical report, Harwell Labortory, 1976.

[87] W. Heisenberg. Uber den anschaulichen Inhalt der quantentheoretischen Kinematik und Mechanik. *Zeitschrift fur Physik*, 43(3-4):172–198 1927.

[88] A. C. Phillips. *Introduction to Quantum Mechanics*. John Wiley and Sons Inc, 2003.

[89] M. Born and A. Lande. The calculation of the compressibility of cubic crystals from the space lattice theory. *Verhandlungen der Deutschen Physik Gesellschaft*, 21(210):210–2016, 1918.

[90] A. Cleave. *Atomic Scale Simulations for Waste Form Applications*. Thesis, Imperial College, 2006.

[91] Max Born and Joseph E. Mayer. Zur Gittertheorie der Ionenkristalle. *Zeitschrift fur Physik*, 75(1-2):1–18 1932.

[92] J. E. Jones. On the Determination of Molecular Fields. II. From the Equation of State of a Gas. *Proceedings of the Royal Society A: Mathematical, Physical and Engineering Sciences*, 106(738):463–477 1924.

[93] R. Eisenschitz and F. London. Über das Verhältnis der van der Waalsschen Kräfte zu den homöopolaren Bindungskräften. *Zeitschrift fur Physik*, 60(7-8):491–527 1930.

[94] F. London. Zur Theorie und Systematik der Molekularkrufte. *Zeitschrift fur Physik*, 63(3-4):245–279 1930.

[95] N. L. Allan, R. G. Bell, I. D. Brown, C. R. A. Catlow, C. M. Freeman, A. M. Gorman, J. H. Harding, N. M. Harrison, R. A. Jackson, P. W. M. Jacobs, W. C. Mackrodt, R. L. McGreevy, J. M. Newsam, S. C. Parker, G. D. Price, S. L. Price, Z. A. Rycerz, P. Tschaufeser, B. Vessal, A. Wall, and G. W. Watson. *Computer modelling in inorganic crystallography*. Academic Press, 1997.

[96] R. A. Jackson, M. E. G. Valerio, and J. F. d. Lima. Computer modelling of BaLiF 3 : I . Interionic potentials and intrinsic defects. *Journal of Physics: Condensed Matter*, 8:10931–10937, 1996.

[97] J. B. Amaral, D. F. Plant, M. E. G. Valerio, and R. A. Jackson. Computer modelling of defect structure and rare earth doping in LiCaAlF 6 and LiSrAlF 6. *Journal of Physics: Condensed Matter*, 15(17):2523–2533 2003.

[98] R. A. Jackson, E. M. Maddock, and M. E. G. Valerio. Computer modelling of rare earth dopants in KYF materials: bulk and surface studies. *IOP Conference Series: Materials Science and Engineering*, 15:012014 2010.

[99] R. A. Buckingham. The Classical Equation of State of Gaseous Helium, Neon and Argon. *Proceedings of the Royal Society A: Mathematical, Physical and Engineering Sciences*, 168(933):264–283 1938.

[100] R. A. Jackson, A. D. Murray, J. H. Harding, and C. R. A. Catlow. The Calculation of Basic Defect Parameters in UO2. *Philosophical Magazine A*, 53(1):27–50, 1986.

[101] C. B. Basak, A. K. Sengupta, and H. S. Kamath. Classical molecular dynamics simulation of UO2 to predict thermophysical properties. *Journal of Alloys and Compounds*, 360(1-2):210–216 2003.

[102] R. W. Grimes, D. J. Binks, and A. B. Lidiard. The extent of zinc oxide solution in zinc chromate spinel. *Philosophical Magazine A*, 72(3):651–668 1995.

[103] D. J. Binks. *Computational Modelling of Zinc Oxide and Related Oxide Ceramics*. PhD thesis, University of Surrey, 1994.

[104] M. S. D. Read and R. A. Jackson. Derivation of enhanced potentials for uranium dioxide and the calculation of lattice and intrinsic defect properties. *Journal of Nuclear Materials*, 406(3):293–303 2010.

[105] I. D. Faux and A. B. Lidiard. The volumes of formation of Schottky defects in ionic crystals. *Zeitschrift fur Naturforschung*, 26:62–68, 1971.

[106] M. Born and K. Huang. *Dynamical Theory of Crystal Lattices*. Oxford University Press, 1954.

[107] U. Schröder. A new model for lattice dynamics (breathing shell model). *Solid State Communications*, 4(7):347–349 1966.

[108] M. J. L. Sangster. Interionic potentials and force constant models for rocksalt structure crystals II. *Journal of Physics and Chemistry of Solids*, 35(2):195–200 1974.

[109] C. R. A. Catlow and W. C. Mackrodt. *Computer Simulation of Solids*. Springer-Verlag, Berlin, 1982.

[110] D. F. Plant. *Computer modelling of the structures and defect properties of some inroganic materials*. Mphil, Keele University, 2001.

[111] W. H. Press, S. A. Teukolsky, W. T. Veterling, and B. P. Flannery. *Numerical Recipes in Fortran*. Cambridge University Press, Cambridge, UK, 1992.

[112] L. N. Kantorovich. Thermoelastic properties of perfect crystals with non- primitive lattices. *Physical Review B*, 51:3520–2534, 1995.

[113] N. L. Allan, T. H. K. Barron, and J. A. O. Bruno. The zero static internal stress approximation in lattice dynamics, and the calculation of isotope effects on molar volumes. *Journal of Chemical Physics*, 195:8300–8303, 1996.

[114] M. E. G. Valerio, R. A. Jackson, and J. F. d. Lima. Derivation of potentials for the rare-earth fluorides, and the calculation of lattice and intrinsic defect properties. *Journal of Physics: Condensed Matter*, 12:7727, 2000.

[115] M. V. Rezende, M. E.G. Valerio, and R. A. Jackson. Modelling the concentration dependence of rare earth doping in inorganic materials for optical applications: Application to rare earth doped barium aluminate. *Optical Materials*, 34(1):109–118 2011.

[116] R. A. Jackson and M. E. G. Valerio. In preparation. 2014.

[117] P. W. Tasker. The stability of ionic crystal surfaces. *Journal of Physics C: Solid State Physics*, 4977, 1979.

[118] W. C. Mackrodt and R. F. Stewart. Defect properties of ionic solids. II. Point defect energies based on modified electron-gas potentials. *Journal of Physics C: Solid State Physics*, 12(3):431–449 1979.

[119] E. A. Colbourn, W. C. MacKrodt, and P. W. Tasker. The segregation of calcium ions at the surface of magnesium oxide: theory and calculation. *Journal of Materials Science*, 18(7):1917–1924 1983.

[120] P. W. Tasker and D. M. Duffy. The structure and properties of the stepped surfaces of MgO and NiO. *Surface Science*, 137:91–102, 1984.

[121] P. J. Lawrence, S. C. Parker, and P. W. Tasker. Computer modelling of the defect properties of chromium III oxide. *Advances in Ceramics*, 23:247–256, 1987.

[122] P. M. Oliver, S. C. Parker, and W. C. Mackrodt. Computer simulation of the crystal morphology of NiO. *Modelling and Simulation in Materials Science and Engineering*, 1(5):755–760 1993.

[123] P. M. Oliver, G. W. Watson, and S. C. Parker. Molecular dynamics simulations of nickel oxide surfaces. *Physical Review B*, 52:5323–5329, 1995.

[124] D. M. Duffy and P. W. Tasker. Computer simulation of 001 tilt grain boundaries in nickel oxide. *Philosophical Magazine A*, 47(6):817–825 1983.

[125] D. M. Duffy and P. W. Tasker. Computer simulation of 011 tilt grain boundaries in nickel oxide. *Philosophical Magazine A*, 48(1):155–162 1983.

[126] G. W. Watson, E. T. Kelsey, N. H. De Leeuw, D. J. Harris, and S. C. Parker. Atomistic simulation of dislocations, surfaces and interfaces in MgO. *Journal of the Chemical Society Faraday Transactions*, 92(3):433, 1996.

[127] D. H. Gay and A. L. Rohl. MARVIN - A new computer code for studying surfaces and interfaces and its application to calculating the crystal morphlogies of corundum and zircon. *Journal of the Chemical Society Faraday Transactions*, 91:925–936, 1995.

[128] D.E. Parry. The electrostatic potential in the surface region of an ionic crystal. *Surface Science*, 49(2):433–440 1975.

[129] P. Hartman and P. Bennema. The attachment energy as a habit controlling factor. *Journal of Crystal Growth*, 49(1):145–156 1980.

[130] N. H. de Leeuw. *Computer Methods in Mineralogy and Geochemistry*, volume 4. Madrid, 2008.

[131] J. W. Gibbs. *Collected Works*. Longman Group Limited, New York, 1928.

[132] G. Wulff. Zur Frage der Geschwindigkeit des Wachstums und der Auflosung der Krystallflachen. *Z Kristallogr Kristall- geom*, 34(949), 1901.

[133] N. H. de Leeuw and S. C. Parker. Surface Structure and Morphology of Calcium Carbonate Polymorphs Calcite, Aragonite, and Vaterite: An Atomistic Approach. *The Journal of Physical Chemistry B*, 102(16):2914–2922 1998.

[134] P. Masri and P. W. Tasker. Surface phonons and surface reconstruction and calcium-doped magnesium oxide. *Surface Science*, 149:209–225, 1985.

[135] J. H. Harding. Defects, Surfaces and Interfaces. In C. R. A. Catlow, editor, *Computer Modelling in Inorganic Crystallography*, chapter 7. Academic Press, 1997.

[136] C. F. Woensdregt. Computation of surface energies in an electrostatic point-charge model. Application to zircon (ZrSiO4). *Physics and Chemistry of Minerals*, 19:52–69, 1992.

[137] M. J. Davies, P. R. Kenway, P. J. Lawrence, S. C. Parker, William C. Mackrodt, and P. W. Tasker. Impurity segregation to the surfaces of corundum-structured oxides. *Journal of the Chemical Society, Faraday Transactions 2*, 85(5):555, 1989.

[138] M. J. Davies. *Computer simulation of oxide surfaces and grain boundaries.* PhD thesis, University of Bath, 1992.

[139] D. McLean. *Grain boundaries in metals.* Clarendon Press, London, UK, 1957.

[140] S. C. Parker, D. J. Cooke, S. Kerisit, A. S. Marmier, S. L. Taylor, and S. N. Taylor. From HADES to PARADISEatomistic simulation of defects in minerals. *Journal of Physics: Condensed Matter*, 16(27):S2735–S2749 2004.

[141] T. X. T. Sayle, S. C. Parker, and C. R. A. Catlow. Surface Segregation of Metal Ions in Cerium Dioxide. *The Journal of Physical Chemistry*, 98(51):13625–13630 1994.

[142] P. R. Kenway, S. C. Parker, and W. C. Mackrodt. Alkaline Earth Impurity Segregation at the Basal {0001} and Prism {1010} Surfaces of α-Al2O3. *Molecular Simulation*, 4(1-3):175–185 1989.

[143] U. Aschauer, P. Bowen, and S. C. Parker. Atomistic Modeling Study of Surface Segregation in Nd:YAG. *Journal of the American Ceramic Society*, 89(12):3812–3816 2006.

[144] M. Alfredsson, F. Corà, D. P. Dobson, J. Davy, J. P. Brodholt, S. C. Parker, and G. D. Price. Dopant control over the crystal morphology of ceramic materials. *Surface Science*, 601(21):4793–4800 2007.

[145] E. Garcia and R. R Ryan. Structure of the laser host material LiYF4. *Acta crystallographica. Section C, Crystal structure communications*, 49:2053–2054, 1993.

[146] M. Schellhorn. High-power diode-pumped Tm:YLF laser. *Applied Physics B*, 91(1):71–74 2008.

[147] A. L. Harmer, A. Linz, D. Gabbe, L. Gillespie, G. M. Janney, and E. Sharp. Fluorescence of Nd3+ in lithium yttrium fluoride. *Bulletin of the American Physical Society*, 12:1068, 1967.

[148] T. M. Pollack, W. F. Wing, R. I. Grasso, E. P. Chicklis, and H. P. Jensenn. . *IEEE Journal of Quantum Electronics*, QE_18(159), 1982.

[149] Example of commerial Nd:YLF laser; http://www.redoptronics.com/Nd-YLF-crystal.html Accessed May 2010.

[150] D. J. Ehrlich, P. F. Moulton, and R. M. Osgood, Jr. Ultraviolet solid-state Ce:YLF laser at 325 nm. *Optics Letters*, 4(6):184 1979.

[151] F. Okada, S. Togawa, and K. Ohta. Solid-state ultraviolet tunable laser: A Ce3+ doped LiYF4 crystal. *Journal Applied Physics*, 75(1):49–54, 1994.

[152] T. Yosida, M. Yamaga, D. Lee, and T. P. J. Han. The electron spin resonance and optical spectra of in. *Journal of Physics:*, 3733, 1997.

[153] Sonia Licia Baldochi, Kiyoshi Shimamura, Kenji Nakano, Na Mujilatu, and Tsuguo Fukuda. Ce-doped LiYF4 growth under CF4 atmosphere. *Journal of Crystal Growth*, 205(4):537–542 1999.

[154] A. Brenier, J. Rubin, R. Moncorge, and C. Pedrini. Excited-state dynamics of the Tm3+ ions and Tm3+ Ho3+ energy transfers in LiYF4. *Journal de Physique*, 50(12):1463–1482, 1989.

[155] L. Tarelho, L. Gomes, and I. Ranieri. Determination of microscopic parameters for nonresonant energy-transfer processes in rare-earth-doped crystals. *Physical Review B*, 56(22):14344–14351 1997.

[156] M. Falconieri and G. Salvetti. Effects of co-dopant concentrations and excitation conditions on the 2 ?m fluorescence dynamics in Tm, Ho:YLF crystals. *Applied Physics A Solids and Surfaces*, 59(3):253–258 1994.

[157] I. M. Ranieri, N. U. Wetter, S. L. Baldochi, L. Gomes, W. De Rossi, L. C. Courrol, E. A. Barbosa, E. P. Maldonado, and S. P. Morato. Laser development of rare-earth doped crystals. *Journal of Alloys and Compounds*, 344:231–239, 2002.

[158] A.M.E. Santo, A.F.H. Librantz, L. Gomes, P.S. Pizani, I.M. Ranieri, N.D. Vieira, and S.L. Baldochi. Growth and characterization of LiYF4:Nd single crystal fibres for optical applications. *Journal of Crystal Growth*, 292(1):149–154 2006.

[159] Y. F. Lü, J. Xia, X. H. Zhang, A. F. Zhang, J. G. Wang, L. Bao, and X. D. Yin. High-efficiency direct-pumped Nd:YLF laser operating at 1321 nm. *Applied Physics B*, 98(2-3):305–309 2009.

[160] N. U. Wetter and A. M. Deana. Diode-side-pumped Nd:YLiF 4 laser emitting at 1053 nm with 53.6% optical efficiency and diffraction-limited beam quality. *Laser Physics Letters*, 10(3):035807 2013.

[161] P. Lacovara, H. K. Choi, C. A. Wang, R. L. Aggarwal, and T. Y. Fan. Room-temperature diode-pumped Yb:YAG laser. *Optics Letters*, 16(14):1089 1991.

[162] T.Y. Fan. Heat generation in Nd:YAG and Yb:YAG. *IEEE Journal of Quantum Electronics*, 29(6):1457–1459 1993.

[163] U. Brauch, A. Giesen, M. Karszewski, Chr. Stewen, and A. Voss. Multiwatt diode-pumped Yb:YAG thin disk laser continuously tunable between 1018 and 1053 nm. *Optics Letters*, 20(7):713 1995.

[164] N. Coluccelli, G. Galzerano, L. Bonelli, a. Toncelli, a. Di Lieto, M. Tonelli, and P. Laporta. Room-temperature diode-pumped Yb3+-doped LiYF4 and KYF4 lasers. *Applied Physics B*, 92(4):519–523 2008.

[165] V. N. Makhov, N. M. Khaidukov, N. Y. Kirikova, M. Kirm, J. C. Krupa, T. V. Ouvarova, and G. Zimmerer. VUV emission of rare-earth ions doped into Fluoride crystals. *Journal of Luminescence*, 89:1005–1007, 2000.

[166] K. Ogasawara, S. Watanabe, H. Toyoshima, T. Ishii, M. G. Brik, H. Ikeno, and I. Tanaka. Optical spectra of trivalent lanthanides in LiYF4 crystal. *Journal of Solid State Chemistry*, 178(2):412–418 2005.

[167] J. Yin, Y. Hang, and L. Zhang. Ab initio calculations of electronic structures of LiYF4 crystals containing F-type color centers. *Optical Materials*, 32(1):194–197 2009.

[168] J. Yin, Q. Zhang, T. Liu, X. Guo, M. Song, X. Wang, and H. Zhang. Ab initio lattice relaxation and electronic structures of LiYF4 crystals containing VF color center. *Physica B: Condensed Matter*, 404(8-11):1053–1057 2009.

[169] J. Yin, Y. Hang, L. Zhang, C. Zhao, J. Xiong, and P. Hu. Origin of the 330nm absorption band and effect of doping Yb in LiYF4 crystals. *Journal of Luminescence*, 130(8):1338–1342 2010.

[170] D. V. Seletskiy, S. D. Melgaard, R. I. Epstein, A. Di Lieto, M. Tonelli, and M. Sheik-Bahae. Local laser cooling of Yb:YLF to 110 K. *Optics Express*, 19(19):18229–18236, 2011.

[171] P. Blanchfield and G. A. Saunders. The elastic constants and acoustic symmetry of LiYF 4. *Journal of Physics C: Solid State Physics*, 12(22):4673–4689 1979.

[172] R. A. Jackson and M. E. G. Valerio. in preparation. 2014.

[173] K. Kalisky. *The Physics and Engineering of Solid State Lasers*. PHI Learning Private Limited, 2006.

[174] N. J. O'Toole and V. A. Streltsov. Synchrotron X-ray analysis of the electron density in CoF 2 and ZnF 2. *Acta Crystallographica Section B Structural Science*, 57(2):128–135 2001.

[175] K. H. Jack and R. Maitland. The crystal structure and interatomic bonding of chromous and chromic fluorides. *Proceedings of the Chemical Society*, pages 232–232, 1957.

[176] J. E. Jorgensen, W. G. Marshall, and R. I. Smith. The compression mechanism of CrF3. *Acta crystallographica. Section B, Structural science*, 60(Pt 6):669–73 2004.

[177] Fritz Ebert and Hans Woitinek. Kristallstrukturen von Fluoriden. II. HgF, HgF2, CuF und CuF2. *Zeitschrift fur anorganische und allgemeine Chemie*, 210(3):269–272 1933.

[178] P. Fischer, W. Halg, D. Schwarzenbach, and H. Gamsjager. Magnetic and crystal structure of copper(II) fluoride. *Journal of Physics and Chemistry of Solids*, 35:1683–1689, 1974.

[179] W. Jauch, A. Palmer, and A. J. Schultz. Single-crystal pulsed neutron diffraction from NiF 2 and FeF 2 : the effect of magnetic order on the fluorine positions. *Acta Crystallographica Section B Structural Science*, 49(6):984–987 1993.

[180] M. A. Hepworth, K. H. Jack, R. D. Peacock, and G. J. Westland. The crystal structures of the trifluorides of iron, cobalt, ruthenium, rhodium, palladium and iridium. *Acta Crystallographica*, 10(1):63–69 1957.

[181] W. Jauch, G. J. McIntyre, and A. J. Schultz. Single-crystal neutron diffraction studies of MnF2 as a function of temperature: the effect of magnetostriction. *Acta Crystallographica Section B Structural Science*, 46(6):739–742 1990.

[182] F. Schroetter and B. G. Mueller. Zur Kristallstruktur von MnF3 und MnPtF6. *Zeitschrift fuer Anorganische und Allgemeine Chemie*, 619(8):1426–1430 1993.

[183] H. Sowa and H. Ahsbahs. Pressure-Induced Octahedron Strain in VF3-Type Compounds. *Acta Crystallographica Section B Structural Science*, 54(5):578–584 1998.

[184] M. M. R. Costa and M. J. M. de Almeida. Asphericity effects in the electron density of VF 2. *Acta Crystallographica Section B Structural Science*, 43(4):346–352 1987.

[185] Pawe E. Tomaszewski. Structural phase transitions in crystals. I. Database. *Phase Transitions*, 38(3):127–220 1992.

[186] K. J. Roberts, G. B. Telfer, R. A. Jackson, P. J. Wilde, and P. Meenan. Determination of a transferable interatomic potential for alkali-metal perchlorates and its application to morphological modelling. *Journal of the Chemical Society Faraday Transactions*, 91(22):4133–4138, 1995.

[187] R. D. Shannon. Revised effective ionic radii and systematic studies of interatomic distances in halides and chalcogenides. *Acta Crystallographica section A*, 32:751–767, 1976.

[188] D. J. Cooke, S. E. Redfern, and S. C. Parker. Atomistic simulation of the structure and segregation to the (0001) and surfaces of Fe2O3. *Physics and Chemistry of Minerals*, 31(8):507–517 2004.

[189] Claude Ederer and Nicola Spaldin. Origin of ferroelectricity in the multiferroic barium fluorides BaMF4: A first principles study. *Physical Review B*, 74(2):024102 2006.

[190] M. Eibschütz, H.J. Guggenheim, S.H. Wemple, I. Camlibel, and M. DiDomenico. Ferroelectricity in BaM2+F4. *Physics Letters A*, 29(7):409–410 1969.

[191] M. DiDomenico, M. Eibschütz, H.J. Guggenheim, and I. Camlibel. Dielectric behavior of ferroelectric BaMF4 above room temperature. *Solid State Communications*, 7(16):1119–1122 1969.

[192] E. T. Keve. Crystal Structure of Pyroelectric Paramagnetic Barium Manganese Fluoride, BaMnF4. *The Journal of Chemical Physics*, 51(11):4928, 1969.

[193] F Gingl. BaMgF4 and Ba2Mg3F10: New examples for structural relationships between hydrides and fluorides. *Zeitschrift fur anorganische und allgemeine Chemie*, 623(1-6):705–709, 1997.

[194] K. Shimamura, E. Villora, K. Muramatsu, and N. Ichinose. Advantageous growth characteristics and properties of compared with for UV/VUV nonlinear optical applications. *Journal of Crystal Growth*, 275(1-2):128–134 2005.

[195] S. C. Buchter, T. Y. Fan, V. Liberman, J. J. Zayhowski, M. Rothschild, E. J. Mason, A. Cassanho, H. P. Jenssen, and J. H. Burnett. Periodically poled BaMgF_4 for ultraviolet frequency generation. *Optics Letters*, 26(21):1693 2001.

[196] K. Shimamura. Growth and characteristics of optical single crystals for UV/VUV applications. *Journal of Fluorine Chemistry*, 132:1040–1046, 2011.

[197] Tomoki Hayashi, Makoto Yoshihara, Syun-ichiro Ohmi, Eisuke Tokumitsu, and Hiroshi Ishiwara. Electrical properties of ferroelectric BaMgF4 films grown on GaAs substrates using AlGaAs buffer layer. *Applied Surface Science*, 117-118(418):418–422 1997.

[198] S. Sinharoy. Growth and characterization of ferroelectric BaMgF4 films. *Journal of Vacuum Science & Technology A: Vacuum, Surfaces, and Films*, 9(3):409 1991.

[199] N. Kodama. Optical and structural studies on BaMgF4:Ce3+ crystals. *Journal of Crystal Growth*, 229(1-4):492–496 2001.

[200] E. Hayashi, K. Ito, S. Yabashi, M. Yamaga, N. Kodama, S. Ono, and N. Sarukura. Vacuum ultraviolet and ultraviolet spectroscopy of BaMgF4 codoped with Ce3+ and Na+. *Journal of Luminescence*, 119-120:69–74 2006.

[201] S. Kuck and I. Sokolska. Observation of photon cascade emission in Pr 3 -doped LuF3 and BaMgF4. *Chemical Physics Letters*, 364(October):273–278, 2002.

[202] J. V. Garcia-Santizo, B. del Rosal, M. O Ramirez, L. E. Bausa, E. G. Villora, P. Molina, V. Vasyliev, and K. Shimamura. Optical spectroscopy of Yb3+ centers in BaMgF4 ferroelectric crystal. *Journal of Applied Physics*, 110(6):063102, 2011.

[203] J. E. Muñoz Santiuste, H. Loro, R. Marino, Ph. Goldner, V. Vasyliev, E. G. Víllora, K. Shimamura, P. Molina, M. O. Ramírez, and L. E. Bausá. Local environment of optically active Nd^{3+} ions in the ultratransparent BaMgF_{4} ferroelectric crystal. *Physical Review B*, 85(18):184110 2012.

[204] H. E. Huang, Z. S. Lin, L. Bai, R. He, and C. T. Chen. Mechanism of the linear and nonlinear optical effects of SrAlF5 and BaMgF4 crystals. *Solid State Communications*, 150(47-48):2318–2321 2010.

[205] S. Watanabe, T. Ishii, K. Fujimura, and K. Ogasawara. First-principles relativistic calculation for 4f5d transition energy of Ce3+ in various fluoride hosts. *Journal of Solid State Chemistry*, 179(8):2438–2442 2006.

[206] S. Janssens, G.V.M. Williams, and D. Clarke. Synthesis and characterization of rare earth and transition metal doped BaMgF4 nanoparticles. *Journal of Luminescence*, 134:277–283 2013.

[207] E. N. Melchakov, M. A. Petrova, I. G. Podkolzina, P. A. Rodnyi, and M. A. Terekhin. Intrinsic luminescence of BaLiF3 and BaMgF4 crystals. *Optics and Spectroscopy*, 69:481–482, 1990.

[208] C. E. W. van Eijk, J. Andrieseen, P. Dorenbos, J. Jansons, N. M. Khaidukov, Z. Rachko, and J. Valbis. *Heavy scintillators for scientific and industrial applications*. 1993.

[209] J. Jansons, Z. Rachko, J. Valbis, J Andriessen, P. Dorenbos, C W E van Eijk, and N. M. Khaidukov. Cross-luminescence of complex halide crystals. *Journal of Physics: Condensed Matter*, 5(10):1589–1596 1993.

[210] T. Yanagida, N. Kawaguchi, Y. Fujimoto, M. Sugiyama, Y. Furuya, K. Kamada, Y. Yokota, A. Yoshikawa, and V. Chani. Growth and scintillation properties of BaMgF4. *Nuclear Instruments and Methods in Physics Research Section A: Accelerators, Spectrometers, Detectors and Associated Equipment*, 621(1-3):473–477 2010.

[211] J. M. Posse, K. Friese, and A. Grzechnik. Structural stability of BaMF4 (M = Mg, Zn and Mn) at high pressures. *Journal of physics. Condensed matter : an Institute of Physics journal*, 23(21):215401 2011.

[212] D. F. Nelson, editor. *Second and Higher Order Elastic Constants*, volume 29a of *Landolt-Börnstein - Group III Condensed Matter*. Springer-Verlag, Berlin/Heidelberg, 1992.

[213] R. A. Jackson, T. E. Littleford, G. E. Newby, and D. F. Plant. Computer modelling of rare earth doping in BMF and YLF. *IOP Conference Series: Materials Science and Engineering*, 15:012048 2010.

[214] T. E. Littleford, R. A. Jackson, and M. S.D. Read. An atomistic surface simulation study predicting morphologies and segregation in yttrium lithium fluoride. *Surface Science*, 606(19-20):1550–1555 2012.

[215] T. E. Littleford, R. A. Jackson, and M. S. D. Read. An atomistic simulation study of the effect of dopants on the morphology of YLiF 4. *physica status solidi (c)*, 10(2):156–159 2013.

[216] T. E. Littleford, R. A. Jackson, and M. S. D. Read. Modelling rare-earth doped BaMgF 4 : a potential laser material. *physica status solidi (c)*, 10(2):153–155 2013.

[217] M. P. Hehlen, W. L. Boncher, S. D. Melgaard, M. W. Blair, R. A. Jackson, T. E. Littleford, and S. P. Love. Preparation of high-purity LiF, YF3, and YbF 3 for laser refrigeration. In Richard I. Epstein, Denis V. Seletskiy, and Mansoor Sheik-Bahae, editors, *SPIE Proceedings*, page 900004 2014.

[218] T. E. Littleford and R. A. Jackson. The impact of rare earth doping on the crystal morphology of Yttrium Lithium Fluoride. *Surface Science*, in prep, 2014.

Appendix 1: $BaMgF_4$ surface results

Rare earth doping defect segregation

The following tables list the defect formation energies for each rare-earth ions and the charge compensation methods at the first four surface sites and at a bulk value. These are corrected using a the factor given to bring them inline with bulk defect formation values from GULP and are used to produce the segregation energy at that depth. Positions highlighted in red are the sites used to in the defect cluster. The values in blue are to indicate which Mg cation site is used in those schemes where more than one Mg site is required.

La: $RE^{\cdot}_{Ba} + V''_{Mg}$

Surface (010)

Position/Å	E(RE$_{Ba}$) /eV	E$_{seg}$ /eV	Position /Å	E(V$_{Mg}$) /eV	E$_{seg}$ /eV
3.322	−24.41	−3.03	0.667	22.09	−3.06
6.115	−24.03	−2.65	2.226	25.20	0.05
10.485	−21.33	0.05	7.189	25.81	0.66
13.593	−21.36	0.01	14.372	25.53	0.38
Bulk	−21.38	-	Bulk	25.15	-
Correction 0.34 eV			Correction 1.12 eV		

Surface (100)

Position /Å	E(RE$_{Ba}$) /eV	E$_{seg}$ /eV	Position /Å	E(V$_{Mg}$) /eV	E$_{seg}$ /eV
0.145	−21.70	−0.32	0.152	23.79	−1.36
1.996	−21.28	0.10	0.269	23.49	−1.66
2.081	−21.45	−0.07	1.920	24.51	−0.64
4.075	−21.58	−0.20	2.247	23.62	−1.53
Bulk	−21.38	-	Bulk	25.15	-
Correction 0.85 eV			Correction −1.26 eV		

Surface (110)

Position /Å	E(RE$_{Ba}$) /eV	E$_{seg}$ /eV	Position /Å	E(V$_{Mg}$) /eV	E$_{seg}$ /eV
0.331	−21.94	−0.56	1.984	22.18	−2.97
1.279	−20.98	0.40	1.684	22.58	−2.57
1.398	−21.83	−0.45	3.072	22.99	−2.16
3.821	−21.76	−0.38	2.791	24.22	−0.93
Bulk	−21.38	-	Bulk	25.15	-
Correction −0.80 eV			Correction 2.02 eV		

La cluster

	(010)		(100)		(110)	
	E($_{cluster}$)/eV	E$_{seg}$ /eV	E($_{cluster}$) /eV	E$_{seg}$ /eV	E($_{cluster}$) /eV	E$_{seg}$ /eV
Surface	−22.08	−2.94	−19.69	−0.55	−21.34	−2.20
Bulk	−19.14	-	−19.14	-	−19.14	-
	Correction0.22 eV		Correction 0.39 eV		Correction 0.44 eV	

Ce 1: $RE^{\cdot}_{Ba} + V''_{Mg}$

Surface (010)

Position /Å	E(RE$_{Ba}$) /eV	E$_{seg}$ /eV
3.322	−25.54	−2.75
6.115	−26.32	−3.53
10.485	−22.74	0.05
13.593	−22.75	0.04
Bulk	−22.79	-
Correction 0.66 eV		

Surface (100)

Position /Å	E(RE$_{Ba}$) /eV	E$_{seg}$ /eV
0.145	−23.24	−0.45
1.996	−22.78	0.01
2.081	−22.92	−0.13
4.075	−23.30	−0.51
Bulk	−22.79	-
Correction 1.85 eV		

Surface (110)

Position /Å	E(RE$_{Ba}$) /eV	E$_{seg}$ /eV
0.331	−23.50	−0.71
1.279	−23.34	−0.55
1.398	−23.52	−0.73
3.821	−23.17	−0.38
Bulk	−22.79	-
Correction 0.19 eV		

Ce cluster

	(010)		(100)		(110)	
	E($_{cluster}$) /eV	E$_{seg}$ /eV	E($_{cluster}$) /eV	E$_{seg}$ /eV	E($_{cluster}$) /eV	E$_{seg}$ /eV
Surface	−24.42	−4.48	−20.93	−0.99	22.14	−2.20
Bulk	−19.14	-	−19.14	-	−19.14	-
	Correction 0.22 eV		Correction 0.31 eV		Correction 0.46 eV	

Pr 1: $RE^{\cdot}_{Ba} + V''_{Mg}$

Surface (010)

Position /Å	E(RE$_{Ba}$) /eV	E$_{seg}$ /eV
3.322	−26.10	−3.90
6.115	−24.44	−2.24
10.485	−22.15	0.05
13.593	−22.16	0.04
Bulk	−22.79	-
Correction−0.35 eV		

Surface (100)

Position /Å	E(RE$_{Ba}$) /eV	E$_{seg}$ /eV
0.145	−22.79	−0.59
1.996	−22.29	−0.09
2.081	−22.40	−0.20
4.075	−22.75	−0.55
Bulk	−22.79	-
Correction 0.84 eV		

Surface (110)

Position /Å	E(RE$_{Ba}$) /eV	E$_{seg}$ /eV
0.331	−22.71	−0.51
1.279	−23.20	−1.00
1.398	−23.01	−0.81
3.821	−22.61	−0.41
Bulk	−22.20	-
Correction−0.81 eV		

Pr cluster

	(010)		(100)		(110)	
	E($_{cluster}$) /eV	E$_{seg}$ /eV	E($_{cluster}$) /eV	E$_{seg}$ /eV	E($_{cluster}$) /eV	E$_{seg}$ /eV
Surface	−25.18	−4.44	−21.91	−1.17	−24.21	−3.46
Bulk	−20.74	-	−20.74	-	−20.74	-
	Correction 0.24 eV		Correction 0.24 eV		Correction 0.49 eV	

Nd: $RE_{Ba}^{\cdot} + V_{Mg}^{''}$

Surface (010)

Position /Å	E(RE$_{Ba}$) /eV	E$_{seg}$ /eV
3.322	−26.10	−3.90
6.115	−24.44	−2.24
10.485	−22.15	0.05
13.593	−22.16	0.04
Bulk	−22.79	-
Correction −0.35 eV		

Surface (100)

Position /Å	E(RE$_{Ba}$) /eV	E$_{seg}$ /eV
0.145	−23.31	−0.69
1.996	−22.78	−0.16
2.081	−22.89	−0.27
4.187	−23.20	−0.58
Bulk	−22.62	-
Correction 0.84 eV		

Surface (110)

Position /Å	E(RE$_{Ba}$) /eV	E$_{seg}$ /eV
0.331	−23.13	−0.51
1.279	−23.62	−1.00
1.398	−23.43	−0.81
3.821	−23.03	−0.41
Bulk	−22.62	-
Correction −0.39 eV		

Nd cluster

	(010)		(100)		(110)	
	E($_{cluster}$)/eV	E$_{seg}$ /eV	E($_{cluster}$) /eV	E$_{seg}$ /eV	E($_{cluster}$) /eV	E$_{seg}$ /eV
Surface	−27.08	−5.36	−23.68	−1.99	−27.04	−5.39
Bulk	−21.68	-	−21.68	-	−21.68	-
	Correction 0.66 eV		Correction 0.30 eV		Correction 0.67 eV	

Sm: $RE_{Mg}^{\cdot} + V_{Ba}^{''}$

Surface (010)

Position /Å	E(RE$_{Mg}$) /eV	E$_{seg}$ /eV	Position /Å	E(V$_{Ba}$) /eV	E$_{seg}$ /eV
0.667	−19.88	−3.07	3.322	15.76	−3.47
2.226	−21.52	−4.71	6.388	18.72	−0.51
7.189	−16.71	0.10	10.485	19.61	0.39
9.689	−16.85	−0.04	13.593	19.42	0.19
Bulk	−16.81	-	Bulk	19.23	-
Correction −0.27 eV			Correction 1.22 eV		

Surface (100)

Position /Å	E(RE$_{Mg}$) /eV	E$_{seg}$ /eV	Position /Å	E(V$_{Ba}$) /eV	E$_{seg}$ /eV
0.152	−18.51	−1.70	0.145	17.33	−1.90
0.269	−17.96	−1.15	1.996	19.18	−0.05
2.247	−17.62	−0.50	2.081	17.38	−1.85
4.216	−17.87	−1.06	4.075	19.05	−0.18
Bulk	−16.81	-	Bulk	19.23	-
Correction 0.95 eV			Correction −1.17 eV		

Surface (110)

Position /Å	E(RE$_{Mg}$) /eV	E$_{seg}$ /eV	Position /Å	E(V$_{Ba}$) /eV	E$_{seg}$ /eV
1.984	−17.85	−1.04	0.331	15.85	−3.38
1.684	−18.53	−1.72	1.279	18.76	−0.47
3.072	-17.35	−0.54	1.398	17.79	−1.44
2.791	−18.34	−1.53	3.821	17.73	−1.50
Bulk	−16.81	-	Bulk	19.23	-
Correction −0.74 eV			Correction 2.13 eV		

Sm cluster

	(010)		(100)		(110)	
	E($_{cluster}$) /eV	E$_{seg}$ /eV	E($_{cluster}$) /eV	E$_{seg}$ /eV	E($_{cluster}$) /eV	E$_{seg}$ /eV
Surface	−23.27	−7.38	−18.99	−3.09	−20.70	−4.80
Bulk	−15.89	-	−15.89	-	−15.89	-
	Correction 0.71 eV		Correction 0.19 eV		Correction 0.19 eV	

Gd: $RE^{\cdot}_{Mg} + V''_{Ba}$

Surface (010)

Position /Å	E(RE_{Mg}) /eV	E_{seg} /eV
0.667	−21.07	−3.05
2.226	−21.46	−3.44
7.189	−17.97	0.09
9.689	−18.03	−0.01
Bulk	−18.02	-
Correction −0.34 eV		

Surface (100)

Position /Å	E(RE_{Mg}) /eV	E_{seg} /eV
0.152	−19.21	−1.19
0.269	−19.07	−1.05
2.247	−18.36	−0.34
4.216	−18.55	−0.906
Bulk	−18.02	-
Correction 0.87 eV		

Surface (110)

Position /Å	E(RE_{Mg}) /eV	E_{seg} /eV
1.984	−18.86	−0.84
1.684	−19.65	−1.63
3.072	−18.78	−0.76
2.791	−19.04	−1.02
Bulk	−18.02	-
Correction −0.81eV		

Gd cluster

	(010)		(100)		(110)	
	E($_{cluster}$) /eV	E_{seg} /eV	E($_{cluster}$) /eV	E_{seg} /eV	E($_{cluster}$) /eV	E_{seg} /eV
Surface	−23.50	−5.01	−21.94	−3.44	−23.32	−4.83
Bulk	−18.50	-	−18.50	-	−18.50	-
	Correction 0.72 eV		Correction 0.26 eV		Correction 0.26 eV	

Tb 1: $RE^{\cdot}_{Mg} + V''_{Ba}$

Surface (010)

Position /Å	E(RE_{Mg}) /eV	E_{seg} /eV
0.667	−21.40	−3.19
2.226	−22.30	−4.09
7.189	−18.12	0.09
9.689	−18.19	0.02
Bulk	−18.17	-
Correction −0.34 eV		

Surface (100)

Position /Å	E(RE_{Mg}) /eV	E_{seg} /eV
0.152	−19.39	−1.18
0.269	−19.24	−1.03
2.247	−18.77	−0.56
4.216	−18.18	−0.84
Bulk	−18.21	-
Correction 0.87 eV		

Surface (110)

Position /Å	E(RE_{Mg}) /eV	E_{seg} /eV
1.984	−18.85	−0.64
1.684	−19.82	−1.61
3.072	−18.82	−0.61
2.791	−19.22	−1.01
Bulk	−18.21	-
Correction −0.81 eV		

Tb cluster

	(010)		(100)		(110)	
	E($_{cluster}$) /eV	E_{seg} /eV	E($_{cluster}$) /eV	E_{seg} /eV	E($_{cluster}$) /eV	E_{seg} /eV
Surface	−24.95	−6.08	−21.77	−2.90	−23.49	−4.62
Bulk	−18.87	-	−18.87	-	−18.87	-
	Correction 0.74 eV		Correction 0.27 eV		Correction 0.27 eV	

Tb 2: $RE_{Mg}^{\cdot} + V_{Mg}^{''}$

Tb cluster

	(010)		(100)		(110)	
	$E(_{cluster})$ /eV	E_{seg} /eV	$E(_{cluster})$ /eV	E_{seg} /eV	$E(_{cluster})$ /eV	E_{seg} /eV
Surface	−19.15	−6.33	−14.75	−1.93	−16.25	−3.99
Bulk	−12.82	-	−12.82	-	−12.82	-
	Correction 0.86 eV		Correction 0.60 eV		Correction 0.55 eV	

Dy: $RE^{\cdot}_{Mg} + V^{''}_{Mg}$

Surface (010)

Position /Å	E(RE_{Mg}) /eV	E_{seg} /eV
0.667	−21.88	−2.92
2.226	−23.04	−4.08
7.189	−18.87	0.09
9.689	−18.93	0.03
Bulk	−18.96	-
Correction −0.34 eV		

Surface (100)

Position /Å	E(RE_{Mg}) /eV	E_{seg} /eV
0.152	−20.32	−1.36
0.269	−19.93	−0.97
2.247	−19.15	−0.19
4.216	−19.40	−0.75
Bulk	−18.96	-
Correction 0.87 eV		

Surface (110)

Position /Å	E(RE_{Mg}) /eV	E_{seg} /eV
1.984	−19.69	−0.73
1.684	−20.64	−1.68
3.072	−19.68	−0.72
2.791	−19.93	−0.97
Bulk	−18.96	-
Correction −0.801 eV		

Dy cluster

	(010)		(100)		(110)	
	E($_{cluster}$) /eV	E_{seg} /eV	E($_{cluster}$) /eV	E_{seg} /eV	E($_{cluster}$) /eV	E_{seg} /eV
Surface	−20.28	−5.94	−16.79	−2.45	−17.56	−4.44
Bulk	−14.34	-	−14.34	-	−14.34	-
	Correction 0.91 eV		Correction 0.92 eV		Correction 1.22 eV	

Ho: $RE^{\cdot}_{Mg} + V''_{Ba}$

Surface (010)

Position /Å	E(RE_{Mg}) /eV	E_{seg} /eV
0.667	−24.07	−4.87
2.226	−22.31	−3.11
7.189	−19.11	0.09
9.689	−19.26	−0.06
Bulk	−19.20	-
Correction −0.35 eV		

Surface (100)

Position /Å	E(RE_{Mg}) /eV	E_{seg} /eV
0.152	−20.40	−1.20
0.269	−20.17	−0.97
2.247	−19.52	−0.32
4.216	−20.17	−0.97
Bulk	−19.20	-
Correction 0.87 eV		

Surface (110)

Position /Å	E(RE_{Mg}) /eV	E_{seg} /eV
1.984	−20.03	−0.83
1.684	−20.90	−1.70
3.072	−19.95	−0.75
2.791	−20.20	−1.00
Bulk	−19.20	-
Correction −0.81 eV		

Ho cluster

	(010)		(100)		(110)	
	E($_{cluster}$) /eV	E_{seg} /eV	E($_{cluster}$) /eV	E_{seg} /eV	E($_{cluster}$) /eV	E_{seg} /eV
Surface	−26.93	−5.80	−23.93	−3.06	−25.63	−4.77
Bulk	−20.86	-	−20.86	-	−120.86	-
	Correction 0.72 eV		Correction 0.33 eV		Correction 0.32 eV	

Er: $RE_{Mg}^{\cdot} + V_{Ba}^{''}$

Surface (010)

Position /Å	E(RE_{Mg}) /eV	E_{seg} /eV
0.667	−22.17	−2.47
2.226	−23.76	−4.06
7.189	−19.61	0.09
9.689	−19.67	0.03
Bulk	−19.70	-
Correction −0.34 eV		

Surface (100)

Position /Å	E(RE_{Mg}) /eV	E_{seg} /eV
0.152	−20.82	−1.12
0.269	−20.62	−0.92
2.247	−20.12	−0.42
4.216	−20.45	−0.75
Bulk	−19.20	-
Correction 0.87 eV		

Surface (110)

Position /Å	E(RE_{Mg}) /eV	E_{seg} /eV
1.984	−20.26	−0.56
1.684	−21.25	−1.55
3.072	−20.38	−0.68
2.791	−20.27	−0.69
Bulk	−19.70	-
Correction−0.81 eV		

Er cluster

	(010)		(100)		(110)	
	E($_{cluster}$) /eV	E_{seg} /eV	E($_{cluster}$) /eV	E_{seg} /eV	E($_{cluster}$) /eV	E_{seg} /eV
Surface	−27.15	−6.08	−24.66	−2.84	−26.72	−4.90
Bulk	−21.82	-	−21.82	-	−21.82	-
	Correction 0.75 eV		Correction 0.33 eV		Correction 0.33 eV	

Tm: $RE_{Mg}^{\cdot} + V_{Mg}^{''}$

Surface (010)

Position /Å	E(RE_{Mg}) /eV	E_{seg} /eV
0.667	−22.72	−2.57
2.226	−22.91	−2.76
7.189	−20.06	0.09
9.689	−20.11	0.04
Bulk	−20.15	-
Correction −0.34 eV		

Surface (100)

Position /Å	E(RE_{Mg}) /eV	E_{seg} /eV
0.152	−20.88	−0.73
0.269	−20.04	−0.89
2.247	−20.18	−0.03
4.216	−20.71	−0.34
Bulk	−20.15	-
Correction 0.87 eV		

Surface (110)

Position /Å	E(RE_{Mg}) /eV	E_{seg} /eV
1.984	−20.67	−0.52
1.684	−21.77	−1.62
3.072	−20.85	−0.70
2.791	−21.06	−0.91
Bulk	−20.15	-
Correction −0.80 eV		

Tm cluster

	(010)		(100)		(110)	
	E($_{cluster}$) /eV	E_{seg} /eV	E($_{cluster}$) /eV	E_{seg} /eV	E($_{cluster}$) /eV	E_{seg} /eV
Surface	−20.10	−3.34	−18.57	−1.18	−19.79	−3.03
Bulk	−16.76	-	−16.76	-	−16.76	-
	Correction 1.02 eV		Correction 0.93 eV		Correction 0.69 eV	

Yb: $RE_{Mg}^{\cdot} + V_{Ba}^{''}$

Surface (010)

Position /Å	E(RE$_{Mg}$) /eV	E$_{seg}$ /eV
0.667	−22.49	−2.35
2.226	−23.88	−3.74
7.189	−20.04	0.10
9.689	−20.11	0.03
Bulk	−20.14	-
Correction −0.34 eV		

Surface (100)

Position /Å	E(RE$_{Mg}$) /eV	E$_{seg}$ /eV
0.152	−21.18	−1.04
0.269	−21.04	−0.90
2.247	−20.36	−0.22
4.216	−20.95	−0.81
Bulk	−20.14	-
Correction 0.87 eV		

Surface (110)

Position /Å	E(RE$_{Mg}$) /eV	E$_{seg}$ /eV
1.984	−20.69	−0.55
1.684	−21.61	−1.47
3.072	−20.86	−0.72
2.791	−21.08	−0.94
Bulk	−20.14	-
Correction −0.80 eV		

Yb cluster

	(010)		(100)		(110)	
	E($_{cluster}$) /eV	E$_{seg}$ /eV	E($_{cluster}$) /eV	E$_{seg}$ /eV	E($_{cluster}$) /eV	E$_{seg}$ /eV
Surface	−27.58	−4.89	−25.38	−3.04	−27.60	−4.91
Bulk	−22.69	-	−22.69	-	−22.69	-
	Correction 0.75 eV		Correction 0.35 eV		Correction 0.35 eV	

Lu: $RE_{Mg}^{\cdot} + V_{Mg}^{''}$

Surface (010)

Position /Å	E(RE_{Mg}) /eV	E_{seg} /eV
0.667	−24.59	−3.36
2.226	−24.83	−3.60
7.189	−21.14	0.08
9.689	−21.18	0.04
Bulk	−20.89	-
Correction −0.34 eV		

Surface (100)

Position /Å	E(RE_{Mg}) /eV	E_{seg} /eV
0.152	−20.88	−0.73
0.269	−20.04	−0.89
2.247	−20.18	−0.03
4.216	−20.71	−0.34
Bulk	−20.15	-
Correction 0.87 eV		

Surface (110)

Position /Å	E(RE_{Mg}) /eV	E_{seg} /eV
1.984	−21.27	−0.38
1.684	−22.45	−1.60
3.072	−21.49	−0.60
2.791	−21.78	−0.89
Bulk	−20.89	-
Correction −0.80 eV		

Lu cluster

	(010)		(100)		(110)	
	E($_{cluster}$) /eV	E_{seg} /eV	E($_{cluster}$) /eV	E_{seg} /eV	E($_{cluster}$) /eV	E_{seg} /eV
Surface	−22.64	−4.37	−20.46	−2.20	−21.89	−3.63
Bulk	−18.26	-	−18.26	-	−18.26	-
	Correction 1.05 eV		Correction 0.94 eV		Correction 0.71 eV	

Appendix 2: Publications

The following publications have resulted from the work presented in this thesis. The list is correct at time of printing. Further publication may follow.

[213] R. A. Jackson, T. E. Littleford, G. E. Newby, and D. F. Plant. Computer modelling of rare earth doping in BMF and YLF. IOP Conference Series: Materials Science and Engineering, 15:012048, November 2010.

[214] T. E. Littleford, R. A. Jackson, and M. S.D. Read. An atomistic surface simulation study predicting morphologies and segregation in yttrium lithium fluoride. Surface Science, 606(19-20):15501555, October 2012.

[215] T. E. Littleford, R. A. Jackson, and M. S. D. Read. An atomistic simulation study of the effect of dopants on the morphology of YLiF 4. physica status solidi (c), 10(2):156159, February 2013.

[216] T. E Littleford, R. A Jackson, and M. S. D. Read. Modelling rare- earth doped BaMgF 4 : a potential laser material. physica status solidi (c), 10(2):153155, February 2013.

[217] M. P. Hehlen, W. L. Boncher, S. D. Melgaard, M. W. Blair, R. A. Jackson, T. E. Littleford, and S. P. Love. Preparation of high purity LiF, YF3, and YbF3 for laser refrigeration. SPIE Proceedings, page 900004 2014.

[218] T. E. Littleford and R. A. Jackson. The impact of rare earth doping on the crystal morphology of Yttrium Lithium Fluoride. Surface Science, in prep, 2014.